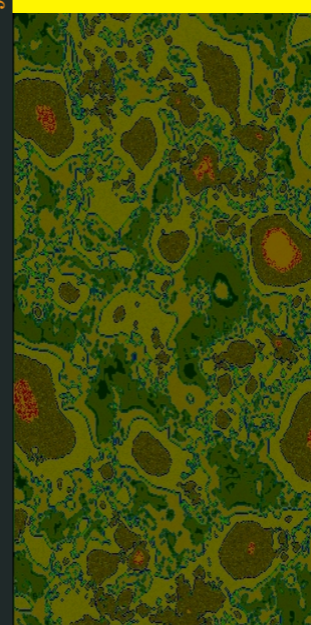
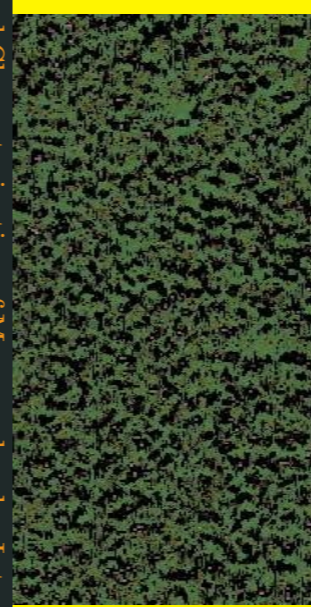


New Approaches in the Engineering and Characterization of Macromolecular Interfaces  
Across the Length Scales: Applications to Hydrophobic and Stimulus Responsive Polymers

Jing Song 2007

ISBN: 978-90-365-2592-3



# New Approaches in the Engineering and Characterization of Macromolecular Interfaces Across the Length Scales:

## Applications to Hydrophobic and Stimulus Responsive Polymers

Jing Song

**New Approaches in the Engineering and  
Characterization of Macromolecular  
Interfaces Across the Length Scales:  
Applications to Hydrophobic and Stimulus  
Responsive Polymers**

**Jing Song**



This research was financially supported by the Dutch Polymer Institute (DPI), PO Box 902, 5600AX Eindhoven, the Netherlands, Project nr. #335.

Samenstelling promotiecommissie:

Prof. dr. ing. D. H. A. Blank, voorzitter	Universiteit Twente
Prof. dr. ir. G. J. Vancso, promotor	Universiteit Twente
Prof. dr. ing. M. Wessling	Universiteit Twente
Prof. dr. ir. J. W. M. Noordermeer	Universiteit Twente
Prof. dr. ir. P. Schoenmakers	Universiteit van Amsterdam
Dr. J. F. L. Duval	CNRS
Dr. H. Hillborg	ABB/KTH

New Approaches in the Engineering and Characterization of Macromolecular Interfaces  
Across the Length Scales: Applications to Hydrophobic and Stimulus Responsive Polymers

By Jing Song  
Ph.D Thesis  
University of Twente, MESA+ Institute for Nanotechnology,  
Enschede, The Netherlands

Copyright © 2007 J. Song, Enschede, the Netherlands.  
All rights reserved.

Cover Design by Jing Song

Printed by Wöhrmann Print Service, 7202 CZ, Zutphen, The Netherlands

ISBN: 978-90-365-2592-3

**NEW APPROACHES IN THE ENGINEERING AND  
CHARACTERIZATION OF MACROMOLECULAR  
INTERFACES ACROSS THE LENGTH SCALES:  
APPLICATIONS TO HYDROPHOBIC AND STIMULUS  
RESPONSIVE POLYMERS**

**PROEFSCHRIFT**

ter verkrijging van  
de graad van doctor aan de Universiteit Twente,  
op gezag van de rector magnificus,  
prof. dr. W.H.M. Zijm,  
volgens besluit van het College van Promoties  
in het openbaar te verdedigen  
op woensdag 28 november 2007 om 15.00 uur

door

Jing Song  
geboren op 18 februari 1974  
te Tianjin, China

Dit proefschrift is goedgekeurd door:

Promotor: Prof. dr. G. J. Vancso

# Contents

<b>Chapter 1 Introduction</b> .....	1
1.1 Overview .....	1
1.2 Concept of this Thesis .....	3
<b>Chapter 2 Engineering, characterization and properties of polymer surfaces</b> .....	7
2.1 Phenomena, methods and materials relevant to this Thesis .....	8
2.1.1 Phenomena .....	8
2.1.1.1 Electrokinetic effects .....	8
2.1.1.2 Double layer model .....	8
2.1.1.3 DLVO theory.....	10
2.1.1.4 Surface mechanical properties of polymers.....	13
2.1.2 Methods.....	13
2.1.2.1 X-ray photoelectron spectroscopy (XPS) .....	14
2.1.2.2 Secondary ion mass spectroscopy (SIMS) .....	15
2.1.2.3 Fluorescence microscopy (FM).....	16
2.1.2.4 Zeta potential .....	17
2.1.3 Materials.....	18
2.1.3.1 Modification of polymer surfaces to enhance adhesion .....	18
2.2 Measuring adhesion from micro- to nanoscale contacts .....	19
2.2.1 Introduction .....	19
2.2.2 Surface forces.....	20
2.2.2.1 Intermolecular forces .....	20
2.2.2.2 Adhesive forces between surfaces .....	21
2.2.3 Adhesion.....	22
2.2.3.1 Thermodynamics of adhesion .....	22
2.2.3.2 Theoretical models of adhesion .....	24
2.2.3.3 Viscoelastic effects.....	29
2.2.3.4 Other factors affecting the adhesion.....	30
2.2.4 Fracture mechanics.....	32
2.2.4.1 Griffith criterion .....	32
2.2.4.2 Adhesion hysteresis .....	35
2.2.4.3 Stress intensity analysis .....	38

2.2.5 Adhesion characterization methods .....	39
2.2.5.1 Surface force apparatus (SFA) .....	39
2.2.5.2. Atomic force microscopy (AFM) .....	41
2.2.5.3. Adhesion testing device (ATD) .....	44
2.2.6 Friction and adhesion .....	46
2.2.7 Frontiers on polymer adhesion applications .....	47
2.2.7.1. High throughput of measurements .....	47
2.2.7.2. Surface patterns for adhesion control .....	47
2.2.7.3. Evaluating adhesion under water .....	48
2.2.8 Summary .....	48
<b>Chapter 3 Flame-treatment of low density polyethylene: Surface chemistry across the length scales .....</b>	<b>55</b>
3.1 Introduction .....	56
3.2 Results and discussion .....	58
3.2.1 Surface wettability .....	58
3.2.2 Surface chemistry modification .....	59
3.2.3 Nano/micro surface topography modification .....	66
3.2.4 Surface ionization state .....	69
3.2.5 Oxidation mechanism by flame-treatment .....	71
3.3 Conclusions .....	72
3.4 Experimental section .....	73
<b>Chapter 4 Effects of flame-treatment on the interfacial energy of LDPE assessed by contact mechanics .....</b>	<b>79</b>
4.1 Introduction .....	80
4.2 Adhesion (adherence) measurements by ATD .....	82
4.3 Results and discussion .....	85
4.4 Conclusions .....	95
4.5 Experimental section .....	95
4.5.1 ATD .....	95
4.5.2 PDMS lenses and flame-treated LDPE preparation .....	97
<b>Chapter 5 Surface ionization state and nanoscale chemical composition of UV-irradiated poly(dimethylsiloxane) probed by chemical force microscopy, force titration, and electrokinetic measurements .....</b>	<b>101</b>
5.1 Introduction .....	102
5.2 Results and discussion .....	104

5.2.1 Time-of flight (ToF)-SIMS .....	104
5.2.2 Adherence (force volume) imaging by AFM .....	106
5.2.3 Force titration .....	107
5.2.4 Surface $pK_a$ shift.....	112
5.2.5 Streaming potential experiments in NaCl solutions .....	115
5.2.6 Streaming potential experiments in phosphate buffer solutions.....	118
5.2.7 Comparison of the streaming potential and AFM results.....	120
5.3 Conclusions .....	123
5.4 Materials and methods .....	124
5.5 Appendix: Gouy-Stern double layer with site dissociation model.....	127
5.5.1 Classical Gouy-Stern double layer .....	127
5.5.2 Modeling with no specific ion adsorption .....	128
5.5.3 Modeling with specific ion adsorption.....	129
<b>Chapter 6 Contact mechanics of UV/ozone treated PDMS by AFM and ATD techniques: Mechanical performance from nanometer to micrometer length scales .....</b>	<b>135</b>
6.1 Introduction.....	136
6.2 Surface Young's modulus at a nanoscopic length scale .....	137
6.2.1 Young's modulus .....	141
6.3 Surface Young's modulus at a mesoscopic length scale.....	150
6.4 Bulk modulus .....	152
6.5 Analysis of the length scale effects .....	153
6.6 Conclusions .....	154
6.7 Experimental section.....	155
<b>Chapter 7 "Smart" organometallic polymer brushes: Switching friction by electrochemical redox stimuli.....</b>	<b>159</b>
7.1 Introduction.....	160
7.2 Tuning of tribological behavior of stimulus responsive PFS by electro-chemistry and its study using in situ electrochemical lateral force microscopy .....	162
7.2.1 Calibration of AFM friction force signals in liquid media .....	164
7.2.2 Nanotribology on PFS films.....	172
7.3 Dependence of adherence of stimulus responsive PFS on the electrical potential by electrochemical atomic force microscopy .....	176



7.4 Discussion .....	178
7.5 Conclusions .....	184
7.6 Experimental section .....	184
<b>Outlook</b> .....	189
<b>Summary</b> .....	191
<b>Samenvatting</b> .....	195
<b>Acknowledgements</b> .....	199
<b>Curriculum Vitae</b> .....	201
<b>Bibliography</b> .....	203
<b>List of abbreviation</b> .....	205

# Chapter 1

## Introduction

### 1.1 Overview

Polymers often exhibit good bulk characteristics in combination with poor surface properties.<sup>1-3</sup> These poor surface properties often limit their applications such as the use of plastic films as substrates for printing (printability),<sup>4</sup> for coatings,<sup>5</sup> as sealants<sup>6</sup> and in biomaterials technology (cell adhesion and biocompatibility of implants).<sup>7</sup> Mechanical wear, friction and the lubrication of surfaces play important roles in machines and in equipments with moving parts, as well as in biomedical devices such as hip joint implants.<sup>8</sup> Wettability can be used to determine (in addition to bulk properties) the performance of contact lenses, textile fibers (washing), and coating films.<sup>9</sup> In other words, the chemical and physical properties of polymer surfaces, such as the chemical composition, hydrophilicity, roughness, crystallinity, conductivity, lubricity, and cross-linking density are crucial factors in order to successfully attain many of these applications.<sup>3, 10-13</sup>

Advances in surface modification techniques have provided polymer surfaces with specific properties to suit the aforementioned applications without affecting the bulk properties. "Surface engineering" is a general term that includes all the techniques by which surface modification can be accomplished. These techniques contain both the more traditional methods, such as flame-treatment, corona treatment, chemical etching, as well as newer ones, such as ion implantation, laser beam melting, plasma modification and polymerization, hot embossing, UV treatment, metallization, sputtering, nano-imprint lithography, etc. These treatments have been applied in order to: 1) produce specific functional groups at a surface for particular interactions with other functional groups; 2) control the surface energy; 3) increase the hydrophobicity or hydrophilicity; 4) improve the chemical inertness; 5) introduce surface cross-linking; 6) remove weak boundary layers or contaminants; 7) modify the surface morphology by increasing or decreasing the surface crystallinity or roughness; 8) increase the

surface electrical conductivity; 9) increase the surface lubricity; 10) introduce designed topological patterns.<sup>1, 3, 10</sup>

Improvements in surface modification techniques cannot be achieved without an in-depth understanding of the chemical and physical properties of polymer surfaces. The nature and the concentration of the functional groups introduced by various surface modification techniques must be determined. Related information and knowledge will enhance our understanding of various surface modification mechanisms. Techniques commonly used for characterization of bulk properties are not always suitable and often display shortcomings. Generally, only the properties of the first few nanometers of a surface are significant in order to achieve the proper targets. X-ray photoelectron spectroscopy (XPS) (often referred to as electron spectroscopy for chemical analysis, ESCA) and secondary ion mass spectroscopy (SIMS) are two important techniques that provide information regarding the chemical composition and structure of a material's top layers. In SIMS, low energy ions are either scattered or stopped by the first few layers of surface atoms. Hence, its sampling depth is only a few angstroms. The sampling depth for XPS, which is determined by the kinetic energy of the emitted photoelectrons, is typically 1 to 10 nm, depending on the take-off angle. For other spectroscopic techniques, such as attenuated total internal-reflection (ATIR), the sampling depth can be up to 1  $\mu\text{m}$  or more. In addition, many other surface-sensitive techniques, such as atomic force microscopy (AFM), have been developed to analyze the outermost layers of polymer surfaces. Contact angle measurements are frequently used to characterize the surface free energy at the depth of a few atoms. Scanning electron microscopy (SEM) is employed to obtain information concerning the topography (outermost layer) as well as the chemical composition (energy dispersive X-ray (EDX) with a sampling depth of *ca.* 1  $\mu\text{m}$ ). Several important factors must be taken into consideration while choosing a surface analysis technique, namely, the sampling depth, surface information, analysis environment, and sample suitability.

The level of surface treatment must also be controlled if optimal results are to be obtained. Hence, it is obvious that polymer surfaces and modified surfaces must be characterized at a molecular level. Although a rapid development in surface analysis techniques during the last 10-20 years has allowed the characterization and investigation of composition and structure of surfaces with a sub-nanometer in-depth spatial resolution, there is still no single instrument or approach available that permits the investigation of the lateral distribution of functional groups and chemical composition on a molecular level. Hence, this

constitutes an area of active scientific interest. Chemical force microscopy (CFM), which uses chemically functionalized probing tips, promises to become a significant alternative in this area. In addition, AFM and adhesion testing device (ATD) can be used to study the nano- to micrometer surface mechanical properties.

Successful applications of surface-treated polymers are generally required to consider bridging information obtained at different length scales. For example, certain adhesion paradoxes have been unraveled, but many questions remain. One adhesion paradox is caused by the distance between interacting bodies. In a macroscopic case, the surfaces are covered with layers of "guest" atoms or contaminating molecules such as oxygen and water, which prevent a true atomic contact between the solid bodies. Moreover, surfaces are rough and jagged at the atomic or molecular scale. The adhesion forces between molecules are of short range, *i.e.* micrometers, so that large gaps exist thus reducing the surface interaction down to a lower value. In addition, Brownian motion, cracking, viscous deformation, *etc.*, lead to a rich variety of adhesion phenomena which may cause the macroscopic adhesion to vary, even though the molecular adhesion remains the same.<sup>14</sup> Thus, surface studies across different length scale are necessary.

Furthermore, various text books and reference articles concerning polymer surfaces have been published.<sup>1-3, 10-17</sup> Some of these focus on analytical techniques and instrumentation, others on surface treatment procedures, on surface forces, or on continuum properties. It is important to reveal the relationship among surface modification, surface analysis and application across a variety of length scales in order to obtain knowledge on surfaces corresponding to the reality.

## 1.2 Concept of this Thesis

The objective of the present Thesis is to test and control physico-chemical changes on modified hydrophobic and stimulus-responsive polymers across different length scales. Efforts have been made to control, characterize and assess the chemical composition of surface-treated polymers by various techniques such as XPS, time-of-flight secondary ion mass spectrometry (ToF-SIMS), CFM, electrochemical atomic force microscopy (ECAFM), and fluorescence microscopy. Electrokinetic properties of treated polymer surfaces were investigated by streaming potential techniques and an AFM force titration procedure.

Adhesion (adherence), friction and mechanical properties were studied by contact mechanics using a custom-built adhesion testing device (ATD), ECAFM, and AFM. Furthermore, a comparison of the techniques was carried out in order to understand the aforementioned properties of the treated polymers.

The scope of this work has been given in *chapter 1*. *Chapter 2* provides the background for the Thesis and presents an overview of surface modification and surface treatment methods with an emphasis on surface treatment for adhesion applications. The summarized aspects include surface force, thermodynamic *work of adhesion*, contact and fracture mechanics, as well as the effects of surface roughness and humidity. Three instruments of micro- and nano-adhesion measurements are also discussed. Finally, the new developments of adhesion applications in polymer science are reviewed.

*Chapter 3* describes the relationship between surface chemistry and morphology of flame-treated low density polyethylene (LDPE) by various characterization techniques across a variety of length scales. The surface concentration of hydroxyl, carbonyl and carboxyl groups, as a function of the number of flame-treatment passes (which is proportional to the treatment time) was obtained. In addition, surface topography of LDPE (before and after flame-treatment) was examined by AFM. Lastly, the ionization state of flame-treated LDPE surfaces was monitored by CFM.

*Chapter 4* demonstrates the effects of the flame-treatment of LDPE on the *work of adhesion* ( $W$ ) and *energy release rate* ( $G$ ) as assessed by a custom-built adhesion testing device (ATD). The *work of adhesion* was studied between an extracted PDMS lens prior to, and following UV/ozone treatment (PDMS and PDMS<sub>OX</sub>) and the LDPE films as a function of the flame-treatment number. A fracture mechanics approach was used to relate the applied load and the radius of the contact area to the energy release rate. Moreover, the difference of the hysteresis ( $G-W$ ) was systematically studied as a function of treatment numbers for both lens types. The origin of hysteresis was discussed.

Studies of the surface chemistry and ionization state of cross-linked poly(dimethylsiloxane) (PDMS) exposed to UV/ozone as a function of treatment time using various complementary and independent experimental techniques are presented in *chapter 5*. It was found that the top 1-2 nm surface layer was dominated by silanol groups ( $-SiOH$ ) for which the concentration increased with increasing treatment dose as unveiled by quantitative studies using ToF-SIMS. The lateral distributions of the silanol groups were analyzed at the

nanometer scale by CFM. The protolytic properties of an oxidized PDMS surfaces in the presence of sodium chloride and phosphate electrolytes were further analyzed by streaming potential measurements as a function of the UV/ozone treatment time. The electrokinetic data were quantitatively interpreted on the basis of a classical double layer model that combined the Gouy-Stern picture and the site dissociation theory.

*Chapter 6* presents the investigation of the Young's modulus of UV/ozone treated PDMS across different length scales. The nanoscale mechanical a property was studied by AFM with different continuum contact mechanics theories (the Hertz and JKR) as well as different tip shape models (spherical and hyperboloid). Moreover, a custom-built ATD set up was used to characterize the Young's modulus across a micrometer scale. Finally, the characteristic length scale effects on mechanical properties were studied.

*Chapter 7* describes quantitative AFM-based friction and adherence (adhesion) measurements between  $\text{Si}_3\text{N}_4$  tip and reversibly oxidized and reduced poly(ferrocenyldimethylsilane) (PFS) layer. AFM cantilever torsional calibration was performed by direct calibration method (the wedge calibration method) using a new calibration standard with fluid refraction corrections. Measurements of interfacial friction as a function of applied load on the nanoscale revealed a significant change in friction between the oxidized and reduced PFS layer. The average friction coefficient (0.47) and adherence (0.61 nN) between oxidized PFS and the  $\text{Si}_3\text{N}_4$  tip were found to be larger than those for neutral PFS (0.3 and 0.03 nN, respectively). Issues related to the interpretation of observed friction and adherence changes were discussed.

## References

- [1] Wu, S. H., *Polymer Interface and Adhesion*. Marcel Dekker: New York, 1982.
- [2] Cheery, B. W., *Polymer Surfaces*. Cambridge University Press: Cambridge, 1981.
- [3] Garbassi, F.; Morra, M.; Occhiello, E., *Polymer Surfaces: From Physics to Technology*. John Wiley & Sons: New York, 1998.
- [4] O'Hare, L. A.; Leadley, S.; Parbhoo, B., *Surf. Interface Anal.* **2002**, *33*, 335.
- [5] Pitt, W. G.; Lakenan, J. E.; Strong, A. B., *J. Appl. Polym. Sci.* **1993**, *48*, 845.
- [6] Richards, J. C., *Adhes. Age* **1970**, *13*, 22.
- [7] Lee, J. H.; Jung, H. W.; Kang, I. K.; Lee, H. B., *Biomaterials* **1994**, *15*, 705.
- [8] Beake, B. D.; Ling, J. S. G.; Leggett, G. J., *J. Mater. Chem.* **1998**, *8*, 2845.
- [9] Ou, S. H.; Ishida, H.; Lando, J. B., *J. Polym. Sci. Pol. Phys.* **1991**, *29*, 67.
- [10] Chan, C. M., *Polymer Surface Modification and Characterization*. Hanser Publishers: Munich, 1994.
- [11] Woodruff, D. P.; Delchar, T. A., *Modern Techniques of Surface Science*. 2nd ed.; Cambridge University Press: Cambridge, 1994.
- [12] Polymer Surfaces and Interfaces Series. In Feast, W. J.; Munro, H. S.; Richards, R. W., Eds. Wiley: Chichester, 1993; Vol. 2.
- [13] Jones, R. A. L.; Richards, R. W., *Polymers at Surfaces and Interfaces*. Cambridge University Press: Cambridge, 1999.
- [14] Kendall, K., *Molecular Adhesion and Its Applications*. Plenum Publishers: New York, 2001.
- [15] Adamson, A. W., *Physical Chemistry of Surfaces*. 5th ed.; John Wiley & Sons: New York, 1990.
- [16] Israelachvili, J. N., *Intermolecular and Surface Forces*. 2nd ed.; Academic Press: London, 1992.
- [17] *Principles of Colloid and Surface Chemistry*. In Hiemenz, P. C.; Rajagopalan, R., Eds. Marcel Dekker: New York, 1997.

# Chapter 2

## **Engineering, characterization and properties of polymer surfaces**

The present Thesis deals with the design, engineering, characterization and study of properties for a selection of polymer surfaces. In this *chapter*, details are provided regarding essential issues for the scientific and technological background necessary to introduce the scope and the state of the art within the chosen subject area. The aim has been to tackle problems which have been notoriously difficult to study until the recent advent of modern approaches to surface analysis as well as the availability of corresponding instrumentation. A high priority has been given to the investigation of adhesion and adherence across the length scales from micro to nanometer contact areas.

Due to the high relevance of this area, a whole section, *i.e.* 2.2, has been devoted to the physical principles and theories of polymer adhesion, and to the various experimental approaches used in adhesion studies. Atomic force microscopy (AFM), employed in the so-called "force volume" imaging mode was utilized to map the adherence force and could thus provide information concerning the nanoscale contact mechanics and adhesion. For the microscale contact, on the other hand, a dedicated adhesion testing device (ATD) had to be built. The underlying theories used to describe the ATD data are under current scientific development.

In the present Thesis, new data and approaches to cross the relevant length scales have been the subject of *chapters* 3-7. The custom-built ATD set up was employed in the studies focusing on microscale contact mechanics. These aspects justified the in-depth treatments provided in section 2.2.

In addition to adhesion and adherence, several other surface phenomena and characterization methods require introduction. Due to the rather large scope, in-depth descriptions are provided in the introductory section of each *chapter*. However, for a clear overview and structure, it was deemed necessary to offer a concise summary of the phenomena, methods and materials with relevance to this Thesis in section 2.1.



## 2.1 Phenomena, methods and materials relevant to this Thesis

### 2.1.1 Phenomena

First, the following sections offer a summary of the main results of surface charging models since these are relevant for understanding *chapter 5*.

#### 2.1.1.1 Electrokinetic effects

Before discussing the theoretical aspects of surface charge, it is necessary to consider the physical nature of charges in an electrolyte medium. Sources of interfacial charges may come from direct ionization of surface groups, differential ion solubility, substitution of surface ions, or specific ion adsorption. An ion or charged particle in an electrolyte exerts an influence on its immediate environment by virtue of its electric field. The term "electrokinetic effects" is used as a general term for four associated phenomena:<sup>1</sup>

- a) *Electrophoresis*: the migration of charged species in an electric field.
- b) *Sedimentation potential*: the potential developed due to the sedimentation of charged particles in an electrolytic medium.
- c) *Electro-osmosis*: the bulk flow of an electrolyte induced by an electric field.
- d) *Streaming potential*: the counterpart of electro-osmosis, *i.e.* the development of a difference in potential (the streaming potential), resulting from the flow of electrolyte.

Electrokinetics has obtained a prominent position in colloid science as an additional approach for electrical surface characterization. Moreover, it is important in practical applications. The study of electrokinetic effects has been developed in connection with the theories of the electrical double layer and of electrostatic surface forces.

#### 2.1.1.2 Double layer model

A charged surface together with the structured electrolyte region associated to it is known as the electrical double layer. This layer is largely responsible for many of the observed electrokinetic effects.

In 1879, Helmholtz<sup>2</sup> was the first to introduce a theoretical model of the electrical double layer, in which its liquid side was conceived as consisting of an immobilized layer of adsorbed counter ions. This model was however inadequate in its explanation of the observed

electrokinetic effects. An alternative was developed by Gouy<sup>3</sup> in 1910 and Chapman<sup>4</sup> in 1913 in which the double layer was considered as a diffuse layer of counter ions, whose concentration decreased with an increasing distance from the surface. Also this view was to some extent inadequate since, according to the model, unrealistically high concentrations of counter ions were predicted at positions close to the surface. The currently accepted model of the double layer combines the ideas of the above versions and was the result of research carried out by Stern in 1924. In the Gouy-Stern model, the electrical double layer is viewed as consisting of two distinct regions, whereby the excess charges in the electrolyte are distributed between a layer of counter ions (the rigid layer), situated at the shortest possible distance from the charged surface, and a diffuse layer. The concentration of counter ions near the surface would be higher than that in the bulk of the solution. There also exists a diffuse layer, extending from the plane of the closest indifferent ions (outer Helmholtz plane, oHp) into the bulk solution. The diffuse layer obeys Boltzmann statistics.

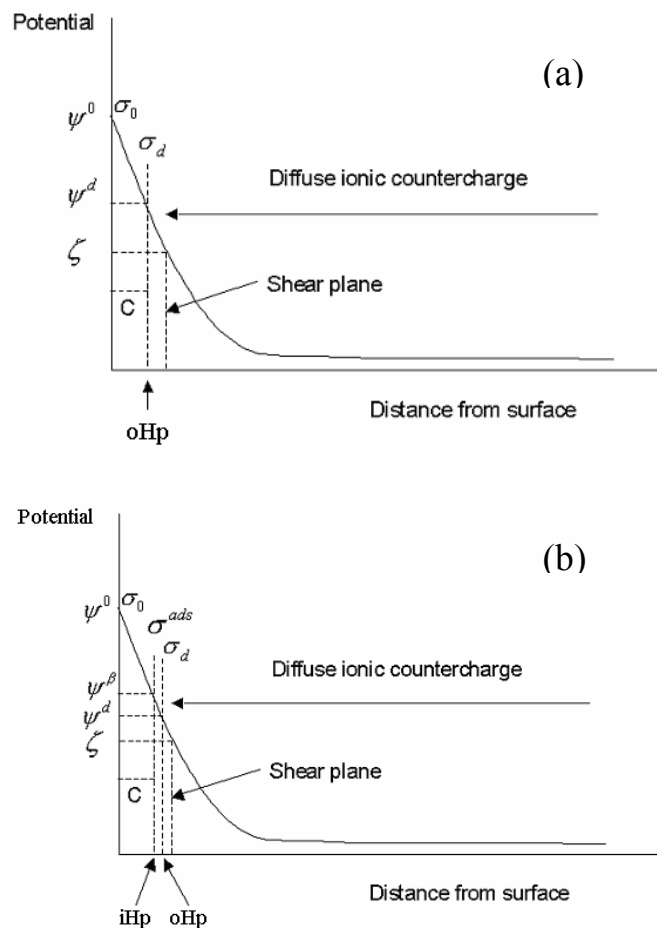


**Figure 2.1** Schematic drawings of the decrease in potential across a double layer as a function of the distance from the surface in the (a) absence and (b) presence of specific ion adsorption.

Figure 2.1 shows a Gouy-Stern double layer structure that considers finite-sized counterions and further includes specific ion adsorption. The charges at and adjacent to the surface cause a potential difference between the region near the surface and the bulk of the solution. The potential decreases within the solution as a function of the distance from the charged surface. The occurrence of specific ion adsorption is inferred from the dependence of certain double layer properties on the nature of counter- and co-ions. Generally, ions that interact specifically (non-electrostatically) with the surface, approach it at a shorter distance. The charge balance as a whole is written as:

$$\sigma^0 + \sigma^d + \sigma^{\text{ads}} = 0 \quad (\text{Eq. 2-1})$$

Here,  $\sigma^0$  is the surface charge;  $\sigma^d$  is the diffuse charge; and  $\sigma^{\text{ads}}$  is the charge that stems from the adsorbed ions. If  $\sigma^{\text{ads}} = 0$ , there is no specific ion adsorption.

There are several potentials shown in Figure 2.1: a) the surface potential,  $\psi_0$ ; b) the potential at the oHp,  $\psi_d$ ; c) the potential at the inner Helmholtz plane (iHp),  $\psi_\beta$ ; and d) the electrokinetic or zeta potential of the shear plane,  $\zeta$ . All these potentials are defined with respect to the potential at an infinite distance from the surface. Although the surface potential is an important parameter, the potential at the oHp is practically even more important since it represents the actual potential influencing the behavior of the charged species. However, as this potential cannot be measured directly, the zeta potential located at the shear plane is often considered as an adequate substitute.<sup>1</sup> The position of the shear plane is close to, and for practical reasons assumed to be identical to, the oHp surface. The  $\zeta$  potential can be determined by electrokinetic measurements, such as streaming potential and electro-osmosis measurements. It is accepted that  $\zeta$  is fully defined by the nature of the surface, its charge, the type of electrolyte and its concentration. It can be said that for any interface with all these parameters known,  $\zeta$  is a well-defined property.

### 2.1.1.3 DLVO theory

The DLVO theory is named after Derjaguin, Landau,<sup>5</sup> Verwey and Overbeek<sup>6</sup> and describes the force between charged surfaces interacting through a liquid medium. The DLVO theory is frequently formulated to colloidal interactions and invoked to investigate a vast array of natural and engineered phenomena, such as particle aggregation,<sup>7</sup> hetero-coagulation, colloid deposition,<sup>8</sup> and a host of processes involving colloidal stability<sup>9</sup> and transport.<sup>10</sup> This theory combines the effects of the van der Waals attraction and the electrostatic repulsion due

to the so called double layer of counterions. The van der Waals interaction potential is largely insensitive to variations in electrolyte concentration and pH. Furthermore, it exceeds the double layer repulsion at small enough distances since it follows a power law interaction (i.e.  $W \propto -1/D^n$ ), whereas the double layer interaction energy remains finite or increases much more slowly as  $D \rightarrow 0$ . Figure 2.2 shows a schematic of the various types of interaction potentials that can occur between two surfaces or colloidal particles under the combined action of these two forces. The van der Waals part of the DLVO interaction of two spheres is computed by Equation 2-2,

$$U_w = -\frac{A}{6D} \frac{R_1 R_2}{R_1 + R_2} \quad (\text{Eq. 2-2})$$

where  $R_1$  and  $R_2$  are the radii of the spheres and  $D$  is the closest distance between the particle surfaces.  $A$  is the so called Hamaker constant and can be computed if these molecular properties are known. Alternatively, it can be derived from macroscopic dielectric properties of the materials, or from experimental measurements. If the Hamaker constant for an interaction between two bodies of the same material  $i$  in vacuum is denoted as  $A_{ii}$ , the Hamaker constant between two bodies of different materials (1 and 2) across a medium 3,  $A_{132}$  is given by  $A_{132} = (\sqrt{A_{11}} - \sqrt{A_{33}})(\sqrt{A_{22}} - \sqrt{A_{33}})$ .

The electrostatic part of the DLVO interaction is calculated with the mean field approximation. For two spheres of radius  $a$  with constant surface charge  $Z$  separated by a center-to-center distance  $r$  in a fluid of dielectric constant  $\epsilon$  containing a concentration  $n$  of monovalent ions, the electrostatic potential takes the form of a screened-Coulomb or Yukawa repulsion,

$$\beta U_e(r) = Z^2 \lambda_B \left( \frac{\exp(\kappa a)}{1 + \kappa a} \right)^2 \frac{\exp(-\kappa r)}{r} \quad (\text{Eq. 2-3})$$

where  $\lambda_B = e^2 / 4\pi\epsilon k_B T$  is the Bjerrum length. This parameter represents the separation at which the electrostatic interaction between two elementary charges is comparable in magnitude to the thermal energy scale. Further,  $e$  is the elementary charge,  $\kappa^{-1}$  is the Debye-Hückel screening length, which is given by  $\kappa^2 = 4\pi\lambda_B n$ , and  $\beta^{-1} = k_B T$  is the thermal energy scale at absolute temperature  $T$ . The results of total potential are:

$$U = U_w + U_e \quad (\text{Eq. 2-4})$$

and depicted in Figure 2.2. This theory proposes that an energy barrier resulting from the repulsive force prevents two highly charged particles from approaching one another and adhering to each other. However, if the particles collide with sufficient energy to overcome that barrier, an attractive force will pull them into contact resulting in a strong and irreversible adherence (Figure 2.2a). Therefore, if the particles have a sufficiently high repulsion, the dispersion will resist aggregation and the colloidal system will be stable. However, if a repulsion mechanism does not exist, coagulation will eventually take place. In certain situations (*e.g.* in high salt concentrations), there is a possibility of a “secondary minimum” where a much weaker and potentially reversible adhesion between particles exists (Figure 2.2b). These weak forces are sufficiently stable not to be broken by Brownian motion, but may dissociate under an externally applied force such as vigorous agitation. For particles of low charge density or potential, the energy barriers are always much lower (Figure 2.2c). Above a certain electrolyte concentration, the energy barrier falls below the  $W = 0$  axis (Figure 2.2d), and the particles then coagulate rapidly. As the surface charge or potential approaches zero, the interaction curve approaches the pure van der Waals curve, and the two surfaces now attract each other strongly at all separations.

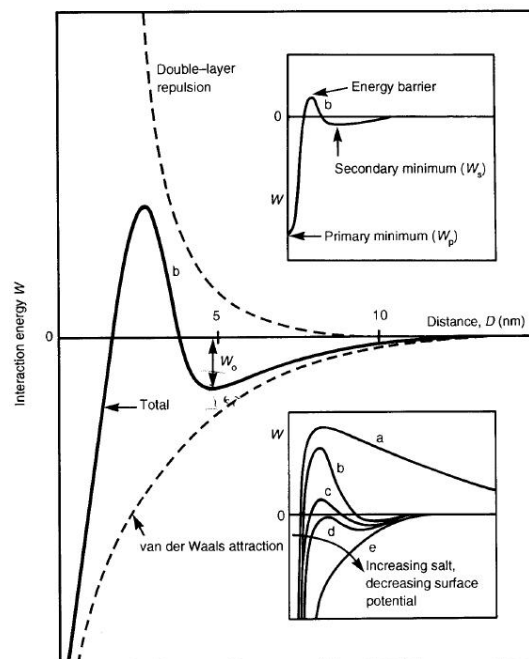


**Figure 2.2** Schematic profiles for energy versus distance of DLVO interaction (adapted from *ref.*<sup>11</sup>).

#### **2.1.1.4 Surface mechanical properties of polymers**

Mechanical properties, including surface viscoelasticity, nanoscale glass transition temperature in the outermost nanometers, indentation, friction and wear, play crucial roles in all applications when polymers are brought into mechanical contact with other materials. The present Thesis reports on investigations concerning friction and nano-indentation features among the surface properties. Friction (from macroscale to nanoscale) is discussed in section 2.2.

In recent years, there has been significant interest in measuring the indentation of thin polymer films with relevance to microelectronics<sup>12</sup> and biomedical systems.<sup>13</sup> Indentation testing is a simple method that essentially consists of touching the material of interest, whose mechanical properties, such as elastic modulus and hardness, are unknown, with a second material with known properties. The establishment of the Brinell, Knoop, Vickers, and Rockwell test follows from a refinement of the method of simply indenting one material with an indenter of a different shape on a sub-micron scale, followed by an *ex-situ* study of the resultant deformation profile with optical or electron microscopy and a surface profiler.<sup>14</sup> In most cases, depth sensing indentation (DSI), JKR measurements and AFM techniques have been used to extract basic mechanical properties and adhesion characteristics.<sup>15-18</sup> Indentation techniques can be used to calculate the elastic modulus, the strain-hardening exponent, the fracture toughness and the viscoelastic properties. More details of the fundamentals of micro- and nano-indentation physics is presented in *chapter 6*.

#### **2.1.2 Methods**

Surface analysis and characterization methods encompass a wide range of experiments. In Table 2.1 below, an overview of the relevant techniques can be seen.

**Table 2.1** An overview of various characterization methods.

Characterized feature	Method	Remarks
Chemical composition	XPS SIMS, ToF-SIMS Optical fluorescence	see below see below see below
Topology	SEM AFM	see ref. <sup>19</sup> see ref. <sup>20</sup>
Surface charge	Streaming potential Zeta potential AFM force titration EC-AFM	see section 5.4 see below see <i>chapter 5</i> see section 7.2
Surface free energy	Contact angle (CA) measurements ATD CFM	see section 2.2 see section 2.2 see section 2.2
Adhesion, adherence	Engineering test of adhesive joints ATD AFM	see ref. <sup>21</sup> see section 2.2 see section 2.2
Surface mechanics	Macroscopic tribology Surface shear ATD contact mechanics Indentation Nano-indentation	see ref. <sup>22</sup> see ref. <sup>23</sup> see section 2.2 see ref. <sup>24, 25</sup> see section 2.2

### 2.1.2.1 X-ray photoelectron spectroscopy (XPS)

XPS has been extensively used in the study of polymer surfaces, including surface modification, chemical reaction, contamination, degradation, polymer chain mobility, adhesion failure, and biocompatibility.<sup>26-29</sup> In polymer analysis, XPS has one noticeable limitation; it lacks molecular specificity although it yields average atomic compositions. Secondary ion mass spectrometry (SIMS) is a powerful complementary technique because of its very high degree of molecular specificity.<sup>28</sup>

XPS involves placing the sample in a high vacuum chamber and irradiating it with a monochromatic or quasi-monochromatic X-ray source. An X-ray photon thus interacts with an inner-shell electron of an atom. This interaction causes a complete transfer of the photon energy to the electron, which subsequently has enough energy to leave the atom and escape from the surface of the sample. The kinetic energy  $E_k$  is related to the binding energy  $E_b$  according to

$$E_k = h\nu - E_b - \psi \quad (\text{Eq. 2-5})$$

where  $h\nu$  is the quantum energy of the X-rays ( $h$  is Planck's constant and  $\nu$  is the X-ray frequency) and  $\psi$  is the work. The binding energy of a particular shell of an atom is unique for each element; therefore, knowing the binding energy allows the identification of the element.

X-ray sources are generally aluminum ( $\text{Al}_{K_\alpha}$  of 1486 eV and linewidth 0.85 eV) or magnesium ( $\text{Mg}_{K_\alpha}$  of 1253.6 eV and linewidth 0.7 eV). It is common to first obtain a survey spectrum which detects all elements in the surface except hydrogen, since hydrogen has no core-electrons. This is then followed, where appropriate, by a high resolution examination of a selected element.

### **2.1.2.2 Secondary ion mass spectroscopy (SIMS)**

SIMS refers to the mass spectrometry of ionized particles which are emitted from the surface when energetic primary particles bombard the surface.<sup>30</sup> Early-stage spectrometry is operated in a mode of dynamic SIMS (DSIMS). In this mode, a high flux of primary ions is directed to the sample surface, rapidly eroding it. This makes DSIMS unsuitable for analyzing ultra-thin surfaces. In addition to elemental composition, SIMS, when operated in a mode referred to as static SIMS (SSIMS), can provide information on the chemical structure of a material surface. In this mode of operation, a low beam-current density and a low voltage are used to minimize surface damage. SSIMS is the most sensitive technique for elemental analysis, allowing the detection of trace impurities.<sup>31</sup>

In the early 1980s, SIMS instruments based on "time-of-flight (ToF) mass spectrometers" were developed at the university of Münster by Benninghoven, Niehus and Steffens.<sup>30, 31</sup> The set-up of ToF-SIMS is shown in Figure 2.3. In this technique, pulsed primary ions with energies of 1-25 keV, typically energetic, such as  $\text{Ar}^+$ ,  $\text{Ga}^+$ ,  $\text{Cs}^+$  and  $\text{O}^-$ , are used to bombard the sample surface, causing the secondary elemental or cluster ions to be emitted from the surface. The ionized particles of one polarity, atomic and molecular secondary ions, are accelerated into a reflectron type spectrometer. A nominal kinetic energy of the secondary ions is:<sup>32</sup>

$$E_k = eV_0 = mv^2 / 2 \quad (\text{Eq. 2-6})$$



Here,  $V_0$  is the accelerating voltage,  $m$  is the mass of ion,  $v$  is the ion's flight velocity, and  $e$  is its charge. They travel through a tube and arrive at an ion detection and counting system. However, since they all depart from the sample simultaneously and are subject to the same accelerating voltage, the lighter particles arrive at the detection system before the heavier ones. The mass separation is obtained in the flight time  $t$  from the sample to the detector. This flight time  $t$  is expressed as:

$$t = L / (2eV_0 / m)^{1/2} \quad (\text{Eq. 2-7})$$

where  $L$  is the effective length of the mass spectrometer. A variety of mass ions are recorded by the detector as a function of the time sequence in order to give the SIMS spectrum.

ToF-SIMS represents a spectroscopy technique that provides characterization of chemical composition, imaging for determining the distribution of chemical species, and depth profiling for thin film characterization. Typically, the primary ion dose in the SSIMS mode is  $\leq 10^{12}$  ions/cm<sup>2</sup> for mass analysis and  $\leq 10^{13}$  ions/cm<sup>2</sup> for imaging.

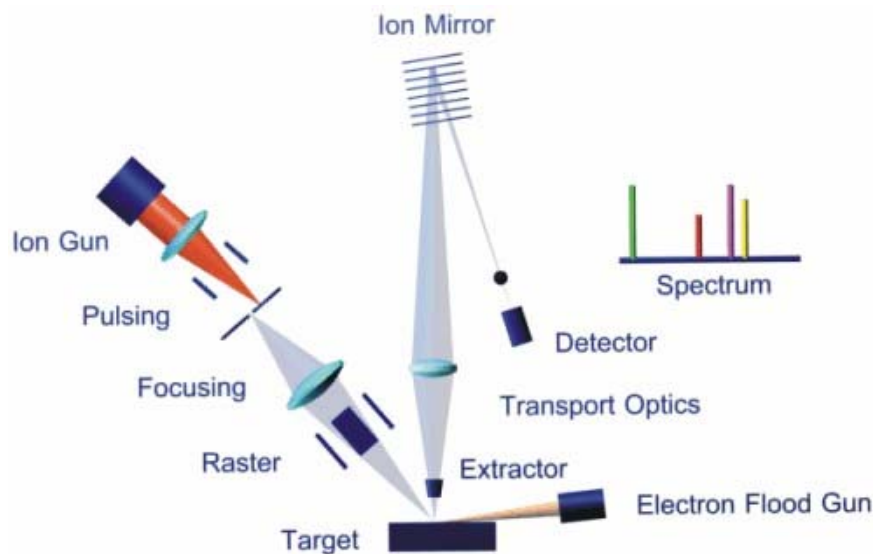


**Figure 2.3** ToF-SIMS set up (adapted from ref.<sup>32</sup>).

### 2.1.2.3 Fluorescence microscopy (FM)

The fluorescence microscopy technique has become an essential tool in biology and biomedical sciences, as well as in materials science.<sup>33</sup> It aims at revealing only the objects of

interest in an otherwise black background. Over the past several decades, organic chemists have devised many thousands of fluorescent probes that provide a means of labeling virtually biological systems.<sup>34</sup>

Only objects of interest fluoresce by FM. Fluorescence is the emission of light that occurs within nanoseconds after the absorption of light that is typically of a shorter wavelength. The Stokes shift, which is defined as the difference between the exciting and emitted wavelengths, is the critical property that renders fluorescence powerful. By completely filtering out the exciting light without blocking the emitted fluorescence, it is possible to see only the fluorescent objects.<sup>35</sup> In contrast to other modes of optical microscopy that are based on macroscopic specimen features, such as phase gradients, light absorption, and birefringence, FM is capable of imaging the distribution of a single molecular species based solely on the properties of fluorescence emission. Thus, by using FM, the precise location of intracellular components labeled with specific fluorophores can be monitored, as can their associated diffusion coefficients, transport characteristics, and interactions with other biomolecules. In addition, the dramatic response in fluorescence to localized environmental variables enables the investigation of pH, viscosity, refractive index, ionic concentrations, membrane potential, and solvent polarity in living cells and tissues. This is excellently reviewed in a paper by Lichtman and Conchello.<sup>35</sup>

#### **2.1.2.4 Zeta potential**

The zeta ( $\zeta$ ) potential (see Figure 2.1) is an important parameter for a number of applications, including the characterization of biomedical polymers, electrokinetic transport of particles or blood cells, membrane efficiency, and microfluidics. The importance of the  $\zeta$  potential for so many applications in science and engineering has led to the development of a number of techniques, based on one of the electrokinetic effects, for measuring this quantity. In the electrophoresis method, the  $\zeta$  potential is determined by placing fine particles in an electric field and measuring their mobility,  $v_E$ , using a suitable microscopic technique. The streaming potential technique has been extensively applied to flat polymer and glass surfaces in order to study the electrical properties of solid-liquid interfaces in a parallel plate microchannel. In this technique the downstream convection of ions via a pressure-driven (with a  $\Delta P$  pressure gradient) flow induces a streaming potential which, for steady incompressible and laminar flow, can be related to the  $\zeta$  potential via:

$$\Delta E_{\text{str}} = \frac{\varepsilon \zeta \Delta P}{\eta \left( \lambda_0 + \frac{2\lambda_s}{r} \right)} \quad (\text{Eq. 2-8})$$

Here,  $\varepsilon$  is the permittivity of the medium,  $\eta$  the viscosity,  $\lambda_0$  the bulk conductivity,  $\lambda_s$  the surface conductivity, and  $r$  the radius of the pore or capillary or half the width of a slit. While this technique is inherently suitable for flat surfaces, accurate measurements of the streaming potential may not be simple in practice.

### 2.1.3 Materials

The present Thesis reports on several surface treatment approaches that have been employed to increase the polarity and subsequently the adhesion of non polar polymers, such as semi-crystalline LDPE and the cross-linked elastomer PDMS. These approaches include flame-treatment (see *chapter 3*) and UV/ozone treatment (see *chapter 5*). A number of "grafting to" approaches have also been employed to obtain surfaces that display a responsive behavior to variations in surface charge (oxidation potential controlled by electrochemistry of oxidizing/reducing agents). In these approaches, PFS chains functionalized with short  $-\text{[CH}_2\text{-CH}_2\text{-S]}-$  segments were grafted to Au substrates (see *chapter 7*).

#### 2.1.3.1 Modification of polymer surfaces to enhance adhesion

A polymer surface is often difficult to be wet or bond to due to its low surface energy, chemical inertness, the presence of contaminants or a weak boundary layer. Surface treatments are used to change the chemical composition, increase the surface energy, modify the crystalline morphology and surface topography or remove contaminants and weak boundary layers. Many processes have been developed to modify polymer surfaces, including chemical and photochemical treatments, plasma processes, surface grafting, etc. These processes generally cause physical or chemical changes to a thin surface layer without affecting the bulk properties. Chemical treatments can cause severe physical and chemical modifications to the surfaces. For instance, sodium etching of fluoropolymers causes defluorination, and consequently the formation of a surface unsaturation. Chromic acid etching of PE causes dissolution of the amorphous regions and thus increases the surface roughness and crystallinity.<sup>36</sup> During flame and thermal treatments, polymer surfaces are oxidized and polar oxygenated groups are introduced. The oxidation proceeds by a free radical mechanism, accompanied by chain scission, and an improved wettability results from the formation of polar groups which in turn leads to an improved bondability as a result of the

increased wettability and interdiffusion. Flame-treatments are used commercially to render polyolefins and polyacetals printable and bondable. Plasma treatments are widely used to improve the wettability and bondability of polyolefins, polyesters and numerous other polymers. UV irradiation of polymer surfaces produces chemical wettability and bondability modifications similar to those induced by plasma treatment. In some cases, the UV radiation during a plasma treatment is the main mode of plasma polymer reaction. UV irradiation causes chain scission, cross-linking and oxidation on polymer surfaces even in an inert atmosphere. Various vinyl monomers have been grafted onto polymer surfaces, and grafting sites on polymers are produced by exposure to plasma, UV radiation or chemical agents. Polymer radicals or polymer peroxides obtained by plasma or UV exposure serve as the initiation and grafting sites. The chemical compositions of these modified surface layers are analyzed by various techniques, and these surface characterization methods include SIMS, XPS, matrix-assisted laser desorption/ionization mass spectrometry, Raman microspectroscopy, near field scanning optical microscopy, etc.

## **2.2 Measuring adhesion from micro- to nanoscale contacts**

Interfacial energy and adhesion (adherence) of solids are important parameters in the science and technology of plastics, fibers, elastomers, coatings, adhesives, etc. This *chapter* provides a theoretical background information that is considered useful for the discussions of surface energy and fracture strength across different length scales. It begins with a brief review of surface forces. Subsequently, the concepts of thermodynamic adhesion and contact mechanical theories are discussed. Furthermore, aspects such as surface roughness and humidity that affect the adhesion are summarized. A number of techniques used to probe adhesion are discussed. These include AFM, surface force apparatus (SFA) and ATD. Special emphasis is placed on reviewing the current status and new perspectives in the practical field of polymer adhesion. Thus, the enhanced understanding of polymer adhesion allows us to make rational predictions and to control the design of the corresponding applications.

### **2.2.1 Introduction**

Adhesion interactions among molecular assemblies comprising surfaces and surroundings occupy a prominent place for a variety of phenomena and applications, span over different length scales, in chemistry, physics and biology. In an extraterrestrial context,

cosmic dust aggregation plays a role in planet formation. On a macroscopic scale, the importance of wetting and lubrication leads to numerous experimental and theoretical investigations. Colloid particles lie in the intermediate region between macro and nano with dimensions that are influenced by interactions on this length scale. Moreover, as nanotechnology begins to set the pace of modern technological advancement in areas as diverse as telecommunications and biomedical engineering, the prominence of intermolecular interactions will only increase. For example, molecular recognition, protein folding and membrane interactions are at the nanoscopic scale. A wider understanding of adhesion will be required to support the current boom in a number of areas such as tribology,<sup>37, 38</sup> biotechnology,<sup>39, 40</sup> mineral separation,<sup>41, 42</sup> and drug delivery systems,<sup>43, 44</sup> etc.

## 2.2.2 Surface forces

### 2.2.2.1 Intermolecular forces

Although the technological arts of adhesion processes have existed since prehistoric times, theories of adhesion have only been developed over last century. As of yet, adhesion is still not fully understood. The understanding of adhesion phenomena requires an extensive knowledge of the intermolecular forces from which they arise. Several reviews concerning intermolecular forces are available.<sup>45-48</sup>

Intermolecular forces can be classified into three categories depending on their physical origins: *electrostatic forces*, *polarization forces* and *forces which are quantum mechanical in nature*.<sup>45</sup> Dispersion forces, for instance, which originally stem from quantum mechanics, make up the most important contribution to the total van der Waals force between atoms and molecules. They play a leading role in a number of important phenomena such as adhesion, surface tension, physical adsorption, wetting, the properties of gases, liquids and thin films, *etc.*<sup>45</sup>

Intermolecular forces can be also grouped into categories based on characteristic phenomena that dominate the essential physical behavior.<sup>47</sup> Thus, one group includes non-specific interactions such as ionic, dipole-dipole, ion-dipole interactions; induced dipolar forces; van der Waals (London dispersive) interactions; hydrophobic and hydrophilic, solvation, structural, and hydration forces; steric and fluctuation forces, *etc.* Another group includes specific (molecule-specific) interactions such H-bonding; ligand-receptor or antibody-antigen type interactions for pairs that are bound together in biological molecules.

At the geometrical surface of the body, interfacial atoms experience forces through interaction with other atoms below or beside them. These interfacial atoms move inward until the repulsive short range forces from the atoms just beneath the surface balance the long range attractive forces from atoms just below and well below the surface. These make an effective contribution to the surface forces (and hence also to the surface tension) up to a characteristic distance of a few atomic (molecular) layers.<sup>47</sup> Thus, different interatomic (intermolecular) forces result in differences in surface tension (surface free energy) and adhesion for various substances.

#### **2.2.2.2 Adhesive forces between surfaces**

In principle, the adhesive forces between surfaces are related to the underlying chemistry and physics of the interfaces themselves. The interfacial forces that hold two bodies together may arise from a sum of interactions of intermolecular forces such as van der Waals forces, chemical bonding, or electrostatic attraction. In 1955, Lifshitz<sup>49-51</sup> proposed a macroscopic theory that considers the interactions of resultant electromagnetic waves (arising from electron motion) emanating from macroscopic bodies, rather than considering the interactions between isolated individual molecules. These electromagnetic fields are completely described in the complex dielectric spectrum, which is therefore the only material property required to completely specify the attractive forces between macroscopic bodies. This theory applies to the distances larger than interatomic distances thus encompassing dispersion, dipole and induction energies. A review as well as refinements of this theory have been given elsewhere.<sup>52-57</sup> When considering the long range interactions between macroscopic surfaces in liquids, four other important forces should be taken into account: solvation, structural and hydration forces, steric forces.<sup>45</sup> Figure 2.4 shows an example of various surface forces vs. the separation distance.

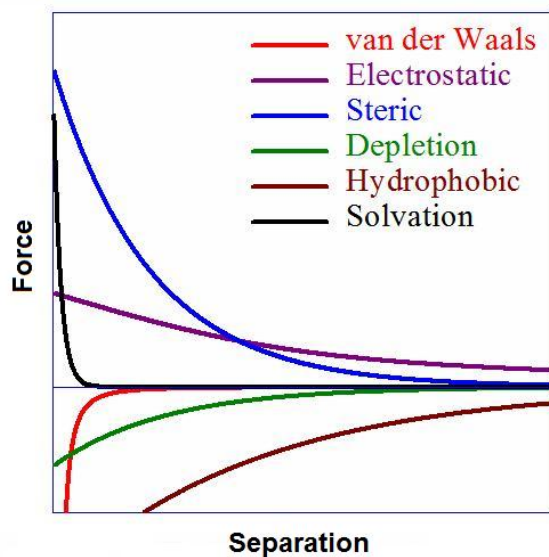


**Figure 2.4** The forces between two surfaces as a function of the separation distance.

In daily life, the adhesive forces between macroscopic surfaces vary largely. There are several reasons for this. 1) The roughness is more significant than the range of the molecular forces keeping the surfaces apart; 2) the ubiquitous presence of contaminants reduces the molecular attraction between the surfaces; and 3) a capillary condensation, as caused by exposure to humid environments, has a consequential effect on the adhesion study. The surface roughness has perhaps the most pronounced effect since even the slightest imperfection, a few nanometers in size, can push the bodies outside the range of atomic forces, thus preventing adhesion. The following section (§2.2.3.4) describes in detail how roughness and humidity alter the adhesion energy.

## 2.2.3 Adhesion

### 2.2.3.1 Thermodynamics of adhesion

There exist numerous definitions for adhesion, but in this *chapter*, *adhesion* refers to the thermodynamic *work of adhesion* ( $W_A$ ), (and cohesion of similar bodies) – a concept first introduced by Harkins.<sup>58</sup> It is defined as the reversible work (the free energy change) per unit area required when separating two phases, from contact to an infinite separation distance. *Adherence* (practical adhesion) is intimately related to a wide range of application fields. The corresponding *work of adhesion* can be easily expressed with surface tension values.<sup>47</sup> In

general, for two solid surfaces in intimate contact, each with a unit area, the *work of adhesion*  $W_{132}$  (when separating two media 1 and 2 in medium 3) can be expressed as:<sup>45</sup>

$$W_{132} = \gamma_{13} + \gamma_{23} - \gamma_{12} \quad (\text{Eq. 2-9})$$

where  $\gamma$  is interfacial tension. This expression is valid for processes that occur through quasi-equilibrium steps, *i.e.* when energy dissipation is negligible.<sup>47</sup>

A commonly used approach for treating solid surface energies is to express surface tension or surface energy as the sum of components due to dispersion forces ( $\gamma^d$ ) and polar forces ( $\gamma^p$ ). The interfacial tension between two phases 1 and 2 can be expressed in terms of two components of each phase. Thus, *work of adhesion* can be expressed

$$W_{132} = 2\{\gamma_3 - [\sqrt{\gamma_1^d \gamma_3^d} + \sqrt{\gamma_1^p \gamma_3^p}] - [\sqrt{\gamma_2^d \gamma_3^d} + \sqrt{\gamma_2^p \gamma_3^p}] + [\sqrt{\gamma_1^d \gamma_2^d} + \sqrt{\gamma_1^p \gamma_2^p}]\} \quad (\text{Eq. 2-10})$$

In an attempt to relate the components more clearly to the chemical nature of the phase, van Oss et al.<sup>59, 60</sup> suggested that the polar component could be better described in terms of acid-base interactions. The total interfacial tension between two phases is the sum of two components,<sup>61</sup> the Lifshitz-van der Waals surface energy  $\gamma^{LW}$  and the acid-base surface energy  $\gamma^{AB} = 2\sqrt{\gamma^+ \gamma^-}$ , where  $\gamma^+$  and  $\gamma^-$  are the electron acceptor and the electron donor components, respectively. For the two components  $\gamma^{LW}$  and  $\gamma^{AB}$  in a binary system, the Good-Girifalco-Fowkes<sup>62</sup> combining rules are applicable:

$$\gamma_{\alpha\beta} = \left(\sqrt{\gamma_{\alpha}^{LW}} - \sqrt{\gamma_{\beta}^{LW}}\right)^2 + 2\left(\sqrt{\gamma_{\alpha}^+ \gamma_{\alpha}^-} + \sqrt{\gamma_{\beta}^+ \gamma_{\beta}^-} - \sqrt{\gamma_{\alpha}^+ \gamma_{\beta}^-} - \sqrt{\gamma_{\alpha}^- \gamma_{\beta}^+}\right) \quad (\text{Eq. 2-11})$$

Hence the *work of adhesion* between two polar samples across a polar medium is:

$$\begin{aligned} \frac{W_{132}}{2} = & \sqrt{\gamma_1^{LW} \gamma_2^{LW}} - \sqrt{\gamma_1^{LW} \gamma_3^{LW}} - \sqrt{\gamma_2^{LW} \gamma_3^{LW}} + \gamma_3^{LW} + \sqrt{\gamma_3^+} \left(\sqrt{\gamma_3^-} - \sqrt{\gamma_1^-} - \sqrt{\gamma_2^-}\right) \\ & + \sqrt{\gamma_3^-} \left(\sqrt{\gamma_3^+} - \sqrt{\gamma_1^+} - \sqrt{\gamma_2^+}\right) + \sqrt{\gamma_1^+ \gamma_2^-} + \sqrt{\gamma_1^- \gamma_2^+} \end{aligned} \quad (\text{Eq. 2-12})$$

Several papers in the literature have proposed a variety of methodologies and theories for estimating surface tension components from contact angle data, as well as their thermodynamic consistency.<sup>63-67</sup>



### 2.2.3.2 Theoretical models of adhesion

Historically, studies of adhesion have approached the subject from two viewpoints: (i) through surface chemistry, trying to correlate adhesive strength to the thermodynamic *work of adhesion*; (ii) through contact mechanics, in an attempt to predict the debonding threshold by analyzing the stresses around the contact area. In the present section, various continuum models describing contact phenomena between both non-deformable and deformable solids are discussed. In all cases, the system of a sphere on a plane is considered.

#### *Nondeformable solids*

For smooth, ideal, rigid solids, the force required to overcome the *work of adhesion* between a rigid sphere and a flat surface (without considering capillary force) written in terms of *work of adhesion* is:

$$F_{\text{pull-off}} = 2\pi RW \quad (\text{Eq. 2-13})$$

This equation is applicable for any type of force as long as the range of interaction and the separation are much shorter than the radius of the sphere. If the sphere and the flat surface consist of the same material:

$$F_{\text{pull-off}} = 4\pi R\gamma \quad (\text{Eq. 2-14})$$

#### *Deformable solids*

The aforementioned models consider incompressible bodies; however, this is never the case in practice. It is important to note that in reality, solid bodies deform elastically and/or plastically under applied loads. Adhesion analysis of these solids requires more accurate contact mechanics models that should include a physical deformation component.

All discussed theories are based on the following assumptions: (1) The deformations are assumed to be purely elastic, governed by linear equations of the classical continuum elasticity theory (Hooke's law). (2) The materials in contact are elastically isotropic. (3) Neither Young's modulus  $E$  nor Poisson's ratio  $\nu$  changes under load. (4) The atomic structure is not taken into account. (5) The contact radius  $a$  is small compared with the radius  $R$  of the sphere.

Differences between the various models in the nature of the forces are shown in Figure 2.5. An idealized "real" interaction force, consisting of long range and short-range forces,<sup>68</sup>

can be seen in Figure 2.5a. The area between the force curve and the base line to the right of the equilibrium distance  $z_0$  (*i.e.* the total shaded area in Figure 2.5a) corresponds directly to the *work of adhesion*

$$W = \int_{z_0}^{\infty} \sigma(z) dz \quad (\text{Eq. 2-15})$$

that is required to separate the two surfaces, in the absence of an external load, from intimate contact (established at the equilibrium distance  $z_0$ ) to an infinite separation distance ( $\sigma(z)$ : force per unit area). The first part  $w_1$  represents the work against the short-range chemical forces (light shading in Figure 2.5a), while  $w_2$  reflects the work against all long-range interactions (visualized as the dark shading).

Hertzian analysis (Figure 2.5b) gives the simplest approximation when adhesive forces are ignored (hence  $W = 0$ ) and also models the repulsive part by a hard wall. In other words, no pull-off force and contact area are zero for an applied load of zero. Adhesion is assumed to play a negligible role in the sample deformation. In the case of adhesion-dominated interactions, a Hertzian analysis underestimates the contact area and effective load experienced by the substrate and results in an overestimation of the sample modulus. For a contact radius  $a$  of the interface region, it predicts that

$$a = \left( \frac{RP}{K} \right)^{1/3} \quad (\text{Eq. 2-16})$$

Here,  $P$  represents the externally applied loading force, and  $R$  the relative radius,

$$\frac{1}{R} = \frac{1}{R_1} + \frac{1}{R_2}, \quad K \text{ is the combined elastic modulus, } K = 4/3 \left[ \frac{(1-\nu_1^2)}{E_1} + \frac{(1-\nu_2^2)}{E_2} \right]^{-1}$$

(where  $E_{1,2}$  are the elastic moduli and  $\nu_{1,2}$  the Poisson ratios of a sphere and plane, respectively) for the vertical displacement  $\delta$  of the two bodies in contact

$$\delta = \frac{a^2}{R} \quad (\text{Eq. 2-17})$$

For the pressure distribution  $p(r)$  within the contact region

$$p(r) = \frac{3Ka}{2\pi R} \sqrt{1 - \left( \frac{r}{a} \right)^2} \quad (\text{Eq. 2-18})$$

where  $r^2 = x^2 + y^2$ .

As an extension of the Hertzian theory, the Johnson Kendall and Roberts (JKR) theory incorporates adhesion via the change in surface energy only where the surfaces are in contact. This is applicable for compliant, elastic samples, large tip radii, and high surface energies. In the JKR theory, a strong adhesive force is supposed to act at the equilibrium distance  $z_0$ , and is described by a delta function including the area  $W$  (Figure 2.5c). However, the interaction vanishes for all distances larger than  $z_0$ . Although this model seems to correspond well to certain experimental observations of contact and separation, the assumption made in its formulation is in fact unphysical. It is assumed that the solids do not interact outside the contact region, whereas in reality electrostatic and van der Waals forces are significant at separation distances of several nanometers. The relationship between the contact radius and the applied load is given by:

$$a^3 = \frac{R}{K} \left[ P + 3\pi RW + \sqrt{6\pi RPW + (3\pi RW)^2} \right] \quad (\text{Eq. 2-19})$$

The indentation of the system follows:

$$\delta = \frac{a^2}{R} - \left( \frac{8\pi Wa}{3K} \right)^{1/2} \quad (\text{Eq. 2-20})$$

And the force necessary to separate the surface from contact and stress distribution is given as:

$$F_{\text{pull-off}}^{\text{JKR}} = -\frac{3}{2} W\pi R \quad (\text{Eq. 2-21})$$

$$p(r) = \frac{3Ka}{2\pi R} \sqrt{1 - \left( \frac{r}{a} \right)^2} - \sqrt{\frac{3WK}{2\pi a} \left( 1 - \left( \frac{r}{a} \right)^2 \right)^{-1/2}} \quad (\text{Eq. 2-22})$$

In comparison, the Derjaguin-Muller-Toporov (DMT) model assumes that the surface forces extend over a finite range and act in the region just outside the contact. It is found to be more appropriate for systems with small radii of curvature, low *work of adhesion* and high moduli. Their analysis includes the adhesion *outside* the contact area by considering long-range attractive forces of basically van der Waals type (Figure 2.5d). The relationship between the force and contact area can be expressed as:

$$P = \frac{Ka^3}{R} - 2\pi RW \quad (\text{Eq. 2-23})$$

The indentation during contact is: 
$$\delta = \frac{a^2}{R} \quad (\text{Eq. 2-24})$$

And the pull-off force is given by: 
$$F_{\text{pull-off}}^{\text{DMT}} = -2\pi RW \quad (\text{Eq. 2-25})$$

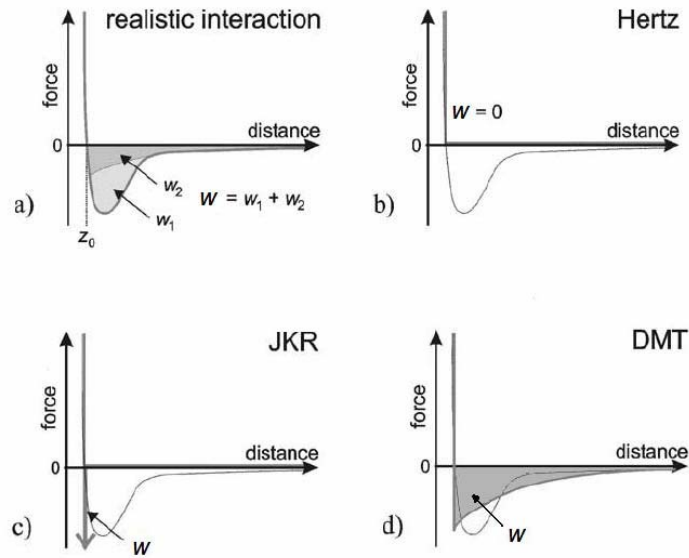


**Figure 2.5** The interaction forces (thick grey lines) used in the various models (b–d), plotted in comparison with a realistic interaction [(a) and thin lines in (b–d)]. All forces are given per unit area; the shaded areas reflect the work of adhesion  $W$ . Attractive forces are not included in the Hertz model (b), whereas they are considered by a delta function in the JKR model (c), and a long-range force in the DMT model (d). All model interactions feature hard-wall repulsion if intimate contact is established at  $z = z_0$ . In (a), the work of adhesion  $W$  is additionally separated into the two components  $w_1$  and  $w_2$  (with  $W = w_1 + w_2$ ), reflecting the individual contributions caused by short-range and long-range interactions, respectively.<sup>69</sup>

A continuous transition regime between JKR-DMT has been developed by Maugis through the application of a Dugdale model to describe the interaction potential between surfaces. It is presented in two coupled analytical equations and solved numerically through iteration.<sup>70</sup> A numerical approximation and curve fit method for non-dimensional data by Carpick<sup>71</sup> provides equations that are more manageable for curve-fitting. A full analytical solution is presented by Schwarz.<sup>69</sup>

To estimate which regime the contact falls within, one can calculate the non-dimensional Tabor parameter,

$$\mu = \left( \frac{R\Delta\gamma^2}{E_r^2 z_0^3} \right)^{1/3} \quad (\text{Eq. 2-26})$$

For  $\mu < 0.1$ , the DMT theory applies, and for  $\mu > 5$ , the JKR theory applies. In between, the transition model is used.

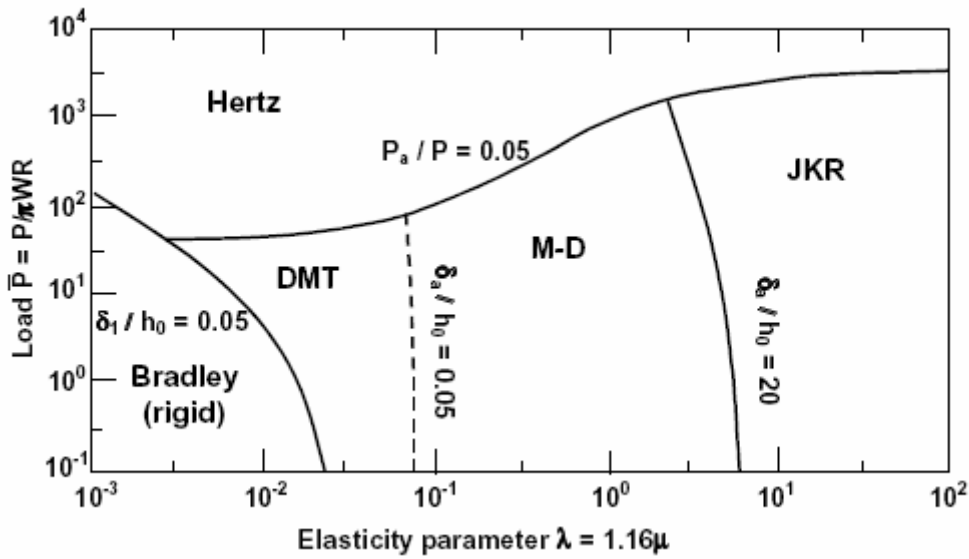


**Figure 2.6** An adhesion map for elastic spheres based on the Maugis-Dugdale model.<sup>72, 73</sup> When the adhesion is negligible, the bodies fall within the Hertz limit (approximately  $F > 10^3 \pi WR$ ).  $\delta_1$  is the elastic compression, and  $h_0$  the equilibrium distance. When  $\delta_1 \ll h_0$ , the bodies are rigid and follow the Bradley theory ( $\lambda < 10^3$ ).  $\delta_a$  is the deformation due to adhesion. When the adhesion is small the behavior of the materials is described by the DMT theory (approximately  $10^2 < \lambda < 10^1$ ), whereas the JKR theory predicts the behavior of highly adhesive bodies (approximately  $\lambda > 10^1$ ). The Maugis theory suits the intermediate region (approximately  $10^1 < \lambda < 10^1$ ).

Johnson and Greenwood<sup>73</sup> discussed the map in Figure 2.6 with coordinates  $\lambda$  or  $\mu$  and  $\bar{F}$ , and could thus cover the complete influence range of the surface forces on the contact of elastic bodies. The elasticity parameter  $\lambda$  or  $\mu$  is a measure of the elastic deformation of the spheres to the effective range of surface forces, and the load parameter  $\bar{F}$  is the ratio of the net contact force to a representative pull-off force. In principle, both the numerical analysis using the Lennard-Jones potential and the Maugis analysis using the Dugdale

approximation apply throughout the map and the Hertz, JKR, DMT and rigid zones comprise subsets in which some simplification is possible. However, in practice, determining the appropriate zone of an adhesion experiment requires the knowledge of a number of parameters, which may not be easily accessible, particularly for nanoscale experiments. Such parameters include the radius of the probe or the combined modulus, which can be affected even by trace amounts of contaminants. In the DMT zone, elastic deformation due to surface forces is negligible and in the rigid zone all elastic deformation is small as compared to the range of the surface forces.

### **2.2.3.3 Viscoelastic effects**

Many materials of interest for interfacial energy measurement, particularly some softer materials with microstructure, such as thermoplastic elastomers, are intrinsically viscoelastic. In these cases, the role of the viscoelasticity in the measurements must be confronted directly. Consequently,  $a$  and  $\delta$  are no longer unique functions of instantaneous load.

Theoretical models for contact between viscoelastic materials in the absence of adhesion have been available since the 1960s.<sup>74, 75</sup> In the early 1970s, Barquins,<sup>76</sup> and Johnson<sup>77</sup> developed models that included adhesion but viscoelastic effects were confined to the periphery of the contact. In the late 1990s, several experiments demonstrated that viscoelastic effects are not confined to the contact periphery but are included in the entire contact zone.<sup>78, 79</sup>

There have been a number of earlier studies of particle deformation and crack propagation that have attempted to incorporate viscoelastic effects both experimentally<sup>78, 80</sup> and theoretically.<sup>74, 75, 77, 81-90</sup> Many of the studies have been limited by the approximate ways that the viscoelastic effects have been incorporated into the theory. It is common to introduce a velocity dependent adhesion energy into the JKR and DMT equations and subsequently solve the resulting differential equation in order to model certain experimental data.<sup>80 90</sup> Haiat<sup>91</sup> recalled the basic equation for the restricted self consistent model in the linear elastic case and then extended this approach to the linear viscoelastic case. Falsafi et al.<sup>78</sup> replaced the Young modulus in JKR equations with a time dependent creep compliance function based on the work of Ting<sup>74</sup> and Schapery.<sup>85, 86, 92, 93</sup> Greenwood and Johnson<sup>87</sup> followed Schapery<sup>85</sup> and simplified the time convolution integral by replacing the creep compliance function with a constant. A power law creep compliance function introduced by Schapery<sup>86</sup> was used by

Hui et al.<sup>88</sup> in a JKR contact theory in the loading phase of adhesive solids. Lin et al.<sup>89</sup> later extended this study to the unloading part.

Johnson<sup>94</sup> and Unert<sup>95</sup> have shown that the crack tip and long range creep phenomena generally occur on very different time scales. Depending on the characteristic relaxation time of the viscoelastic material as well as the experimental measurement time, both can be important. Recently, Hui and coworkers have put forward a model that accounts for linear viscoelastic response at all length and times scales.<sup>89,96</sup>

#### 2.2.3.4 Other factors affecting adhesion

External factors that are important in evaluating the adhesion between two surfaces include temperature, humidity, surface roughness, contaminants and the total interfacial contact time. In this section, the discussion mainly concerns the effects of surface roughness and humidity.

##### *Surface roughness*

The real contact area influences several physical properties such as the contact resistivity, adhesion, friction, etc. Hertz studied the frictionless contact between elastic solids with smooth surface profiles. This theory predicts that the contact area  $A$  increases non-linearly with the loading force  $F$  as  $A \sim F^{2/3}$ . In a sphere-plane configuration, where the sphere is considered to have a rough surface, the simplest model of a rough but nominal surface consists of a regular array of spherical bumps of equivalent radii of curvature  $R$  and equivalent heights. If such a surface is in contact with a flat surface of an elastic solid, the Hertz contact model can be (approximately) applied to each asperity contact region. Moreover, the area of real contact should be proportional to  $F_N^{2/3}$ . However, this does not hold true in experiments with randomly rough surfaces, which show that, even when the contact is purely elastic (*i.e.*, without plastic flow), the area of real contact is proportional to  $F_N$  as long as the contact area  $A$  is small in comparison with the nominal contact area  $A_0$ .

In a pioneering study, Archard<sup>97</sup> showed that in a more realistic model of rough surfaces, where the roughness is described by a hierarchical model consisting of small spherical bumps on top of larger spherical bumps and so on, the real contact area is proportional to the load. This model explains the basic physics in a clear manner, but it cannot be used in practical calculations since real surfaces cannot be represented by the idealized

surface roughness assumed by Archard. A somewhat more useful and applicable model, presented by Greenwood and Williamson,<sup>87</sup> describes the rough surface as consisting of spherical bumps of equal radii of curvature  $R$ , but where the height follows a Gaussian distribution. This model predicts that the area of real contact is almost proportional to the load. The Greenwood-Williamson theory is valid strictly at a low loading force. It also neglects the elastic coupling between micro-asperity contact regions. A more refined model based on the same assumptions was developed by Bush et al.<sup>98,99</sup> Here, the height distribution is described by a random process, and it was found that at a low loading force, the area of real contact increased linearly with  $F_N$ . In summary, for a rough surface, conventional contact mechanics models require modification.

### **Humidity**

In an environment of high humidity, the formation of a capillary condensation becomes possible when the sphere approaches the flat surfaces as shown in Figure 2.7a. Capillary forces can then dominate the interaction between the sphere and plane. The general formula for the adhesive force between two bodies with capillary condensation is given by:<sup>100</sup>

$$F = F(\Delta P) + F_{\text{solid-solid}} + F(\gamma_{LV}) \quad (\text{Eq. 2-27})$$

where  $F(\Delta P) = 4\pi R \gamma_{LV} \cos\theta$  is the force due to the Laplace pressure  $\Delta P$  within the meniscus,  $F_{\text{solid-solid}}$  is the force due to direct solid-solid interaction, and  $F(\gamma_{LV}) = 2\pi R \gamma_{LV} \sin\phi \sin(\theta + \phi)$  is the resolved force due to the liquid/vapor surface tension.<sup>101, 102</sup>

When the sphere and plane are separated by a small distance  $D$ , as shown in Figure 2.7b, the force due to the Laplace pressure in the liquid bridge may be calculated according to:<sup>103</sup>

$$F = 4\pi R^2 \phi \gamma_L \cos\theta \frac{d\phi}{dD} \quad (\text{Eq. 2-28})$$

Assuming that the liquid volume remains constant, Equation 2-28 then becomes:

$$F = \frac{4\pi R \gamma_L \cos\theta}{1 + D/d} \quad (\text{Eq. 2-29})$$



One alternative can be to consider the Kelvin equilibrium condition. The Kelvin equation relates the equilibrium meniscus curvature to the relative vapor pressure; and if the Kelvin equilibrium is maintained during the separation process, the adhesive force becomes:

$$F = -4\pi R \gamma_{LV} \cos \theta \left( 1 - \frac{D}{2r_m \cos \theta} \right) \quad (\text{Eq. 2-30})$$

Here,  $r_m = (1/r_1 + 1/r_2)^{-1}$  is the meniscus curvature. When limited to small surface separations, the adhesive force and its gradient strive toward the same value for both the constant-meniscus-volume and Kelvin-equilibrium conditions.

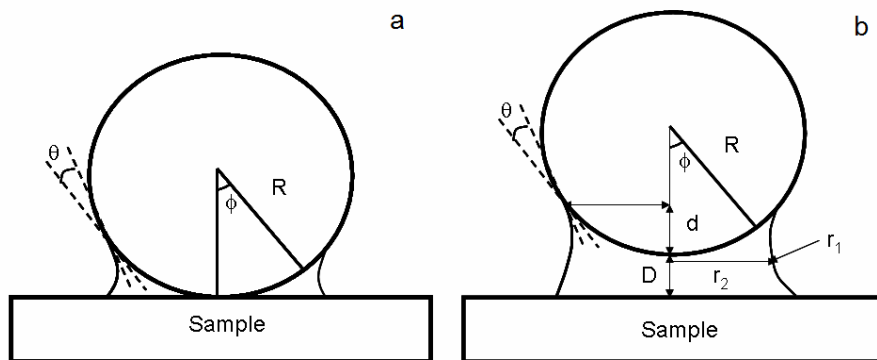


**Figure 2.7** a) A schematic of a liquid meniscus around the sphere. b) A schematic of a liquid meniscus between the sphere and plane at finite separation.<sup>100, 104</sup>

## 2.2.4 Fracture mechanics

Practical adhesion (adherence) comes from real destructive adhesion tests. In other words, the adherence, which is expressed in terms of fracture energy, is the energy required to separate bonded asymmetric bodies. As a first step, a relationship between the fundamentals of adhesion (thermodynamic *work of adhesion*) and adherence is clarified.

### 2.2.4.1 Griffith criterion

The values of the thermodynamic *work of adhesion*  $W$  occupy only a small range from 0.1-10 Jm<sup>-2</sup>. In practice, the measured adherence is larger than this value. A relatively simple way to understand their relationship is via an energy balance approach following the theory of *Griffith*.<sup>105</sup>

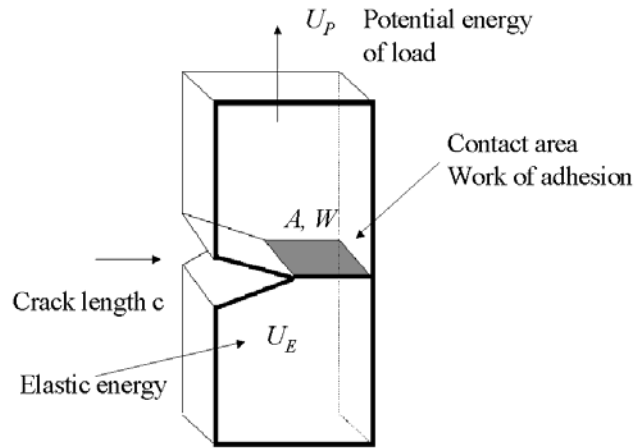


**Figure 2.8** A schematic view of the Griffith fracture mechanics theory.<sup>106</sup>

When two elastic bodies are in contact over an area  $A$  under a tensile load (as shown in Figure 2.8), the separation of the two bodies can be seen as the propagation of a crack toward the center of contact. The crack extension is here demonstrated in mode I (opening mode, with the crack faces moving apart perpendicularly). The equilibrium of the system under a force  $P$  can be tested by varying the  $dA$  of the contact area, at a constant temperature. For an isolated system, the free energy  $F$  cannot be increased, whereas for a reversible and isothermal change, the variation in free energy is equal to the variation in total energy  $U_T$ :

$$dF = dU_T = dU_E + dU_P + dU_S \leq 0 \quad (\text{Eq. 2-31})$$

Here,  $U_E$ ,  $U_P$ ,  $U_S$  represent respectively the stored elastic energy, the potential energy of the load  $P$  and the stored energy at the interface defined by :

$$dU_S = -WdA \quad (\text{Eq. 2-32})$$

The energy release rate, defined as the fracture energy per unit area can be written as:

$$G = \partial U_E / \partial A + \partial U_P / \partial A \quad (\text{Eq. 2-33})$$

Consequently, the variation in free energy during a spontaneous change becomes:

$$dF = dU_T = (G - W)dA \leq 0 \quad (\text{Eq. 2-34})$$

The equilibrium is thus given by:

$$G = W \quad (\text{Eq. 2-35})$$

This equilibrium relation is called *Griffith's criterion*. It links  $P$  to  $A$  during equilibrium at a fixed load. When  $G > W$ , the fracture will proceed provided that the release of potential energy is sufficient to supply the energy required for creating new fracture surfaces (crack propagation).  $GdA$  is the mechanical energy released when the crack extends by  $dA$ . The breaking of interface bonds requires the energy  $WdA$ . The excess  $(G-W) dA$  is converted into kinetic energy assuming there is no dissipative factor. Thus, there exists a “crack extension force”  $G-W$  applied to a unit area of crack. Under this force, the crack has a limited speed  $v$ , which is a function of the temperature (through the Williams-Landel-Ferry (WLF) shift factor  $a_T$ ), and one can write:<sup>80, 107</sup>

$$G = W \{1 + \Phi(a_T \cdot v)\} \quad (\text{Eq. 2-36})$$

The right hand side of Equation 2-36 corresponds to the drag due to viscoelastic losses at the crack tip and is proportional to  $W$  as proposed by Gent et al.,<sup>108</sup> and Andrews et al.<sup>109</sup> When the function  $\Phi$ , a characteristic of the viscoelastic material, is known, the equation enables the prediction of the detachment kinetics, provided that the failure is an adhesive failure and the viscoelastic losses are limited to the crack tip.<sup>110</sup>

In some papers, the *Griffith* theory is written as

$$G = G_0 \{1 + \Phi(a_T \cdot v)\} \quad (\text{Eq. 2-37})$$

In this expression, a larger value for the *work of adhesion*  $G_0$ , known as the “threshold energy” or zero-rate fracture energy is introduced instead of  $W$ .

Another modification to Equation 2-37, which incorporates a mechanism-dependent interfacial term, has been proposed by Shull and Crosby<sup>111</sup>, as shown below:

$$G = W \{1 + \Psi(v', t_c, \dots)\} \{1 + \Phi(a_T v)\} \quad (\text{Eq. 2-38})$$

Here,  $G_0$  takes on a rate dependence of the form  $W(1 + \Psi)$  where  $\Psi$  is a microscopic loss function that accommodates the energy dissipated by any non-dispersive interaction at the interface. Included in this term are energy losses incurred as a result of irreversible rupture of interfacial bonds established through specific interactions (the Lake-Thomas effect),<sup>112</sup> such as hydrogen bonding or contact electrification, or through strong physical interactions such as interdigitation.

The difference between  $G_0$  and  $W$  has been interpreted as the enhancement of the zero rate adhesion energy that arises from the change of state of the interface after adhesive contact. This difference might be a result of specific chemical interactions, interfacial rearrangements etc. The development of such interfacial bonds usually requires certain conditions described by measurable parameters, such as the contact time ( $t_c$ ), annealing temperature, or substrate polarity, which may be incorporated into the  $\Psi$  term. Seeing as interfacially bonded polymer chains will not behave in a purely elastic manner,  $\Psi$  must also include a velocity dependence. It is however independent of that arising from bulk viscoelasticity. Although the term "bulk" is used to describe the parameter  $\Phi$ , the underlying dissipative processes at the crack tip may also be confined to micrometer or even submicrometer length scales. However, the length scale for the "interfacial" effects that contribute to  $\Psi$  is typically limited to a few nanometers, as defined by the distance between interfacial bonds. Equation 2-38 simply presents one possible example of a more general method for separating interfacial and bulk energy loss contributions.

Contacts involving viscoelastic materials are more difficult to analyze since not all of the applied energy reaches the crack tip instantaneously. Several authors have by means of different approaches and various criteria studied either the local crack zone or the global system and the energy conservation principle is applied to the overall system.<sup>85, 92, 93, 113, 114</sup>

#### **2.2.4.2 Adhesion hysteresis**

An interesting aspect of the adhesion between two elastomers brought into contact is the fact that the strain energy release rate required for the crack to grow during unloading is larger than that required for the crack to propagate during loading. This difference,  $G_{ul} - G_l$  or  $G_{ul} - W$  (during loading,  $G_l = W$  at an equilibrium state) called adhesion hysteresis, may arise from a bulk viscoelasticity or from mechanical electrical and/or chemical changes of the materials at the interface. The adhesion hysteresis has been the subject of numerous studies. However, the complex bulk and surface phenomena and their relative importance in determining the adhesion hysteresis is still not fully understood.<sup>62, 115-125</sup>

Silberzan et al.<sup>119</sup> observed the hysteresis upon the unloading of two PDMS hemispheres that had been extracted in chloroform and dried under vacuum. It was postulated that excess unreacted Si-H bonds in the elastomer were oxidized at room temperature to Si-OH and thus promoted hydrogen bonding between the surfaces. Perutz et al.<sup>126</sup> observed

the adhesion hysteresis between PDMS networks that had been deliberately hydrolyzed through exposure to 0.1 M HCl aqueous solutions. The hysteresis was here attributed to a surface reconstruction reaction between silanol groups. In contrast, Emerson et al.<sup>127</sup> demonstrated that the presence of SiH groups was not essential for the hysteresis to form between toluene extracted hemispheres. Unreacted SiH groups were removed in a reaction with ethylene gas, but the hysteresis still remained. In this case it was argued that the hysteresis resulted from the entanglement of chains across the interface. Choi et al.<sup>120</sup> also observed an adhesion hysteresis between PDMS elastomers after extraction in toluene. Entanglements were given as the reason for the observed hysteresis, also in this case. Pickering et al.<sup>128</sup> measured the adhesion of PDMS against both glass and mica in either air or dry nitrogen. It was observed that the adhesion hysteresis depended strongly on the initial contact time, the ambient humidity, and the hydrophilicity of the surface. It could thus be deduced that the capillary forces increased the observed hysteresis.

Israelachvili classified his surface as crystalline or solid-like, amorphous and liquid-like (as displayed in Figure 2.9) layers. The crystalline surfaces tended not to reorganize, thus giving rise to a low hysteresis. The liquid-like surfaces reorganized very quickly both upon loading and unloading, and the hysteresis was low also in this case. For the amorphous surfaces, on the other hand, reorganization could take place over a significant time scale, and this case generally displayed the largest hysteresis.

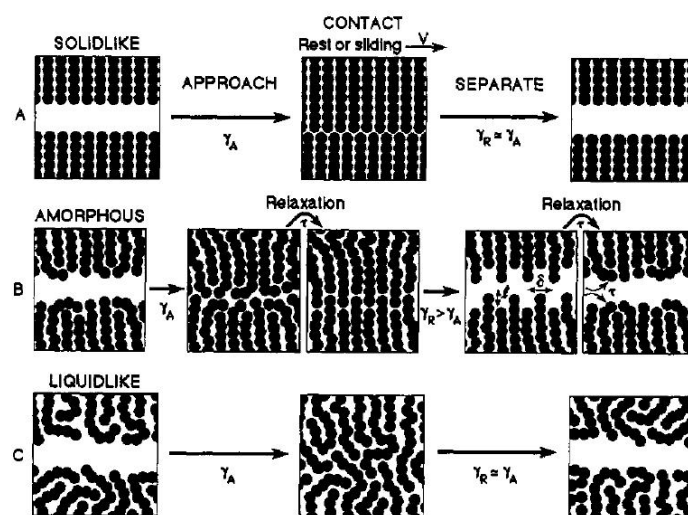


**Figure 2.9** A schematic representation of crystalline or solid-like, amorphous and liquid-like layers.<sup>129</sup>

Knowledge of the mechanisms behind hysteresis formation is helpful when making practical decisions. The separability of the interfacial and bulk factors in Equation 2-38 suggests two general classes of strategies for controlling the elastomer adhesion, *i.e.* strategies based on changing  $G_0$  through interface modification and those that alter  $\Phi$  by manipulation of the elastomer's bulk properties. On a simplistic level, the analogy with viscoelastic loss is obvious. It is not surprising to find that the adhesion hysteresis is considered to have a temperature/rate dependence (as shown in Figure 2.10). Additionally, a combination of these effects may be used to modify the adhesive properties, as large-scale changes in bulk properties are often coupled to changes in surface energy.

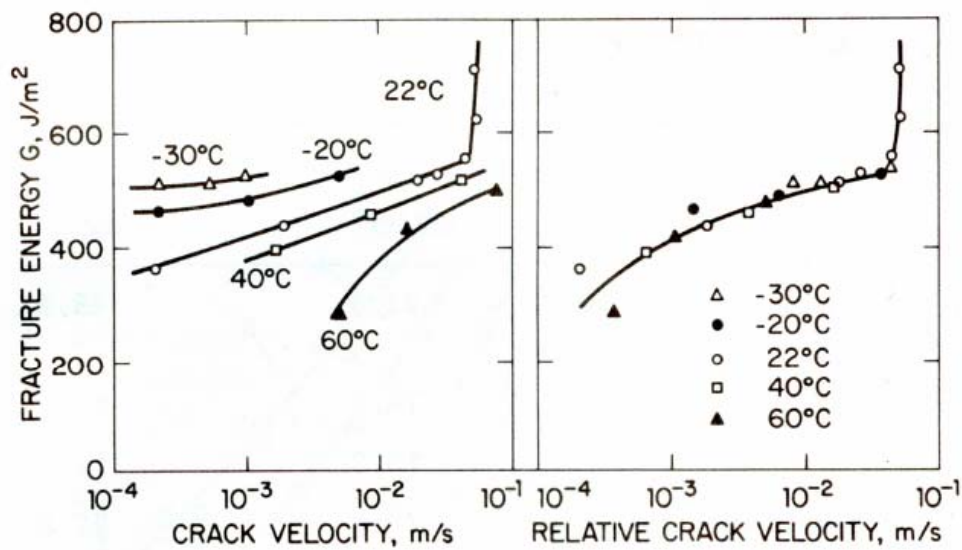


**Figure 2.10** The temperature dependence of the fracture energy for a slow crack propagation in poly(methyl methacrylate).<sup>237</sup>

In many cases, it is undesirable as well as impractical to alter the bulk properties of an elastomer. Hence, the preferred route is often to alter the interfacial properties by surface modification of the substrate, as commonly exemplified by the use of poly-(tetrafluoroethylene) (PTFE or Teflon)-coated surfaces in order to minimize adhesion. A number of so-called chain pullout models have been developed to predict the adhesion enhancement attained through substrate modification by adsorbed or grafted polymer chains. These models have been compared with experimental results for several elastomeric systems.<sup>123, 130, 131</sup> The fracture toughness increases in an essentially linear manner with the molecular weight of the polymer brush and shows a maximum as a function of the areal brush density.

In other words, it first increases as a result of the interpenetration into the elastomer brush but then falls back to the thermodynamic *work of adhesion* as the brush density becomes too high to allow for significant penetration.<sup>132-135</sup>

### 2.2.4.3 Stress intensity analysis

The connection between the strain energy release rate, which is a global quantity, and the stress intensity factor, which expresses the strength of the local elastic stress field in the neighbourhood of the crack tip, is of great importance. Irwin<sup>136</sup> has analyzed fracture in terms of crack tip stress fields. There are three major loading modes. Mode I is defined as the opening mode or tensile mode. In this mode the crack surfaces move directly apart, as shown in Figure 2.11, and this is encountered in an overwhelming majority of practical situations. By using the crack tip stress function of Westergaard,<sup>137</sup> Irwin gave the following relations of stress:

$$\sigma_x = \frac{K_I}{\sqrt{2\pi r}} \cos \frac{\theta}{2} \left( 1 - \sin \frac{\theta}{2} \sin \frac{3\theta}{2} \right) \quad (\text{Eq. 2-39})$$

$$\sigma_y = \frac{K_I}{\sqrt{2\pi r}} \cos \frac{\theta}{2} \left( 1 + \sin \frac{\theta}{2} \sin \frac{3\theta}{2} \right) \quad (\text{Eq. 2-40})$$

$$\tau_{xy} = \frac{K_I}{\sqrt{2\pi r}} \left( \sin \frac{\theta}{2} \cos \frac{\theta}{2} \cos \frac{3\theta}{2} \right) \quad (\text{Eq. 2-41})$$

where  $\sigma$  is the normal stress,  $\tau$  the shear stress,  $\theta$  the polar angle and  $r$  the radial coordinate. The constant  $K_I$  is the parameter that determines the magnitude of the local stress for a given specimen configuration and applied stress, and is termed the stress intensity factor.

The periphery of the contact is viewed as the tip of a crack. If  $a$  increases, the crack closes, whereas if  $a$  decreases, the crack opens. The crack propagates with the speed  $v = -da/dt$ . The energy flow to the crack tip per unit area of crack extension is given by the strain energy release rate,  $G$ , which is related to the stress intensity factor as:

$$G = K_I^2 / E \quad (\text{Eq. 2-42})$$

for plane stress and as:

$$G = K_I^2 (1 - \nu^2) / E \quad (\text{Eq. 2-43})$$

for plane strain.

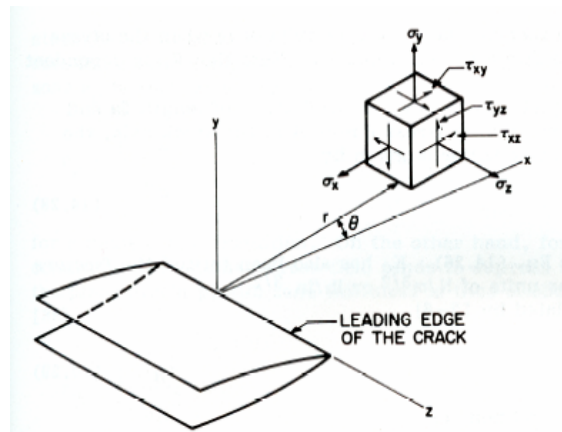


**Figure 2.11** Coordinates measured from the leading edge of a crack and stress components in the crack tip stress field.<sup>106</sup>

## 2.2.5 Adhesion characterization methods

In order to understand adhesion phenomena, a variety of adhesion tests have been developed in addition to the modeling of contact mechanics. Traditionally, the adhesion between two materials has been investigated by tack or peel measurements. Many of the fundamental concepts have been introduced in the context of various experimental geometries based on the work of Rivlin and Thomas,<sup>138</sup> Lake and Thomas,<sup>112</sup> Gent et al.<sup>139-144</sup>, Maugis et al.,<sup>80, 145</sup> De Gennes,<sup>146-148</sup> and many others. These measurements have provided a wealth of information about nonspecific interactions, but understanding the true nature of the adhesion still requires a direct measurement. Experimental techniques that are able to measure forces in this range under a variety of ambient conditions and solvents have only become available during recent decades. Specifically, three techniques are capable of such measurements: a surface force apparatus (SFA), a JKR apparatus or an ATD and AFM. This section mainly discusses these three methods as they are the most popular and capable of directly measuring the adhesive forces.

### 2.2.5.1 Surface force apparatus (SFA)

The surface force apparatus is the first equipment to successfully measure forces between surfaces as a function of their separation for distances below 100 nm.<sup>149, 150</sup> It consists of crossed mica cylinders with radii on the order of centimeters. The configuration of the set up is shown in Figure 2.12. One surface is fixed while the other is mounted on a



flexible force sensing beam. The distance between the two cylinders is usually measured by white light interferometry using fringes of equal chromatic order (FECO). Nowadays, the equipment is capable of measuring forces in the range  $10^{-8}$ -1 N with a vertical distance resolution of  $\pm 0.5$ -1 Å.<sup>151</sup> A modified version has been developed by Klein,<sup>152</sup> Parker et al.<sup>153</sup>, and Israelachvili and McGuigan.<sup>154</sup> Furthermore, Tonck et al.<sup>155</sup> have extended the SFA method to opaque materials, replacing the optical technique for measuring distances by a capacitance method. The SFA has also been used to study various forces, including van der Waals forces, double layer forces, viscous and hydration forces, as well as adhesion and friction.

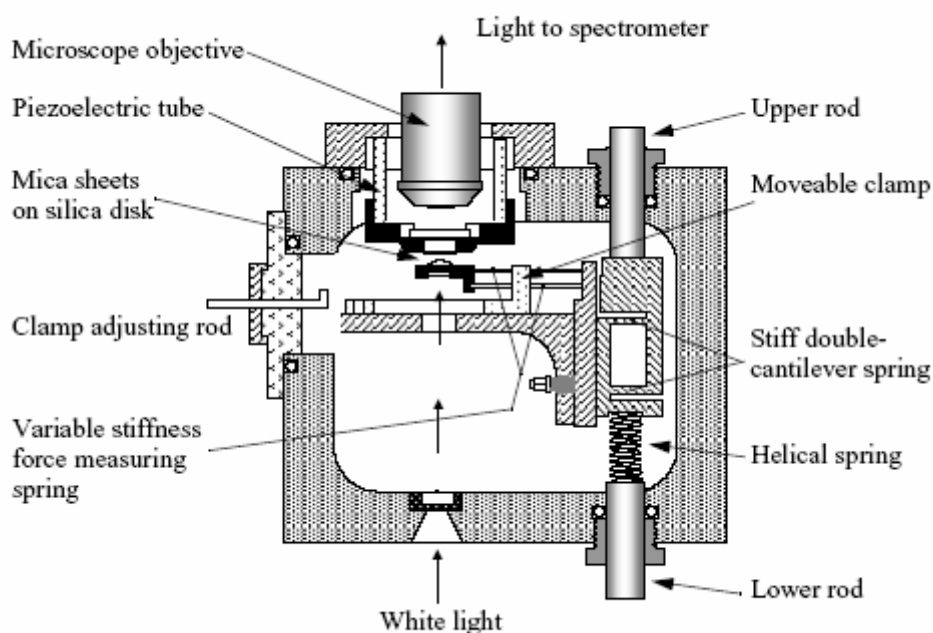


**Figure 2.12** A schematic of the surface forces apparatus.<sup>45</sup>

An approach to studying the molecular details of surface interactions is to directly measure the forces between the surfaces of interest. In particular, force distance profiles measured with the surface force apparatus,<sup>45, 154, 156-161</sup> can be quantitatively analyzed in terms of the various contributing fundamental surface forces. These include van der Waals, electrostatic double layer,<sup>159, 160</sup> hydration,<sup>161, 162</sup> osmotic,<sup>156</sup> steric<sup>163</sup> and hydrophobic interactions.<sup>164</sup> Direct force measurements of specific receptor-ligand binding events,<sup>165-168</sup> as well as non-specific protein interactions<sup>165, 169</sup> have also been carried out with the SFA technique.

SFA provides a means of measuring the thermodynamic or intrinsic *work of adhesion* between polymer surfaces in a direct mechanical manner. This is possible because of the small contact area between the surfaces and the slow rate of crack propagation in the SFA.<sup>170</sup>

Although the SFA has produced many interesting results, it is subject to several limitations. However, one of the biggest limitations is that the surfaces must be smooth over a large area, as well as flexible. Moreover, the instrument does not provide any mapping or imaging of the surface.

### **2.2.5.2 Atomic force microscopy (AFM)**

AFM possesses both the sub-nanometer spatial resolution and pico-newton force resolution necessary for characterizing the strength and spatial distribution of intermolecular interactions. A sensitive spring is used to determine the force. A piezo electric crystal, which is sufficiently well calibrated, is employed to alter the separation of the tip and surface. With commercially available cantilevers, AFM may be utilized to measure forces accurately down to approximately 10 pN.<sup>171</sup>

AFM development envelopes numerous measurements that utilize a range of physico-chemical interactions between a tip and sample surface. AFM not only generates images of sample surface permitting the observation of their structural or dynamic features; but has also been successfully applied to studies of polymers,<sup>172-175</sup> biologic systems<sup>174, 176</sup> and interfacial phenomena.<sup>177-179</sup>

One can routinely quantify both the net surface force and its separation dependence as the probe approaches the sample, and consequently any adhesion or pull-off force on retraction. A practical experiment of interest is to attach a colloid particle to the end of the cantilever in order to study the interaction with a sample of choice. This method is often referred to as colloid probe microscopy.

Two detailed reviews concerning adhesion as measured by AFM have been put forward by Cappella<sup>180</sup> and Butt.<sup>181</sup> Much of the present understanding of elastic adhesion mechanics of spheres on planar substrates is based on the theoretical work of JKR and DMT. The point of contact is defined as the intersection between the contact region and the non-contact region of the force curve, *i.e.* it is the point of contact at which height the tip would have touched the sample.<sup>182</sup> The contact area can be described and expressed by several theories of continuum contact mechanics,<sup>180</sup> in addition to modern molecular dynamic

calculations that have been the source of many important insights into nano-scale mechanics. Choosing the appropriate theory depends on the relative magnitudes of the material properties and surface forces.

There are several features of AFM that make it ideal for force sensing, such as the sensitivity of the displacement (round 0.01 nm), the small contact area between tip and sample, and the ability to operate under physiological conditions.<sup>183</sup> Through AFM measurements it is possible to obtain the following information. 1) the magnitude of the force that depends on long-range attractive and adhesion forces; 2) an estimation of the point of tip-sample contact; 3) the tip-sample contact area; and 4) the elastic modulus and plasticity of thin and thick films.<sup>180</sup> It is also possible to investigate the complex inter- and intramolecular interactions, the ranges in magnitude, the time dependence of rupture forces, the mechanical properties of molecules and the strength of individual bonds.<sup>175, 184-188</sup>

However, the utility of the standard AFM setup for measuring specific forces is severely limited by the unknown chemical composition of the AFM tip. Standard silicon and silicon nitride probes present a poorly defined chemical interface and often pick up contaminations during a measurement. A concept of chemical force microscopy (CFM), introduced by Lieber and coworkers,<sup>189</sup> replaces the poorly characterized tip-sample interface with a well-defined interface produced by deliberate functionalization of the AFM tip surface. These modifications render AFM a useful tool for measuring specific and well-defined chemical interactions. A careful design of the probe modification can also prevent contaminations, control the number of interacting molecules, and even spatially separate different types of interactions. Researchers have used chemically modified AFM probes for a number of applications, including adhesion and friction measurements, as well as high resolution imaging.<sup>36, 189-193</sup> The Lieber group showed that covalent modifications of the AFM probes allowed them to distinguish between the interactions of basic functional groups.<sup>189-191, 194, 195</sup> Researchers quickly expanded these studies to include a larger number of functional groups as well as solvents, and Table 2.2 summarizes some of these data (certain data adapted from ref. <sup>196, 197</sup>). However, even a quick look at these data shows that an idea of determining a defined bond strength which would be characteristic for a particular interaction is too simplistic. Interaction forces measured between identical functionalities in a variety of solvents can differ by almost one order of magnitude. Measurements performed by several research groups, where a similar probe functionalization has been used in one type of solvent can also produce different results. It is thus clear that the interaction force can be influenced

by a number of different parameters and in order to understand the situation, the microscopic dynamics of the unbinding process should be taken into account.<sup>197</sup>

Furthermore, the emerging kinetic view of intermolecular interactions has introduced a completely new paradigm for understanding these interactions. The kinetic model shows that the strength of the measured interactions depends not only on the energy landscape of the system, but also on the loading history prior to the bond breakup.<sup>198, 199</sup> This new paradigm refocuses our attention on the energy landscape as a fundamental characteristic for the interaction. Moreover, the dynamic force spectroscopy approach derived from the kinetic model allows a direct characterization of the potential energy barrier geometry.<sup>200-202</sup> Further investigation of the interactions in various systems, especially bimolecular interactions, will uncover numerous interesting intermolecular characteristics. These studies have the potential to, for the first time, reveal a true picture of the energy landscapes in complex chemical and biological systems.<sup>203-209</sup>

**Table 2.2** The interaction strength between AFM tips and samples functionalized with specific functional groups measured in various solvents. The results were obtained by selected pull-off force measurements performed with thiol-modified tips.

Functionality	Solvent	Pull-off force (nN)	Reference
CH <sub>3</sub> -CH <sub>3</sub> , C <sub>18</sub>	EtOH	1.0±0.4	190
CH <sub>3</sub> -CH <sub>3</sub> , C <sub>12</sub>	EtOH	2.3±1.1	210
COOH-CH <sub>3</sub> , C <sub>11</sub> , C <sub>18</sub>	EtOH	0.3±0.2	190
COOH-COOH, C <sub>11</sub>	EtOH	2.3±0.8	190
COOH-COOH, C <sub>11</sub>	EtOH	0.27±0.04	210
COOH-COOH, C <sub>11</sub>	PrOH	1.37±0.26	211
CH <sub>2</sub> OH-CH <sub>2</sub> OH, C <sub>11</sub>	EtOH	0.18±0.18	210
CH <sub>3</sub> -NH <sub>2</sub> , C <sub>11</sub>	EtOH	0.3±0.06	212
CH <sub>3</sub> -COOH, C <sub>11</sub>	EtOH	0.3±0.06	212
CH <sub>3</sub> -CONH <sub>2</sub> , C <sub>11</sub>	EtOH	0.3±0.06	212
NH <sub>2</sub> -NH <sub>2</sub> , C <sub>11</sub>	EtOH	0.8±0.16	212
CONH <sub>2</sub> -CONH <sub>2</sub> , C <sub>11</sub>	EtOH	1.8±0.36	212
CONH <sub>2</sub> -OH, C <sub>11</sub>	EtOH	1.3±0.26	212
CONH <sub>2</sub> -NH <sub>2</sub> , C <sub>11</sub>	EtOH	1.2±0.24	212
CONH <sub>2</sub> -COOH, C <sub>11</sub>	EtOH	2.2±0.44	212
NH <sub>2</sub> -COOH, C <sub>11</sub>	EtOH	0.7±0.14	212
NH <sub>2</sub> -OH, C <sub>11</sub>	EtOH	0.5±0.1	212
COOH-OH, C <sub>11</sub>	EtOH	1.2±0.24	212
OH-OH, C <sub>11</sub>	EtOH	0.9±0.18	212
CH <sub>3</sub> -CH <sub>3</sub> , C <sub>12</sub>	CH <sub>3</sub> (CH <sub>2</sub> ) <sub>14</sub> CH <sub>3</sub>	0.07±0.05	210
COOH-COOH, C <sub>11</sub>	CH <sub>3</sub> (CH <sub>2</sub> ) <sub>14</sub> CH <sub>3</sub>	0.11±0.02	210
COOH-COOH, C <sub>11</sub>	Hexane	0.95±0.26	211
CH <sub>3</sub> -CH <sub>3</sub> , C <sub>12</sub>	Water	12.5±4.4	210
CH <sub>3</sub> -CH <sub>3</sub> , C <sub>18</sub>	Water	60±5	213
COOH-COOH, C <sub>11</sub>	Water	2.8±0.2	211
COOH-COOH, C <sub>11</sub>	Water, pH<5	7.0±0.2	213
COOH-COOH, C <sub>11</sub>	Water, DI	2.3±1.1	210
COOH-CH <sub>2</sub> OH, C <sub>11</sub>	Water, pH<5	1.1±0.5	213
CH <sub>2</sub> OH-CH <sub>2</sub> OH, C <sub>11</sub>	Water, pH<5	1.0±0.2	213
CH <sub>2</sub> OH-CH <sub>2</sub> OH, C <sub>11</sub>	Water, DI	0.3±0.5	210

### 2.2.5.3 Adhesion testing device (ATD)

A device within microscopic contact mechanics known as the "JKR equipment" or "adhesion testing device (ATD)", based upon the contact mechanical theory of Johnson, Kendall, and Roberts (JKR), is becoming an increasingly popular technique for studying the adhesion of elastomers.<sup>62, 117, 119, 124, 132, 214-218</sup> The JKR apparatus introduced by Chaudhury and Whitesides<sup>117, 219</sup> was found to be particularly sensitive to interfacial effects since bulk viscoelastic losses due to sample deformation are minimized by the small volume of the lenses typically used. In these experiments, the contact radius was studied as a function of the

applied load. The method is relatively simple as compared to that of the SFA. A typical scheme of the apparatus is illustrated in Figure 2.13.<sup>62</sup> In JKR or ATD experiments, typically two caps, or alternatively one cap and one flat surface, of either identical or varying materials are brought into contact. Two regimes, *loading* and *unloading*, are conducted within the experiment and these represent rough counterparts of the advancing and receding angles in contact angle measurements. The actual amount of work necessary to separate the surfaces is related to the adherence, which in turn depends on the  $W$ , surface energies, mechanical properties, surface roughness, contact time and a number of other factors. Parallel attempts have been carried out to investigate the hysteresis between loading and unloading.<sup>119, 120, 126, 128, 215, 220</sup>

One of the most important differences between the ATD and AFM techniques is the length scale. Thus, AFM and ATD measurements can be used as complementary methods in order to bridge the nano- and micro-scale adhesion measurements, and ultimately provide more comprehensive information from the studied surfaces.

In the ATD experiment, the PDMS lens is able to interact with the surface on the micrometer scale, elastically following the surface topography in a conformal fashion.<sup>217</sup> The ATD method utilizes a multi-asperity contact geometry for rough surfaces, whereas AFM essentially encompasses quasi-single asperity contacts.<sup>221, 222</sup> The influence of the surface roughness on the obtained values of  $W$  must differ between these techniques, as a result of their different nature and scales. In addition, the ATD probe is a soft, flexible elastomeric lens, while the AFM tip is a stiff, solid material. The hard tip can penetrate the soft surface of the material prior to the pull-off adhesion measurement, thus allowing more complex interactions between the interacting bodies and resulting in apparently higher adhesion data.<sup>223</sup> Furthermore, AFM possesses both the sub-nanometer spatial resolution and pico-Newton force resolution necessary for characterizing the strength and spatial distribution on intermolecular interactions.

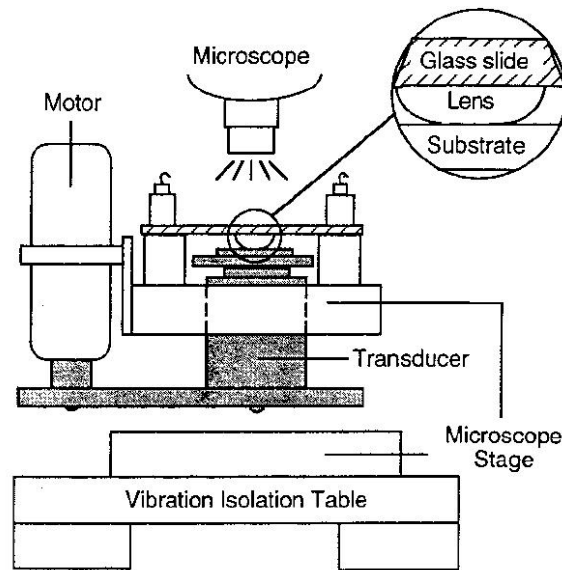


**Figure 2.13** A schematic of the apparatus for JKR adhesion studies, displaying the elastomeric lens and substrate in the inset.<sup>62</sup>

### 2.2.6 Friction and adhesion

When two polymers slide over each other, or when one polymer slides over a rigid substrate, the force of friction between them can be examined. However, a quantitative treatment can be used to explain the basic laws of friction which were presented by Amontons as early as 1699:

- (i) The frictional force between two bodies is independent of their area of contact.
- (ii) The frictional force between two bodies is directly proportional to the load perpendicular to the interface.
- (iii) The frictional force is independent of velocity.

Friction was considered to be the interlocking of surface asperities prior to Hardy's observation that a monolayer of lubricant reduces friction. Following the inadequacy of the theory of interlocking, adhesion was considered a better explanation. The modern study of friction started in the 1950's and was headed by Bowden and Tabor. They found that friction is independent of the apparent contact area, but is proportional to the true contact area. The relationship between adhesion and friction has subsequently been at the center of the interest of tribologists. If two surfaces adhere to each other, a finite friction force can arise even in the absence of any weight or externally applied load. This is a result of the two surfaces

experiencing an effective additional load  $L_0$  due to the attractive forces between them. Thus, between two adhering surfaces, the total friction force can be expressed as:

$$F = \mu(L_0 + L) = F_0 + \mu L \quad (\text{Eq. 2-44})$$

where  $F_0 = \mu L_0$  is a constant arising from the friction force due to adhesion and  $\mu = dF / dL$  is the normal friction coefficient, determined by the structure of the interlocking asperities as before. Israelachvili et al.<sup>129</sup> have reported that the absolute magnitude of adhesion is not directly correlated with the friction force value, and have suggested that the adhesion hysteresis is in close relation with friction. All mechanisms of friction and wear should be related to adhesive mechanisms since no one has denied that atomic bonding may take place during sliding. However, there is no general relationship between adhesion and friction forces, even though in specific situations the two may well be highly correlated.<sup>224, 225</sup> Further investigations are thus needed.

### 2.2.7 Frontiers on polymer adhesion applications

Polymeric solids have been used in numerous industrial applications. In this section, new trends within the study of polymer adhesion are reviewed.

#### 2.2.7.1 High throughput of measurements

Combinational and high throughput experimental design has been advocated by both industry and academia in areas such as coating, tissue scaffolds and mechanical property measurements. Current high-throughput methodologies for measuring the interfacial adhesion typically rely on serial or sequential testing of discrete or continuous libraries. Forster et al.<sup>226</sup> developed a measurement platform that employs an array of micro-lenses to simultaneously measure the adhesion at multiple points on a library of planar specimens. This technique relies on the accurate measurement of the overall lens array displacement, rather than the load and the individual lens contact areas, to quantify the *work of adhesion* using the JKR model. The multilens arrays require a different type of analysis as compared to the traditional JKR tests. This is due to the inability to accurately measure the load on each lens.

#### 2.2.7.2 Surface patterns for adhesion control

Defined surface structures of various shapes and length scales can impact the adhesion of polymer interfaces. Most recent research has focused on the use of post-like structures with high aspect ratios in order to modify the formation and separation mechanisms for an



interface. These mechanisms for controlling the adhesion are inspired by the natural mechanisms present in species such as the gecko and the jumping spider. Although post-like structures are effective, numerous other geometries can impact adhesion properties through a variety of mechanisms. Several research groups have demonstrated how micro- and nano-fabricated structures on polymer surfaces can control the adhesion of an interface.<sup>227-232</sup> The primary mechanism for controlling adhesion is the balance of initiation and propagation events during the interfacial separation.<sup>230, 233 234</sup>

### **2.2.7.3 Evaluating adhesion under water**

With a proper control of experimental conditions, the JKR technique can be extended to evaluate adhesion properties under water. Techniques suitable for underwater adhesion measurements are essential for understanding adhesion phenomena in aqueous environments. Some examples of such phenomena include fouling, antifouling, protein adsorption, blood coagulation, and cell adhesion. The method has also been applied for monitoring the adsorption of non-ionic surfactants onto a solid surface in an aqueous solution.<sup>235, 236</sup>

### **2.2.8 Summary**

Interfacial energy, structure and adhesion are important parameters in the science and technology concerning the formulation of materials, the design of engineering structures, and thin film applications. Miniaturization down to the micro and now to the nano level of mechanical, electrical and optical devices has relied heavily on the understanding and the technology of adhesion. The physical and mechanical properties of materials are significantly affected by the structure and strength of interfaces. To understand this, a discussion was carried out on how an interface is formed and interfacial science, stress analysis and fracture mechanics were combined with an interdisciplinary approach. It was demonstrated that direct tests are possible with AFM, SFA and ATD measurements at a nano- to microscale, and ultimately, the frontier between adhesion and friction between polymers was discussed.

## References

- [1] Lyklema, J., *Fundamentals of Interface and Colloid Science*. Academic Press: San Diego, 1995.
- [2] von Helmholtz, H. L. F., *Ann. Physik* **1879**, 7, 337.
- [3] Gouy, G., *J. Phys. Radium* **1910**, 9, 457.
- [4] Champman, D. L., *Philos. Mag.* **1913**, 25, 475.
- [5] Derjaguin, B. V.; Landau, L. D., *Acta Physicochim. USSR* **1941**, 14, 633.
- [6] Verwey, E. J. W.; Overbeek, J. T. G., *Theory of the Stability of Lyophobic Colloids*. Elsevier: New York, 1948.
- [7] Russel, W. B.; Saville, D. A.; Schowalter, W. R., *Colloidal Dispersions*. Cambridge University Press: Cambridge, 1989.
- [8] Kihira, H.; Matijevic, E., *Adv. Colloid Interfac.* **1992**, 42, 1.
- [9] Ryan, J. N.; Elimelech, M., *Colloid Surface A* **1996**, 107, 1.
- [10] Elimelech, M.; Gregory, J.; Jia, X.; Williams, R. A., *Particle Deposition and Aggregation: Measurement, Modelling and Simulation*. Butterworth-Heinemann: Oxford, 1995.
- [11] Israelachvili, J. N., *Surf. Sci. Rep.* **1992**, 14, 109.
- [12] Lotters, J. C.; Olthuis, W.; Veltink, P. H.; Bergveld, P., *J. Micromech. Microeng.* **1997**, 7, 145.
- [13] Abu Bakar, M. S.; Cheang, P.; Khor, K. A., *Compos. Sci. Technol.* **2003**, 63, 421.
- [14] Fischer-Cripps, A. C., *Nanoindentation*. Springer-Verlag: New York, 2002.
- [15] Buchko, C. J.; Slattery, M. J.; Kozloff, K. M.; Martin, D. C., *J. Mater. Res.* **2000**, 15, 231.
- [16] van Landingham, M. R.; Villarrubia, J. S.; Guthrie, W. F.; Meyers, G. F., *Macromol. Symp.* **2001**, 167, 15.
- [17] Briscoe, B. J.; Fiori, L.; Pelillo, E., *J. Phys. D Appl. Phys.* **1998**, 31, 2395.
- [18] Vaenkatesan, V.; Li, Z. L.; Vellinga, W. P.; de Jeu, W. H., *Polymer* **2006**, 47, 8317.
- [19] Sawyer, L.; Michael, J., *Scanning Electron Microscopy and X-Ray Microanalysis*. Kluwer Academic/Plenum Publishers: New York, 2003.
- [20] Magonov, S. N.; Whangbo, M. H., *Surface Analysis with STM and AFM: Experimental and Theoretical Aspects of Image Analysis*. VCH Publishers: New York, 1996.
- [21] Comyn, J., *Adhesion Science*. Royal Society of Chemistry: Cambridge, 1997.
- [22] Bhushan, B., *Modern Tribology Handbook*. CRC Press Inc.: Boca Raton, 2001; Vol. 2.
- [23] Okada, Y., *B. Seismol. Soc. Am.* **1985**, 75, 1135.
- [24] Hill, L. W., *Mechanical Properties of Coatings*. Federation of Societies for Coatings Technology: Philadelphia, 1987.
- [25] Ward, I. M., *Mechanical Properties of Solid Polymers*. John Willey & Sons: London, 1971.
- [26] Briggs, D.; Seah, M. P., *Practical Surface Analysis: Auger and X-Ray Photoelectron Spectroscopy*. John Wiley & Sons: New York, 1983.
- [27] Briggs, D., *Handbook of X-ray and Ultraviolet Photoelectron Spectroscopy*. Heyden: London, 1977.
- [28] Chan, C. M., *Polymer Surface Modification and Characterization*. Hanser Publishers: Munich, 1994.
- [29] Andrade, J. D., *Surface and Interfacial Aspects of Biomedical Polymers*. Plenum Press: New York, 1985.
- [30] Benninghoven, A.; Rudenauer, F. G.; Werner, H. W., *Secondary Ion Mass Spectrometry. Basic Concepts, Instrumental Aspects, Applications and Trends*. John Wiley & Sons: New York, 1987.
- [31] Vickerman, J. C.; Briggs, D., *ToF-SIMS Surface Analysis by Mass*. IM Publications and Surface Spectra Limited: Chichester, 2001.
- [32] [http://www.fkf.mpg.de/ga/machines/sims/How\\_does\\_TOF\\_SIMS\\_work.html](http://www.fkf.mpg.de/ga/machines/sims/How_does_TOF_SIMS_work.html).
- [33] Rost, F. W. D., *Fluorescence Microscopy*. Cambridge University Press: Cambridge, 1995.
- [34] *A Guide to Fluorescent Probes and Labeling Technologies*. <http://probes.invitrogen.com/handbook>.
- [35] Lichtman, J. W.; Conchello, J. A., *Nat. Methods* **2005**, 2, 910.
- [36] Schönherr, H.; Vancso, G. J., *J. Polym. Sci. Pol. Phys.* **1998**, 36, 2483.
- [37] Yamada, S.; Israelachvili, J., *J. Phys. Chem. B.* **1998**, 102, 234.

- [38] Maeda, N.; Chen, N. H.; Tirrell, M.; Israelachvili, J. N., *Science* **2002**, 297, 379.
- [39] Razatos, A.; Ong, Y. L.; Sharma, M. M.; Georgious, g., *P. Natl. Acad. Sci. USA*. **1998**, 95, 11059.
- [40] Reich, Z.; Kapon, R.; Nevo, R.; Pilpel, Y.; Zmora, S.; Scolnik, Y., *Biotechnol. Adv.* **2001**, 19, 451.
- [41] Nagaoka, T.; Ohmura, N.; Saiki, H., *Appl. Environ. Microb.* **1999**, 65, 3588.
- [42] Lower, S. K.; Tadanier, C. J.; Hochella, M. F., *Geochim. Cosmochim. Ac.* **2000**, 64, 3133.
- [43] Hubbell, J. A., *Curr. Opin. Biotech.* **1999**, 10, 123.
- [44] Lehr, C. M., *Crit. Rev. Ther. Drug.* **1994**, 11, 119.
- [45] Israelachvili, J. N., *Intermolecular and Surface Forces*. Academic press: London, 1991.
- [46] Fowler, P. W.; Jenneskens, I. W.; Nillot, C.; Popelier, P. L. A.; Price, S. L.; Soncini, A.; Tsuzuki, S.; Wales, D., *Intermolecular Forces and Clusters I (Structure and Bonding)*. Springer: Berlin, 2005.
- [47] Vancso, G. J.; Hillborg, H.; Schönherr, H., *Adv. Polym. Sci.* **2005**, 182, 55.
- [48] Margenau, H.; Kestner, N. R., *Theory of Intermolecular Forces 3rd ed.* Pergamon Press: New York, 1971.
- [49] Lifshitz, E. M., *Zh. Eksp. Teor. Fiz.* **1955**, 29, 94.
- [50] Lifshitz, E. M., *Sov. Phys.* **1956**, 2, 73.
- [51] Dzyaloshinskii, I. E.; Lifshitz, E. M.; Pitaevskii, L. P., *Adv. Phys.* **1961**, 10, 165.
- [52] Langbein, D., *Solid State Commun.* **1973**, 12, 853.
- [53] McLachlan, A. D., *Proc. R. Soc. Lon. Ser-A* **1963**, 271, 387.
- [54] McLachlan, A. D., *Proc. R. Soc. Lon. Ser-A* **1963**, 274, 80.
- [55] Israelachvili, J. N., *Proc. R. Soc. Lon. Ser-A* **1972**, 331, 39.
- [56] Langbein, D., *J. Adhesion* **1972**, 3, 213.
- [57] Langbein, D., *Phys. Rev. B Solid St.* **1970**, 2, 3371.
- [58] Harkins, W. D., *Z. Phys. Chem.* **1928**, 139, 647.
- [59] van Oss, C. J., *Interfacial Forces in Aqueous Media*. Marcel Dekker, Inc., New York: 1994.
- [60] van Oss, C. J.; Good, R. J.; Chaudhury, M. K., *Langmuir* **1988**, 4, 884.
- [61] Clint, J. H., *Curr. Opin. Colloid In.* **2001**, 6, 28.
- [62] Ahn, D.; Shull, K. R., *Macromolecules* **1996**, 29, 4381.
- [63] Kwok, D. Y.; Gietzelt, T.; Grundke, K.; Jacobasch, H. J.; Neumann, A. W., *Langmuir* **1997**, 13, 2880.
- [64] Neumann, A. W., *Adv. Colloid Interfac.* **1974**, 4, 105.
- [65] Kwok, D. Y.; Neumann, A. W., *Colloid. Surface A* **2000**, 161, 49.
- [66] Correia, N. T.; Ramos, J. J. M.; Saramago, B. J. V.; Calado, J. C. G., *J. Colloid Interf. Sci.* **1997**, 189, 361.
- [67] Douillard, J. M., *J. Colloid Interf. Sci.* **1997**, 188, 511.
- [68] Schwarz, U. D.; Holscher, H.; Wiesendanger, R., *Phys. Rev. B* **2000**, 62, 13089.
- [69] Schwarz, U. D., *J. Colloid Interf. Sci.* **2003**, 261, 99.
- [70] Maugis, D., *J. Colloid Interf. Sci.* **1992**, 150, 243.
- [71] Carpick, R. W.; Ogletree, D. F.; Salmeron, J., *J. Colloid Interf. Sci.* **1999**, 211, 395.
- [72] Johnson, K. L., *Tribol. Int.* **1998**, 31, 413.
- [73] Johnson, K. L.; Greenwood, J. A., *J. Colloid Interf. Sci.* **1997**, 192, 326.
- [74] Ting, T. C. T., *J. Appl. Mech.* **1966**, 33, 845.
- [75] Ting, T. C. T., *J. Appl. Mech.* **1968**, 35, 248.
- [76] Barquins, M.; Courtel, R., *Wear* **1975**, 32, 133.
- [77] Johnson, K. L.; Roberts, A. D., *Proc. R. Soc. Lon. Ser-A* **1974**, 337, 217.
- [78] Falsafi, A.; Deprez, P.; Bates, F. S.; Tirrell, M., *J. Rheol.* **1997**, 41, 1349.
- [79] Wahl, K. J.; Stepnowski, S. V.; Unertl, W. N., *Tribol. Lett.* **1998**, 5, 103.
- [80] Maugis, D.; Barquins, M., *J. Phys. D Appl. Phys.* **1978**, 11, 1989.
- [81] Hunter, S. C., *J. Mech. Phys. Solids* **1960**, 8, 219.
- [82] Lee, E. H.; Radok, J. R. M., *J. Appl. Mech.* **1960**, 27, 438.
- [83] Yang, W. H., *J. Appl. Mech.* **1966**, 33, 395.
- [84] Graham, G. A., *Int. J. Eng. Sci.* **1967**, 5, 495.
- [85] Schapery, R. A., *Int. J. Fracture* **1975**, 11, 369.

- [86] Schapery, R. A., *Int. J. Fracture* **1989**, *39*, 163.
- [87] Greenwood, J. A.; Johnson, K. L., *Philos. Mag. A* **1981**, *43*, 697.
- [88] Hui, C. Y.; Baney, J. M.; Kramer, E. J., *Langmuir* **1998**, *14*, 6570.
- [89] Lin, Y. Y.; Hui, C. Y.; Baney, J. M., *J. Phys. D Appl. Phys.* **1999**, *32*, 2250.
- [90] Barthel, E.; Roux, S., *Langmuir* **2000**, *16*, 8134.
- [91] Haiat, G.; Huy, M. C. P.; Barthel, E., *J. Mech. Phys. Solids* **2003**, *51*, 69.
- [92] Schapery, R. A., *Int. J. Fracture* **1975**, *11*, 549.
- [93] Schapery, R. A., *Int. J. Fracture* **1975**, *11*, 141.
- [94] Johnson, K. L. In *Microstructure and Microtribology of Polymer Surfaces*, Tsukruk, V. V.; Wahl, K. J., Eds.; American Chemical Society: Washington, DC, 2000; p 24.
- [95] Unertl, W. N. In *Microstructure and Microtribology of Polymer Surfaces*, Tsukruk, V. V.; Wahl, K. J., Eds.; American Chemical Society: Washington, DC, 2000; p 66.
- [96] Hui, C. Y.; Baney, J.; Kramer, E. J., *Langmuir* **1988**, *4*, 6570.
- [97] Archard, J. F., *Proc. R. Soc. Lon. Ser-A* **1957**, *243*, 190.
- [98] Bush, A. W.; Gibson, R. D.; Thomas, T. R., *Wear* **1975**, *35*, 87.
- [99] Bush, A. W.; Gibson, R. D.; Keogh, G. P., *Mech. Res. Commun.* **1976**, *3*, 169.
- [100] Fisher, L. R.; Israelachvili, J. N., *Colloid. Surface* **1981**, *3*, 303.
- [101] Tabor, D., *J. Colloid Interf. Sci.* **1977**, *58*, 2.
- [102] Visser, J., *Surface Colloid Sci.* **1976**, *8*, 3.
- [103] Carpick, R. W.; Ogletree, D. F.; Salmeron, J., *J. Colloid Interface Sci.* **1999**, *211*, 395.
- [104] Christenson, H. K., *J. Colloid Interf. Sci.* **1985**, *104*, 234.
- [105] Griffith, A. A., *Phil. Trans. Roy. Soc. London A* **1920**, *221*, 163.
- [106] Fischer-Cripps, A. C., *Introduction to Contact Mechanics*. Springer: Berlin, 2000.
- [107] Barquins, M.; Maugis, D., *J. Adhesion* **1981**, *13*, 53.
- [108] Gent, A. N.; Schultz, J., *J. Adhesion* **1972**, *3*, 281.
- [109] Andrews, E. H.; Kinloch, A. J., *Proc. R. Soc. Lon. Ser-A* **1973**, *332*, 385.
- [110] Vallet, D.; Barquins, M., *Int. J. Adhes. Adhes.* **2002**, *22*, 41.
- [111] Shull, K. R.; Crosby, A. J., *J. Eng. Mater.-T. Asme.* **1997**, *119*, 211.
- [112] Lake, G. J.; Thomas, A. G., *Proc. R. Soc. London, Ser. A* **1967**, *300*, 108.
- [113] Bitner, J. L.; Rushford, J. L.; Rose, W. S.; Hunston, D. L.; Riew, C. K., *J. Adhesion* **1981**, *13*, 3.
- [114] Hui, C. Y.; Xu, D. B.; Kramer, E. J., *J. Appl. Phys.* **1992**, *72*, 3294.
- [115] Chaudhury, M. K.; Owen, M. J., *J. Phys. Chem.* **1993**, *97*, 5722.
- [116] Chaudhury, M. K.; Owen, M. J., *Langmuir* **1993**, *9*, 29.
- [117] Chaudhury, M. K.; Whitesides, G. M., *Langmuir* **1991**, *7*, 1013.
- [118] Chen, Y. L.; Helm, C. A.; Israelachvili, J. N., *J. Phys. Chem.* **1991**, *95*, 10736.
- [119] Silberzan, P.; Perutz, S.; Kramer, E. J.; Chaudhury, M. K., *Langmuir* **1994**, *10*, 2466.
- [120] Choi, G. Y.; Kim, S. J.; Ulman, A., *Langmuir* **1997**, *13*, 6333.
- [121] Ellul, M. D.; Gent, A. N., *J. Polym. Sci. Pol. Phys.* **1984**, *22*, 1953.
- [122] Reichert, W. F.; Brown, H. R., *Polymer* **1993**, *34*, 2289.
- [123] Brown, H. R., *Macromolecules* **1993**, *26*, 1666.
- [124] Deruelle, M.; Leger, L.; Tirrell, M., *Macromolecules* **1995**, *28*, 7419.
- [125] Israelachvili, J. N.; Chen, Y. L.; Yoshizawa, H.; Steinberg, S.; Vigil, G.; Xu, Z. G., *Vide-Sci. Tech. Appl.* **1994**, *272*, 8.
- [126] Perutz, S.; Kramer, E. J.; Baney, J.; Hui, C. Y., *Macromolecules* **1997**, *30*, 7964.
- [127] Emerson, J. A.; Miller, G. V.; Sorensen, C. R.; Pearson, R. A., *Proc. ACS Div. Poly. Mat. Sci. Eng.* **1999**, *81*, 385.
- [128] Pickering, J. P.; van der Meer, D. W.; Vancso, G. J., *Proc. ACS Div. Poly. Mat. Sci. Eng.* **1999**, *81*, 389.
- [129] Yoshizawa, H.; Chen, Y. L.; Israelachvili, J., *J. Phys. Chem.* **1993**, *97*, 4128.
- [130] Creton, C.; Brown, H. R.; Shull, K. R., *Macromolecules* **1994**, *27*, 3174.
- [131] Deruelle, M.; Leger, L.; Tirrell, M., *Macromolecules* **1995**, *28*, 7419.
- [132] Brown, H. R., *Annu. Rev. Mater. Sci.* **1991**, *21*, 463.
- [133] Raphael, E.; Degennes, P. G., *J. Phys. Chem.* **1992**, *96*, 4002.
- [134] Ji, H.; Gennes, P. G., *Macromolecules* **1993**, *26*, 520.

- [135] Ligoure, C., *Macromolecules* **1996**, *29*, 5459.
- [136] Irwin, G. R., *J. Appl. Mech.* **1957**, *24*, 361.
- [137] Westergaard, H. M., *J. Appl. Mech.* **1939**, *6*, 49.
- [138] Rivlin, R. S.; Thomas, A. G., *J. Polym. Sci.* **1953**, *10*, 291.
- [139] Gent, A. N.; Lindley, P. B.; Thomas, A. G., *J. Appl. Polym. Sci.* **1964**, *8*, 455.
- [140] Gent, A. N.; Kinloch, A. J., *J. Polym. Sci. A2* **1971**, *9*, 659.
- [141] Gent, A. N.; Hamed, G. R., *Rubber Chem. Technol.* **1982**, *55*, 483.
- [142] Gent, A. N.; Tobias, R. H., *J. Polym. Sci. B* **1984**, *22*, 1483.
- [143] Gent, A. N.; Kim, H. J., *Rubber Chem. Technol.* **1990**, *63*, 613.
- [144] Gent, A. N.; Lai, S. M., *J. Polym. Sci. Pol. Phys.* **1994**, *32*, 1543.
- [145] Maugis, D., *Langmuir* **1995**, *11*, 679.
- [146] Degennes, P. G., *J. Phys-Paris* **1989**, *50*, 2551.
- [147] Raphael, E.; Degennes, P. G., *J. Phys. Chem.* **1992**, *96*, 4002.
- [148] Degennes, P. G., *Langmuir* **1996**, *12*, 4497.
- [149] Tabor, D.; Winterto.Rh, *Proc. R. Soc. Lon. Ser-A* **1969**, *312*, 435.
- [150] Israelachvili, J. N.; Tabor, D., *Proc. R. Soc. London A* **1972**, *331*, 19.
- [151] Landman, U.; Luedtke, W. D.; Burnham, N. A.; Colton, R. J., *Science* **1990**, *248*, 454.
- [152] Klein, J., *Nature* **1980**, *288*, 248.
- [153] Parker, J. L.; Christenson, H. K.; Ninham, B. W., *Rev. Sci. Instrum.* **1989**, *60*, 3135.
- [154] Israelachvili, J. N.; McGuiggan, P. M., *J. Mater. Res.* **1990**, *5*, 2223.
- [155] Tonck, A.; Georges, J. M.; Loubet, J. L., *J. Colloid Interf. Sci.* **1988**, *126*, 150.
- [156] Kuhl, T. L.; Leckband, D. E.; Lasic, D. D.; Israelachvili, J. N., *Biophys. J.* **1994**, *66*, 1479.
- [157] Leckband, D., *Nature* **1995**, *376*, 617.
- [158] Israelachvili, J. N.; Pashley, R. M., *J. Coll. Int. Sci.* **1984**, *98*, 500.
- [159] Marra, J., *J. Phys. Chem.* **1986**, *90*, 2145.
- [160] Marra, J.; Hair, M. L., *J. Phys. Chem.* **1988**, *92*, 6044.
- [161] Pashley, R. M.; McGuiggan, P. M.; Ninham, B. W.; Brady, J.; Evans, D. F., *J. Phys. Chem.* **1986**, *90*, 1637.
- [162] Leikin, S.; Parsegian, V. A.; Rau, D. C.; Rand, R. P., *Annu. Rev. Phys. Chem.* **1993**, *44*, 369.
- [163] Claesson, P. M.; Paulson, O. E. H.; Blomberg, E.; Burns, N. L., *Colloid. Surface A* **1997**, *123*, 341.
- [164] Israelachvili, J.; Pashley, R., *Nature* **1982**, *300*, 341.
- [165] Leckband, D. E.; Schmitt, F. J.; Israelachvili, J. N.; Knoll, W., *Biochemistry* **1994**, *33*, 4611.
- [166] Davies, D. R.; Padlan, E. A.; Sheriff, S., *Annu. Rev. Biochem.* **1990**, *59*, 439.
- [167] Leckband, D.; Kuhl, T. L.; Wang, H. K.; Herron, J.; Muller, W.; Ringsdorf, H., *Biochemistry* **1995**, *34*, 11467.
- [168] Leckband, D. E.; Muller, W.; Schmitt, F. J.; Ringsdorf, H., *Biophys. J.* **1995**, *69*, 1162.
- [169] Blomberg, E.; Claesson, P. M.; Froberg, J. C.; Tilton, R. D., *Langmuir* **1994**, *10*, 2325.
- [170] Mangipudi, V.; Tirrell, M.; Pocius, A. V., *Langmuir* **1995**, *11*, 19.
- [171] Viani, M. B.; Schaffer, T. E.; Chand, A.; Rief, M.; Gaub, H. E.; Hansma, P. K., *J. Appl. Phys.* **1999**, *86*, 2258.
- [172] Mizes, H. A.; Loh, K. G.; Miller, R. J. D.; Ahuja, S. K.; Grabowski, E. F., *Appl. Phys. Lett.* **1991**, *59*, 2901.
- [173] Nakajima, K.; Yamaguchi, H.; Lee, J. C.; Kageshima, M.; Ikehara, T.; Nishi, T., *Jpn. J. Appl. Phys. I* **1997**, *36*, 3850.
- [174] Bliznyuk, V. N.; Assender, H. E.; Briggs, G. A. D., *Macromolecules* **2002**, *35*, 6613.
- [175] Aime, J. P.; Elkaakour, Z.; Odin, C.; Bouhacina, T.; Michel, D.; Curely, J.; Dautant, A., *J. Appl. Phys.* **1994**, *76*, 754.
- [176] Gimzewski, J. K.; Joachim, C., *Science* **1999**, *283*, 1683.
- [177] Crassous, J.; Charlaix, E.; Gayvallet, H.; Loubet, J. L., *Langmuir* **1993**, *9*, 1995.
- [178] Attard, P., *J. Adhes. Sci. Technol.* **2002**, *16*, 753.
- [179] Mugele, F.; Becker, T.; Nikopoulos, R.; Kohonen, M.; Herminghaus, S., *J. Adhes. Sci. Technol.* **2002**, *16*, 951.
- [180] Cappella, B.; Dietler, G., *Surf. Sci. Rep.* **1999**, *34*, 1.
- [181] Butt, H. J.; Cappella, B.; Kappl, M., *Surf. Sci. Rep.* **2005**, *59*, 1.

- [182] Radmacher, M.; Cleveland, J. P.; Fritz, M.; Hansma, H. G.; Hansma, P. K., *Biophys. J.* **1994**, *66*, 2159.
- [183] Lee, G. U.; Kidwell, D. A.; Colton, R. J., *Langmuir* **1994**, *10*, 354.
- [184] Hoh, J. H.; Cleveland, J. P.; Prater, C. B.; Revel, J. P.; Hansma, P. K., *J. Am. Chem. Soc.* **1992**, *114*, 4917.
- [185] Heinz, W. F.; Hoh, J. H., *Trends Biotechnol.* **1999**, *17*, 143.
- [186] Mareanukroh, M.; Eby, R. K.; Scavuzzo, R. J.; Hamed, G. R.; Preuschen, J., *Rubber Chem. Technol.* **2000**, *73*, 912.
- [187] Pethica, J. B.; Oliver, W. C., *Phys. Scripta* **1987**, *T19A*, 61.
- [188] Burnham, N. A.; Colton, R. J.; Pollock, H. M., *J. Vac. Sci. Technol. A* **1991**, *9*, 2548.
- [189] Frisbie, C. D.; Rozsnyai, L. F.; Noy, A.; Wrighton, M. S.; Lieber, C. M., *Science* **1994**, *265*, 2071.
- [190] Noy, A.; Frisbie, C. D.; Rozsnyai, L. F.; Wrighton, M. S.; Lieber, C. M., *J. Am. Chem. Soc.* **1995**, *117*, 7943.
- [191] Noy, A.; Vezenov, D.; Lieber, C. M., *Annu. Rev. Mater. Sci.* **1997**, *27*, 381.
- [192] Tsukruk, V. V., *Rubber Chem. Technol.* **1997**, *70*, 430.
- [193] Hillborg, H.; Tomczak, N.; Olah, A.; Schönherr, H.; Vancso, G. J., *Langmuir* **2004**, *20*, 785.
- [194] Vezenov, D. V.; Zhuk, A. V.; Whitesides, G. M.; Lieber, C. M., *J. Am. Chem. Soc.* **2002**, *124*, 10578.
- [195] Clear, S. C.; Nealey, P., *J. Coll. Int. Sci.* **1999**, *213*, 238.
- [196] Vezenov, D. V.; Noy, A.; Ashby, P., *J. Adhes. Sci. Technol.* **2005**, *19*, 313.
- [197] Noy, A., *Surf. Interface Anal.* **2006**, *38*, 1429.
- [198] Evans, E., *Annu. Rev. Bioph. Biom.* **2001**, *30*, 105.
- [199] Zepeda, S.; Yeh, Y.; Noy, A., *Langmuir* **2003**, *19*, 1457.
- [200] Evans, E.; Ritchie, K., *Biophys. J.* **1997**, *72*, 1541.
- [201] Friedsam, C.; Wehle, A. K.; Kuhner, F.; Gaub, H. E., *J. Phys.-Condens. Mat.* **2003**, *15*, S1709.
- [202] Williams, P. M., *Anal. Chim. Acta* **2003**, *479*, 107.
- [203] Strunz, T.; Oroszlan, K.; Schafer, R.; Guntherodt, H. J., *P. Natl. Acad. Sci. USA.* **1999**, *96*, 11277.
- [204] Rotto, T. V.; Langry, K.; Rudd, R.; Balhorn, R.; McElfresh, M., *Biophys. J.* **2004**, *86*, 322A.
- [205] Bustamante, C.; Marko, J. F.; Siggia, E. D.; Smith, S., *Science* **1994**, *265*, 1599.
- [206] Brockwell, D. J.; Paci, E.; Zinober, R. C.; Beddard, G. S.; Olmsted, P. D.; Smith, D. A.; Perham, R. N.; Radford, S. E., *Nat. Struct. Biol.* **2003**, *10*, 731.
- [207] Fernandez, J. M.; Li, H. B., *Science* **2004**, *303*, 1674.
- [208] Tskhovrebova, L.; Trinick, J.; Sleep, J. A.; Simmons, R. M., *Nature* **1997**, *387*, 308.
- [209] Rief, M.; Oesterhelt, F.; Heymann, B.; Gaub, H. E., *Science* **1997**, *275*, 1295.
- [210] Sinniah, S. K.; Steel, A. B.; Miller, C. J.; ReuttRobey, J. E., *J. Am. Chem. Soc.* **1996**, *118*, 8925.
- [211] Han, T.; Williams, J. M.; Beebe, T. P., *Anal. Chim. Acta* **1995**, *307*, 365.
- [212] vanderVegte, E. W.; Hadziioannou, G., *Langmuir* **1997**, *13*, 4357.
- [213] Vezenov, D.; Noy, A.; Rosznyi, L. F.; Lieber, C. M., *J. Am. Chem. Soc.* **1997**, *119*, 2006.
- [214] Tirrell, M., *Langmuir* **1996**, *12*, 4548.
- [215] Kim, S. J.; Choi, G. Y.; Ulman, A.; Fleischer, C., *Langmuir* **1997**, *13*, 6850.
- [216] Mowery, C. L.; Crosby, A. J.; Ahn, D.; Shull, K. R., *Langmuir* **1997**, *13*, 6101.
- [217] Johnson, K. L.; Kendall, K.; Roberts, A. D., *Proc. R. Soc. Lon. Ser-A* **1971**, *324*, 301.
- [218] Deruelle, M.; Tirrell, M.; Marciano, Y.; Hervet, H.; Leger, L., *Faraday Discuss.* **1994**, *98*, 55.
- [219] Chaudhury, M. K.; Whitesides, G. M., *Science* **1992**, *255*, 1230.
- [220] Choi, G. Y.; Zurawsky, W.; Ulman, A., *Langmuir* **1999**, *15*, 8447.
- [221] Binnig, G.; Rohrer, H., *Helv. Phys. Acta.* **1982**, *55*, 726.
- [222] Binnig, G.; Quate, C. F.; Gerber, C., *Phys. Rev. Lett.* **1986**, *56*, 930.
- [223] Bhushan, B., *J. Vac. Sci. Technol. B* **2003**, *21*, 2262.
- [224] Rabinowicz, E., *Friction and Wear of Materials*. John Wiley & Sons: New York, 1965.
- [225] Homola, A. M.; Israelachvili, J. N.; McGuiggan, P. M.; Gee, M. L., *Wear* **1990**, *136*, 65.
- [226] Forster, A. M.; Zhang, W. H.; Crosby, A. J.; Stafford, C. M., *Meas. Sci. Technol.* **2005**, *16*, 81.

- [227] Autumn, K.; Liang, Y. A.; Hsieh, S. T.; Zesch, W.; Chan, W. P.; Kenny, T. W.; Fearing, R.; Full, R. J., *Nature* **2000**, *405*, 681.
- [228] Geim, A. K.; Dubonos, S. V.; Grigorieva, I. V.; Novoselov, K. S.; Zhukov, A. A.; Shapoval, S. Y., *Nat. Mater.* **2003**, *2*, 461.
- [229] Sitti, M.; Fearing, R. S., *J. Adhes. Sci. Technol.* **2003**, *17*, 1055.
- [230] Gao, H. J.; Yao, H. M., *P. Natl. Acad. Sci. USA.* **2004**, *101*, 7851.
- [231] Persson, B. N. J.; Gorb, S., *J. Chem. Phys.* **2003**, *119*, 11437.
- [232] Arzt, E.; Gorb, S.; Spolenak, R., *P. Natl. Acad. Sci. USA.* **2003**, *100*, 10603.
- [233] Crosby, A. J.; Hageman, M.; Duncan, A., *Langmuir* **2005**, *21*, 11738.
- [234] Bhushan, B.; Peressadko, A. G.; Kim, T. W., *J. Adhesion Sci. Technol.* **2006**, *20*, 1475.
- [235] Haidara, H.; Chaudhury, M. K.; Owen, M. J., *J. Phys. Chem.* **1995**, *99*, 8681.
- [236] Loskofsky, C.; Song, F.; Newby, B. M. Z., *J. Adhesion* **2006**, *82*, 713.
- [237] Rosenfield, A. R.; Kannien, M. F., *J. Macromol, Sci. B* **1973**, *7*, 609.

# Chapter 3

## **Flame-treatment of low density polyethylene: Surface chemistry across the length scales<sup>\*</sup>**

The relationship between surface chemistry and morphology of flame-treated low density polyethylene (LDPE) was studied by various characterization techniques across different length scales. The chemical composition of the surface was determined on the micrometer scale by X-ray photoelectron spectroscopy (XPS) as well as with time-of-flight secondary ion mass spectrometry (ToF-SIMS), while surface wettability was obtained through contact angle (CA) measurements on the millimeter scale. The surface concentration of hydroxyl, carbonyl and carboxyl groups, as a function of the "number" of the flame-treatment passes (which is proportional to the treatment time) was obtained. Moreover, a correlation was found with chemical composition and polarity, emphasizing the role of oxygen-containing functional groups introduced during the treatment. Carboxyl functional groups were specifically identified by fluorescent labeling and the results were compared with the ToF-SIMS data. In addition, atomic force microscopy (AFM) was used to evaluate changes in surface topography and roughness on the nanometer to micrometer length scales. After flame-treatment, water soluble low molecular weight oxidized materials (LMWOM), which were generated as products of oxidation and chain scission of the LDPE surface, agglomerated into small topographical mounds that were visible in the AFM micrographs. After rinsing the samples with water and ethanol, nodular surfaces were observed. The ionization state of flame-treated LDPE surfaces was monitored by chemical force microscopy (CFM). The effective surface  $pK_a$  values of carboxylic acid ( $-COOH$ ) obtained by AFM were revealed by chemical force titration curves and the effective surface  $pK_a$  values were found to be around 6.

---

<sup>\*</sup> This *chapter* has been published in the following article: J. Song; U. Gunst, H. F. Arlinghaus, G. J. Vancso *Applied Surface Science* **2007**, 253, 9489.



### 3.1 Introduction

Low density polyethylene (LDPE) has been widely used in various applications owing to its excellent physical and chemical bulk properties. These include light mass, low toxicity, excellent electric insulation, mechanical durability, good chemical resistance and ease of processing and molding.<sup>1, 2</sup> However, the polymer rarely possesses surface properties that promote successful applications in fields requiring adhesion, printability, and biocompatibility.<sup>3</sup> For instance, the non-polar LDPE surfaces are fairly hydrophobic, *i.e.* water contact angles around 100° (advancing) and 70° (receding) are typically found. It is therefore difficult to bind these hydrophobic polymer surfaces directly with other substances, such as adhesives, printing inks, paints, and various metal surfaces. Thus, technologies that involve surface engineering to convert inexpensive LDPE into valuable finished goods have become more important. In order to address these issues, treatments to increase the surface energy of the polymer by introducing polar functionalities are essentially desirable.<sup>4-6</sup>

In recent decades, numerous technologies have been extensively developed to modify the surface properties of polymeric materials in order to yield valuable finished products. Examples of such technologies include plasma, chemical, corona, flame, and ion implantation treatments.<sup>6-14</sup> These techniques affect only the chemical and physical properties of the outermost surface layer with an effective skin layer depth depending on the type of treatment and treatment conditions, and thus, they do not alter the bulk properties.<sup>13-15</sup> As is well known, plasma treatment has become increasingly important in the last 20 years and it is possible to treat even substrates with complex shapes. The various high energy species present in the plasma induce the formation of free radicals in the polymeric chains and thus permit the formation of certain polar functional groups on the polymeric surface which enhance the surface adhesion. In addition, the treatment is fast, clean, environmentally safe, uniform and precisely controllable.<sup>6, 13, 16-24</sup> On the other hand, clear disadvantages of plasma treatment include the fact that it encompasses a complex process and that the adjustment of the plasma discharge parameters constitutes a complicated task.<sup>14, 22</sup> Moreover, changes in the surface chemistry obtained by plasma treatment are not permanent and this may affect industrial applications.<sup>23</sup>

Wet chemical treatments are simple and benign methods for modifying polymer surfaces. Noteworthy studies have focused on changes in surface chemical composition and morphology upon etching with strong acids to convert smooth hydrophobic polymer surfaces

to rough hydrophilic ones.<sup>25-27</sup> However, wet chemical treatments involve a number of additional processing steps, such as washing, rinsing and drying. It is rather expensive and gives rise to the environmental problem of disposing a large amount of toxic waste.<sup>28</sup>

For the last 50 years, corona discharges and flame are the most widely used pre-treatment methods for polymer films in industry. Corona discharge treatment is generally used for the pre-treatment of polyolefin films whereas the flame-treatment is used for thicker sections. Corona discharge treatment produces significant changes in the surface topography of polymers, and flame is probably the oldest type of plasma known. This latter method is extensively used for treating plastic bottles and other moldings.<sup>11</sup> Compared with corona treatment, flame-treatment offers a number of practical advantages, including the ability to achieve extensive surface oxidation and excellent wettability at extremely short processing times. In addition, this method does not generate toxic corrosive ozone and displays no significant loss of treatment effect upon aging.<sup>29</sup> Though a straightforward set-up is required for this technique, a certain craftsmanship is still needed to obtain consistent results.<sup>30</sup> Currently, flame-treatment is receiving a renewed industrial interest as a technique for modifying films because of major improvements in its safety, reliability and ease of operation.<sup>31</sup> An in depth understanding and a close survey of the physical and chemical properties of flame-treated polymer surfaces are required to gain an understanding in order to optimise the process. Unfortunately, available knowledge is currently insufficient.

In the present work, the chemical nature of flame-treated LDPE surfaces have been extensively examined by various surface sensitive analytical techniques, including XPS, ToF-SIMS, fluorescence microscopy (FM) and CA. In addition, AFM was used to investigate the surface structure and topography of the films on a nanometer resolution before and after treatment. Moreover, the surface ionization state of flame-treated LDPE was studied by CFM. The experimental results displayed a multifunctional and responsive surface after flame-treatment of LDPE, and should be helpful in developing PE commodities with designer surfaces for a variety of applications.

## 3.2 Results and discussion

### 3.2.1 Surface wettability

The wetting properties of the LDPE samples on the millimeter length scale were evaluated by contact angle measurements. Figure 3.1 shows the variation of the water contact angle following the flame-treatment as a function of treatment number. The observed advancing angle changed from  $100^\circ$  for the untreated sample to  $47.5^\circ$  for the sample treated 200 times. The receding angle changed from  $72^\circ$  to  $12^\circ$ . The reduction in contact angle demonstrated an expected increase in the surface wettability and surface energy following the flame-treatment. The decrease in the water contact angle occurred rapidly at first and then slowed down as the number of flame-treatments exceeded 100. This behavior indicated that the amount of polar functional groups at the LDPE surface increased for an increasing number of flame-treatments up to 100 after which the surface became saturated. Interestingly, no significant difference was observed between the contact angles of treated and washed samples. The difference between the advancing and receding contact angles, *i.e.* the contact angle hysteresis, was also found to increase with an increasing number of treatments. It has been widely accepted that contact angles are sensitive to changes in both the surface topography and the chemical behavior<sup>32</sup>. For the flame-treated LDPE in the present report, the surface roughness only displayed minor changes on the micrometer scale (as will be shown in the following AFM study). Thus, with respect to the lowering of the water contact angle, the effect of the roughness was expected to be small. Contact angle hysteresis is usually ascribed to a variety of causes including structural disorder, surface roughness and heterogeneity.<sup>33</sup> In the present case, the observed hysteresis may result from the combination of an increasing amount of polar groups at the surface and their reorientation under the influence of the liquid phase. This raises the question regarding what kind of surface functional groups were introduced by the flame-treatment and what the mechanism behind the wettability changes was. In the following section, the atomic percentage of oxygen on treated and washed samples were compared from XPS results to identify the chemical nature of the species introduced through the treatment.

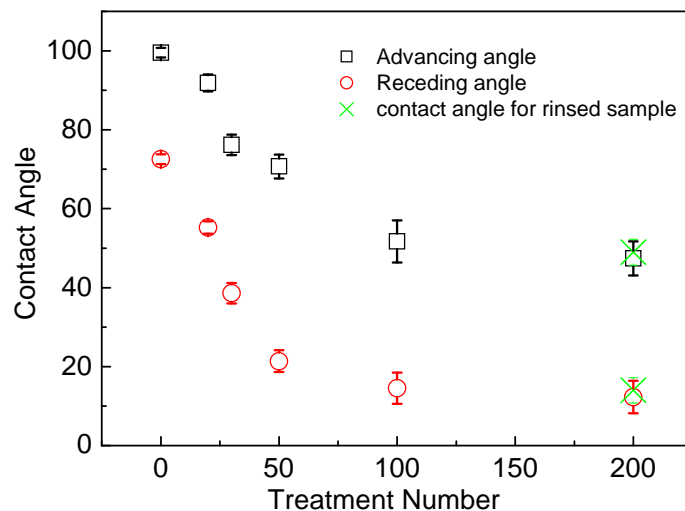


**Figure 3** The variation of surface contact angles measured with  $H_2O$  as a function of the number of passes of flame-treatment of LDPE.

### 3.2.2. Surface chemistry modification

XPS is utilized to probe the chemical composition and identity of the functional groups that are present within the outermost layer of a film surface. In order to study the in-depth distribution of the chemical composition on the flame-treated LDPE films, angle resolved XPS (AR-XPS) was used at take-off angles varying from  $10^\circ$  to  $60^\circ$ . The sampling depth of XPS is related to the relative orientation of the incident X-ray beam and the sample surface. The value of the sampling depth,  $l$ , for each take-off angle can be calculated according to Equation 3.1,

$$l = 3\lambda \times \sin\theta \quad (\text{Eq. 3-1})$$

where  $\lambda$  is the inelastic mean free path of the electrons, (ca.  $40\text{\AA}$  for C 1s from PE) and  $\theta$  is the take-off angle.<sup>34</sup>

The surface concentration of oxygen in the LDPE films as determined by XPS is shown in Table 3.1. The untreated LDPE sample was analyzed to determine the cleanliness of the original surface, and it can be noted that the untreated LDPE surface showed less than 2% oxygen. It was also observed that the oxygen concentration was significantly greater in the treated films than in their untreated counterparts. The oxygen concentration increased with an increasing number of treatments. The surface concentration of oxygen was found to be 10.71% (take-off angle was  $60^\circ$ ) whereas 12% was detected by Briggs et al. in an independent

study (take-off angle was  $90^\circ$ ).<sup>35</sup> The LDPE film treated 200 times was rinsed for 1 min in a mixture of ethanol and water and this procedure resulted in a drop in the O concentration as observed by XPS. This was attributed to the presence of small amounts of oxidized, low molar mass fractions of the polymer which were weakly bound to the surface and removed by the solvent.<sup>36</sup> Moreover, for the same flame-treated specimen, the O concentration was found to increase with a decreasing take-off angle *i.e.* with decreasing sample depth. For the sample treated 200 times, the oxygen concentration decreased by  $\sim 18\%$  when comparing measurements with sampling depths of  $\sim 10.4$  nm and  $\sim 2.1$  nm. Although the angle-dependent XPS experiment was a valuable tool to obtain information about the chemical differentiation in the surface layer, care should be taken when interpreting the sampling depth value. Since our LDPE film had a rough surface, it could not be definitively concluded that the flame-treatment could modify the LDPE surface any deeper than the XPS sampling depth. Nevertheless, the suggested depth of oxidation was in the range of 20 to 50 nm.

Table 3.1 The oxygen concentration of flame-treated LDPE surface versus the number of treatments as obtained by angle resolved XPS at varying take-off angles.

$\theta (^\circ)^a$	$l (nm)^b$	Untreated LDPE	Treated 100 times	Treated 200 times	Rinsed Sample
10	2.1	1.2	-	13.1	11.9
20	4.1	1.3	-	11.3	9.2
30	6.0	1.6	-	10.8	8.3
40	7.7	1.4	-	10.8	8.5
45	8.5	1.0	6.7	9.6	8.0
60	10.4	1.3	-	10.7	7.2

<sup>a</sup>  $\theta$  is the take-off angle

<sup>b</sup>  $l$  is the estimated sampling depth value calculated by Equation 3.1.

As has been proposed elsewhere,<sup>35, 37</sup> flame-treatment introduces hydroxyl, carbonyl, and carboxyl groups on the surface of PE films. In addition to giving qualitative atomic concentrations on the sample surface, XPS spectra can also provide chemical bonding information. Typical spectra for LDPE surfaces before and after flame-treatment are shown in Figure 3.2. The C 1s spectrum of the untreated LDPE contained a symmetric C–C peak and no chemical shift was observed for this signal after treatment for 200 times (Figure 3.2a). This result indicated the presence of only one valence state for carbon corresponding to  $C_xH_y$  functionalities (*i.e.*  $-CH$ ,  $-CH_2$ ,  $-CH_3$ ). In contrast, flame modification led to the appearance of a shoulder at higher binding energies (BE), which was taken as an indication of the build up of oxygenated carbon centers. This result was also consistent with the observed variation

in the O concentration. A simple deconvolution of the C 1s spectrum for the LDPE treated 200 times demonstrated three peaks at higher BE relative to the primary hydrocarbon peak. These peaks were assigned to alcohol and/or ether (C–O), as well as carbonyl (C=O) and carboxyl (O–C=O) groups (Figure 3.2b). The deconvoluted O 1s spectra for the flame-treated LDPE were not particularly informative due to contributions of every possible chemical environment for O except O–C=O which has a binding energy some 1.5 eV higher. The relative concentrations of functional groups were obtained by normalizing the integrated peak areas. It was also observed that the relative concentration remained constant with increasing the number of flame-treatments; *i.e.* the ratio among C–O: C=O: O–C=O groups was found to be 46: 44: 10.

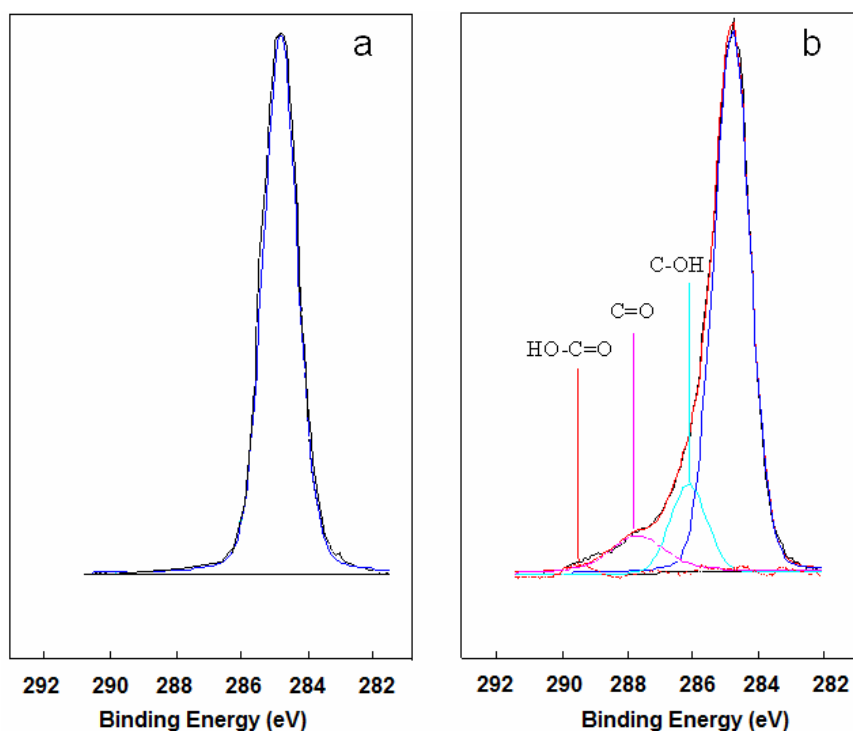


**Figure 3.2** High resolution C 1s XPS spectra of (a) untreated LDPE; and (b) LDPE treated 200 times.

SIMS has a shallower observation depth than XPS. In other words, the observed fragments are emitted from the first 1 ~ 3 top monolayers of the surface, as compared to in the ca. 1 ~ 10 nm layer in XPS analysis. Therefore, ToF-SIMS measurements were also carried out in order to quantitatively study the surface composition of flame-treated LDPE as a function of the number of treatments. As mentioned above, by analyzing and deconvolution, the XPS results concerning the C 1s peak could provide information about the chemical

species formed as a result of the surface modification. A direct indication of the composition of these species can be obtained by analyzing the ToF-SIMS data. But the difference in the sampling depths must be kept in mind.

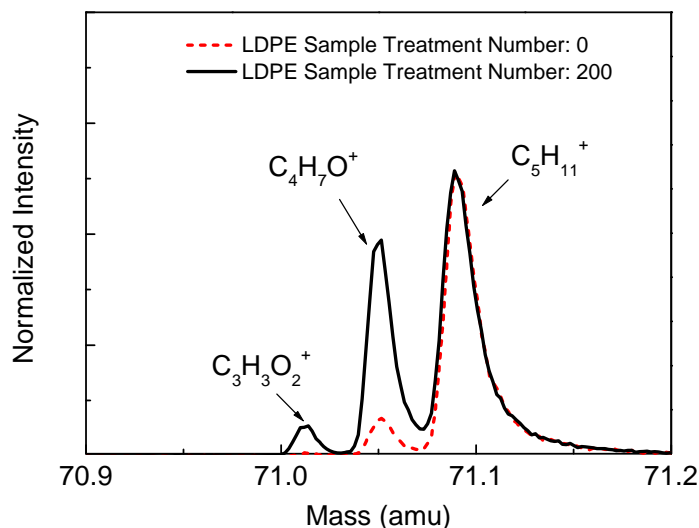


**Figure 3.3** Positive ToF-SIMS spectrum of untreated and flame-treated LDPE surface of fragments at  $m/z$  around 71.

All the treated LDPE films exhibited qualitatively similar ToF-SIMS spectra. The secondary ion intensities of oxygen-containing functional species show an enhancement with the treatment number. Figure 3.3 shows the typical spectra of untreated LDPE and the LDPE sample treated 200 times at different  $m/z$  range. Apart from the presence of hydrocarbon peaks, *i.e.*  $C_nH_m^+$ , due to fragmentation of the polymer, the formation of oxygen-containing functional species was directly observed. Table 3.2 compares the relative intensities of all the significant oxygen-containing fragments up to  $m/z$  100 from these positive ion spectra. The intensity of the  $C_2H_3^+$  peak was used as an internal reference for the quantitative treatment of relative peak intensity data as shown in an earlier independent study for a hydrocarbon polymer.<sup>38</sup>

**Table 3.2** The relative intensity  $\times 10^{+3}$  of positive ions for flame-treated LDPE as obtained by ToF-SIMS using  $C_2H_3^+$  as a standard.

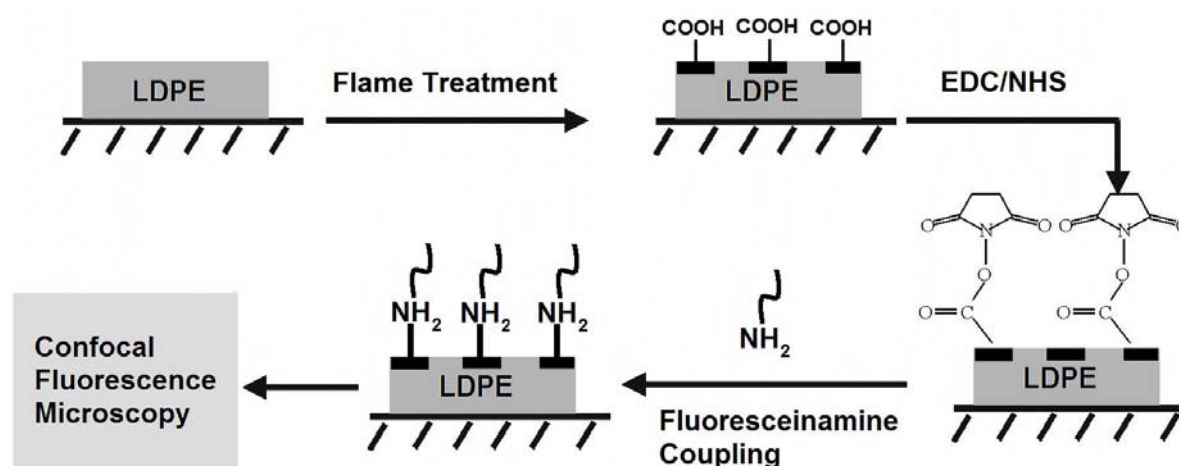
Treatment number	$CHO^+$	$CH_3O^+$	$C_2H_3O^+$	$CHO_2^+$	$C_2H_5O^+$	$C_2H_4O_2^+$	$C_4H_7O^+$	$C_3H_5O_2^+$
50	6.5	7.3	51.6	0.4	11.5	0.2	15.7	1.0
100	34.3	43.2	311.8	3.4	59.5	2.9	83.6	9.1
150	35.9	55.8	415.3	4.1	73.1	3.9	105.6	11.7
200	45.3	46.1	471.0	5.9	83.4	5.4	119.3	16.0

It should be kept in mind that for the original LDPE sample a small amount of oxygen was observed. The sample surface of LDPE is a "real world" sample surface. It has been exposed to air and the environment. Thus the presence of surface contamination can be anticipated. Because we prepared all samples by the same procedure (except for different flame-treatment numbers), the contamination is expected to be similar. We used pure LDPE as background, and all data shown in Table 2 were background corrected to obtain "real" concentration values. In Table 3.2, the ions  $CHO_2^+$  (m/z 45),  $C_2H_4O_2^+$  (m/z 60), and  $C_3H_5O_2^+$  (m/z 73) were candidates for fragments derived from carboxylic acid functional groups. Alcohol formed  $CH_3O^+$  (m/z 33),  $C_2H_5O^+$  (m/z 45) and carbonyl was from  $CHO^+$  (m/z 29),  $C_2H_3O^+$  (m/z 43) and  $C_4H_7O^+$  (m/z 71). It was observed that the total amount of oxygen-related species increased with the number of treatments. Also the amount of the individual molecular ions increased. The ratio among C–O: C=O: O–C=O groups was found to be 80: 16: 4. When compared with XPS, the ToF-SIMS observations displayed a relatively larger concentration of C–O fragments. One reason for this difference was presumably the variations in sampling depth indicating the existence of a gradient in the reaction products already for the outermost 10 nm. Finally, when comparing samples treated 50 and 100 times, the concentration of the O–C=O groups increased *ca.* ten fold while the other two functionalities increased *ca.* six fold. This is an indication of an enhanced formation of –COOH groups with an increasing number of treatments.

The nature and density of surface functional groups are the essential characteristics that affect the properties and applications of a surface, *e.g.* in surface wetting, and biocompatibility.<sup>39</sup> As discussed above, XPS and ToF-SIMS measurements allowed us to identify and quantify the oxidized functional groups. Often, one of these functional groups is of critical importance, *e.g.* to provide a specific interaction or to allow the attachment of a chemical entity through synthesis. A quantitative characterization of such a specific functional



group is clearly crucial and fluorescent labeling offers a possibility in this area. The ease of operation is also important when performing surface analysis. XPS and ToF-SIMS need to be operated in ultrahigh vacuum environments. Fluorescent labeling, on the other hand, is a promising method because of its high sensitivity, ease of operation and *in situ* applicability. It has been widely used in biological applications<sup>40, 41</sup>, polymer chemistry<sup>42-45</sup>, and study of self assembled monolayers.<sup>46-49</sup>



**Scheme 3.1** A schematic portrayal of the immobilization of fluoresceinamine on flame-treated LDPE.

Fluorescent labeling of surface species enables the identification and quantification of surface functional groups with very low concentrations. However, as any other surface derivatization technique, it provides a lower limit to detect surface coverage.<sup>50</sup> Fluoresceinamine is usually used to label surface aldehyde and carboxyl groups. As was shown in the XPS and SIMS results, carboxyl was the most likely binding group for this dye. In other words, the use of such labeling rendered it possible to selectively detect this functional group. The scheme of fluorescent labeling emphasized in this study is presented in Scheme 3.1.

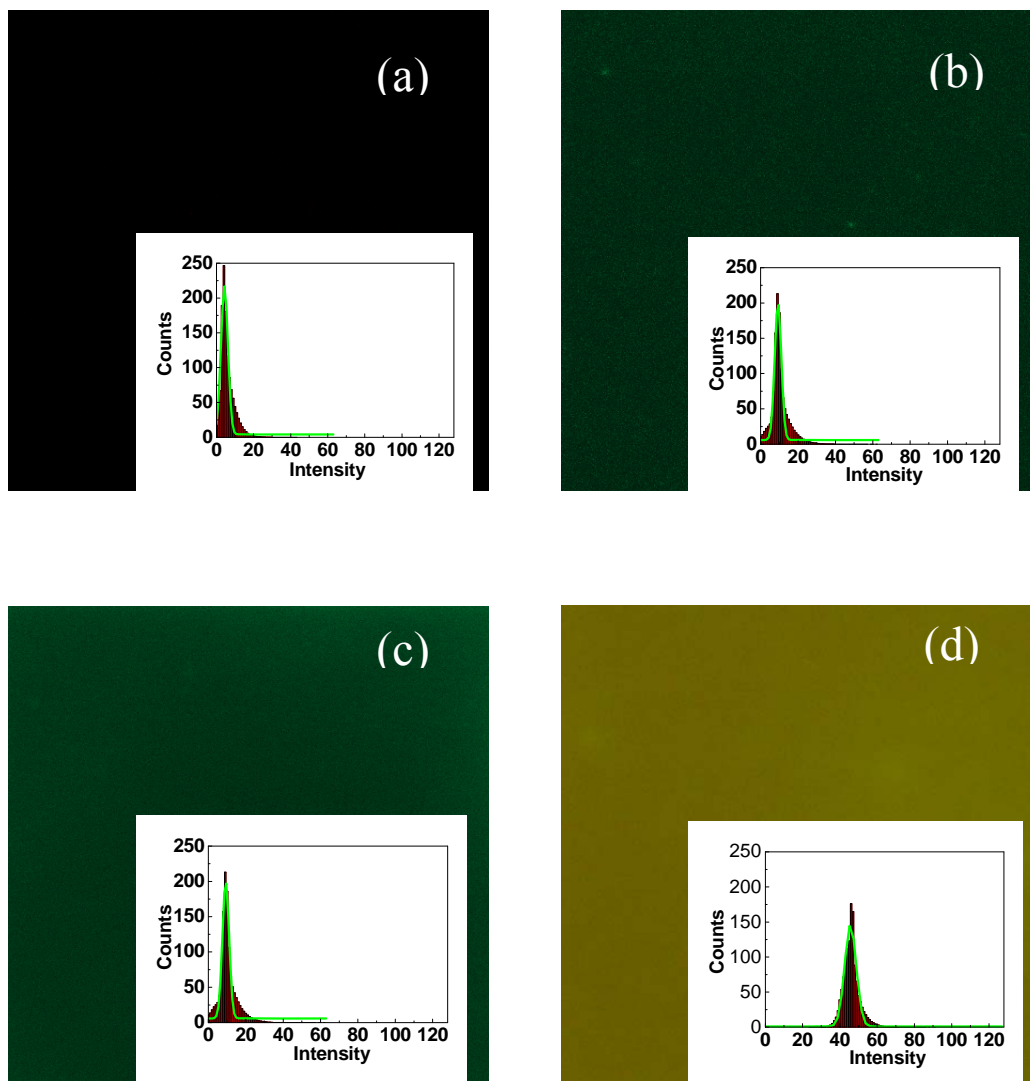


**Figure 3.4** Fluorescence microscopy images and fluorescence emission intensity histograms of (a) untreated LDPE; (b) LDPE treated 50 times; (c) LDPE treated 100 times; and (d) LDPE treated 200 time coupled with fluoresceinamine.

Carboxylic acid groups were converted to reactive N-hydroxysuccinimide ester groups by reaction with 1-ethyl-3-(dimethylamino)-propylcarbodiimide (EDC) and N-hydroxysuccinimide (NHS). Generally, primary amino groups react efficiently with these active esters (also in aqueous media) and yield robust derivatized layers owing to covalent coupling. Thus, the concentration of  $\text{-COOH}$  groups could be investigated by fluorescence microscopy using fluoresceinamine as the label. Figure 3.4 shows fluorescence microscopy images (image area  $200\ \mu\text{m} \times 200\ \mu\text{m}$ ) of four LDPE samples flame-treated a varying number of times and reacted with the dye in aqueous medium. The figure displays a clear increase in fluorescence intensity, and the integrated intensities are also shown in the insets as histograms.

For the untreated LDPE film, a fluorescence emission of very low intensity was observed. It can also be noticed that the intensity of the fluorescence emission was enhanced with an increasing number of treatments. In addition, a homogeneous fluorescence emission was observed.

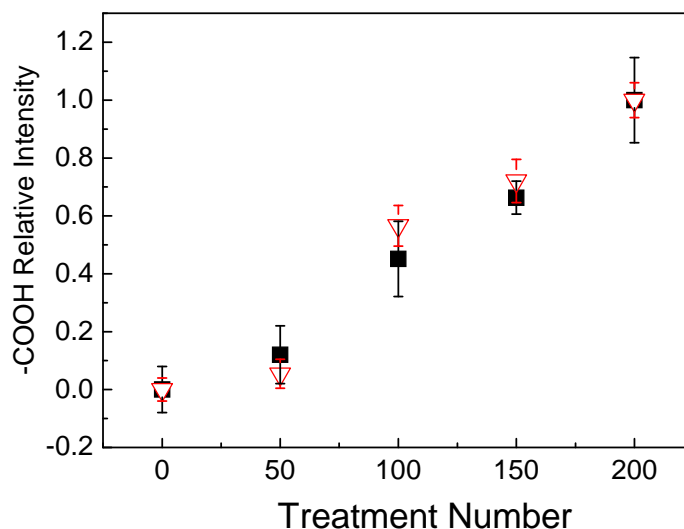


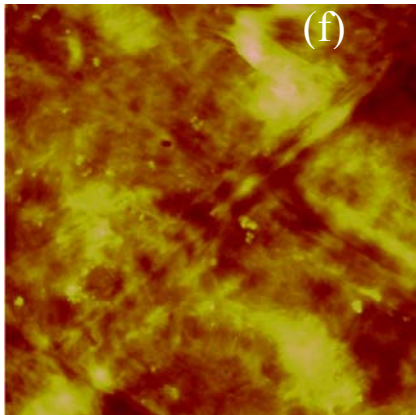
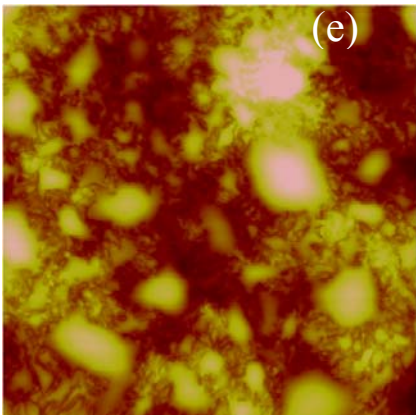
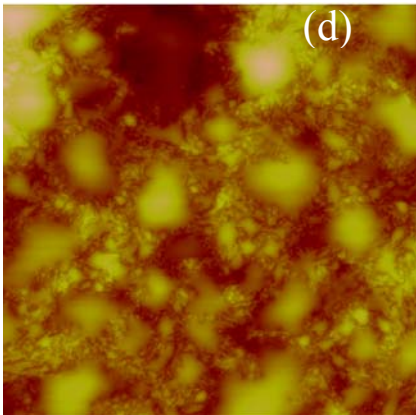
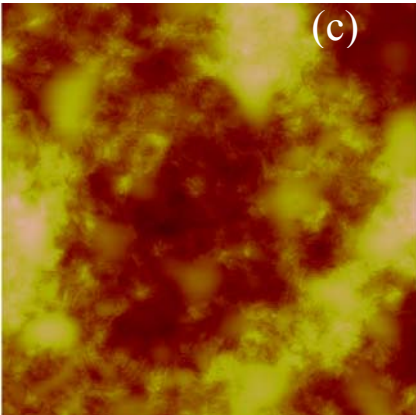
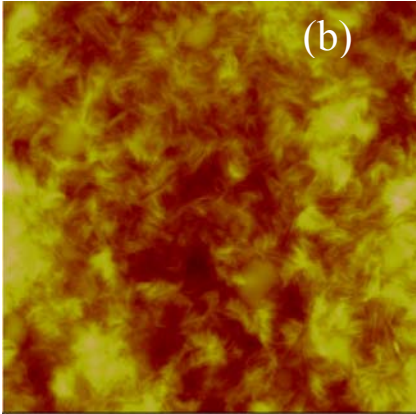
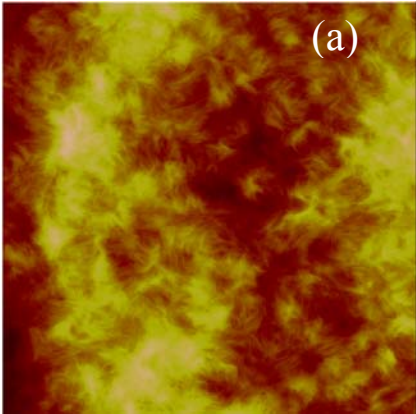
**Figure 3.5** The normalized  $[-\text{COOH}]$  of flame-treated LDPE as measured by (a) ToF-SIMS ( $\nabla$ ); and (b) Fluorescence Microscopy ( $\blacksquare$ ) as a function of the number of treatment passes.

An independent confirmation for the increased concentration of carboxylic acid groups was already observed in the SIMS experiment. Figure 3.5 shows the normalized  $-\text{COOH}$  concentration as a function of treatment frequency as obtained by both ToF-SIMS and fluorescent labeling methods. A normalization was performed using the sample treated 200 times as a reference. Both methods gave a nearly linear increase in the  $-\text{COOH}$  concentration and showed a remarkable quantitative agreement. As for the contact angle measurement, the contact angle reached saturation after 100 treatment cycles. This may be explained by certain of the polar groups reorienting under influence of the liquid phase.

### 3.2.3 Nano/micro surface topography modification

AFM analysis was carried out in order to observe the topographical changes of flame-treated LDPE from the micrometer to the nanometer length scales. Figure 3.6 shows representative height images of untreated as well as treated samples. All these images were captured at the scan area of  $5\ \mu\text{m} \times 5\ \mu\text{m}$ , with the corresponding  $z$  ranges given below the

images. For the original untreated LDPE (Figure 3.6a), a clearly visible lamellar surface structure was observed, indicating the presence of surface spherulites throughout the film. The lighter areas corresponded to higher regions rendering it possible to observe individual lamellae. After flame-treatment of the surface, it became somewhat smoother and exhibited round-shaped features which formed a nodular structure (Figure 3.6 (b-e)). The large nodular features were  $0.5 \sim 1 \mu\text{m}$  in diameter, and the number of larger features increased for prolonged treatment times. It is known that the original structure of the polymer surface breaks down by some kind of chain scission upon flame-treatment.<sup>51</sup> Degradation products and active constituents are thus formed during the treatment. Overney et al.<sup>51</sup> observed that droplet-like structures were formed on polypropylene surfaces at high doses of plasma treatment. These features were identified as low molar mass decomposition products of the polymer. The large round feature that was apparent in the present case (Figure 3.6(d-e)) resembled the droplets observed by Overney et al., leading us to believe that escape and rearrangement of degradation products originating from the LDPE surface took place on the treated surface. Figure 6f shows the topography of a treated sample rinsed with water and ethanol that displayed a different topography. Following the rinsing, neither a mound-like nor a lamella structure could be observed for the sample treated 200 times. The shape of the globular features (aggregated LMWOM) was explained in terms of the difference in surface energy.<sup>52, 53</sup> The LMWOM was easily removed through rinsing with water, due to the fact that it was probably loosely bound to the surface. In addition, it was also found that the rinsed sample displayed small bead-like structures. This means that oxidized polymer would also remain at the surface following rinsing. We propose that corresponding oxidation products of PE were formed in polymer-analogous reactions, by introducing e.g. carbonyl groups and hydroperoxides. Such products would not be washed off by water.<sup>54, 55</sup> This was consistent with the XPS results indicating a high oxygen concentration for the rinsed sample. Figure 3.6g shows the RMS roughness obtained from AFM images of the sample surface as a function of the flame-treatment number. The data was obtained from an average of 3-5 RMS values from a number of AFM images over an area of  $5 \mu\text{m} \times 5 \mu\text{m}$ . The error bars present the maximum standard deviations. Surprisingly, the RMS roughness did not display a significant change during the flame-treatment at the investigated length scale.



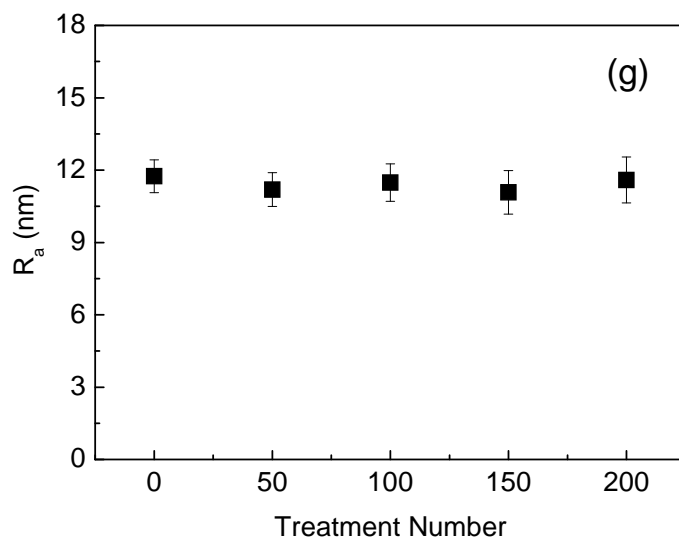


**Figure 3.6** Tapping mode AFM height images (z-scale 300 nm) of (a) untreated LDPE; (b) LDPE treated 5 times; (c) LDPE treated 50 times; (d) LDPE treated 100 times (e) LDPE treated 200 times; and (f) LDPE treated 200 times and subsequently rinsed. (g) The average roughness  $R_a$  versus the number of treatments. The scan area was  $5 \mu\text{m} \times 5 \mu\text{m}$ .

### 3.2.4 Surface ionization state

CFM measurements were carried out by bringing a self-assembled-monolayer (SAM)-modified tip terminated by  $-\text{OH}$  entities into contact with the LDPE film followed by retracting the tip. To further investigate the surface ionization state, average pull-off forces in a  $500 \text{ nm} \times 500 \text{ nm}$  area were obtained by performing force volume (FV) mode scanning on various flame-treated samples as a function of solution pH. The corresponding normalized force titration curves (average pull-off force as a reference of values at  $\text{pH} = 4$  vs.  $\text{pH}$ ) on flame-treated LDPE are shown in Figure 3.7. As was already seen in Figure 3.6g, the mean roughness ( $R_a$ ) was not influenced by the flame-treatment. Consequently, only a minor influence of the sample topography on the force measurements was expected.

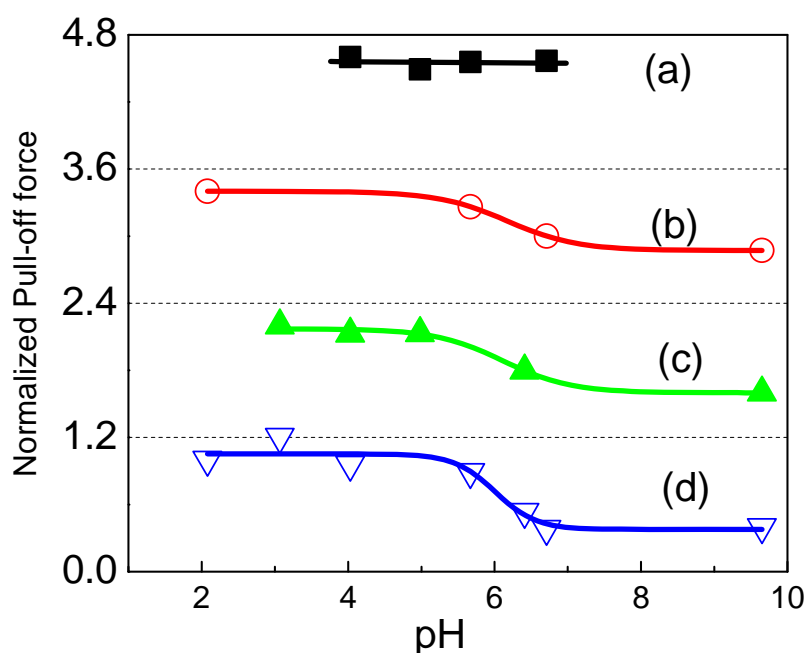


**Figure 3.7** Normalized chemical force titration curves showing the adhesive force between hydroxyl functionalized tips and flame-treated LDPE films as a function of the solution pH. The average pull-off force at pH = 4 was set as a reference for each sample. The solid lines were added as guides to the eye. (a) Untreated LDPE (■);  $\varepsilon = 0.27$ . (b) LDPE treated 50 times (○);  $\varepsilon = 0.44$ . (c) LDPE treated 100 times (▲);  $\varepsilon = 0.69$ . (d) LDPE treated 200 times (▽);  $\varepsilon = 0.43$ .  $\varepsilon$  was the average deviation in the adherence as obtained from Force Volume images.

The force titration curves for the flame-treated LDPE films exhibited a typical sigmoidal pattern. However, the untreated polymer exhibited a high and almost constant pull-off force over the entire pH range investigated. It was suggested that the adherence variation observed by CFM at low pH values was related to a heterogeneous distribution of protonated carboxyl functional groups ( $-\text{COOH}$ ), as revealed by the ToF-SIMS and XPS experiments. For the flame-treated samples, the interactions between the ionizable functional (carboxylic acid) groups and the hydroxyl groups at the tip influenced the pH-dependence of the pull-off force. Since the hydroxyl-terminated tips did not show any pH dependence, the titration behavior could be directly attributed to varying degrees of protonation of the  $-\text{COOH}$  groups at the LDPE surface. Based on the force titration curves, it was apparent that the strength of adhesion and the extent of attractive interaction diminished with increasing the pH.

When the pH is increased, these protonated functional groups give rise to a force-effective surface  $pK_a$ . Such behavior was also observed on the surface-treated LDPE in the

present study. The value of the surface  $pK_a$  was evaluated from the force titration curves and was found to be approx. 6.

Similar to previous studies,<sup>27</sup> it was proposed that for the flame-treated LDPE surfaces, the carboxylic acid groups were stabilized by the surrounding methyl groups, leading to the deprotonation occurring at higher pH values, as compared with the listed homogenous –COOH solutions.<sup>56, 57</sup>

### **3.2.5 Oxidation mechanism by flame-treatment**

The combustion of hydrocarbons is a highly complex process and many excited species were present in the flame, including free radicals, ions, atoms and electrons.<sup>58</sup> The ion concentration in a hydrocarbon flame is usually low,<sup>59</sup> and UV emissions from hydrocarbon flames are primarily due to OH radicals. Ground state molecular oxygen and long-lived excited oxygen molecules were thought to be non-reactive toward saturated polymers such as PE. Hydrogen abstraction by oxygen molecules is unlikely to occur in a flame. Thus, it was far more likely that the free radicals in the flame were the species responsible for the formation of polymer radicals.<sup>9, 10, 30, 31, 60</sup> The mechanism has been unanimously considered to occur by a radical process. In addition, it is known that the chemical reactions involving in a flame usually proceed through free radical intermediates.<sup>61</sup> The mechanism of surface oxidation by flame-treatment likely involves polymer radical formation through abstraction of hydrogen by O and OH, followed by rapid reaction of the polymer radicals with O, OH, and O<sub>2</sub>. The alkoxy, peroxy and hydroperoxy polymer radicals formed by this oxidative attack lead to a wide range of oxidized products through further reactions with O and polymer, or through reactions between the radicals themselves.<sup>10, 31</sup>

It was found that chain scission<sup>53, 62, 63</sup> accompanied by oxidative attack leads to the formation of low molecular weight oxidized material which agglomerated into globules at the surface. Such low molecular weight fragments of the polymer at the surface acted as a weak boundary layer. For a larger number of treatments, the degradation was more emphasized. After washing with water, the flame-treated LDPE was still oxidized but no longer included scission products with the low molecular weight moieties at the surface. The insoluble oxidized products of flame-treatment were probably composed of high or intermediate molecular weight material.



Degradation of polyethylene is also induced by other external factors and mechanisms such as thermal effect.<sup>54, 55</sup> Elevated temperatures can significantly increase the rate of various chemical reactions, such as oxidation, and therefore lead to the degradation of the polymer in an indirect way. The hydroxyl and carbonyl groups usually account for most of the oxidation products on thermooxidative degradation of polyethylene. Such products would not be washed off by water treatment.

### 3.3 Conclusions

In this paper, the surface of flame-treated LDPE was studied by various techniques. A comprehensive view of the effects of the flame-treatment at different sampling depths with respect to the sensitivities of the various techniques was obtained. The surface modification of LDPE by this process appeared to be simple and environmentally friendly. Surface physicochemical modification could be attributed to interactions of the polymer with high energy excited species in the flame. These induce modifications characterized by the presence of oxygenated groups at the surface. The introduction of high energy oxidized groups enhanced the LDPE surface energy thus improved its wettability by polar liquids. The number of polar groups showed a constant increase with the number of flame-treatments, and the depth of oxidation was also found to be a function of the number of treatments. XPS analysis, using high energy resolution and a refined approach to C 1s curve fitting, provided insights into the quantitative assessment of the type and concentration of functional groups. Positive ToF-SIMS spectra were obtained at high mass resolution. The oxygen-containing fragments were identified by accurate mass analysis and subjected to a detailed comparison with the XPS results. The dominating functional groups as a result of the flame-treatment were identified as hydroxyl, carbonyl and carboxyl groups. The formation of a heterogeneous surface topology exhibiting drop-like features was observed by AFM. The degradation reaction resulted in the formation of low mass by-products via chain scission, which coagulated and appeared as "drops". Washing the film with water after the flame-treatment reduced a small percentage of the atomic percentage of oxygen on the surface and removed droplike features exhibiting a nodular topography. The surface ionization state was studied by chemical force titration curves. Characteristic surface  $pK_a$  values of approx. 6 were obtained for carboxyl acid groups at the surface. This indicated a nanoscale heterogeneity of the –COOH functional groups. However, on the microscale and above, the lateral distribution of

the functional groups was homogeneous (*i.e.* beyond the resolution of optical diffraction limit) as evidenced by FM.

### **3.4 Experimental section**

**Materials.** Additive free LDPE films (with thicknesses of 0.2 mm) were obtained from DSM (Geleen, the Netherlands). The melting point and weight percentage of crystallinity, as measured by differential scanning calorimetry (DSC) at a scan rate of 10 K/min (Perkin-Elmer DSC-7), were 113.5°C and 32.1%, respectively. Samples of the films were cut into pieces of ca. 1cm × 1cm prior to treatment. After refluxing in dichloromethane (Merck) for 30 min, the films were rinsed in ethanol (Merck) and dried in a stream of nitrogen immediately prior to use.

**Flame-treatment.** A mixture of natural gas and air were combusted by a nozzle type burner and this procedure constituted the film flame-treatment in our experiments. For an efficient treatment, variables such as the air to gas ratio, air and gas flow rates, the distance between the tip of the flame and the object to be treated, as well as the treatment time had to be controlled.<sup>11</sup> The flow rate of the mixture of natural gas and air was ca. 12.3 cm<sup>3</sup>/s and the equivalence ratio, which is defined as the stoichiometric oxidizer: fuel ratio divided by the actual oxidizer: fuel ratio was ca. 0.93. A longer exposure to the high temperature flame caused the films to become easily destroyed and was not very effective in increasing the amount of functional groups. In order to increase the degree of oxidation at the surface, repeated cycles of flame-treatment were carried out. The LDPE films were repeatedly pulled across the tip of the flame at a distance of ca. 0-1 mm with a speed of ca. 0.5 m/s. The flame cone length is ca. 1 cm so that the exposure time of the film to the flame is about ca. 0.02s. The frequency of repetitions was defined as the treatment number which was proportional to the total treatment time. Thus the total treatment time varied from 0 to 4 s. For all experiments, the flame-treatment number had to be lower than 200 or else the LDPE films became deformed.

**Contact angle experiments.** The contact angles were determined by the sessile drop technique using Milli-Q water and a contact angle microscope (Data Physics, OCA 15plus) at room temperature and ambient humidity. All contact angles were measured on both sides of the

drop and the results were averaged. Each contact angle reported in this work was an average of the values obtained for a minimum of 3 points on the sample surface.

**X-ray photoelectron spectroscopy (XPS).** The atomic compositions of the surfaces of the flame-treated LDPE samples were analyzed by angle-resolved XPS on a PHI Quantum 2000 Scanning ESCA microprobe (Chanhasen, MN) using a  $Al_{K\alpha}$  X-ray source at a variable take-off angle between  $10^\circ$  and  $60^\circ$ . A 25 Watt X-ray beam with a  $100\ \mu\text{m}$  diameter scanned over a  $700\ \mu\text{m} \times 300\ \mu\text{m}$  area. Atomic concentrations were determined by numerical integration of the relative peak areas using the Multipak software with supplied sensitivity factors (C 1s: 0.312; O 1s: 0.733).<sup>64</sup>

**Fluorescence microscopy (FM).** Fluorescence micrographs were obtained with a Zeiss LSM 510 confocal fluorescence microscopy. Images of dry samples on glass cover slips were recorded at room temperature on a Plan-Apochromat<sup>®</sup>  $63 \times / 1.4$  numerical aperture oil-immersion objective. Fluoresceinamine, excited with the 488 nm line of an  $Ar^+$  laser, was used as dye. The fluorescence emission of the dye was recorded with photomultiplier tubes (Hamamatsu R6357) after spectral filtering with a 500-550 nm bandpass filter and a 650 nm longpass filter. Images with maximum pinhole diameters were acquired.

**Coupling of fluoresceinamine.** First, untreated and flame-treated LDPE films were rinsed thoroughly with water and ethanol. After that, the LDPE films were activated for fluorescence studies by immersion for  $2 \times 30$  min in aqueous solutions of 1 M 1-ethyl-3-(dimethylamino)-propylcarbodiimide (EDC), and 0.2 M N-hydroxysuccinimide (NHS), successively. Subsequently, the films were immersed in a fluoresceinamine solution (100 mM, PB buffer, pH = 7.4) for an additional 30 min, after which they were taken out, rinsed with PB buffer and Milli-Q water, and dried in a stream of nitrogen. Fluoresceinamine, EDC and NHS were all purchased from Aldrich and were used as received.

**Time-of-flight secondary ion mass spectrometry (ToF-SIMS).** In ToF-SIMS, a pulsed, focused, energetic ion beam bombards a surface, leading to interactions that cause the emission of positive and negative secondary ions.<sup>65, 66</sup> A reflectron type time-of-flight mass spectrometer, with a design equivalent to that of the "ToF-SIMS IV". An electron impact ion source (10 keV,  $^{40}Ar^+$ ) was used for generating primary ion pulses for static ToF-SIMS. The pulsed ion beam was raster-scanned over an area of  $200\ \mu\text{m} \times 200\ \mu\text{m}$ . The detected mass range from 1 to 3500 amu and the mass resolution  $m/\Delta m$  was better than 5000 at mass 41. For

charge compensation, a low energy electron flood gun was utilized.

**Atomic force microscopy (AFM).** Surface topography measurements were carried out with a NanoScope IIIa multimode AFM [Veeco-Digital Instruments (DI), Santa Barbara, CA]. Tapping mode AFM scans was performed in air using a non-coated silicon tip with a spring constant of 10 N/m ~ 20 N/m (Nanosensors, Wetzlar, Germany). Features on the nanometer scale were imaged on a minimum of three different areas on the samples.

Force Volume experiments as described in a previous published paper.<sup>67</sup> which give information about laterally resolved surface adherence were performed in a liquid environment with the AFM controller fitted with a DI liquid cell (volume ~ 50  $\mu$ L). Triangular shaped silicon nitride cantilevers and silicon nitride tips (DI) coated with ca. 2 nm Ti as the adhesion layer and ca. 50 nm Au in high vacuum were used in these AFM FV experiments. Functional groups for chemical force microscopy were introduced at the AFM tip surface by modifying gold-coated Si<sub>3</sub>N<sub>4</sub> cantilevers with self-assembled monolayers (SAMs). The functionalized tips were prepared by immersion in a 1 mM 11-mercapto-1undecanol solution in ethanol for 10 ~ 40 h at room temperature. The so-obtained tips were kept in solution between measurements, rinsed in ethanol and dried in a stream of nitrogen immediately prior to use. The spring constants of the cantilevers ranged from 0.14 to 0.18 N/m, as obtained by the method of Hutter and Bechhoefer<sup>68</sup> according to the equipartition method which consists in measuring the thermal excitation of the tip to compute its spring constant. The specific details of the CFM procedure were similar to those reported for previous studies.<sup>69</sup>

## References

- [1] Caldwell, R. A.; Woodell, J. E.; Ho, S. P.; Shalaby, S. W.; Boland, T.; Langan, E. M.; Laberge, M., *J. Biomed. Mater. Res.* **2002**, *62*, 514.
- [2] Tajima, S.; Komvopoulos, K., *J. Phys. Chem. B* **2005**, *109*, 17623.
- [3] Owen, M. J.; Smith, P. J., *J. Adhes. Sci. Technol.* **1994**, *8*, 1063.
- [4] Kim, K. S.; Ryu, C. M.; Park, C. S.; Sur, G. S.; Park, C. E., *Polymer* **2003**, *44*, 6287.
- [5] Chan, C. M.; Ko, T. M., *Surf. Sci. Rep.* **1996**, *24*, 1.
- [6] Liston, E. M.; Martinu, L.; Wertheimer, M. R., *J. Adhes. Sci. Technol* **1993**, *7*, 1091.
- [7] Chen, J. S.; Sun, Z.; Guo, P. S.; Zhang, Z. B.; Zhu, D. Z.; Xu, H. J., *J. Appl. Phys.* **2003**, *93*, 5103.
- [8] Iwata, H.; Kishida, A.; Suzuki, M.; Hata, Y.; Ikada, Y., *J. Polym. Sci. Pol. Chem.* **1988**, *26*, 3309.
- [9] Severini, F.; Di Landro, L.; Galfetti, L.; Meda, L.; Ricca, G.; Zenere, G., *Macromol. Symp.* **2002**, *181*, 225.
- [10] Strobel, M.; Jones, V.; Lyons, C. S.; Ulsh, M.; Kushner, M. J.; Dorai, R.; Branch, M. C., *Plasmas Polym.* **2003**, *8*, 61.
- [11] Desai, S. M.; Singh, R. P., *Adv. Polym. Sci.* **2004**, *169*, 231.
- [12] Salleo, A.; Chabinye, M. L.; Yang, M. S.; Street, R. A., *Appl. Phys. Lett.* **2002**, *81*, 4383.
- [13] Kim, B. K.; Kim, K. S.; Cho, K.; Park, C. E., *J. Adhes. Sci. Technol.* **2001**, *15*, 1805.
- [14] Chan, C. M., *Polymer Surface Modification and Characterization*. Hanser Publishers: Munich, 1994.
- [15] Brewis, D. M.; Briggs, D., *Polymer* **1981**, *22*, 7.
- [16] Momose, Y.; Tamura, Y.; Ogino, M.; Okazaki, S.; Hirayama, M., *J. Vac. Sci. Technol. A* **1992**, *10*, 229.
- [17] Clouet, F.; Shi, M. K., *J. Appl. Polym. Sci.* **1992**, *46*, 1955.
- [18] Hansen, R. H.; Pascale, J. V.; De Benedictis, T.; Rentzepis, P. M., *J. Polym. Sci. A* **1965**, *3*, 2205.
- [19] Strobel, M.; Corn, S.; Lyons, C. S.; Korba, G. A., *J. Polym. Sci. Pol. Chem.* **1985**, *23*, 1125.
- [20] Hollahan, J. R.; Bell, A. T., *Techniques and Applications of Plasma Chemistry*. John Wiley & Sons: New York, 1974.
- [21] Vasilets, V. N.; Tikhomirov, N. A.; Ponomarev, A. N., *Khim. Vys. Energ.* **1978**, *12*, 442.
- [22] Olander, B.; Wirsen, A.; Albertsson, A. C., *J. Appl. Polym. Sci.* **2004**, *91*, 4098.
- [23] Truica-Marasescu, F.; Jedrzejowski, P.; Wertheimer, M. R., *Plasma Process. Polym.* **2004**, *1*, 153.
- [24] Klapperich, C.; Pruitt, L.; Komvopoulos, K., *J. Mater. Sci.: Mater. M.* **2001**, *12*, 549.
- [25] Rasmussen, J. R.; Bergbreiter, D. E.; Whitesides, G. M., *J. Am. Chem. Soc.* **1977**, *99*, 4746.
- [26] Rasmussen, J. R.; Stedronsky, E. R.; Whitesides, G. M., *J. Am. Chem. Soc.* **1977**, *99*, 4736.
- [27] Schönherr, H.; Hruska, Z.; Vancso, G. J., *Macromolecules* **2000**, *33*, 4532.
- [28] Fonseca, C.; Perena, J. M.; Fatou, J. G.; Bello, A., *J. Mater. Sci.* **1985**, *20*, 3283.
- [29] Strobel, M.; Branch, M. C.; Ulsh, M.; Kapaun, R. S.; Kirk, S.; Lyons, C. S., *J. Adhes. Sci. Technol.* **1996**, *10*, 515.
- [30] Garbassi, F.; Morra, M.; Occhiello, E., *Polymer Surfaces From Physics to Technology*. John Wiley & Sons: Chichester, 1998.
- [31] Strobel, M.; Sullivan, N.; Branch, M. C.; Park, J.; Ulsh, M.; Kapaun, R. S.; Leys, B., *J. Adhes. Sci. Technol.* **2000**, *14*, 1243.
- [32] Adamson, A. W.; Gast, A. P., *Physical Chemistry of Surfaces*. John Wiley and Sons: New York, 1997.
- [33] Johnson, R. E.; Dettre, R. H., *J. Colloid Interf. Sci.* **1966**, *21*, 610.
- [34] Le, Q. T.; Pireaux, J. J.; Caudano, R., *J. Adhes. Sci. Technol.* **1997**, *11*, 735.
- [35] Briggs, D.; Brewis, D. M.; Dahm, R. H.; Fletcher, I. W., *Surf. Interface Anal.* **2003**, *35*, 156.
- [36] Beamson, G.; Briggs, D., *High Resolution XPS of Organic Polymers: the Scienta ESCA300 Database*. Wiley: Chichester, 1992.
- [37] Briggs, D.; Kendall, C. R.; Blythe, A. R.; Wootton, A. B., *Polymer* **1983**, *24*, 47.

- [38] Vickerman, J. C.; Briggs, D., *ToF-SIMS: Surface Analysis by Mass spectrometry*. IMPublications: Chichester, 2001.
- [39] Ferraz, M. P.; Knowles, J. C.; Olsen, I.; Monteiro, F. J.; Santos, J. D., *Biomaterials* **2000**, *21*, 813.
- [40] Benters, R.; Niemeyer, C. M.; Wohrle, D., *Chembiochem* **2001**, *2*, 686.
- [41] Apostolova, E.; Krumova, S.; Tuparev, N.; Molina, M. T.; Filipova, T.; Petkanchin, I.; Taneva, S. G., *Colloid. Surface B* **2003**, *29*, 1.
- [42] Herold, M.; Brunner, H.; Tovar, G. E. M., *Macromol. Chem. Physic.* **2003**, *204*, 770.
- [43] Lee, K. B.; Yoon, K. R.; Woo, S. I.; Choi, I. S., *J. Pharm. Sci.* **2003**, *92*, 933.
- [44] Wang, W. L.; He, Q. G.; Zhai, J.; Yang, J. L.; Bai, F. L., *Polym. Advan. Technol.* **2003**, *14*, 341.
- [45] Hollander, A., *Surf. Interface Anal* **2004**, *36*, 1023.
- [46] Ye, T.; McArthur, E. A.; Borguet, E., *J. Phys. Chem. B* **2005**, *109*, 9927.
- [47] Flink, S.; van Veggel, F. C. J. M.; Reinhoudt, D. N., *J. Phys. Org. Chem* **2001**, *14*, 407.
- [48] Montalti, M.; Prodi, L.; Zaccheroni, N.; Baxter, R.; Teobaldi, G.; Zerbetto, F., *Langmuir* **2003**, *19*, 5172.
- [49] Sagiv, J., *J. Am. Chem. Soc.* **1980**, *102*, 92.
- [50] McArthur, E. A.; Ye, T.; Cross, J. P.; Petoud, S.; Borguet, E., *J. Am. Chem. Soc.* **2004**, *126*, 2260.
- [51] Overney, R. M.; Luthi, R.; Haefke, H.; Frommer, J.; Meyer, E.; Guntherodt, H. J.; Hild, S.; Fuhrmann, J., *Appl. Surf. Sci.* **1993**, *64*, 197.
- [52] Strobel, M.; Dunatov, C.; Strobel, J. M.; Lyons, C. S.; Perron, S. J.; Morgen, M. C., *J. Adhes. Sci. Technol.* **1989**, *3*, 321.
- [53] Boyd, R. D.; Kenwright, A. M.; Badyal, J. P. S., *Macromolecules* **1997**, *30*, 5429.
- [54] Gugumus, F., *Polym. Degrad. Stabil.* **1996**, *52*, 131.
- [55] Dilara, P. A.; Briassoulis, D., *J. Agric. Engng. Res.* **2000**, *76*, 309.
- [56] Bain, C. D.; Whitesides, G. M., *Langmuir* **1989**, *5*, 1370.
- [57] Risch, K.; Seitz, H., *Organische Chemie*. Schroedel: Hannover, 1981.
- [58] Gaydon, A. F., *The Spectroscopy of Flames*. Springer: London, 1974.
- [59] Lewis, B.; von Elbe, G., *Combustion, Flames and Explosions of Gases*. Academic Press: Orlando, 1987.
- [60] Sheng, E.; Sutherland, I.; Brewis, D. M.; Heath, R. J.; Bradley, R. H., *J. Mater. Chem.* **1994**, *4*, 487.
- [61] Briggs, D.; Kendall, C. R., *Polymer* **1979**, *20*, 1053.
- [62] Penney, W. R.; Bell, K. J., *Ind. Eng. Chem* **1967**, *59*, 40.
- [63] Yun, H. K.; Cho, K.; Kim, J. K.; Park, C. E.; Sim, S. M.; Oh, S. Y.; Park, J. M., *J. Adhes. Sci. Technol* **1997**, *11*, 95.
- [64] Reilman, R. F.; Msezane, A.; Manson, S. T., *J. Electron Spectrosc.* **1976**, *8*, 389.
- [65] Benninghoven, A., *Angew. Chem. Int. Edit.* **1994**, *33*, 1023.
- [66] Leeson, A. M.; Alexander, M. R.; Short, R. D.; Briggs, D.; Hearn, M. J., *Surf. Interf. Anal.* **1997**, *25*, 261.
- [67] Song, J.; Duval, J. F. L.; Cohen Stuart, M. A.; Hillborg, H.; Gunst, U.; Arlinghaus, H. F.; Vancso, G. J., *Langmuir* **2007**, *23*, 5430.
- [68] Hutter, J. L.; Bechhoefer, J., *Rev. Sci. Instrum.* **1993**, *64*, 1868.
- [69] Hillborg, H.; Tomczak, N.; Olah, A.; Schönherr, H.; Vancso, G. J., *Langmuir* **2004**, *20*, 785.



# Chapter 4

## **Effects of flame-treatment on the interfacial energy of LDPE assessed by contact mechanics<sup>†</sup>**

In this *chapter*, the effects of flame-treatment of LDPE on *work of adhesion* ( $W$ ) and *energy release rate* ( $G$ ) were assessed by a custom-built adhesion testing device (ATD). The contact area and the vertical displacement between LDPE films and PDMS lenses (untreated and UV/ozone treated) were varied as functions of the applied load,  $P$ . The adhesion and pull-off forces between the extracted PDMS lenses and the LDPE films were studied as functions of the duration of the flame-treatment expressed in “treatment numbers”. A fracture mechanics approach was used to relate the applied load and the radius of the contact area to the energy release rate. The difference between the energy release rate and the thermodynamic *work of adhesion*, defined as the adhesion hysteresis ( $G-W$ ), increased systematically with increasing treatment numbers for both lens types. In addition, the adhesion hysteresis appeared to be dependent on the contact time. Finally, the origin of the adhesion hysteresis was discussed. It was concluded that bonding by surface functional groups may be the dominating mechanisms for the observed hysteresis.

---

<sup>†</sup> This *chapter* is submitted for publication.



## 4.1 Introduction

In recent years, a fast growth in polyethylene (PE) films for engineering applications has taken place due to excellent combinations of PE properties such as easy processability, surface finishing versatility, excellent barrier behavior, etc. However, many of these applications require good adhesion properties. Unfortunately, due to the inherent low surface tension of hydrocarbons, PE films exhibit low *work of adhesion* and are hydrophobic. Thus, the control and tailoring of the adhesion (adherence) by various surface treatment methods and related surface characterization and physical/chemical investigation have attracted special attention.<sup>1,2</sup>

In *chapter 3*, the relationship between surface chemistry and morphology of flame-treated LDPE has been studied by various characterization techniques. The LDPE was flame-treated in order to raise the surface activity of the polymer and enhance its wettability without modifying the bulk properties. The design of an adhesion (adherence) measurement for such flame-treated LDPE is described in this *chapter*. Traditional adhesion measurement techniques such as peel test or blister test reflect the practical adhesion of the tested materials and involve large bulk deformations which is no doubt useful from a design point of view.<sup>3</sup> However, they offer only a limited sensitivity and are not well suited for capitalizing on "tunable interfaces". The *Work of adhesion* and surface energy play vital roles in understanding the theories of adhesion. In addition to contact angle measurements which infer or estimate solid *surface energy* and *work of adhesion* from the deposition of liquid droplets of varying liquid-vapour surface tensions on the surface,<sup>4</sup> the so-called adhesion testing device (ATD) or JKR apparatus provides an alternative direct contact mechanics approach for characterizing the adhesion behavior via the change in surface energy when two solid surfaces (vs. liquid-solid in contact angle measurement) are in contact.<sup>5,6</sup> Basically, contact mechanics encompass the mechanics of solids spreading their interfacial area under normal pressure on contacting (curved) surfaces.<sup>7</sup> Preferentially, contact mechanics should be studied in a thermodynamically reversible fashion, for example, by performing static or zero rate adhesion measurements.<sup>6</sup> The ATD or JKR apparatus is an acceptable technique since slow loading rates can be applied and the system is in a quasi-equilibrium condition. Adhesion measurements by ATD implies the determination of the thermodynamic *work of adhesion* ( $W$ ) between two curved surfaces (with the geometric mean radius of curvature  $R$ ), often a soft hemisphere and a hard flat surface,<sup>8</sup> less often crossed cylinders.<sup>9,10</sup> This hemisphere is called

a lens and should be fabricated of compliant, elastic materials with low surface energy. From early ATD experiments with natural and synthetic rubbers,<sup>8, 11-13</sup> gelatin<sup>8</sup> and polyurethanes,<sup>14, 15</sup> to more recent studies with PDMS<sup>5, 13, 16-18</sup> and polyisoprene elastomers,<sup>19, 20</sup> the usefulness and potential of this technique have been well established. In addition, the technique minimizes the sample volume to reduce bulk viscoelastic losses and permit testing at a lower range of crack velocities where interfacial effects are unobscured by bulk effects.

Furthermore, the method is even anticipated for contact between dissimilar materials. This opens for the possibility of greatly expanding our knowledge of interfacial energies between different solid polymers. Lastly, the ATD test geometry is readily adaptable to sliding experiments, as shown by Brown,<sup>21</sup> a potentially very significant advantage for the development of our understanding of the relationships between adhesion and friction, between normal pressure and sliding force, measured nearly simultaneously at the same interfaces. However, in parallel with the successes, many poorly understood phenomena remain to be solved. The reliability and interpretation of JKR experiments for largely dissimilar interfaces are still problematic. This assures further in-depth studies, e.g. in the case of surface-treated polymers.

Interfacial energies were determined from contact mechanics experiments in the loading mode, analyzed by the Johnson-Kendall-Roberts (JKR) theory of adhesive elastic contacts.<sup>7</sup> Although this approach yields results that correspond satisfactorily with those from contact experiments, in which the load on the sample is increased with time, a substantial hysteresis is very often observed when the sample is unloaded. The deformation is irreversible as would be required by the JKR theory. The origin of this hysteresis is not always understood; is sometimes controversial, and may well vary for different situations. To investigate the origin of such adhesion hysteresis, the JKR approach can be extended by using fracture mechanics.<sup>14</sup> In this *chapter*, energy release rate,  $G$ , during crack propagation introduced by Maugis,<sup>22</sup> in order to characterize the practical interfacial energy or the fracture toughness.

The ability to tailor adhesion properties of surfaces and interfaces for specific application is a challenge. In this *chapter*, the contact between PDMS lenses and LDPE films was studied in the framework of the JKR method by an ATD set-up. The aim was to explore the change of the *work of adhesion* as a function of surface treatment, and defined the source of the adhesion hysteresis that was generated. The fracture energy,  $G$ , was studied as a

function of the crack speed, contact time, and flame-treatment level. We believe that these studies carry both fundamental and technological significance.

## 4.2 Adhesion (adherence) measurements by ATD

The ATD set-up was used to describe the mechanics of contact that developed when a solid, hemispherical PDMS lens was pressed onto a rigid flat substrate.<sup>23,24</sup> An ATD set-up usually consists of the sample (an elastomeric lens in contact with a substrate), a mechanical load cell, an optical microscope for measuring the contact area (equipped e.g. with a CCD camera), a stepper motor, a force transducer, a sample stage and various control accessories (see experimental part, Figure 4.9). The measurements were performed at a fixed motor movement speed (0.17; 0.42; 0.84  $\mu\text{m/s}$  respectively) until a maximum contact area ( $A_{\text{max}}$ ) was reached (loading regime). The maximum diameter of the contact area was limited to 150  $\mu\text{m}$  in order for the deformations to be kept within the elastic regime.<sup>25</sup> The load was then released (unloading regime) and the motor was moved in a reverse direction, either directly after loading or after the system had been held in contact for a given time. A typical dynamic loading/unloading cycle of a cross-linked PDMS lens on a flame-treated LDPE film is shown in Figure 4.1, where the features of the curves are also depicted. In this plot, the recorded load,  $P$ ; the imposed displacement of the bodies,  $\delta$ ; and the radius of the circular contact area,  $a$ , are presented as functions of time. Initially, before contact, the force transducer recorded a so called zero force ( $t < t_1$ ). As the surface were approached, at the so-called snap-on point, the elastomeric lens "jumps" into contact with the substrate. The corresponding force is a measure of the adhesion and acts as an additional effective load. In the moment of the snap-on, a detectable contact area ( $t = t_2$ ) is formed. The loading part ( $t = [t_2, t_3]$ ) lasts until the motion is reversed. Upon retraction of the surfaces, the unloading commences with a slowly descending curve. This region ( $t = [t_3, t_4]$ ) is dominated by the mechanical response of the device, namely the gearbox and the shaft hysteresis. The unloading curve ( $t = [t_3, t_7]$ ) usually goes through a minimum, the so-called maximum adherence force or pull-off force ( $t = t_6$ ) and ends with a sudden separation (snap-off) ( $t = t_7$ ) of the contacting surfaces. The final part of the cycle is characterized by zero contact force ( $t > t_7$ ), where separated surfaces are far from each other. It should also be noted that there is a difference between the time of the unloading and that of the loading part, which reflects the longer time required for the contacting interfaces to break rather than to form.

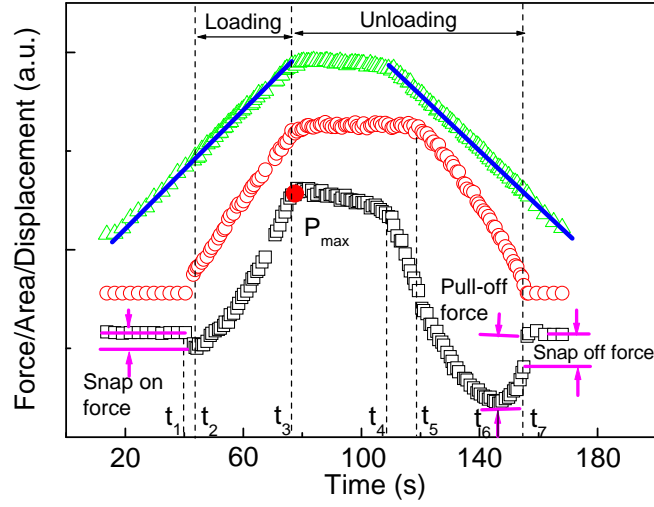


**Figure 4.1** A typical loading and unloading cycle of the LDPE sample system with explanations of the characteristic features. The curves of the load,  $P$  ( $\square$ ), contact area,  $A$  ( $\circ$ ), and motor displacement,  $\delta$  ( $\Delta$ ) are represented in real time of the measurement.

The relationship between the force and the contact radius of the loading and unloading part for contact between a PDMS lens and an untreated commercial LDPE film is illustrated in Figure 4.2a. These data are representative of all the data in this *chapter*. The values of thermodynamic *work of adhesion* ( $W$ ) and combined *elastic modulus* ( $K$ ) were obtained by fitting the recorded loading part using the JKR theory with Equation 4-1.

$$a^3 = \frac{R}{K} \left[ P + 3\pi R W_{12} + \left( 6\pi R P W_{12} + (3\pi R W_{12})^2 \right)^{1/2} \right] \quad (\text{Eq. 4-1})$$

Here,  $R$  is the relative radius,  $1/R = 1/R_1 + 1/R_2$  (for ideally flat surface,  $R_2 \rightarrow \infty$ ),  $K$  is the combined elastic modulus  $K = 4/3 \left[ (1-\nu_1^2)/E_1 + (1-\nu_2^2)/E_2 \right]^{-1}$  (with  $E_{1,2}$  and  $\nu_{1,2}$  as the elastic moduli and Poisson's ratios of the lens and sample film, respectively), and  $W$  is the thermodynamic *work of adhesion* at the interface. For symmetrical contacts  $W = 2\gamma$ , whereas for asymmetrical contacts  $W = \gamma_1 + \gamma_2 - \gamma_{12}$ . The basis of this equation is a balance of attractive energy exerted through the adhesive contact producing a deformation that tends to increase " $a$ " and a countervailing elastic energy that tends to reduce " $a$ " (once more, in

thermodynamic equilibrium). In Figure 4.2a, the solid line (purple) corresponds to the data from the loading part with the fitting parameters by the JKR model. Another solid line (yellow) shows the relationship between the load and contact radius as predicted by the Hertz model (see *chapter 2*) where the value of the combined elastic modulus is kept constant or obtained from the bulk material. Because of the quasi-equilibrium nature of the experiment,  $W$  can not be associated with the true thermodynamic *work of adhesion*, especially when strong interactions exist at the interface.  $K$  is not an idealized parameter, and often deviates from known values of the bulk elastic constant. However, utilization of the equation continues to be used since there is no alternative theory.

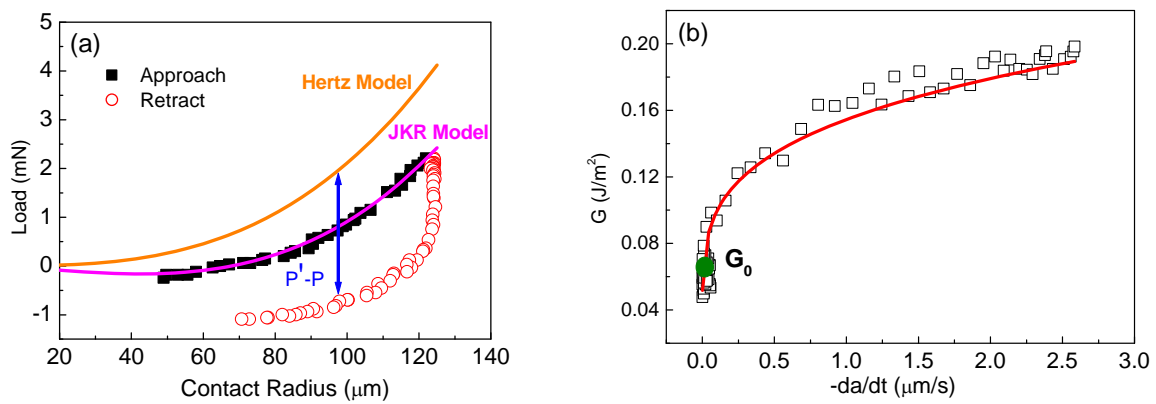


**Figure 4.2** a) A JKR fit to the advancing part of the loading-unloading cycle of the untreated LDPE sample. b) The dependence of  $G$  on the crack growth rate for the unloading data shown in (a).

For a quantitative analysis of the unloading data, a rearrangement of the JKR theory (Equation 4-2) to explicitly solve the energy release rate,  $G$ .

$$G = \frac{1}{6\pi K a^3} \left( P' - P \right)^2 \quad (\text{Eq. 4-2})$$

$$P' = \frac{K a^3}{R} \quad (\text{Eq. 4-3})$$

Here,  $P'$  is the effective load that would have been necessary in a purely Hertzian situation, i.e. where no adhesion exists between the surfaces, to produce the observed contact radius. Of course, in reality, the actual load  $P$ , required to maintain the same contact radius, is smaller than  $P'$  since the surface forces tend to enlarge the interfacial area. The difference  $P' - P$  is

shown in Figure 4.2a. It follows that the square of this difference is proportional to  $G$  (Equation 4-2). For equilibrium data, the *work of adhesion*,  $W$ , is exactly matched by the strain energy release rate,  $G$ , and this is the classical *Griffith* criterion of fracture mechanics,  $G = W$ . During unloading, equilibrium is usually not achieved and therefore the data of  $a$  versus  $P$  yields a nonequilibrium value of  $G$  which drives the relaxation of the contact of the opening of the crack as the contact radius decreases. Therefore, a nonequilibrium time-dependent form of Equation 4-2 was used to determine the strain energy release rate. Hence,  $G$  was calculated from the data of  $a$  versus  $P$  inserted in Equation 4-2 and a predetermined value of  $K$  obtained from the loading curves was assumed (see results and discussion).<sup>26</sup> This procedure is derived from the analysis of Maugis and Barquins<sup>14, 27</sup> and has been widely employed.<sup>17, 19-21</sup>

Upon unloading from the maximum load,  $P_{\max}$ , the contact area was progressively reduced until the lens was completely separated from the substrate. Thus, at the periphery of the contact circle, there existed a growing interfacial crack whose velocity was given by the first derivative of the contact radius with respect to time, i.e.  $-da/dt$ . In order to examine more precisely the rate dependence of adhesion, it was necessary to relate  $G$  to the true interfacial crack velocity,  $v'$ , Figure 4.2b presents the data of energy release rate as a function of the crack propagation rate for the adhesion between PDMS the lens and the untreated LDPE surfaces. It can be noticed that the unloading  $G$  initially increased without any variation of  $a$  (that remained equal to the maximum contact area) and  $v' = 0$  before a critical fracture energy,  $G_0$ , is reached from which  $a$  shrunk while  $G$  continued to increase monotonically, ( $G$  refers to an energy release rate value that was obtained while the crack was propagating and thus contact patch was shrinking and  $G_0$  refers to the initial value of  $G$  where the propagation started). Such behavior has already been reported in the literature without much discussion of the criteria required for its observation. During unloading,  $G$  significantly exceeds  $W$  and gives rise to a positive driving force in order for the crack to propagate at a velocity  $v'$ .

### 4.3 Results and Discussion

Two kinds of PDMS lenses were used in our experiments. 1) Conventional, untreated PDMS lenses which are widely applied in JKR measurements. 2) UV/ozone treated PDMS lenses which were obtained to enhance surface free energy. The oxidation processes and their effects on the PDMS surfaces after exposure to UV/ozone irradiation have been investigated

by various techniques. A detailed account of this process will be shown in *chapter 5*. Following the surface modification with UV/ozone plasma, the PDMS surface changed from hydrophobic to hydrophilic. Thus, the surface energy of the oxidized PDMS surface also changed, thereby having an effect on the final results of adhesion and adherence between the lens and sample film. In comparison with the results obtained with untreated PDMS lens, corresponding experiments will help to fully understand the adhesion phenomena in this system.

A series of experiments with a PDMS or oxidized PDMS (PDMS<sub>OX</sub>) lens and LDPE films (untreated and flame-treated) at three different dynamic loading/unloading rates were performed. Figure 4.3 shows the obtained pull-off forces as functions of the flame-treatment numbers which are proportional to the duration of the flame-treatment (see *chapter 3*).

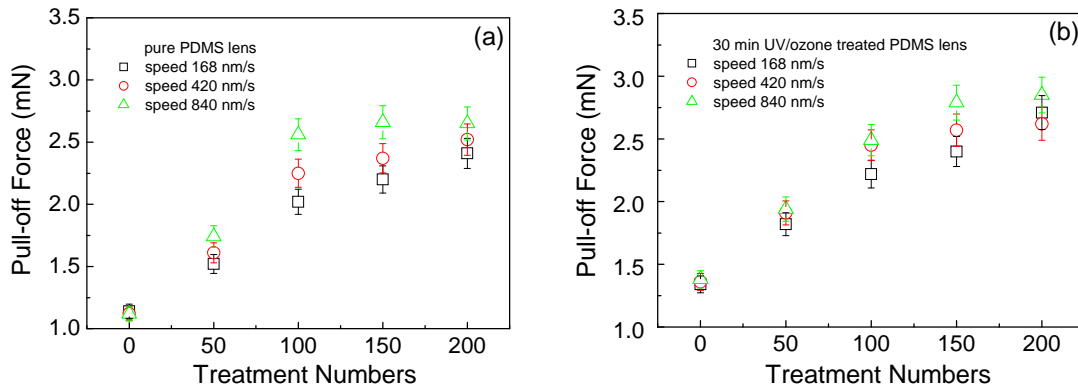


**Figure 4.3** The effects of flame-treatment on pull-off force of LDPE film with a) PDMS lens; b) PDMS<sub>OX</sub> lens at different loading speeds.

In a typical unloading part of the experiment, the contact radius decreased as the load was reduced from a compressive (positive) to a tensile (negative) value until pull-off occurred. The adherence between the contacting surfaces was analysed. It was found that with increasing treatment numbers, the adherence force between the PDMS lens and the LDPE film increased from 1.1 mN (untreated LDPE film) to 2.3 mN (sample treated 200 times). Increasing the unloading rate, generally increased the value of the pull-off force. For the surface treated PDMS<sub>OX</sub> lens, the pull-off force was enhanced from 1.6 mN (untreated LDPE film) to 2.7 mN (sample treated 200 times). A similar increase of the pull-off force, when increasing the unloading rate was observed. The adherence, as measured by the pull-off force,

is related to the *work of adhesion* in the thermodynamic limit. A thermodynamic adhesion energy  $W$  can be calculated from the JKR model (Equation 4-4):

$$F_{\text{pull-off}} = -\frac{3}{2}\pi RW_{12} \quad (\text{Eq. 4-4})$$

The JKR analysis predicts that the finite pull-off force required to separate the solids depends only on the value of the combined radius,  $R$ , and on the surface energies. However, it does not depend on the loading rate or on the magnitude of the initial maximum applied load, i.e. it neglects viscoelastic and dissipative phenomena. The enhanced surface energy of flame-treated LDPE and the UV/ozone treated PDMS lens were obtained from water contact angle experiments. For PDMS, a reduction in the advancing contact angle from  $\theta_a = 116^\circ$  (untreated) to  $\theta_a = 89^\circ$  (treated 30 min) was obtained, and for LDPE, the contact angle was decreased from  $\theta_a = 101^\circ$  (untreated) to  $\theta_a = 56^\circ$  (treated 200 times). These trends regarding the decrease of contact angle indicate (as expected) an increase in surface polarity (i.e. surface energy) as a result of the surface treatment. Changes in the surface energy can cause large changes in adherence, and thus allows the control of the adhesion in an engineering context.

It is worth to point out that the pull-off force and the value of adhesion energy in thermodynamic control should be constant at different loading rates when using the JKR model. However, in the present experiments, for the flame-treated LDPE films, an increase in the pull-off force was observed when the loading rate was increased. This increase was attributed to the onset of viscous dissipation processes at higher rates. Such effects of viscous dissipation at the periphery of the contact zone on the adhesive contact have been investigated.<sup>28-30</sup> In addition, JKR pull-off is a transient, fast process of "disjoining" a deformed, soft lens from a surface. The relaxation time of this deformation and the timescale of the pull-off event can be very different, which introduces experimental uncertainty. In addition to the pull-off force, the amplitude of the free energy increment corresponding to newly created free surfaces is another quantity related to adhesion phenomena. Therefore, in the following part, thermodynamic and practical adhesion will be discussed separately.

Figure 4.4 shows the fitted *work of adhesion* from the loading part of the JKR experiment as a function of treatment numbers. An increase in the obtained *work of adhesion* between the untreated PDMS lens and the LDPE film was observed for increasing treatment numbers.



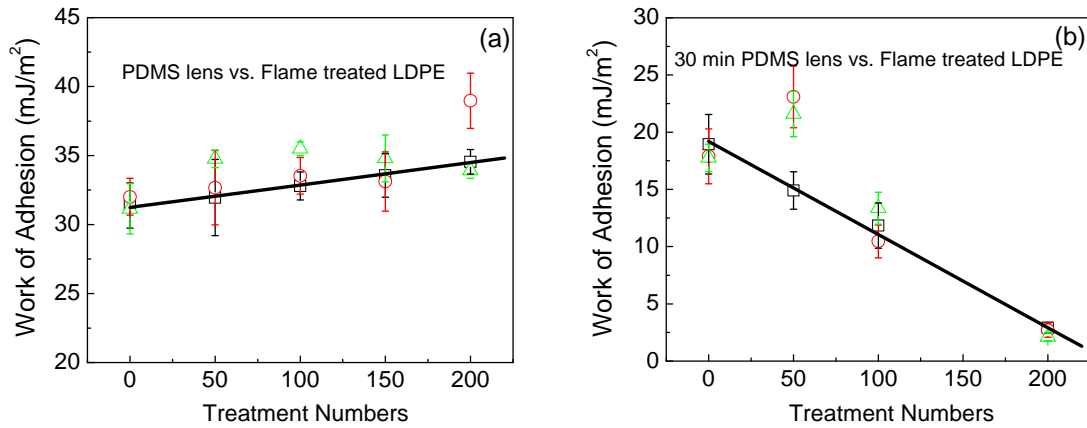


**Figure 4.4** The calculated work of adhesion as a function of treatment numbers. a) PDMS lens b) PDMS<sub>OX</sub> lens.

A theoretical value for  $W$  between a PDMS lens and a LDPE film can be calculated from the definition of the *work of adhesion*,

$$W = \gamma_{LDPE} + \gamma_{PDMS} - \gamma_{LDPE-PDMS} \quad (\text{Eq. 4-4})$$

where the surface tensions  $\gamma_{LDPE}$  and  $\gamma_{PDMS}$  are 33 and 21.7 mJ/m<sup>2</sup>, as taken from the literature.<sup>31, 32</sup> In a previous investigation, a value of 5.6 mJ/m<sup>2</sup> was obtained for the interfacial tension,  $\gamma_{LDPE-PDMS}$ , between PE and PDMS.<sup>33</sup> These numbers yield a predicted value of 48 mJ/m<sup>2</sup> for the *work of adhesion* between LDPE and PDMS. The value obtained from our experiment is 42 mJ/m<sup>2</sup> which was smaller than what was predicted. This difference may be due to surface roughness effects, since the surface roughness decreases the effective contact area. With an increased flame-treatment level, the density of polar functionalities on the surface increases, resulting in an enhancement of the surface energy and the *work of adhesion*.

However, the experiment with the PDMS<sub>OX</sub> lens showed a reversed trend. The *work of adhesion*,  $W$ , dropped from 42 mJ/m<sup>2</sup> on untreated LDPE to 8 mJ/m<sup>2</sup> on an LDPE treated 200 times as depicted in Figure 4.4 with PDMS<sub>OX</sub> lens. The obtained value of  $W_{PDMS_{OX}/LDPE}$  obtained was smaller as compared to the value for  $W_{PDMS/LDPE}$  mentioned above. This result seems contradictory. From our pervious study, the surface energy of PDMS will be enhanced after UV/ozone irradiation. The *work of adhesion*,  $W_{PDMS_{OX}/LDPE}$ , should thus increase as

compared to  $W_{\text{PDMS/LDPE}}$ . Similar observations displaying reduced  $W$  values from contact mechanics (JKR) experiments, were reported in studies of the self contact between model pressure-sensitive adhesives.<sup>34, 35</sup> For acrylate-based cross-linked elastomers, copolymerized with 10% acrylic acid a significant reduction of the *work of adhesion* was measured at room temperature with respect to the pure elastomer. The authors reasoned that this effect had its origin from the enhanced inelastic nature of the acid-containing polymer. In our experiments, the flame-treatment of the LDPE films enabled an enhancement of the stiffness of the films at the surface. However, more important phenomena were also identified. In the ATD measurements, a low modulus elastomer PDMS lens (with a Young's modulus around 3 MPa) deformed as compared to the hard substrate with LDPE thin film during the loading procedure. After UV/ozone irradiation, a thin silica-like layer was formed and the value of the surface Young's modulus will increase to 30 MPa on the micrometer length scale (see *chapter 6*). Such an increased inelastic nature of the PDMS lens resulted in the decrease of  $W$ . Another possible explanation for the deviation of the JKR measurements from theory was offered by Tirrell et al.,<sup>34, 35</sup> who reasoned that dipoles at the approaching surfaces are oriented such that they repel each other (net repulsion) during the dynamic process of approach. Only after contact is established, can the dipoles reorient themselves and relax in order to yield a net attractive electrostatic force. Thus, additional analysis of the unloading part of the experiment is necessary to understand the trend shown in Figure 4.4b. In addition, the presence of surface ionization effects was considered. There is always a condensed, thin water layer present at polar surfaces, such as  $-\text{COOH}$  (flame-treated LDPE) and  $-\text{SiOH}$  (UV/ozone treated silicon). Surface deprotonation of these two materials can in both cases yield a negatively charged contact area which water expelled from contact. This effect can considerably reduce adhesion.

A determination of the dependence of the interfacial fracture energy on the flame-treatment level and on the rate of crack propagation is an important objective, to understand the mechanical strength of interfaces. An interesting aspect of the ATD experiment is that the energy release rate required as the contact area decrease during unloading is much larger than the *work of adhesion* required for the growth of the contact area during loading. This means that *Griffith's criterion* which assumes  $G = W$  is not fulfilled. The corresponding difference,  $G - W$ , is called the adhesion hysteresis. When  $G > W$ , the fracture continues to propagate provided that the release of potential energy is sufficient to supply the energy required for creating new fracture surfaces (crack propagation). Since the thermodynamics of the *work of adhesion* is unchanged for each sample, the degree of adhesion hysteresis can be translated

into a better understanding of the dynamic chemical processes occurring during disjoining mechanical contact. Figure 4.5 shows the evaluation of the energy release rate,  $G$ . This energy release rate is a function of crack propagation rate ( $v'$ ) for a given sample. An increase of  $G$  was observed with increasing  $v'$ .

Technical elastomers are not purely elastic, i.e. they exhibit internal viscous losses when mechanically excited. If the separation is performed at a finite rate, a certain amount of energy is dissipated at the fracture line. By considering viscoelastic losses at the crack lens, as proposed by Gent et al.,<sup>36</sup> and Andrews et al.,<sup>37</sup> the energy release rate changes as functions of the unloading rate.

$$G - W = W\Phi(a_T v') \quad (\text{Eq. 4-5})$$

Where,  $a_T$  is the Williams-Landel-Ferry (WLF) shift factor, which is a function of the temperature.

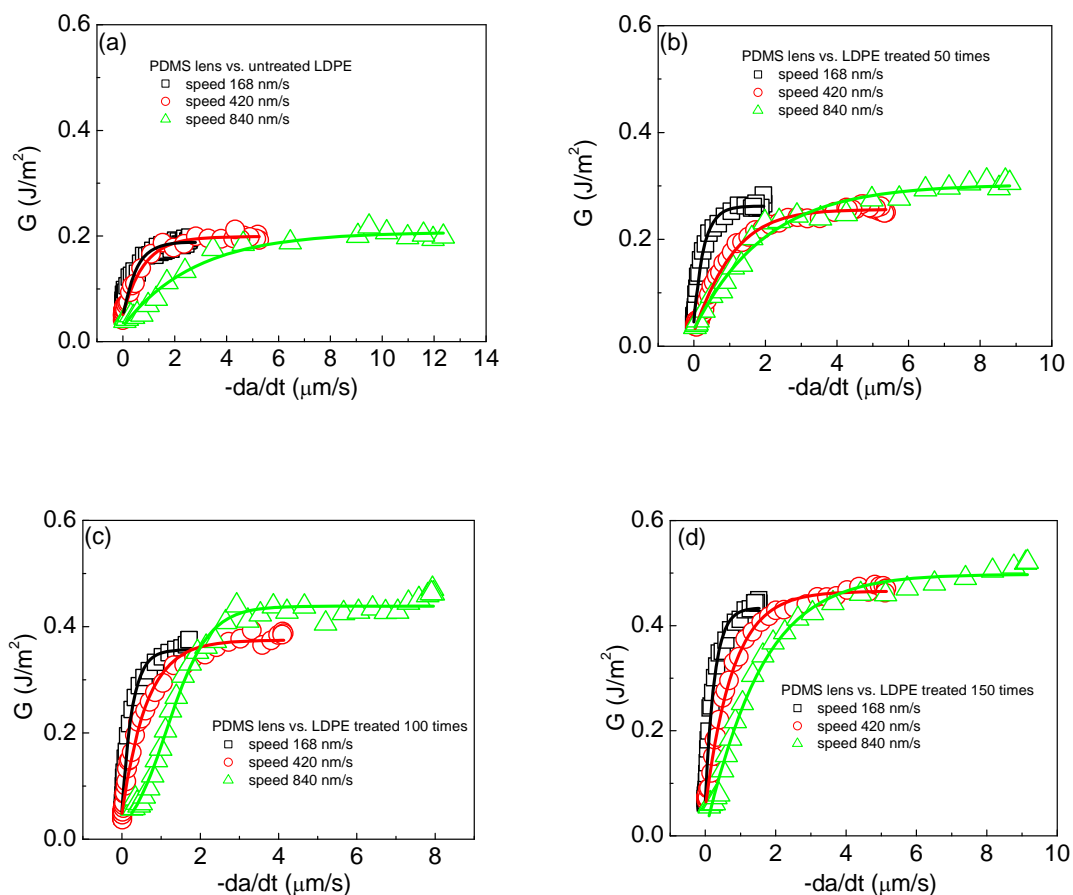


**Figure 4.5** The dependence of the energy release rate,  $G$ , on the crack growth rate obtained from unloading data for various flame-treated samples with a pure PDMS lens. (a) no treatment; (b) treated 50 times; (c) treated 100 times; (d) treated 150 times.

For all treatment levels, the energy release rate was also found to depend on the unloading rate; i.e. it decreased with an increasing withdrawal speed at a given crack propagation rate  $-da/dt$  (certainly for low  $-da/dt$  values). In Figure 4.6, the  $G$  values are plotted as functions of the crack propagation rate at a constant unloading rate for both untreated, as well as treated PDMS (Figure 4.6a and Figure 4.6b, respectively). Clearly, the treatment level of oxidized LDPE and PDMS lens had an effect on the magnitude of the energy release rate (Figure 4.6). The fracture energy was increased with increasing flame-treatment number of LDPE for both the untreated and treated PDMS lens. For a constant treatment level of the LDPE film, the energy release rate was enhanced with the PDMS<sub>OX</sub> lens. The fracture energy in the unloading regime became larger than  $0.5 \text{ J/m}^2$  in the case of the LDPE film treated 150 times measured with the PDMS<sub>OX</sub> lens at a crack propagation rate of  $v' \geq 1 \text{ } \mu\text{m/s}$  (e.g.  $v' = 2.0 \text{ } \mu\text{m/s}$ ): This was later used as an arbitrarily chosen reference point.

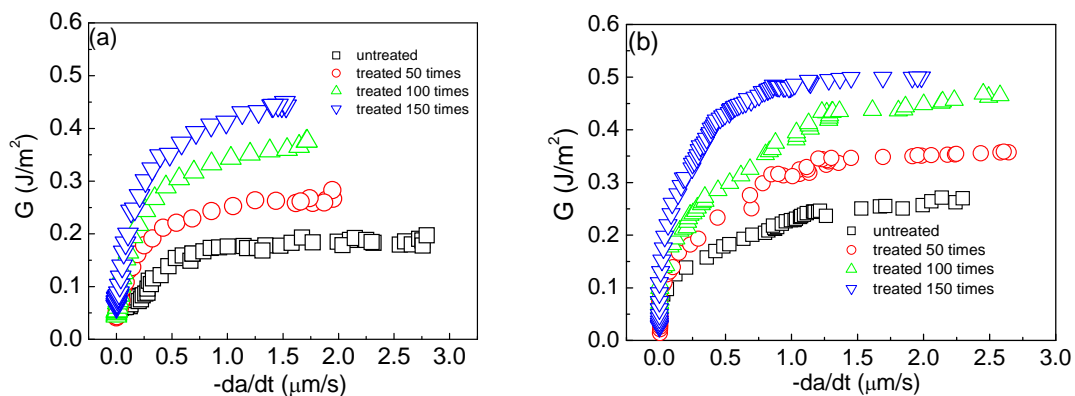


**Figure 4.6** The Dependence of the energy release rate,  $G$ , on the crack growth rate for the unloading data for various treated samples with a) a pure PDMS lens; b) a PDMS<sub>OX</sub> lens. All data were obtained at an unloading rate of  $168 \text{ nm/s}$ .

The critical unloading fracture energy  $G_0$  from which  $a$  started to decrease thus became the relevant parameters to describe the energy per area necessary for separating the solids. The increase in  $G$  upon unloading at a fixed  $v'$  (e.g. at the reference point of  $2.0 \text{ } \mu\text{m/s}$ ) as a function of the treatment number which we was defined as  $G_m$ , was the evidence that additional adhesion forces have developed within the contact area between the materials.

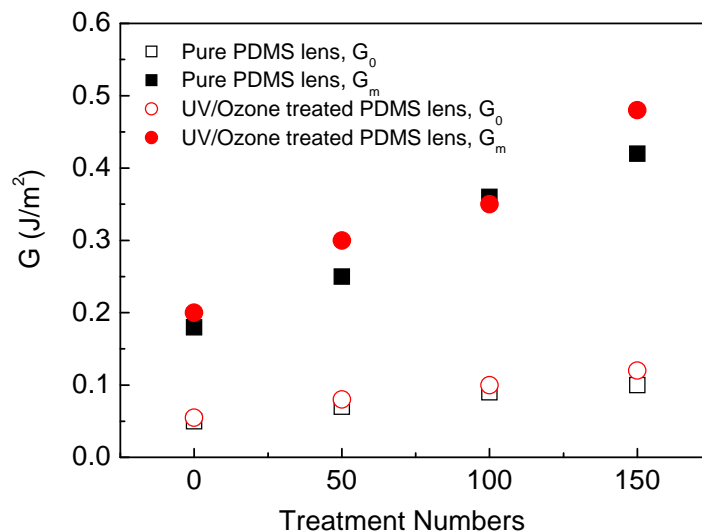


**Figure 4.7** The dependence of  $G_0$ , and  $G_m$  on the treatment number at  $v' = 2\mu\text{m/s}$  for the unloading data of samples with various treatment.

As compared to the untreated LDPE,  $G_0$  and  $G_m$  increased with the treatment number. Furthermore,  $G_0$ ,  $G_m$  displayed slight increments when the oxidized PDMS lens was used. This indicated that an additional hysteresis was introduced when a more polar PDMS was utilized.

According to literature,<sup>9</sup> a number of mechanisms have been considered to be the cause of the adhesion hysteresis as reported. For example, the hysteresis may be caused by energy dissipation due to impact upon contact of two surfaces, viscoelastic or plastic bulk deformation of the contacting materials and surface roughness or chemical heterogeneity. The hysteresis can also result from the rearrangement or reconfiguration of molecular groups at the interfaces due to chemical interaction between two surfaces. Terms such as interdigitation, interdiffusion, and interpenetration have been used by a number of authors describing such processes.<sup>5, 9, 38</sup> In addition, if the surface exhibits ionizable groups, protonation/deprotonation can also contribute to the hysteresis. In practice, the hysteresis occurs by a combination of numerous effects, including those listed above. If one wishes to understand the dominating contribution to the hysteresis for a given material's interfaces, the possible underlying mechanism must be separately considered.

Certainly, in the present case, viscoelastic effects were not the sole origin of the adhesion hysteresis since an increase in  $G$  could be observed with increasing treatment dose.

In certain papers, the *Griffith* theory is written as

$$G = G_0 \{1 + \Phi(a_T \cdot \nu)\} \quad (\text{Eq. 4-6})$$

In this expression, the threshold energy,  $G_0$ , is used instead of  $W$  and  $\Phi$  describe a function associated with viscoelasticity.

A modification to Equation 4-6, which incorporates a mechanism-dependent interfacial term, has been proposed by Shull and Crosby,<sup>39</sup> as shown below:

$$G = W \{1 + \Psi(\nu', t_c, \dots)\} \{1 + \Phi(a_T \nu)\} \quad (\text{Eq. 4-7})$$

Here,  $G_0$  exhibits a rate dependence on the crack propagation rate of the form  $W(1 + \Psi)$  where  $\Psi$  is a microscopic loss function that accommodates the energy dissipated by any non-dispersive interaction at the interface. Included in this term are the energy losses incurred as a result of irreversible rupture of interfacial bonds established through specific interactions (the Lake-Thomas effect),<sup>40</sup> such as hydrogen bonding, contact electrification, or rupture of strong physical interactions such as interdigitation.

The difference between  $G_0$  and  $W$  has been interpreted as the enhancement of the zero rate adhesion energy that arises from the change of state of the interface after adhesive contact (see Figure 4.2a). For the extracted PDMS lens, interdigitation, interdiffusion, and interpenetration may not be the dominant factors behind the adhesion hysteresis. Rather, a possible explanation may be that, during the time of contact, some primary or secondary bonds, e.g. hydrogen bonding, were formed. The values of  $G_0$  between the PDMS lens and the LDPE exceeded those of  $W$ , suggesting that specific interactions such as hydrogen bonding may be significant.

In commercial PDMS networks, an excess of the silane-functional cross-linker is added to prevent the surface from blooming. For the pure PDMS lens, excess silane groups play a major role in the chemical adhesion hysteresis. It is known that at ambient condition, in the presence of water vapor in the air, silane groups may hydrolyze to form silanol groups:



The silanol groups can then form hydrogen bonds across the interface. In order to confirm that such hydrogen bonds were related to the observed adhesion enhancement, JKR testing was performed using also PDMS<sub>OX</sub> lenses. Figure 4.6 compares  $G$  as a function of  $\nu$

for the two lens types. It is clear that the fracture energy for the oxidized lens was larger than for the untreated lens. In the case of PDMS<sub>OX</sub> lens, additional silanol functional groups were formed as a result of the surface treatment (see *chapter 5*). When two polar surfaces are brought into contact, a surface reconstruction may occur and the groups on opposite sides of the interface can combine to form hydrogen bonds. The energies required in order to break such bonds are much higher than those for separating neat PDMS-LDPE surfaces (bound primarily by van der Waals forces). Another important point to add is that, although  $W_{\text{PDMS}_{\text{OX}}/\text{LDPE}}$  was smaller than  $W_{\text{PDMS}/\text{LDPE}}$ , the practical energy,  $G_0$  and  $G_m$  show a reverse trend (i.e. it increased with increasing treatment dose).

Additionally, it is desirable to determine whether the contact time affects the adhesion. In order to assess this possibility, the maximum load,  $P_{\text{max}}$ , of the loading experiment was maintained for a given contact time,  $t_c$ , prior to unloading. The results of unloading  $G$  as a function of  $a$  after various contact times,  $t_c$ , are presented in Figure 4.8 for an untreated and sample treated 150 times respectively. The additional hysteresis can be seen to evolve with contact time for both samples.

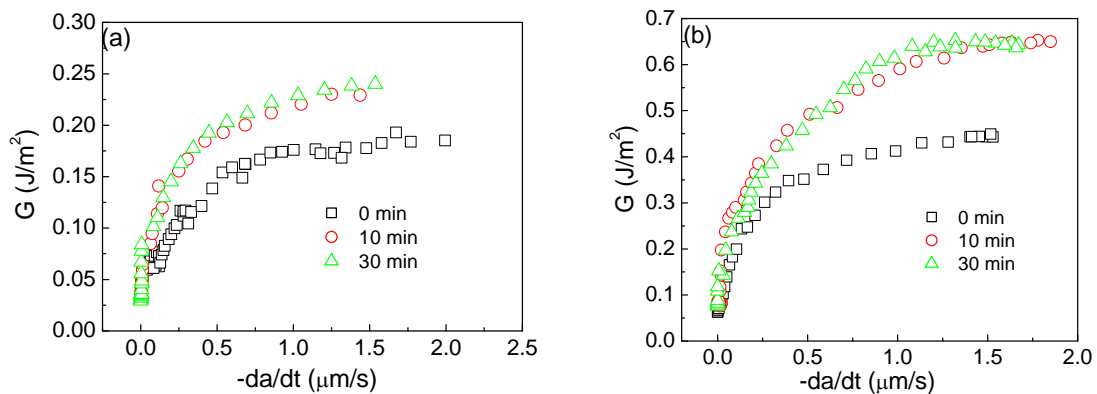


**Figure 4.8** The dependence of  $G$  on crack growth rate as a function of dwelling time with pure PDMS lens. a) untreated LDPE; b) LDPE treated 150 times.

The effect of increasing the contact dwelling time from 0 min to 10 min was evident for both the untreated sample, as well as LDPE treated 150 times. However, a further increase of the dwelling time to 30 min resulted did not further increase  $G$ . This may be interpreted by

larger scale (segment) rearrangement processes that reach equilibrium (at room temperature) on a time scale of *ca.* 10 min.

## **4.4 Conclusions**

In this *chapter*, values of interfacial energy and fracture toughness between PDMS and LDPE were obtained using a custom-built ATD set-up. The dependence of the measured energy release rate values on the rate of separation, contact time, flame-treatment effects were considered. The *work of adhesion* was observed to decrease upon approaching the surfaces towards one another and this decrease was related to an electrostatic repulsion. Upon withdrawal of the surfaces, an increase in the adherence (energy release rate) was expected measured with an increasing treatment dose. It can thus be concluded that the adhesion hysteresis was primarily caused by the formation of a hydrogen bond across the interface. The results presented in this *chapter* lead us to conclude that the JKR method gives useful insights into the adhesion between LDPE and PDMS and the underline mechanism that accompany adhesion hysteresis.

## **4.5 Experimental section**

### **4.5.1 ATD**

Contact mechanical measurements were carried out on a custom-built ATD set-up (JKR apparatus) which is shown schematically in Figure 4.9. It was designed to measure the adhesion between two bodies, typically a hemisphere lens and a flat surface, where at least one of the bodies was elastic. In our experiments, a PDMS lens was attached directly to the upper glass microscope slide and mounted in the device as a stationary part. An LDPE film was then firmly clamped into the sample holder frame and attached directly to the transducer head (Thames-side Maywood Ltd.) as a moving part. A precision gram range load cell was fixed to the movable stage of an XYZ table (Time and Precision Inds. Ltd.). This movable stage was driven by a bipolar stepper motor with a resolution of  $\sim 42 \text{ nm step}^{-1}$  in the vertical direction and measured with a force transducer with a 25 g peak sensitivity (Thames-side Maywood Ltd.). The movement of the stage was monitored by a displacement transducer with



an accuracy of 77.42 mV/mm (Omega Engineering Inc.). The device could be operated in either a stepwise mode, or in continuous measurements.

The contact area between PDMS lens and sample was continuously monitored through a transparent elastomer lens by a CCD camera (Sony XC-999P) with a custom-made reflected light optical microscope utilizing a 10 × magnification. The area of the field of view was 535 × 414 μm. Images were captured by a video camera and can be imported directly into a computer image analysis program. The contact area is measured with a circle fitting function in the custom-built software. A typical photomicrograph of the contact area is shown in Figure 4.10a. Off-line edge detection software was applied for obscured contact areas. The program saved a series of images to disk for off line manual analysis. In spite of the time consuming procedure, in some cases the visual image by image visual analysis proved to be the only way to accomplish the measurements of unclear contact areas.

The signals were transmitted to a National Instrument data acquisition board, and connected to a desktop computer for subsequent data analysis and processing. Values of the temperature ( $T = 21^\circ$ ) and relative humidity ( $RH = 28\%$ ) were monitored by a combined sensor (T&RH) with an accuracy of  $\pm 3.5\%$  (Sensiron SHT 11). The signals from the load cell, displacement transducer, T&RH sensor, and CCD camera were processed by a computer using a custom-written LabVIEW™ software. The use of the computer-controlled interface enabled a precise control of both the rate and displacement of the motor shaft.

This device was initially developed, built and tested in a previous project by Dr. A. Olah.<sup>23</sup>

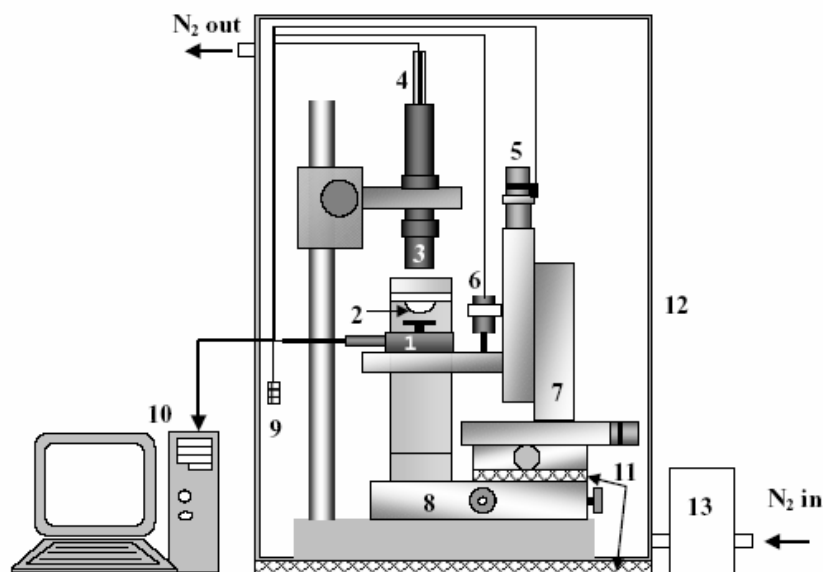


**Figure 4.9** The scheme of the ATD used to measure surface and interfacial properties between an elastomeric lens and a substrate. 1) load cell and the flat sheet sample; 2) elastomeric lens; 3) optical microscope; 4) CCD camera; 5) stepper motor; 6) displacement transducer; 7) XYZ table; 8) XY table; 9) humidity and temperature sensor; 10) computer; 11) vibration dumping rubber; 12) glove box; 13) humidity controller (adapted from ref<sup>23</sup>).

All measurements were carried out after an equilibration time of at least 10 min after mounting the samples onto the sample holder stage. For the same sample, ATD measurements were performed in sequence at three different places.

#### 4.5.2 PDMS lenses and flame-treated LDPE preparation

Cross-linked poly(dimethylsiloxane) PDMS elastomers have been used in various adhesion studies since their elastic modulus is in a range ideal with regard to the JKR theory. Moreover, it is relatively easy to prepare samples with optically smooth surfaces and transparency. For the JKR adhesion (adherence) measurements, sphere-cap-like PDMS lenses were applied. Sylgard 184 (Dow Corning), consisting of PDMS and a reinforcing silica filler was prepared by carefully mixing the precursors Sylgard 184A/Sylgard 184B at a 10:1 mass ratio. The mixtures were subsequently degassed in a vacuum oven at ambient temperature for 1 hour. For the lens preparation, small drops (1–2  $\mu\text{l}$ ) of the mixed and degassed precursors were applied with a micro syringe onto glass microscope slides, which had previously been treated with 1H, 1H, 2H, 2H perfluorodecyltrichlorosilane to prevent a complete wetting to reduce adhesion. The curing reaction was carried out at 120°C for 24 h. The residual polymers and

oligomers not covalently bound to the elastomer networks in the lenses were removed by subsequent Soxhlet extraction for at least 24 h using n-hexane, boiled at 120°C as the solvent. After extraction, the lenses were dried in a vacuum oven at ambient temperature and stored in glass vials until use. Glass and silicon substrates were cleaned using Piranha solutions (1:4 mixtures of 30% H<sub>2</sub>O<sub>2</sub> and 70% concentrated H<sub>2</sub>SO<sub>4</sub>) at ambient temperature, carefully rinsed several times in Millipore water and ethanol, and finally dried in a stream of nitrogen gas. After each JKR experiment, an image of the lens side view profile was analyzed to determine the radius of curvature (shown in Figure 4.10b). The prepared lenses had radii of curvature in the range of 1 ~ 1.5 mm.

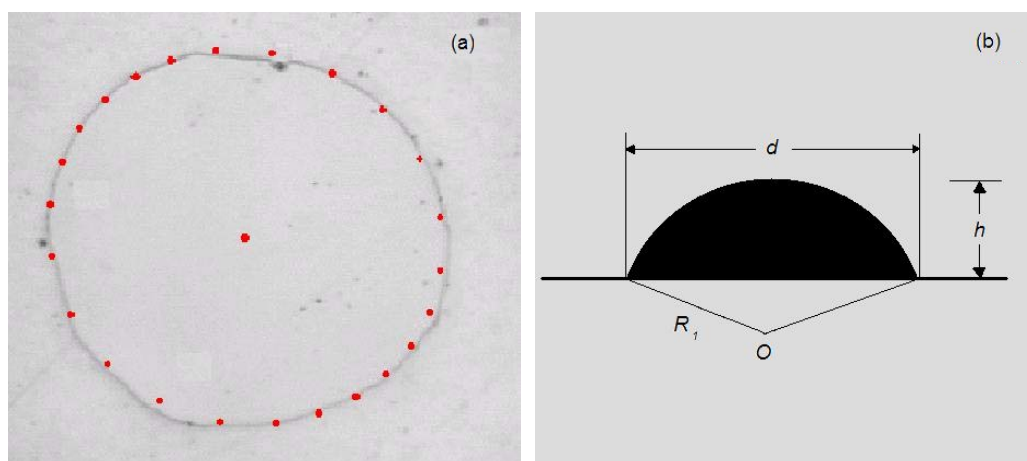


**Figure 4.10** a) Photomicrograph of the contact area between a PDMS lens ( $R = 1.12$  mm) and a flat sheet of LDPE. The edge of the lens is outside the field of view; b) schematic side-view of a PDMS lens. The radius of the lens,  $R_1$ , is calculated by  $R_1 = h / 2 + d^2 / 8h$ .

Polar groups were introduced to the surface of the PDMS lenses by partial oxidation; the lenses were partially oxidized in UV/ozone plasma for 30 min. The UV/ozone technique will be described in *chapter 5*. All ATD experiments were performed immediately following the oxidation treatment to limit surface reconstruction of the lens (polar groups with a higher surface energy than that of the PDMS network would relax and return back to below the surface). The preparation procedure of flame-treated LDPE has been described in *chapter 3*. Treated LDPE films were fixed on a glass slide with transparent glue (Pattex Uni-rapid, Henkel) for the experiment.

## References

- [1] Choi, D. M.; Park, C. K.; Cho, K.; Park, C. E., *Polymer* **1997**, *38*, 6243.
- [2] Lin, J. C.; Cooper, S. L., *Biomaterials* **1995**, *16*, 1017.
- [3] Packham, D. E., *Handbook of adhesion*. John Wiley & Sons: Harlow, 1992.
- [4] van Oss, C. J., *Interfacial Forces in Aqueous Media*. Marcel Dekker: New York, 1994.
- [5] Chaudhury, M. K.; Whitesides, G. M., *Langmuir* **1991**, *7*, 1013.
- [6] Tirrell, M., *Langmuir* **1996**, *12*, 4548.
- [7] Johnson, K. L., *Contact Mechanics*. Cambridge University Press: Cambridge, 1985.
- [8] Johnson, K. L.; Kendall, K.; Roberts, A. D., *Proc. R. Soc. Lon. Ser-A* **1971**, *324*, 301.
- [9] Chen, Y. L.; Helm, C. A.; Israelachvili, J. N., *J. Phys. Chem.* **1991**, *95*, 10736.
- [10] Merrill, W. W.; Pocius, A. V.; Thakker, B. V.; Tirrell, M., *Langmuir* **1991**, *7*, 1975.
- [11] Roberts, A. D., *Rubber Chem. Technol.* **1979**, *52*, 23.
- [12] Roberts, A. D.; Thomas, A. G., *Wear* **1975**, *33*, 45.
- [13] Vallat, M. F.; Ziegler, P.; Vondracek, P.; Schultz, J., *J. Adhesion* **1991**, *35*, 95.
- [14] Maugis, D.; Barquins, M., *J. Phys. D Appl. Phys.* **1978**, *11*, 1989.
- [15] Rimai, D. S.; DeMejo, L. P.; Vreeland, W.; Bowen, R.; Gaboury, S. R.; Urban, M. W., *J. Appl. Phys.* **1992**, *71*, 2253.
- [16] Chaudhury, M. K.; Whitesides, G. M., *Science* **1992**, *255*, 1230.
- [17] Silberzan, P.; Perutz, S.; Kramer, E. J.; Chaudhury, M. K., *Langmuir* **1994**, *10*, 2466.
- [18] Leger, L.; Hervet, H.; Marciano, Y.; Deruelle, M.; Massey, G., *Israel J. Chem.* **1995**, *35*, 65.
- [19] Brown, H. R., *Macromolecules* **1993**, *26*, 1666.
- [20] Creton, C.; Brown, H. R.; Shull, K. R., *Macromolecules* **1994**, *27*, 3174.
- [21] Brown, H. R., *Science* **1994**, *263*, 1411.
- [22] Maugis, D., *J. Mater. Sci.* **1985**, *20*, 3041.
- [23] Olah, A.; Hillborg, H.; Vancso, G. J., *Appl. Surf. Sci.* **2005**, *239*, 410.
- [24] Olah, A.; Hernpenius, M. A.; Zou, S.; Vancso, G. J., *Appl. Surf. Sci.* **2006**, *252*, 3714.
- [25] Chin, P.; McCullough, R. L.; Wu, W. L., *J. Adhesion* **1997**, *64*, 145.
- [26] Ahn, D.; Shull, K. R., *Macromolecules* **1996**, *29*, 4381.
- [27] Maugis, D., *J. Colloid Interf. Sci.* **1992**, *150*, 243.
- [28] Muller, V. M., *Colloid J.* **1996**, *58*, 612.
- [29] Greenwood, J. A.; Johnson, K. L., *Philos. Mag.* **1981**, *43*, 697.
- [30] Maugis, D., *J. Adhes. Sci. Technol.* **1987**, *1*, 105.
- [31] Wu, S., *J. Macromol. Sci. R. M. C.* **1974**, *C10*, 1.
- [32] Jalbert, C.; Koberstein, J. T.; Hariharan, A.; Kumar, S. K., *Macromolecules* **1997**, *30*, 4481.
- [33] Wu, S. H., *Polymer interface and adhesion*. John Wiley & Sons: 1982.
- [34] Li, L. H.; Macosko, C.; Korba, G. L.; Pocius, A. V.; Tirrell, M., *J. Adhesion* **2001**, *77*, 95.
- [35] Li, L. H.; Tirrell, M.; Korba, G. A.; Pocius, A. V., *J. Adhesion* **2001**, *76*, 307.
- [36] Gent, A. N.; Schultz, J., *J. Adhesion* **1972**, *3*, 281.
- [37] Andrews, E. H.; Kinloch, A. J., *Proc. R. Soc. Lon. Ser-A* **1973**, *332*, 385.
- [38] Merrill, W. W.; Pocius, A. V.; Thakker, B. V.; Tirrell, M., *Langmuir* **1991**, *7*, 1975.
- [39] Shull, K. R.; Crosby, A. J., *J. Eng. Mater.-T. Asme.* **1997**, *119*, 211.
- [40] Lake, G. J.; Thomas, A. G., *Proc. R. Soc. London, Ser. A* **1967**, *300*, 108.



# Chapter 5

## **Surface ionization state and nanoscale chemical composition of UV-irradiated poly(dimethylsiloxane) probed by chemical force microscopy, force titration, and electrokinetic measurements<sup>‡</sup>**

The surface chemistry and ionization state of cross-linked poly(dimethylsiloxane) (PDMS) exposed to UV/ozone were studied as a function of treatment time. Various complementary and independent experimental techniques were utilized, which yielded information on the macroscopic as well as the nanometric scale. The average chemical composition of the PDMS surface was quantitatively investigated by time-of-flight secondary ion mass spectrometry (ToF-SIMS). It was found that the top 1-2 nm surface layer was dominated by silanol groups ( $-\text{SiOH}$ ) for which the concentration increased with increasing treatment dose. The lateral distributions of the silanol groups were analyzed on the nanometer scale by means of atomic force microscopy (AFM) with chemically functionalized tip probes in aqueous buffer solutions at varying pHs. Spatially dependent pull-off force curves (also called “force volume” imaging) indicated the presence of strong chemical heterogeneity of the probed surface. This heterogeneity took the form of patches of silanol functionalities with high local concentration surrounded by a matrix of predominantly hydrophobic domains at low pH. The average pull-off forces for the entire surface scanned were significantly reduced for pH values larger than a characteristic  $\text{p}K_{\text{a}}$  constant (in the range between 4.5 and 5.5). The extent of the decrease in the pull-off force and the particular value of  $\text{p}K_{\text{a}}$  were found to be a function of treatment time and to differ from the commonly reported values for silanol functional groups on a homogeneous silica surface. These dependences were ascribed to the evoking of a protonation/deprotonation process of the surface silanol groups which was sensitive to the hydrophobic/hydrophilic balance of their close molecular environment. Intermolecular hydrogen bonding may also account for the shifts in the surface  $\text{p}K_{\text{a}}$ . Furthermore, depending on the nature of the electrolyte, a third effect related to double layer composition, as determined by specific ion adsorption, was quantitatively analyzed by streaming potential measurements in the presence of sodium chloride and phosphate electrolytes.

---

<sup>‡</sup> This *chapter* has been published in the following article: Song, J.; Duval, J.F.L.; Cohen-Stuart, M.A.C.; Hillborg, H.; Gunst, U.; Arlinghaus, H.F.; Vancso, G.J. *Langmuir* **2007**, *23*,5430.

## 5.1 Introduction

Poly(dimethylsiloxane) (PDMS) is a unique polymer with a variety of intriguing properties related to the chemical structure of its Si–O backbone and substitution on Si.<sup>1</sup> Cross-linked PDMS elastomers are widely used as insulating and protective materials in both high- and low-temperature rubber applications, in soft lithography as stamps for microcontact printing, and in the microfabrication of micro-electromechanical system (MEMS) devices.<sup>2-7</sup> However, despite the very useful bulk properties, including a modulus which does not vary significantly over a broad temperature range, selective gas permeability,<sup>8</sup> and long-term endurance, the low surface tension of PDMS limits its use in surface-related applications.

Reduction of the hydrophobicity can be achieved by exposing PDMS to various types of oxidizing plasmas, corona discharges, or UV radiation.<sup>9-12</sup> Such surface treatments have been adopted for controlling the wettability and to render the PDMS surface more hydrophilic. For instance, in microfluidic applications, a decrease in the hydrophobicity of PDMS improves the wettability of aqueous solutions and leads to the reduction of air bubble nucleation in the microchannels.<sup>13</sup> To properly adjust the surface characteristics of PDMS for the aforementioned applications, it is critical to understand the changes that the PDMS surface undergoes when exposed to various surface treatments.

It has been shown that, during treatment-dependent surface modifications of PDMS, silanol groups are introduced at the surface.<sup>14</sup> Recently, Graubner et al. thoroughly investigated the mechanism of photochemical alteration of PDMS.<sup>15</sup> They concluded that the photochemical conversion of surface methylsilane groups to silanol groups is responsible for the large increase in surface free energy. Oxidative cross-linking via Si–O bridges was found to cause the gradual formation of a continuous “silica-like” barrier layer of SiO<sub>2</sub>. The oxidation process within the top 10 nm of the surface has been extensively investigated by X-ray photoelectron spectroscopy (XPS), proving the existence of this silica-like layer.<sup>14-18</sup> To gain further understanding of the oxidizing processes, it is important to elucidate the development of lateral heterogeneities in the surface chemistry on a submicrometer scale as a function of treatment time.

Compared to other vacuum-based surface characterization techniques such as XPS and scanning electron microscopy (SEM), atomic force microscopy (AFM) can be utilized with surface functionalized tips and is in this case often referred to as chemical force microscopy (CFM). This technique exhibits the advantage that measurements can be carried out in

solvents and salt solutions (electrolytes).<sup>19-20</sup> CFM thus combines the high spatial resolution of AFM with further chemical discrimination as introduced by chemically functionalized scanning probe tips that, upon approach, locally interact with the surface to be analyzed.

The subject of mapping the surface hydrophobicity of UV/ozone-treated PDMS as a function of storage time by CFM has already been addressed in one of our earlier studies.<sup>21</sup> However, the coverage and surface distribution of the functional groups as well as the ionic state introduced during their oxidization process have received little attention. In this paper, UV/ozone irradiation was used to mimic the oxidation process since the resulting chemical changes were similar to those introduced by the fast (and therefore less controlled) oxygen plasma techniques.<sup>22-24</sup> The interaction forces (adherence) between the chemically modified tip and the PDMS surface were measured by CFM and were found to be highly sensitive to the changes in the ionization state of the terminal surface functionalities as induced by varying the solution composition (pH, ionic strength) and the surface treatment time. Force titration curves, monitoring the tip-sample adherence as a function of pH, were used to determine and map the  $pK_a$  of the functional surface groups at a  $\sim 20$  nm resolution.<sup>25</sup>

To gain further insights into the molecular origins of the  $pK_a$  shifts when varying the electrolyte composition and/or UV/ozone exposure time, the knowledge of the overall surface ionization state (macroscopic scale) was also essential. Therefore, UV/ozone-treated PDMS surfaces were further investigated by streaming potential measurements in various electrolytes of which the ion concentrations were varied. A critical examination of the variations in the so-determined isoelectric points (IEP)<sup>26-28</sup> with surface treatment and electrolyte composition was performed. Hence, it was possible to address the role played by the specific ionic interaction in the determination of the effective surface  $pK_a$ . The measured streaming potentials were quantitatively interpreted on the basis of a double layer model that coupled the classical Gouy-Stern scheme with the site dissociation theory.<sup>29</sup> The combination of the nano- and macro-scale analyses of the PDMS surface leads to the identification of the physicochemical processes that affect the effective  $pK_a$  of the PDMS surface, namely the presence of hydrophobic nanometer-sized domains stabilized by UV/ozone irradiation, the formation of lateral hydrogen bonding, and specific ion adsorption phenomena.



## 5.2 Results and discussion

### 5.2.1 Time-of-flight (ToF)-SIMS results

As a first step, we should discuss the chemical composition of PDMS by ToF-SIMS to identify in detail the surface functional groups. Static secondary ion mass spectrometry (SSIMS)<sup>41</sup> has been used to characterize the structure of polymers on the basis of their fingerprint spectra that reveal specific spectroscopic features of the fragments located in the backbone and pendant groups. In the static ToF-SIMS regime, the emission of parent-like ion species (cationized:  $[M + Me]^+$ , protonated:  $[M + H]^+$ , deprotonated  $[M - H]^-$ , or loss of functional groups  $[M - CH_3]^+$ ,  $[M - OH]^+$ , and so forth) or of molecular fragments is reached by very low total primary ion fluencies (less than  $10^{13}$  ions/cm<sup>2</sup>).<sup>42-44</sup> Furthermore, molecule fragmentation can be reduced by using primary ion cluster beams such as  $Au_5^+$  or  $Bi_3^+$ . In the present study, we used  $^{40}Ar^+$  as the primary ion, which was adequate for the evaluation of the PDMS fragments.

ToF-SIMS has previously been used to study the molar mass distribution<sup>45</sup> and fragmentation mechanism of PDMS<sup>46</sup> in the high mass range. In the current analysis, various low-mass oxygen-containing fragments from the ToF-SIMS positive ion spectra were identified as representing the various possible oxygen effects seen in the chemical shift of the O 1s and Si 2p by XPS.<sup>15</sup> The ToF-SIMS spectra as obtained for various PDMS surfaces irradiated by UV/ozone were compared in detail. Differences in surface functionality across the whole sample series including the entire range of oxidation were identified by the analysis of low-mass range spectra. In Figure 5.1, extensive fragmentation can be observed in the mass range from 0 to 300 Da. The spectra recorded for varying exposure times of the PDMS surfaces are similar in this mass range. In the mass range below 100 Da, the dominant peak was at 73.05 Da, which corresponds to the mass of the major isotopes  $(CH_3)_3Si^+$ . Peaks at 43.00 Da ( $CH_3Si^+$ ) and 27.98 Da ( $Si^+$ ) can also be observed in the figure.

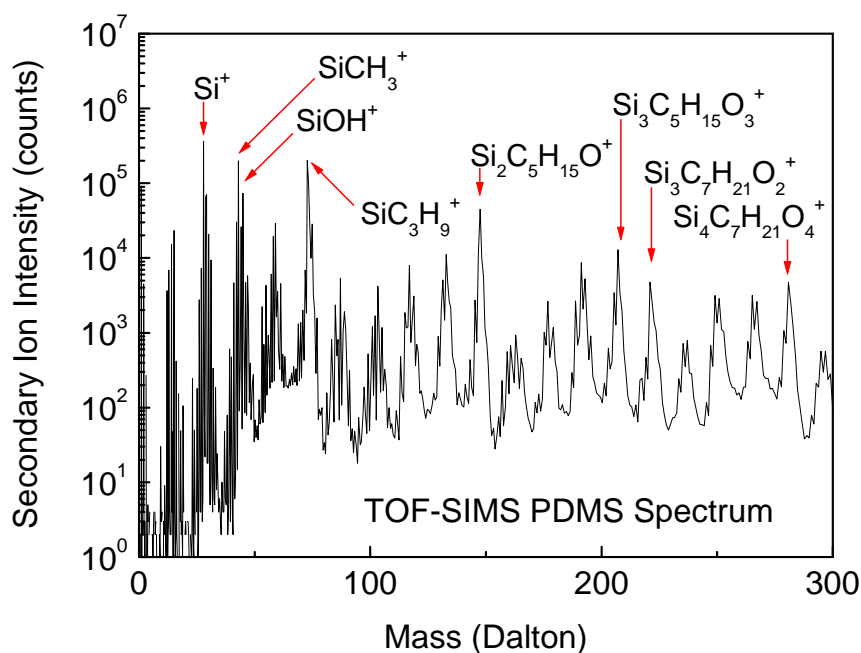


**Figure 5.1** Representative ToF-SIMS spectrum of a UV/ozone treated PDMS surface with characteristic secondary ion species.

The relative intensities of the oxygen containing fragments from the positive ion spectra are collected in Table 5.1. The  $\text{Si}^+$  peak intensity was chosen as an internal reference. Based on the data presented in Table 5.1, it could be concluded that, with increasing oxidation time, the silanol group was the major ionizable functional group favored, and the concentration of this surface entity was significantly enhanced when increasing the duration of the treatment time.

**Table 5.1** Relative Intensity ( $\times 10^{+3}$ ) of Positive Ions by ToF-SIMS for UV/ozone-treated PDMS Using  $\text{Si}^+$  as a Standard.

Time (min)*	$\text{C}^+$	$\text{O}^+$	$\text{SiCH}^+$	$\text{SiOH}^+$	$\text{SiCHO}^+$	$\text{SiC}_2\text{H}_6\text{O}^+$	$\text{SiC}_2\text{H}_6\text{O}_2^+$
0	9.15	0.21	9.35	22.4	0.26	1.26	0.22
5	7.58	0.20	9.21	32.5	0.28	1.35	0.24
10	8.11	0.24	9.00	40.7	0.28	1.49	0.21
30	7.11	0.24	8.86	44.7	0.33	1.16	0.15
60	7.04	0.22	9.05	65.7	0.37	2.20	0.25

\*Time refers to the UV/ozone treatment time

### 5.2.2 Adherence (force volume) imaging by AFM

For FV imaging and subsequent AFM experiments, we employed Au-coated tips that were hydroxyl functionalized by thiol-based self-assembled monolayers and were reported to have stable and robust properties in CFM.<sup>18-19</sup> These tips met the two essential requirements for probing the particular  $pK_a$  features of the investigated surface: (a) they did not exhibit a pH-dependent change in ionization and (b) they were hydrophilic.<sup>47</sup> Figure 5.2 displays a typical FV image as obtained for a 30 min UV-treated PDMS surface in a phosphate buffer at two distinct pH values with a  $\pm 20$  nm resolution. Figure 5.2a shows a marked heterogeneous distribution of the surface functional entities introduced during the UV treatment. As revealed by the ToF-SIMS experiments and based on previous knowledge on the chemical nature ( $pK_a$ ) of silanol functionalities,<sup>48</sup> it is suggested that the adherence variation observed by CFM at low pH values was related to a heterogeneous distribution of protonated silanol functional groups ( $-\text{SiOH}_2^+$ ). We have added representative pull-off force curves showing pull-off events in bright-colored, low-adherence domains (Figure 5.2c, curve (1)) and in dark-colored, high-adherence domains (Figure 5.2c, curve (2)). The typical size of the high adherence domains lies in the range of 20–100 nm. When the pH of the buffer system was adjusted to 7.2, the adherence displayed a dramatic decrease and clearly revealed a homogeneous distribution of adherence over the entire sample surface (Figure 5.2b). Typical corresponding force curves are shown in Figure 5.2d. A gradual increase of the solution pH caused deprotonation of the silanol groups, and the surface then became more negatively charged. This caused electrostatic (dipolar) repulsion between the tip and the ionized surface, as reflected in Figure 5.2b and 5.2d. To further investigate the surface ionization state, FV imaging was performed on various UV/ozone-irradiated PDMS samples immersed in electrolytes as a function of the solution pH.

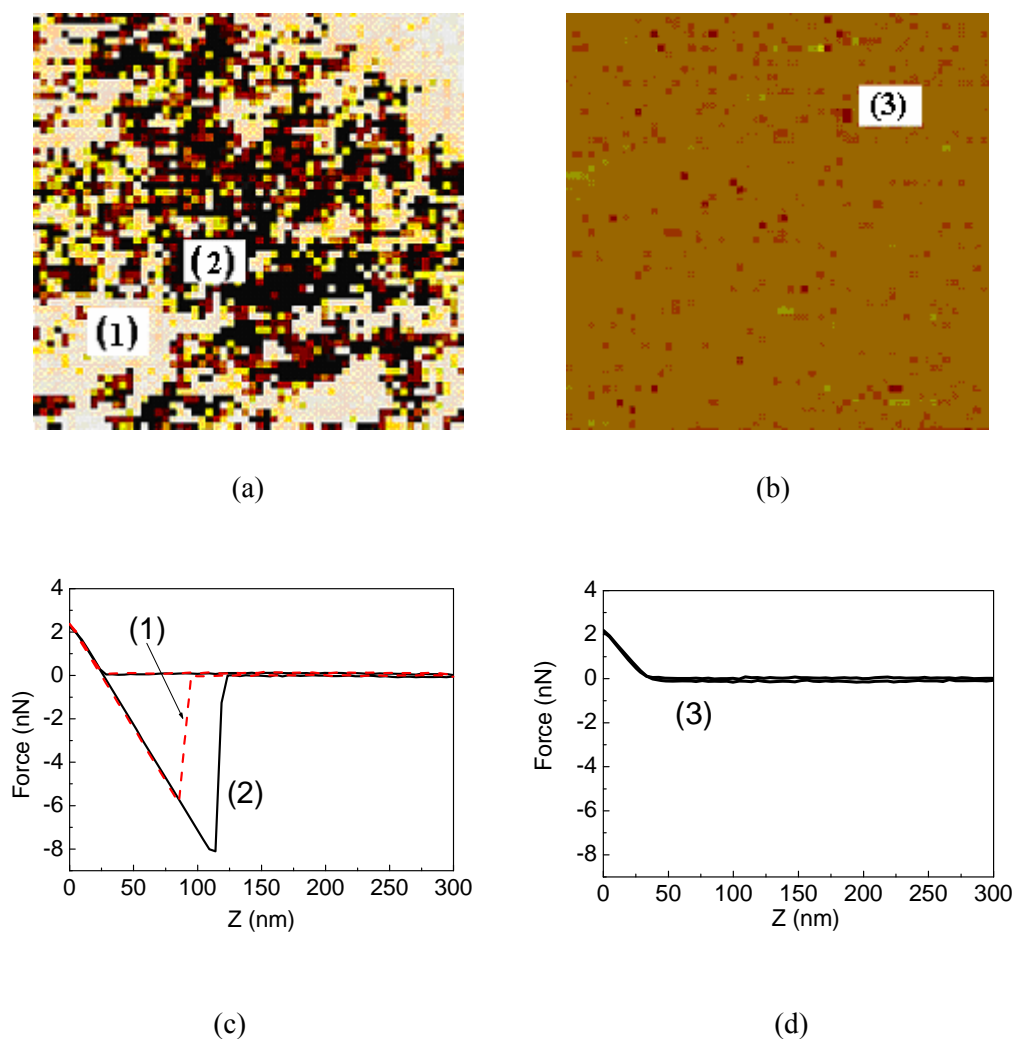


**Figure 5.2** Contact mode AFM force volume images of a PDMS surface after 30 min of UV/ozone treatment phosphate buffer solution (ionic strength = 300 mM) at: (a) pH = 3,  $F_{\text{pull-off}} = 8.06 \pm 0.97$  nN and (b) pH = 7.2,  $F_{\text{pull-off}} = 0.20 \pm 0.10$  nN. The color scale ranges from dark (high adherence) to bright (low adherence). Scan area: 500 nm  $\times$  500 nm. The Z range of the force volume was 20 nm. (c) Typical force curve from a region with (1) low and (2) high adherence at pH = 3. (d) Typical force curve obtained for the same surface at pH = 7.2.

### 5.2.3 Force titration

For oxidized PDMS films, Hillborg et al.<sup>21</sup> showed that the mean roughness ( $R_a$ ) was not influenced by the UV/ozone exposure, so that only a minor influence of the sample topography on the force measurements was expected<sup>49</sup>. To analyze the pull-off force distributions over the imaged sections, data were plotted in the form of force histograms at various pH values shown in Figure 5.3.

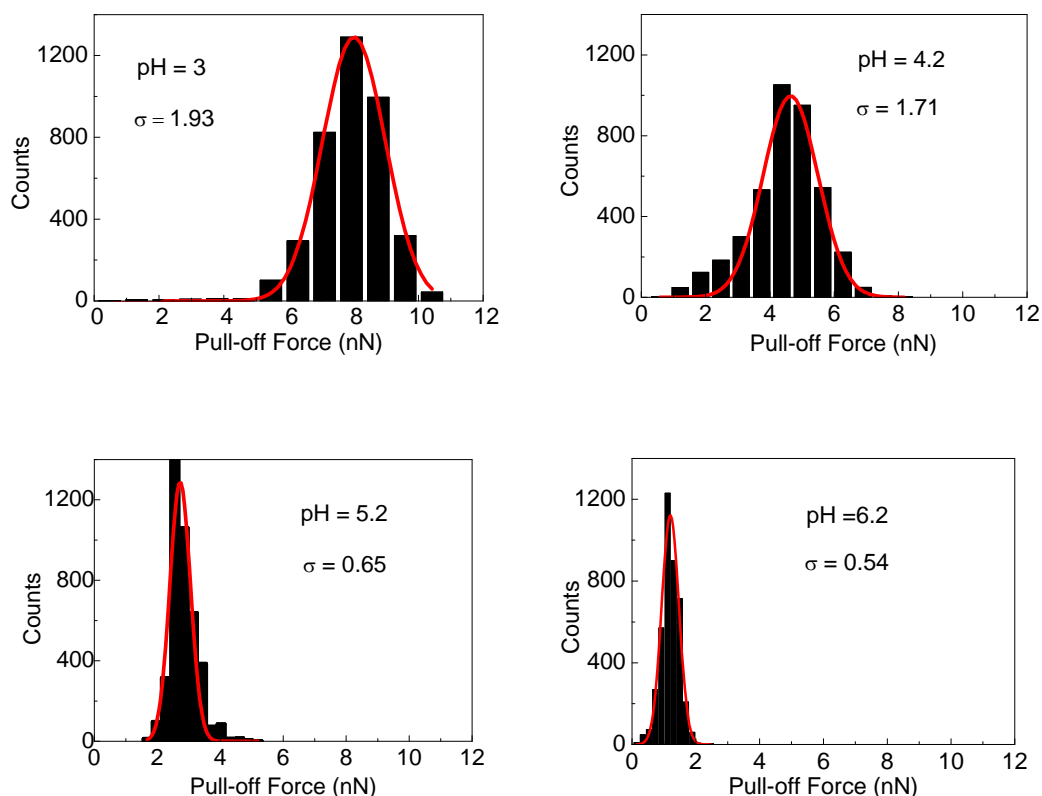


**Figure 5.3** Representative histograms of the pull-off force recorded for PDMS exposed to 30 min UV/ozone at different pH. Scan area: 500 nm  $\times$  500 nm (4096 force curves per histogram). The histograms were fitted using a Gaussian distribution ( $\sigma$  = standard deviation).

It is clear that when using a hydroxyl functionalized tip, the average pull-off force decreases with increasing pH. The histograms are fitted according to a Gaussian statistical distribution. The standard deviation of the Gaussian distribution ( $\sigma$ ) decreases from 1.93 to 0.54 with increasing pH, reflecting a more homogenous distribution of pull-off force. The most probable values of the pull-off forces, which correspond to the peaks in the Gaussian statistics, were plotted as a function of pH to yield force titration curves as those shown in Figure 5.4. The force titration curves for the exposed samples exhibited a typical sigmoidal pattern. The force values decreased with increasing exposure time, from 13 nN (untreated) to 4 nN (treated for 1 h) at low pH and from 12 nN (untreated) to 0 nN (treated for 1 h) at high pH. However, untreated PDMS exhibited a high and almost constant pull-off force of 12–13 nN over the entire pH range investigated.

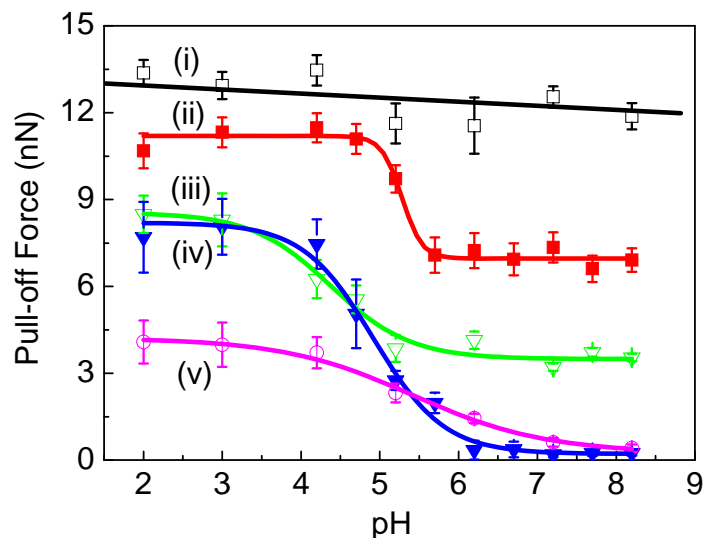


**Figure 5.4** Chemical force titration curves showing the adhesive force between the hydroxyl-functionalized tips and the treated PDMS samples as a function of solution pH. Error bars represent the standard deviation in the adherence as obtained from Force Volume images. The solid lines have been added as guides to the eye. (i) Untreated PDMS ( $\square$ ); (ii) PDMS treated for 5 min ( $\blacksquare$ ); (iii) PDMS treated for 15 min ( $\nabla$ ); (iv) PDMS treated for 30 min ( $\blacktriangledown$ ); (v) PDMS treated for 60 min ( $\circ$ ).

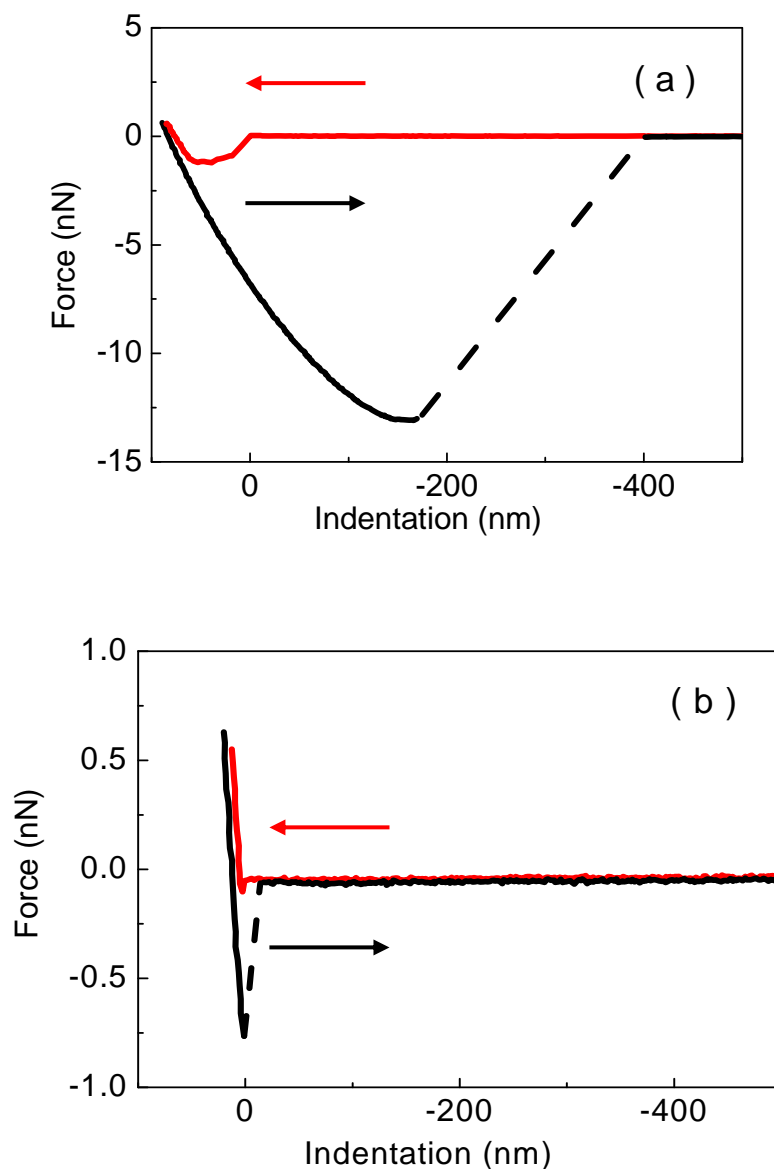
The trends in the average pull-off force for low pH values as a function of treatment time should be discussed at this juncture. To this end, we first need to recall the variation of the surface elastic modulus for PDMS during treatment. UV/ozone-treated PDMS samples have been shown to exhibit increasing surface elastic moduli with increasing treatment doses.<sup>21</sup> Such an increased modulus influences the contact area and indentation depth between the CFM tip and the sample. The elastic deformation of PDMS in the absence of external normal forces is determined by the adhesive interactions between the tip and the surface.<sup>50-51</sup>

Figure 5.4 shows the force versus indentation plots for a  $\text{Si}_3\text{N}_4$  AFM tip interacting with (a) an untreated PDMS surface and (b) PDMS exposed to 60 min of UV/ozone. From the approaching part of the force versus the indentation curve, it can be easily inferred that untreated PDMS had a larger adhesion-induced indentation than the oxidized sample. At the same maximum load, the oxidized PDMS surface showed less indentation. For a pyramidally shaped AFM tip, this smaller indentation results in a decrease in the effective contact area. Moreover, from the retracting part of the force versus indentation curves, it could be seen that untreated PDMS, as compared to the treated sample, was deformed and “pulled up” by the tip over a longer distance before the AFM tip detached.

Compared to a UV/ozone-treated sample, pure PDMS has free polymer chains with high segmental mobility in the probed surface region, which effectively increases the friction force as a result of an adhesive interaction between the tip and the viscoelastic surface during the pull-off event. This friction force corresponds to a significant contribution in the force balance. The increased friction force and the increased effective contact area between the tip and the surface can account for the higher pull-off forces for the untreated samples and the samples with shorter treatment times.

For UV/ozone-treated samples, the interactions between the ionizable functional (silanol) groups and the hydroxyl groups at the tip influence the magnitude and the pH dependence of the pull-off force. Since the hydroxyl-terminated functionalized tips did not show any pH dependence, the titration behavior could be directly attributed to varying degrees of protonation of the silanol groups at the PDMS surface. Based on the force titration curves, it was apparent that the strength of adhesion and the extent of attractive interaction diminished with increasing pH. To reduce the influence of variations concerning the tip radius and contact area, the normalized pull-off force values were calculated by dividing the actual values with the pull-off force value obtained for the original nontreated PDMS pull-off force.

Normalized pull-off force data for the  $\text{Si}_3\text{N}_4$  tips and for the hydroxyl-functionalized tips at  $\text{pH} = 3$  are compared in Figure 5.5. After 5 min of UV/ozone treatment, the average pull-off force decreased to 55% of the initial value when using  $\text{Si}_3\text{N}_4$  tips and to 15% of the initial value when using hydroxyl-terminated tips. This large difference is a strong indication of hydrogen bond formation between the surface of the oxidized PDMS and the hydroxyl-terminated tips. Such hydrogen bonding was nearly absent in the case of the  $\text{Si}_3\text{N}_4$  tips.



**Figure 5.5** Typical plots representing AFM force versus indentation for a  $\text{Si}_3\text{N}_4$  tip interacting with (a) an untreated PDMS surface and (b) a PDMS surface treated for 60 min. Both sets of data were obtained at  $\text{pH} = 3$ .

The transition pH range from complete protonation (low pH values) to complete deprotonation (high pH values) of the silanol groups (compare Figure 5.4) was clearly reflected in the force titration curves. The corresponding inflection points, denoted as  $\text{p}K_{1/2}$  at which value half of the surface sites were ionized (as obtained from force curves versus pH), were used to estimate the surface effective thermodynamic equilibrium constant. Its value at the inflection point for PDMS studied, denoted hereinafter as  $\text{p}K_a$ , was evaluated from the force titration curves and lies in the range of 4.5–5.5, depending on the treatment dose. Based



on the surface site dissociation theory and the Gouy-Chapman-Stern double layer models, as proposed by Yates,<sup>29, 52</sup> and later extended by Davis<sup>53-54</sup> and James,<sup>55</sup> the relevant protolytic reactions of –SiOH groups may be summarized as follows:



where  $K_{a_1}$  and  $K_{a_2}$  are the constants associated to the protolytic reactions (1) and (2), respectively. From the literature<sup>56-57</sup>  $\text{p}K_{a_1}$  is  $\sim 1$  and  $\text{p}K_{a_2}$   $\sim 4$ . In our force titration experiments, the surface effective  $\text{p}K_a$  was obviously shifted to higher pH values and no significant or systematic variation with treatment time could be unambiguously established.

#### 5.2.4 Surface $\text{p}K_a$ shift

In Figure 5.6, the representative force volume images of UV/ozone-treated PDMS are shown as a function of treatment time. The characteristic size of the hydrophilic domains (dark areas in the images) was within the range of 20 ~ 200 nm. The ionizable silanol groups were surrounded in their molecular environment by hydrophobic methyl groups. Similar to previous studies<sup>25, 58</sup> we propose that, for the UV/ozone-treated PDMS surfaces, the silanol groups were stabilized by the surrounding methyl groups, leading to the deprotonation occurring at higher pH values, as compared to those for the listed homogeneous silanol surface.<sup>56, 57</sup>

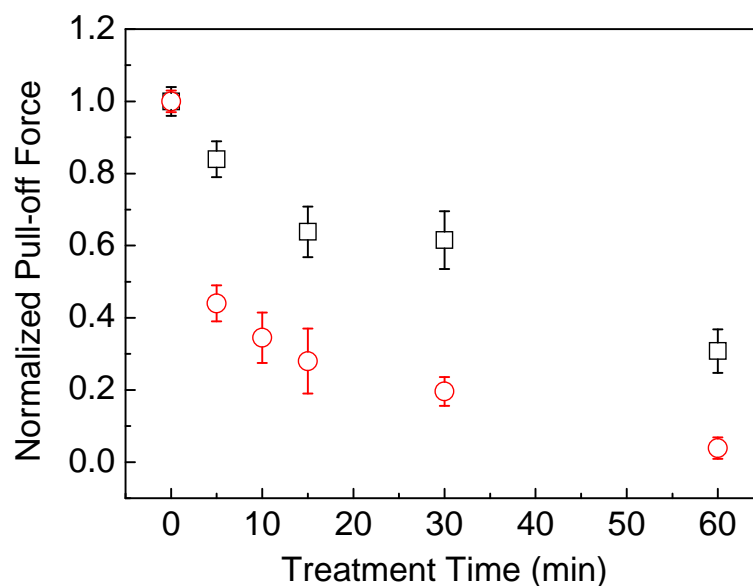


**Figure 5.6** Normalized pull-off force between the AFM tip and the PDMS surface as a function of UV/ozone treatment time ( $t$ ). The force values were normalized with respect to the force obtained for the untreated specimen ( $t = 0$ ) at  $\text{pH} = 3$ . Interactions with a hydroxyl-functionalized tip ( $\square$ ); Interactions with a  $\text{Si}_3\text{N}_4$  tip ( $\circ$ ).

Moreover, we also consider the possibility of intermolecular lateral hydrogen bond formation between the surface silanol groups. In Figure 5.7, it can be clearly seen that the  $-\text{SiOH}$  rich hydrophilic domains were, on average, larger for the samples exposed to UV/ozone for 1 h, as compared to those exposed for 5 min. The aforementioned intermolecular lateral hydrogen bonding may cause the acidic protons to be held more tightly on the surface, resulting in the dissociation of the functional group at higher pH values. Furthermore, in Figure 5.4, the  $\text{p}K_a$  transition range for the sample exposed to UV/ozone for 1 h appears to be broader than that for the sample exposed for merely 5 min. This is in line with the aforementioned explanation.

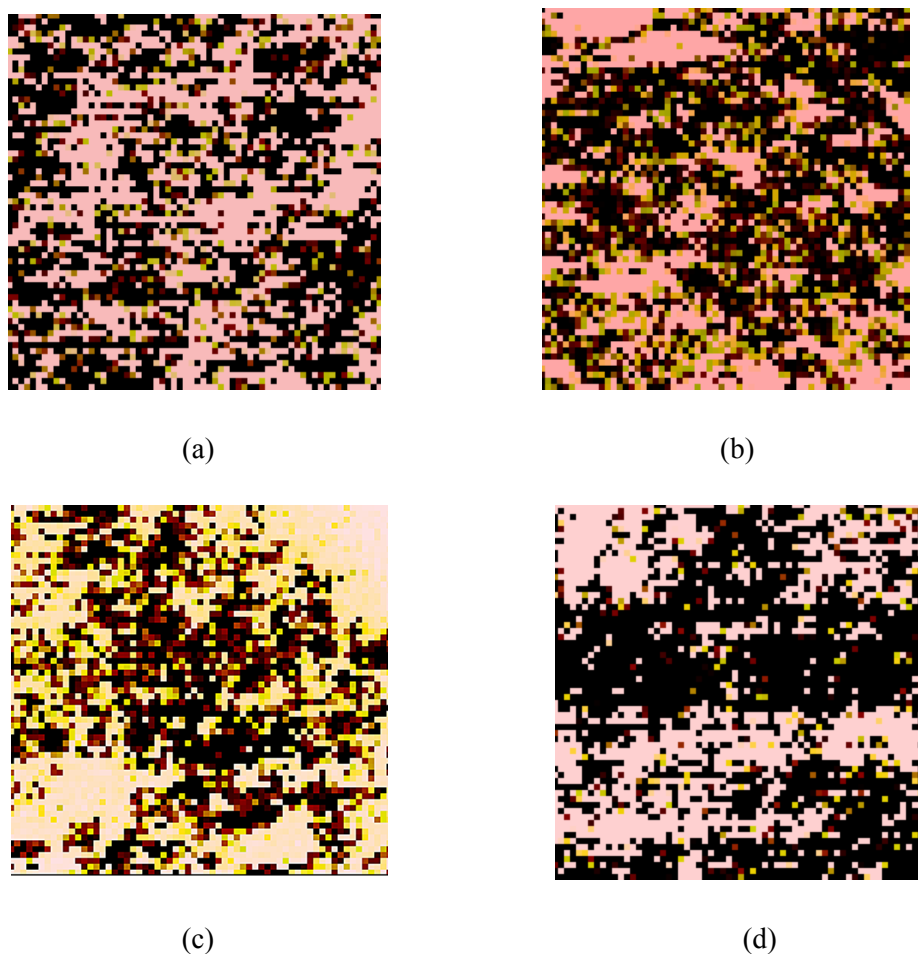


**Figure 5.7** Contact mode AFM force volume images of oxidized PDMS surfaces in a phosphate electrolyte solution ( $\text{pH} = 3$ ) obtained with a hydroxyl-terminated tip. Scan area:  $500 \text{ nm} \times 500 \text{ nm}$ . The color scale ranges from dark (high pull-off, high adherence) to bright (low pull-off, low adherence). The Z range of the force volume was 20 nm. (a) 5 min UV/ozone treatment ( $F_{\text{pull-off}} = 11.33 \pm 0.52 \text{ nN}$ ); (b) 15 min UV/ozone treatment ( $F_{\text{pull-off}} = 8.29 \pm 0.92 \text{ nN}$ ); (c) 30 min UV/ozone treatment ( $F_{\text{pull-off}} = 8.06 \pm 0.97 \text{ nN}$ ); (d) 1 h UV/ozone treatment ( $F_{\text{pull-off}} = 3.99 \pm 0.77 \text{ nN}$ ).

In addition to the previously mentioned stabilization effects, another possible explanation could be the influence of a double layer at the polymer surface giving rise to a shift in the  $\text{pK}_a$  to higher pH values. Figure 5.8 shows the force titration curves measured at two different ionic strengths ( $10^{-2} \text{ M}$  and  $10^{-1} \text{ M}$ ) using phosphate buffer solutions. For the higher ionic strength solution, the magnitude of the pull-off force was reduced. It is likely that, for the corresponding high electrolyte concentrations, the counterions screened the surface functional groups taking part in the interactions with the  $-\text{OH}$  tip, resulting in lower pull-off forces. Moreover, the transitions from low to high pH ionization states broadened with increasing ionic strength. As can also be seen in Figure 5.8, no clear shift for the surface  $\text{pK}_a$  was observed when varying the electrolyte concentration. Despite the uncertainty inherent to the experimental data, the latter result suggests that, for the system under study, the impact of

the double layer (surface proton concentration as compared to bulk proton concentration) on the stabilization of the surface charge was not predominant.

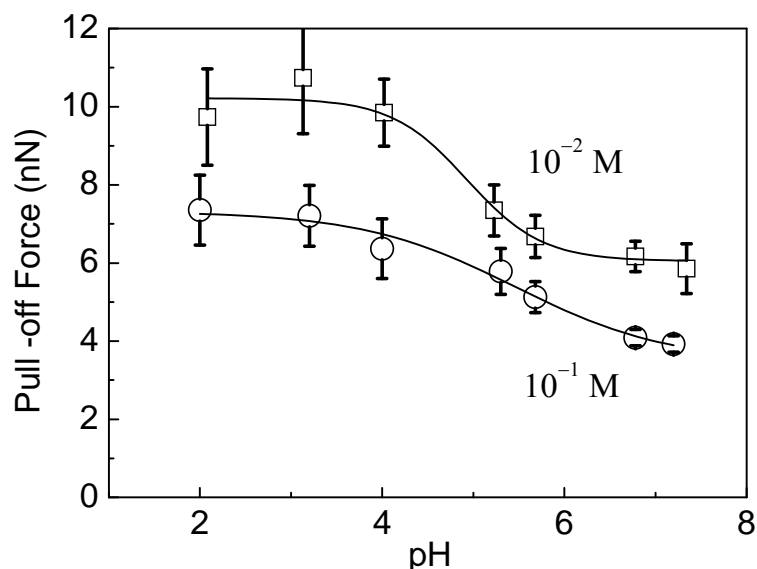


**Figure 5.8** Force titration curves for a PDMS surface oxidized for 15 min in a phosphate buffer at two ionic strengths.

### 5.2.5 Streaming potential experiment in NaCl solutions

To gain further understanding of the surface ionization behavior of oxidized PDMS surfaces, streaming potential measurements were carried out on PDMS with varying degrees of oxidation (i.e., treated with UV/ozone for various exposure times) at different pH values in  $10^{-2}$ ,  $10^{-3}$  or  $10^{-4}$  M aqueous sodium chloride and phosphate solutions. From the linear dependence of the measured streaming potential with the applied pressure drop, one can determine the electrokinetic potential, also called the zeta potential ( $\zeta$ ) for the surface under investigation.<sup>59</sup> It should be noted that the PDMS surface was assimilated to a rigid, ion-impenetrable surface with *a priori* a well-defined location for the slip plane and thus a clear physical meaning for the electrokinetic potential.<sup>60</sup> This rigid nature of PDMS was justified by the very low water permeability, as reported in the literature,<sup>61</sup> for PDMS substrates used in microfluidic devices to prevent leakage.<sup>62-63</sup> Also, the positioning of the relevant ionogenic silanol groups, responsible for the PDMS surface charge, within a 1 ~ 2 nm top layer,<sup>18</sup> was in line with the notion of surface charge density as classically used for impermeable materials (for soft objects, the electrokinetic features are interpreted in terms of space charge density).

All these elements basically justify the use of the classical Smoluchowski equation which becomes approximate when dealing with substrates such as gels or charged polyelectrolytes for which flow penetration (or hydrodynamic permeability) is significant.<sup>64</sup>

In Figure 5.9a,  $\zeta$  potential values as a function of pH are shown for samples in a  $10^{-3}$  M NaCl electrolyte solution. The lines in Figure 5.9a correspond to simulation results obtained using the double layer model outlined in the Appendix. The  $\zeta$  potential values were positive at low pH since the surface was positively charged, and they were found to decrease with increasing pH due to the gradual deprotonation of the surface silanol groups. After passing the IEP, where  $\zeta = 0$ , a negative potential was reached (negatively charged surface). The IEP was estimated from the sigmoidal shape of the curves. Moreover, around the IEP, the slopes of these curves increased with increasing treatment time. This behavior indicates an increasing number of surface-ionizable groups with treatment time, as previously shown by the ToF-SIMS experiments mentioned earlier.

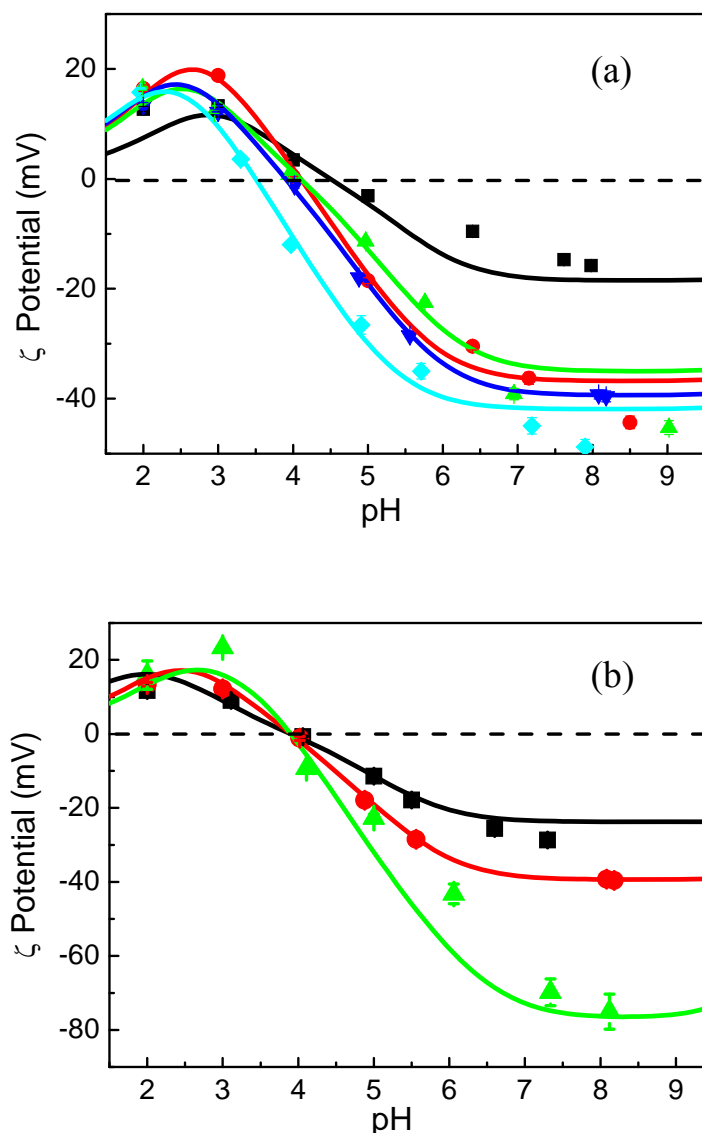


**Figure 5.9** (a)  $\zeta$  potential versus pH for varying treatment times of PDMS with a  $10^{-3}$  M NaCl electrolyte solution. The points represent experimental data, and the solid lines correspond to simulation results according to the double layer model outlined in the Appendix. Untreated PDMS ( $\square$ ); PDMS treated for 5 min ( $\circ$ ); PDMS treated for 15 min ( $\triangle$ ); PDMS treated for 30 min ( $\nabla$ ); PDMS treated for 60 min ( $\diamond$ ). (b)  $\zeta$  potential vs. buffer pH for a 30 min oxidized PDMS surface as measured in a NaCl solution at various ionic strengths. The points represent the experimental data and the solid lines correspond to simulation results according to the double layer model outlined in the Appendix. NaCl:  $10^{-2}$  M ( $\square$ );  $10^{-3}$  M ( $\circ$ );  $10^{-4}$  M ( $\triangle$ ).

All the observed IEP values were higher than the values reported in the literature for silanol groups on silica surfaces (IEP  $\approx 2 \sim 2.5$ ).<sup>56</sup> The shift of the IEP with treatment time may be related to the heterogeneity of the surface (hydrophobic/hydrophilic balance) and/or to specific ion adsorption ( $\text{Na}^+$  or  $\text{Cl}^-$ ) onto the PDMS surface. To discriminate between these

two processes, streaming potential experiments were performed at various levels of NaCl concentrations. Figure 5.9b shows the pH dependence of the  $\zeta$  potential as a function of pH for three ionic strengths obtained from NaCl buffer solutions for samples oxidized for 30 min. At a given pH, the magnitude of the  $\zeta$  potential decreased with increasing ionic strength. This is consistent with expectations from the classical double layer theory (i.e., increased amounts of ions in the solution increase the surface charge screening).<sup>65</sup> Furthermore, the IEP did not show any measurable variations when varying the salt level in the solution. This excludes the impact of the NaCl ionic specificity for PDMS on the IEP variations with UV/ozone exposure time.

### 5.2.6 Streaming potential experiments in phosphate buffer solutions

To mimic the conditions of the AFM experiments, a phosphate salt buffer was also used as the electrolyte solution in streaming potential measurements. Figure 5.10a shows the resulting  $\zeta$  potentials for varying treatment times of PDMS with a  $10^{-3}$  M ionic strength phosphate salt at different pH values. The overall shape of the  $\zeta$ -pH curves was similar to those obtained with the NaCl electrolytic solution. The associated IEP values also decreased as a function of the treatment time but quantitatively differed from those determined for PDMS in the presence of NaCl. Furthermore, Figure 5.10b shows the  $\zeta$  potential for a PDMS sample oxidized for 15 min as measured with a phosphate solution at various ionic strengths. As opposed to that for the NaCl electrolyte solution, the IEP decreased upon increase of the ionic strength of the phosphate solution. This indicates an occurrence of anion adsorption onto the PDMS surface.

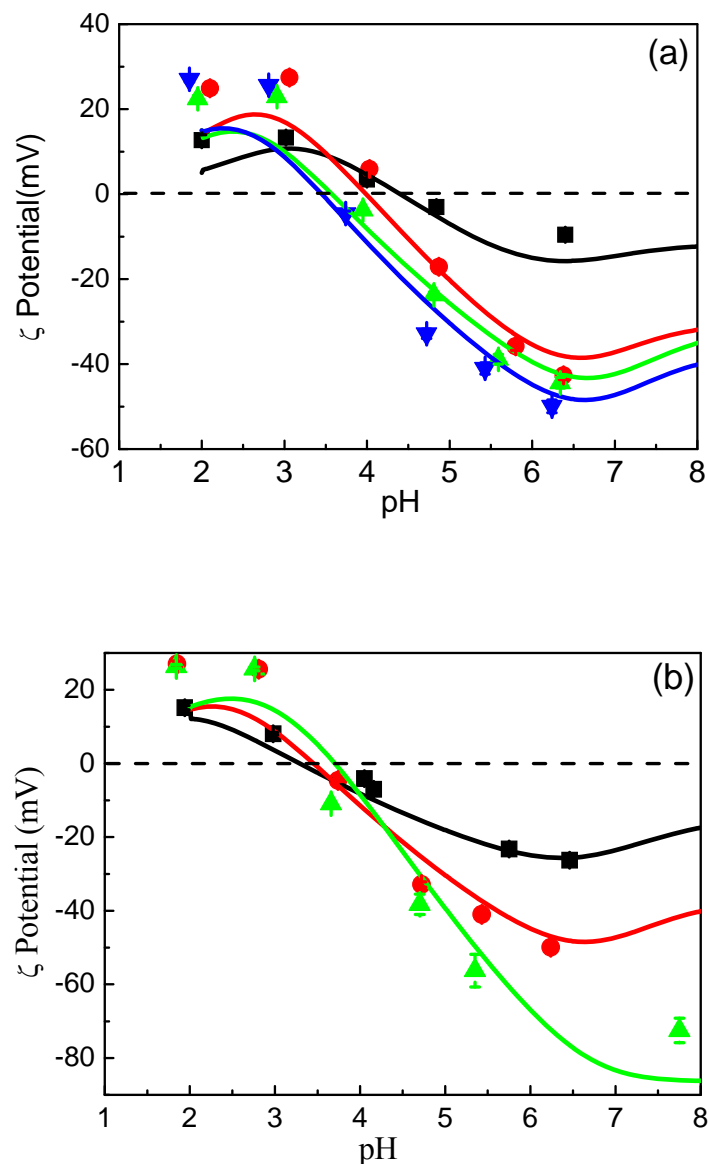


**Figure 5.10** (a)  $\zeta$  potential versus buffer pH for various treatment times of PDMS with a  $10^{-3}$  M phosphate salt electrolyte solution. The points represent experimental data, and the solid lines correspond to simulation results according to the double layer model outlined in the Appendix. Untreated PDMS ( $\square$ ); PDMS treated for 5 min ( $\circ$ ); PDMS treated for 15 min ( $\triangle$ ); PDMS treated for 30 min ( $\nabla$ ). (b)  $\zeta$  potential for a 15 min oxidized PDMS sample measured with phosphate solution at various ionic strengths. The points represent experimental data, and the solid lines correspond to simulation results according to the double layer model outlined in the Appendix. Phosphate salt buffer:  $10^{-2}$  M ( $\square$ );  $10^{-3}$  M ( $\circ$ );  $10^{-4}$  M ( $\triangle$ ).



### 5.2.7 Comparison of the streaming potential and AFM results

Streaming potential and AFM force titration experiments were used to characterize the surface ionization state of untreated and UV/ozone-irradiated PDMS on varying length scales. Streaming potential data are averaged over large sample areas (on the order of  $\text{cm}^2$ ), and the surface IEP is used as a characteristic ionization state parameter. This is compared to the surface  $\text{p}K_a$  determined on the nanoscale by AFM force titration experiments. In the case of AFM, the probed area had a characteristic size of 20–30 nm. It was found from the streaming potential experiments that there were low amounts of charge at the pure PDMS surface. This can be explained by pointing out that the PDMS precursor, Sylgard 184 (Dow Corning), contains a reinforcing silica filler, and the hydrolysis of this silica in an aqueous electrolyte environment would introduce some surface charge. In contrast, in the AFM titration curves, we could not find any pH dependent behavior for the untreated samples. As mentioned before, the pull-off force obtained included both hydrogen bond interactions as well as van der Waals forces between the tip and the sample. For untreated PDMS samples, the pull-off forces were predominantly determined by the van der Waals interactions and did not show titration behavior with variations in pH.

A summary of the IEP and surface  $\text{p}K_a$  values for the UV/ozone-treated PDMS surfaces is visualized in Figure 5.11. It can be seen that the IEP values in NaCl solution decreased with increasing treatment time, approaching the reported literature data. This indicates that the surface heterogeneity was reduced with treatment time, proceeding toward a more homogeneous silanol-functionalized surface. In addition, there were clear differences between the two buffers (NaCl and phosphate) and those differences were strongly dependent on the UV/ozone exposure time. Overall, the IEP values in the phosphate solution were lower than those in the NaCl solution. This IEP shift in the phosphate buffer suggested that *specific anions* were adsorbed onto the surface and that the phosphate anions therefore could contribute to the double layer charging taking place at the PDMS surface. Furthermore, whereas the IEP of NaCl buffered systems did not show any dependence on ionic strength, that of the phosphate buffered system did. In other words, the IEP decreased to a certain extent when the phosphate concentration increased and this was as a result of (mono- and multivalent) anionic ( $\text{H}_2\text{PO}_4^-$  and  $\text{HPO}_4^{2-}$ ) surface adsorption (see the Appendix). Thus, on average, more than one electron charge was added to the surface per adsorbed ion. With increasing ionic strength of the buffer, the magnitude of the specific adsorption increased,

making the surface more negatively charged. This explains the difference between the electrokinetic results as obtained for the NaCl buffer versus for the phosphate buffer.

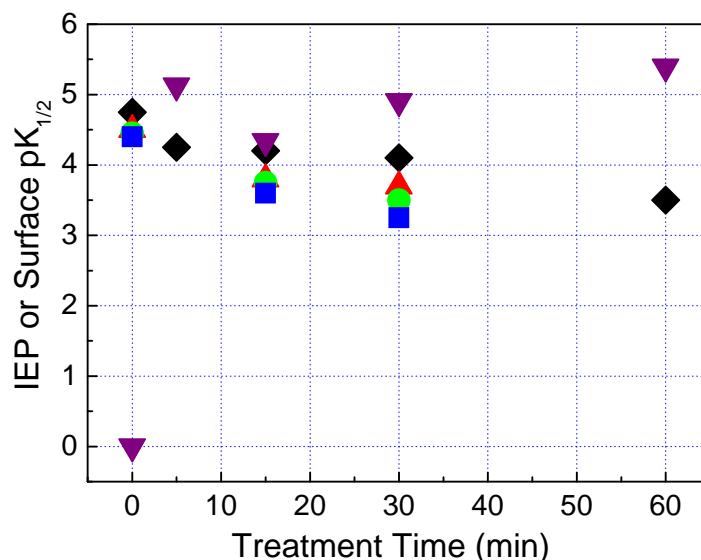


**Figure 5.11** Summary of the IEP and surface  $pK_a$  values as obtained for UV/ozone-treated PDMS surfaces. The IEP was evaluated from streaming potential experiments. Buffers: NaCl (◇);  $10^{-2}$  M (□);  $10^{-3}$  M (○);  $10^{-4}$  M (△) phosphate salt. Surface  $pK_a$  as obtained by an AFM titration curve in a 0.3M phosphate buffer solution (▽).

In Figure 5.11, one can see that both the IEP and the “effective surface  $pK_a$ ” values in phosphate buffer changed with increasing treatment dose and were higher than the values published in the literature for silanol (see related discussion above). However, the differences between the IEP and the effective surface  $pK_a$  should be noticed and explained as follows. The IEP value was obtained in a “direct” manner from the analysis of the surface charge, while the effective force  $pK_a$  was derived on the basis of analyzing differences in the pull-off force. Thus, the measurement and interpretation of the adherence remain difficult in view of the uncertainties pertaining to the tip shape and surface roughness (use of granular gold coating).<sup>66</sup> The surface parameters were averaged according to radically different ways since the physical-chemical processes probed by either electrokinetics or AFM were on different scales, that is, macro versus nano, respectively.

Referring to the surface charge formation mechanism expressed in Equations 5-2 and 5-3, the relationship between the IEP and the surface ionization  $pK_a$  values can be expressed as:

$$\text{IEP} = \frac{1}{2} (\text{p}K_{a_1} + \text{p}K_{a_2}) \quad (\text{Eq. 5-3})$$

Relation (3) is valid for indifferent electrolyte solutions. By applying the Gouy-Stern equation with the site dissociation model, as described in the Appendix, the values for  $\text{p}K_{a_1}$  and  $\text{p}K_{a_2}$  could be obtained by fitting the streaming potential data obtained in an indifferent NaCl electrolyte with least square regression (LSR) methods. The values obtained are shown in Figure 5.12. It was found that both  $\text{p}K_{a_1}$  and  $\text{p}K_{a_2}$  were higher than the values suggested in the literature, as previously mentioned. With an increase in the treatment dose,  $\text{p}K_{a_1}$  and  $\text{p}K_{a_2}$  were shifted to more acidic values. These values were subsequently considered for the quantitative analysis of the electrokinetic data measured in phosphate buffer solutions (see below).

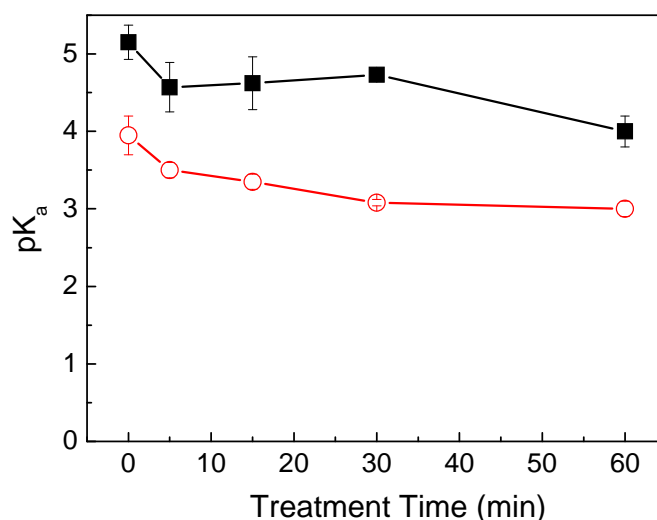
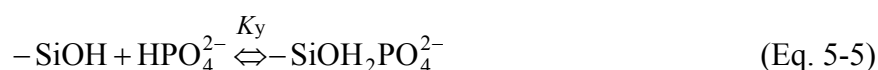
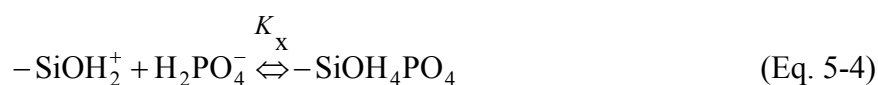


**Figure 5.12** Values of  $\text{p}K_{a_1}$  (○) and  $\text{p}K_{a_2}$  (■) as obtained by the double layer model outlined in the Appendix. Electrolyte: NaCl.

Taking into account specific ion adsorption, a modified site dissociation model was applied (shown in the Appendix). In this model, we further include two types of specifically adsorbed ions onto the treated sample surface.



Here,  $K_x$  and  $K_y$  are the corresponding equilibrium constants. Figure 5.13 shows the simulation results based on this ion-exchange equilibrium mechanism. The parameter  $N_s$  denotes the total number of active surface sites. It was found that  $N_s$  increased with an increasing dose of the UV/ozone treatment. In addition, the values of the specific ion adsorption equilibrium constants  $K_x$  and  $K_y$  also increased. These results confirm that, for higher concentrations of the ionizable sites, specific ion adsorption took place to a larger extent. Similarly, on a molecular scale, it seems possible that the phosphate ion adsorption contributes to the local double layer composition although it was very difficult to picture this in a quantitative way on the basis of merely the AFM titration curves. Returning to Figure 5.8, the broadening of the transition area with increasing solution ionic strength may be due to the specific phosphate ion adsorption at the surface, which altered the adherence between the tip and the functional groups.

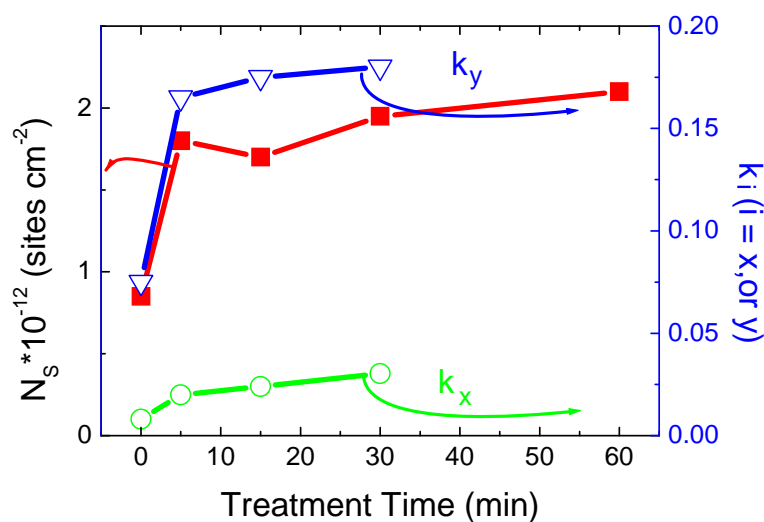


**Figure 5.13** Number of active surface sites, denoted  $N_s$ , in a buffer solution (■) and the specific ion adsorption parameters  $k_x$  (○) and  $k_y$  (▽) defined by  $k_x = RT \ln(K_x)/F$  and  $k_y = RT \ln(K_y)/2F$  (with  $R$ ,  $T$ , and  $F$  in SI units) as a function of treatment time for UV/ozone-treated PDMS. Electrolyte:  $10^{-3}$  M phosphate buffers.

### 5.3 Conclusions

The average chemical composition of UV/ozone-treated PDMS was monitored by ToF-SIMS in a quantitative way. Corresponding results showed that silanol functional groups

were the most probable ionizable groups on the surface. Their concentration increased with increasing treatment time. AFM pull-off force measurements were carried out on oxidized PDMS films as a function of pH by using hydroxyl-functionalized tips. A change in the surface charge induced by the dissociation of silanol groups could be detected by monitoring the adhesive forces between the surface and the modified AFM probes. Laterally resolved force “imaging” gave clear evidence for heterogeneous functional group distributions over the surface of the oxidized samples. Oxidized hydrophilic patches (initially 20 ~ 100 nm in size) grew with increasing treatment time. Force titration curves revealed that the effective surface  $pK_a$  values were in the range of 4.5 ~ 5.5. This is higher than the typical literature value of uniform silanol groups on a silica surface. We concluded that this shift was primarily due to the hydrophobic environment having stabilizing effects on the surface ionization. The broadening of the  $pK_a$  range that could be observed with increasing treatment dose was interpreted as a result of an increasing probability of intermolecular hydrogen bonding and specific ion adsorption. By interpreting streaming potential experiments on the basis of a Gouy-Stern site dissociation model, it was confirmed that specific ion adsorption took place in phosphate electrolyte solutions, thus contributing to the overall (as probed by electrokinetics) and local (as probed by AFM) states of ionization of the surface silanol groups.

## 5.4 Materials and methods

**PDMS film preparation.** All experiments were performed using an elastomeric PDMS kit manufactured by Dow Corning. Sylgard-184A (elastomer) and Sylgard-184B (curing agent) were used without modification and mixed at a mass ratio of 10:1. Glass cover slides were cleaned using a Piranha solution (1:4 mixture of 30%  $H_2O_2$  and concentrated  $H_2SO_4$ ), carefully rinsed several times in Milli-Q water and ethanol, and finally dried in a stream of nitrogen gas. *Caution! Piranha solution is a very strong oxidant, which reacts violently with organic materials and should therefore be handled with the utmost care!* The PDMS was then spin coated onto the cleaned glass substrates using a spin coater model P6700 (Specialty Coating Systems, Inc). The film thickness was  $800 \text{ nm} \pm 100 \text{ nm}$  according to the ellipsometry measurements (Plasmos SD 2002 ellipsometer). After spin coating, the films were cured overnight at  $120^\circ \text{C}$  and then stored individually in plastic containers at ambient temperature.

**UV/ozone treatment.** UV/ozone treatment of the PDMS surface was carried out in a commercially available UV/ozone chamber (Ultra-Violet Products PR-100). A typical treatment chamber contains a low-pressure mercury UV light, generating UV emissions at 185 nm ( $1.5 \text{ mW cm}^{-2}$ ) and 254 nm ( $15 \text{ mW cm}^{-2}$ ). The distance between the UV source and the PDMS films was 20 mm for the particular setup used in this study. A nominal steady-state concentration of ozone at 55 ppm was produced in a two-step photochemical process initiated by the photolysis of molecular oxygen at 185 nm. The 254 nm radiation can be absorbed by most hydrocarbons, as well as by ozone. The organic samples reacted with atomic oxygen to form simpler, volatile molecules, which desorbed from the surface.

Since the surface energy of the UV/ozone-treated PDMS was a function of storage time,<sup>21</sup> all the following characteristic measurements were performed directly after the treatment.

**AFM tip modification.** Triangular shaped silicon nitride cantilevers and silicon nitride tips (Veeco-Digital Instruments (DI), Santa Barbara, CA) coated with  $\sim 2 \text{ nm}$  Ti as the adhesion layer and  $\sim 50 \text{ nm}$  Au in high vacuum were used in the AFM experiments. The SAM-functionalized tips were prepared by immersion in a 1 mM 11-mercapto-1-undecanol solution, with ethanol as the solvent, for 10 – 40 h at room temperature. The functionalized tips were kept in solution between measurements and then rinsed in ethanol and dried in a stream of nitrogen immediately before use. The spring constants of the cantilevers ranged from 0.14 to  $0.28 \text{ nN nm}^{-1}$ , as obtained by the method of Hutter and Bechhoefer.<sup>30</sup>

**Chemical force microscopy (CFM).** CFM was carried out with a NanoScope III multimode AFM (DI). A hydroxyl-terminated tip was brought into contact with a modified substrate and then retracted. For laterally resolved pull-off force measurements, the AFM was operated in the so-called force volume (FV) mode<sup>31</sup> using a  $10 \mu\text{m} \times 10 \mu\text{m}$   $x$ - $y$ -range scanner. Arrays of  $64 \times 64$  points (corresponding to 4096 consecutive force measurements (force-distance curves)) were acquired on scan areas of  $500 \text{ nm} \times 500 \text{ nm}$ . Cycles of tip approach, contact, and retraction were recorded at a rate of 4 Hz with a vertical ( $Z$ ) scan size on the order of 500 nm. The photodiode signal data and piezo displacement curves were transformed into force-distance data using a custom built LabVIEW<sup>TM</sup> application.<sup>21, 32</sup> Histograms of adherence were obtained.

This approach-contact-retract cycle was performed as a function of the solution pH. The most probable force of rupture versus pH, as derived from the aforementioned histograms, was referred to as chemical force titration curve. All the force-distance curves were obtained in a

liquid cell filled with buffer solution. The cell was thoroughly cleaned and then rinsed with ethanol and water prior to use. The buffer solution was freshly prepared using a phosphate salt ( $\text{H}_3\text{PO}_4$ ,  $\text{NaH}_2\text{PO}_4$ ,  $\text{Na}_2\text{HPO}_4$ ) and kept at a constant ionic strength of 300 mM and at a pH ranging from 2 to 8. The measurements were carried out after an equilibration period of at least 1 h to minimize any instrument drift. More importantly, the pull-off force data did not change over time, indicating that the surface was in equilibrium with the buffer. For FV imaging, only subsequent up and down scans that showed the same force characteristics were considered. After the experiments, the tip radii were characterized by scanning an array of sharp spikes, resulting in so-called tip imaging. No obvious tip apex enlargement was observed.

***Time-of-flight secondary ion mass spectrometry (ToF-SIMS).*** In ToF-SIMS, a pulsed, focused, energetic ion beam bombards a surface, leading to interactions that cause the emission of positive and negative secondary ions.<sup>33</sup> The instrument used was a reflectron type time-of-flight mass spectrometer, with a design equivalent to that of the “ToF-SIMS IV”.<sup>34</sup> An electron impact ion source (10 keV,  $^{40}\text{Ar}^+$ ) was used for generating primary ion pulses for static ToF-SIMS. The pulsed ion beam was raster-scanned over an area of  $200\ \mu\text{m} \times 200\ \mu\text{m}$ . The mass range was from 1 to 3500 amu, and the mass resolution  $m/\Delta m$  was better than 4500 at mass 41. For charge compensation, a low-energy electron flood gun was utilized.

***Streaming potential measurements.*** Streaming potentials<sup>35-36</sup> were measured in a rectangular microchannel cell consisting of two planar sample surfaces as published in a previous study.<sup>37-40</sup> The cell consisted of two Plexiglas parts and contained a sample holder, Pt electrodes, and channels for in- and outlet of the liquid. The samples were spin-coated PDMS on glass slides. The liquid flow between the sample surfaces in the cell was achieved by applying a pressure regulator and a transducer. All functions were monitored by a computer and a customized interface.

## 5.5 Appendix: Gouy-Stern double layer with site dissociation model

### 5.5.1 Classical Gouy-Stern double layer

Anisotropic ion accumulation exists at the contact interface between an electrochemically active surface and a liquid electrolyte.<sup>67</sup> The charges at and adjacent to the surface will cause a potential difference between the region near the surface and the bulk of the solution. The potential decreases within the solution as a function of the distance from the charged surface. Specific ion adsorption occurrence is inferred from the dependence of certain double layer properties on the nature of counter and co-ions. Generally, ions that interact specifically (non-electro statically) with the surface approach it at a shorter distance.

The charge balance as a whole is written as

$$\sigma^0 + \sigma^d + \sigma^{\text{ads}} = 0 \quad (\text{Eq. 5-6})$$

$\sigma^0$  is the surface charge;  $\sigma^d$  is the diffuse charge;  $\sigma^{\text{ads}}$  is the charge that stems from the adsorbed ions.

If  $\sigma^{\text{ads}} = 0$ , there is no specific ion adsorption.

The Stern layer acts as a molecular condenser represented by a capacitance  $C$ . The surface potentials  $\psi^0$ , the potential at the outer Helmholtz plane (oHp)  $\psi^d$  and the surface charges  $\sigma^d$  are related via the capacitances.<sup>67</sup>

$$C = \frac{d\sigma^d}{d(\psi^0 - \psi^d)} \quad (\text{Eq. 5-7})$$

The plane where these specifically adsorbed ions reside is called the inner Helmholtz plane (iHp). The iHp layer capacitance and the oHp layer capacitances are given by

$$C_1 = \frac{d\sigma^0}{d(\psi^0 - \psi^d)} \quad (\text{Eq. 5-8})$$

and

$$C_2 = \frac{d\sigma^d}{d(\psi^{\beta} - \psi^d)} \quad (\text{Eq. 5-9})$$

respectively.



$\psi^\beta$  is the potential at the inner Helmholtz plane (iHp). Within the framework of our analysis, the capacitance is considered constant (integral capacitances are then assimilated to differential capacitances), as commonly adopted in the literature.<sup>67</sup>

### 5.5.2 Modeling with no specific ion adsorption

For the description of charge and potential at the oxide-electrolyte interface, different models can be used.<sup>67-69</sup> The surface charge at the oxidized PDMS-electrolyte interface originates from the dissociation of silanol groups when in contact with a NaCl buffer solution. The equilibrium constants of silanol ionization processes are  $K_{a_1}$  and  $K_{a_2}$  given by

$$K_{a_1} = \frac{[-\text{SiOH}][\text{H}^+] \exp(-e\psi^0/kT)}{[-\text{SiOH}_2^+]} \quad (\text{Eq. 5-10})$$

$$K_{a_2} = \frac{[-\text{SiO}^-][\text{H}^+] \exp(-e\psi^0/kT)}{[-\text{SiOH}]} \quad (\text{Eq. 5-11})$$

where  $[\text{H}^+]$  is the concentration of protons in the bulk and the other quantities in brackets are surface concentrations;  $k$  is the Boltzmann factor;  $T$  is the absolute temperature,  $\psi^0$  is the surface potential and  $e$  is the elementary charge.

Surface charge  $\sigma_0$  derives from the acid-base interactions of the solution components and is defined by

$$\sigma_0 = e([- \text{SiOH}_2^+] - [- \text{SiO}^-]) \quad (\text{Eq. 5-12})$$

Consequently the pH of the solution is the primary externally adjustable variable, which together with the electrolyte concentration determines the sign and the magnitude of  $\sigma_0$ . In this study, neither the formation nor the disappearance of silanol groups is taken into account and the parameter  $N_s$  (effective number of ionizable surface sites) is therefore supposed to remain constant upon changing the electrolyte composition. The total amount of reactive silanol groups is directly dependent on the UV/ozone treatment dose. We have

$$N_s = [-\text{SiOH}_2^+] + [-\text{SiO}^-] + [\text{SiOH}] \quad (\text{Eq. 5-13})$$

Diffuse ionic charge  $\sigma^d$  can be derived from the Gouy-Chapman theory for a 1:1 electrolyte.

$$\sigma^d = -(8I\varepsilon_0\varepsilon_{rw}RT)^{1/2} \sinh(y^d/2) \quad (\text{Eq. 5-14})$$

where  $\varepsilon_0$  is the dielectric permittivity of vacuum;  $\varepsilon_{rw}$  is the relative permittivity of water;  $I$  is the ionic strength of the solution;  $R$  is the gas constant;  $T$  is the temperature.  $y^d$ , the dimensionless potential defined by

$$y^d = F\psi^d / RT \quad (\text{Eq. 5-15})$$

and 
$$\psi^d = \zeta \quad (\text{Eq. 5-16})$$

where  $\psi^d$  is generally assimilated to the electrokinetic potential ( $\zeta$ ).

The set of Equations 5-10 to 5-13 can be transformed into

$$\sigma^0 = eN_s \frac{([H^+] / K_{a_1}) \exp(-e\psi^0 / kT) - (K_{a_2} / [H^+]) \exp(e\psi^0 / kT)}{1 + ([H^+] / K_{a_1}) \exp(-e\psi^0 / kT) + (K_{a_2} / [H^+]) \exp(e\psi^0 / kT)} \quad (\text{Eq. 5-17})$$

A consistent resolution -as achieved by numerical analysis- of Equations 5-6, 5-7, 5-9, 5-16 and 5-17 allows for a quantitative determination of the double layer parameters that include the various potentials and charges entering the description of the interfacial structure. Further comparison with experimental data (i.e. electrokinetic potentials derived from streaming potential measurements) obtained for a broad range of ionic strengths and pH values enable the evaluation of the quantities  $K_{a_1}$  and  $K_{a_2}$  and  $N_s$ . For that purpose, a Least Square Regression (LSR) method was considered.

### 5.5.3 Modeling with specific ion adsorption

Ions of the background electrolyte, which are not primarily charge-determining for a particular type of surface, may specifically adsorb onto the surface. The non-electrostatic forces involved in this process result in shifts of the point of zero charge and the IEP. For such a reversible interface, the amount of specifically adsorbed ions is, for a given concentration and affinity of these ions, determined by the solution pH. In our experiment, the influence of specific ion adsorption is taken into account by formulating the appropriate equilibrium equations for phosphate groups.

In the low pH range,  $\text{SiOH}_2^+$  are expected to be the predominant species present at the surface. The surface concentrations of  $-\text{SiOH}$  and  $-\text{SiO}^-$  increase upon increasing the pH

value. In the analysis, we considered adsorption of ions onto oppositely charged surface sites, which constitutes the most favorable situation from an energetic point of view. As revealed by electrokinetic experiments performed in NaCl solutions,  $\text{Na}^+$  and  $\text{Cl}^-$  may be considered as indifferent ions. Considering the neutral and negatively charged ions in the phosphate buffer solution, the adsorbability sequence for the various ions present in phosphate solutions onto oxide like surfaces for low to intermediate pH values is as follows  $\text{H}_3\text{PO}_4 \ll \text{H}_2\text{PO}_4^- \ll \text{HPO}_4^{2-}$ . The binding of the pertaining anions onto PDMS surface are expressed by Equations 5-6 in section 3.7. The binding process equilibrium constants are  $K_x$  and  $K_y$ . It is noted that the respective bulk concentrations of the various relevant phosphate ions were evaluated according to classical calculations based on the first two dissociation  $\text{p}K_a$  values reported in the literature.<sup>70, 71</sup> The charge density at the solid surface can be calculated from the total amount of charged surface groups that is now written:

$$N_s = [\text{SiOH}] + [\text{SiOH}_2^+] + [\text{SiO}^-] + [\text{SiOH}_4\text{PO}_4] + [-\text{SiOH}_2\text{PO}_4^{2-}] \quad (\text{Eq. 5-18})$$

$$\sigma^0 = [-\text{SiOH}_2^+] - [\text{SiO}^-] - 2[-\text{SiOH}_2\text{PO}_4^{2-}] \quad (\text{Eq. 5-19})$$

The charge density at the inner Helmholtz plane  $\sigma^\beta$  is determined by the total concentration of adsorbed electrolyte ions:

$$\sigma^\beta = [-\text{SiOH}_4\text{PO}_4] - 2[-\text{SiOH}_2\text{PO}_4^{2-}] \quad (\text{Eq. 5-20})$$

Due to the charge neutrality requirement in a stationary equilibrium, all charge densities must compensate each other as expressed by Equation (10-11). From these basic equations the expressions for the concentrations of the different charged groups can be derived as a function of  $N_s$ ,  $K_{a_1}$ ,  $K_{a_2}$ ,  $K_x$  and  $K_y$ . The parameters,  $N_s$ ,  $K_{a_1}$ , and  $K_{a_2}$  were obtained from the analysis of the electrokinetic data obtained in NaCl indifferent electrolyte. On the basis of an iterative numerical analysis of Equations 6, 7, 9-11, 14, 16, 18-21 and subsequent comparison (following a LSR strategy) with experimental data ( $\zeta$  potentials) at various ionic strength and pH conditions, we could evaluate the searched quantities  $K_x$  and  $K_y$ . We add that the values of the different electrical capacitances introduced in the model and chosen for the analysis were  $C = 100 \mu\text{F cm}^{-2}$  (used for the case where no specific adsorption takes place),  $C_1 = 120 \mu\text{F cm}^{-2}$ , and  $C_2 = 20 \mu\text{F cm}^{-2}$  as used for the case of specifically

adsorbing ions.<sup>68</sup> The (assumed) constancy of these is certainly an abstraction from reality in view of the variation of the silanol distributions (or equivalent of the local balance between hydrophobic and hydrophilic silanol patches) with UV/ozone treatment time. However, for the lack of better and for the sake of simplicity, we considered oxide-type capacitances as commonly reported in the literature.<sup>67, 69</sup> For that reason, the analysis of the data should certainly be considered at a semi-quantitative level but it has however the merit to reproduce the experimentally observed PDMS surface features, particularly the IEP shifts when varying the phosphate concentration in solution and/or the treatment time and the increase of the surface site concentration with increasing UV/ozone time exposure. Those features are qualitatively in line with the independent AFM analysis.

## References

- [1] Brook, M. A. *Silicon in Organic, Organometallic, and Polymer Chemistry*: John Wiley & Sons: New York, 2000.
- [2] Xia, Y. N.; Whitesides, G. M. *Annu. Rev. Mater. Sci.* **1998**, *28*, 153.
- [3] Kane, R. S.; Takayama, S.; Ostuni, E.; Ingber, D. E.; Whitesides, G. M. *Biomaterials* **1999**, *20*, 2363.
- [4] Lahiri, J.; Ostuni, E.; Whitesides, G.M. *Langmuir* **1999**, *15*, 2055.
- [5] Degenhart, G. H.; Dordi, B.; Schönherr, H.; Vancso, G. J. *Langmuir* **2004**, *20*, 6216.
- [6] Hillborg, H.; Gedde, U. W. *IEEE. Trans. Dielectr. Electr. Insul.* **1999**, *6*, 703.
- [7] Hall, J. F. *IEEE Trans. Power Delivery* **1993**, *8*, 376.
- [8] Merkel, T. C.; Bondar, V. I.; Nagai, K.; Freeman, B. D.; Pinnau, I. *J. Polym. Sci., Part B: Polym. Phys.* **2000**, *38*, 415.
- [9] Efimenko, K.; Wallace, W. E.; Genzer, J. J. *Colloid Interface Sci.* **2002**, *254*, 306.
- [10] Fateh-Alavi, K.; Gedde, U. W. *Polym. Degrad. Stab.* **2004**, *84*, 469.
- [11] Kind, H.; Bonard, J. M.; Emmenegger, C.; Nilsson, L. O.; Hernadi, K.; Maillard-Schaller, E.; Schlapbach, L.; Forro, L.; Kern, K. *Adv. Mater.* **1999**, *11*, 1285.
- [12] Berdichevsky, Y.; Khandurina, J.; Guttman, A.; Lo, Y. H. *Sens. Actuators, B* **2004**, *97*, 402.
- [13] Martin, B. D.; Brandow, S. L.; Dressick, W. J.; Schull, T. L. *Langmuir* **2000**, *16*, 9944.
- [14] Hillborg, H.; Sandelin, M.; Gedde, U. W. *Polymer* **2001**, *42*, 7349.
- [15] Graubner, V. M.; Jordan, R.; Nuyken, O.; Schnyder, B.; Lippert, T.; Kotz, R.; Wokaun, A. *Macromolecules* **2004**, *37*, 5936.
- [16] Toth, A.; Bertoti, I.; Blazso, M.; Banhegyi, G.; Bogнар, A.; Szaplanczay; P. *J. Appl. Polym. Sci.* **1994**, *52*, 1293.
- [17] Owen, M. J.; Smith, P. J. *J. Adhes. Sci. Technol.* **1994**, *8*, 1063.
- [18] Hillborg, H.; Gedde, U. W. *Polymer* **1998**, *39*, 1991.
- [19] Frisbie, C. D.; Rozsnyai, L. F.; Noy, A.; Wrighton, M. S.; Lieber, C. M. *Science* **1994**, *265*, 2071.
- [20] Noy, A.; Frisbie, C. D.; Rozsnyai, L. F.; *J. Am. Chem. Soc.* **1995**, *117*, 7943.
- [21] Hillborg, H.; Tomczak, N.; Olah, A.; Schönherr, H.; Vancso, G. J. *Langmuir* **2004**, *20*, 785.
- [22] Vasilets, V. N.; Nakamura, K.; Uyama, Y.; Ogata, S.; Ikada, Y. *Polymer* **1998**, *39*, 2875.
- [23] Huck, W. T. S.; Bowden, N.; Onck, P.; Pardoен, T.; Hutchinson, J. W.; Whitesides, G. M. *Langmuir* **2000**, *16*, 3497.
- [24] Ouyang, M.; Yuan, C.; Muisener, R. J.; Boulares, A.; Koberstein, J. T. *Chem. Mater.* **2000**, *12*, 1591.
- [25] Schönherr, H.; Hruska, Z.; Vancso, G.J. *Macromolecules* **2000**, *33*, 4532.
- [26] Duval, Y.; Mielczarski, J. A.; Pokrovsky, O. S.; Mielczarski, E.; Ehrhardt, J. J. *J. Phys. Chem. B* **2002**, *106*, 2937.
- [27] Kim, K. J.; Fane, A. G.; Nyström, M. *J. Membr. Sci.* **1997**, *134*, 1999.
- [28] Franks, G. V.; Meagher, L. *Colloids Surf., A* **2003**, *214*, 99.
- [29] Yates, D. E.; Levine, S.; Healy, T. W. *J. Chem. Soc., Faraday Trans.* **1974**, *70*, 1807.
- [30] Hutter, J.L.; Bechhoefer, J. *Rev. Sci. Instrum.* **1993**, *64*, 1868.
- [31] A force volume image contains an array of force curves over the entire sample area and is generated by ramping the *z* piezo as the tip scans across the area. Each force curve is measured at a unique *x-y* position in the area, and force curves from an array of *x-y* points are combined into a three-dimensional array, or “volume”, of force data. The value at a point (*x,y,z*) in the volume is the deflection (force) of the cantilever at that position in space.
- [32] Vancso, G. J.; Hillborg, H.; Schönherr, H. *Adv. Polym. Sci.* **2005**, *182*, 55.
- [33] Benninghoven, A. *Angew. Chem., Int. Ed. Eng.* **1994**, *33*, 1023.
- [34] Gunst, U.; Zabel, W. R.; Poll, G.; Arlinghaus, H. F. *Surf. Interface Anal.* **2004**, *36*, 1231.
- [35] Delgado, A. V. *Interfacial Electrokinetics and Electrophoresis*, Marcel Dekker Ltd: New York, 2001.
- [36] The streaming potential is defined as the difference in potential ( $V_{str}$ ) at zero current caused by the flow of liquid under a pressure gradient in a capillary with flat walls made of the investigated specimen (PDMS).

- [37] Van Wagenen, R. A.; Andrade, J. D. *J. Colloid Interface Sci.* **1980**, *76*, 305.
- [38] Scales, P. J.; Grieser, F.; Healy, T. W. *Langmuir* **1990**, *6*, 582.
- [39] Duval, J. F. L.; Huijs, G. K.; Threels, W. F.; Lyklema, J.; van Leeuwen, H. P. *J. Colloid Interface Sci.* **2003**, *260*, 95.
- [40] Norde, W.; Rouwendal, E. *J. Colloid Interface Sci.* **1990**, *139*, 169.
- [41] Arlinghaus, H. F. Static Secondary Ion Mass Spectrometry (SSIMS). In *Surface and Thin Film Analysis*; Eds.; Bubert, H.; Jenett, H., Wiley-VCH: New York, 2002.
- [42] Steffens, P.; Niehuis, E.; Friese, T.; Greifendorf, D.; Benninghoven, A. *J. Vac. Sci. Technol., A* **1985**, *3*, 1322.
- [43] Benninghoven, A. *J. Vac. Sci. Technol. A* **1985**, *3*, 451.
- [44] Bletsos, I. V.; Hercules, D. M.; Magill, J. H.; van Leyen, D.; Niehuis, E.; Benninghoven, A. *Anal. Chem.* **1988**, *60*, 938.
- [45] Hagenhoff, B.; Benninghoven, A.; Barthel, H.; Zoller, W. *Anal. Chem.* **1991**, *63*, 2466.
- [46] Dong, X.; Proctor, A.; Hercules, D. M. *Macromolecules* **1997**, *30*, 63.
- [47] Vezenov, D. V.; Noy, A.; Rozsnyai, L. F.; Lieber, C. M. *J. Am. Chem. Soc.* **1997**, *119*, 2006.
- [48] Parks, G. A. *Chem. Rev.* **1965**, *65*, 177.
- [49] Eaton, P. J.; Graham, P.; Smith, J. R.; Smart, J. D.; Nevell, T. G.; Tsibouklis, J. *Langmuir* **2000**, *16*, 7887.
- [50] Sun, Y. J.; Walker, G. C. *Langmuir* **2005**, *21*, 8694.
- [51] Sun, Y. J.; Akhremitchev, B.; Walker, G. C. *Langmuir* **2004**, *20*, 5837.
- [52] Yates, D. E.; Healy, T. W. *J. Colloid Interface Sci.* **1976**, *55*, 9.
- [53] Davis, J. A.; James, R. O.; Leckie, J. O. *J. Colloid Interface Sci.* **1978**, *63*, 480.
- [54] Davis, J. A.; Leckie, J. O. *J. Colloid Interface Sci.* **1978**, *67*, 90.
- [55] James, R. O.; Davis, J. A.; Leckie, J. O. *J. Colloid Interface Sci.* **1978**, *65*, 331. (a) Ong, S. W.; Zhao, X. L.; Eienthal, K. B. *Chem. Phys. Lett.* **1992**, *191*, 327. (b) Lyklema, J. *Fundamentals of Interface and Colloid Science Vol. II*: Academic Press: San Diego, 1995.
- [56] Wang, B.; Abdulali-Kanji, Z.; Dodwell, E.; Horton, J. H.; Oleschuk, R. D. *Electrophoresis* **2003**, *24*, 1442.
- [57] Schönherr et al. (see ref 25) previously suggested that the surface  $pK_a$  of  $-COOH$  groups introduced on oxyfluorinated isotactic polypropylene shifted to higher values as compared to the bulk  $pK_a$ . The observed shifts in  $pK_a$  were due to the presence of a surrounding hydrophobic environment, which retarded the ionization process.
- [58] Werner, C.; Kärber, H.; Zimmermann, R.; Dukhin, S.; Jacobasch, H. J. *J. Colloid Interface Sci.* **1998**, *208*, 329.
- [59] Duval, J. F. L.; Ohshima, H. *Langmuir* **2006**, *22*, 3533.
- [60] Graubner, V. M.; Jordan, R.; Nuyken, O.; Kötz, R.; Lippert, T.; Schnyder B.; Wokaun A. *Polym. Mater. Sci. Eng.* **2003**, *88*, 489.
- [61] Sia, S. K.; Whitesides, G. M. *Electrophoresis* **2003**, *24*, 3563.
- [62] McDonald, J. C.; Whitesides, G. M. *Acc. Chem. Res.*, **2002**, *35*, 491.
- [63] Duval, J. F. L.; Wilkinson, K. J.; van Leeuwen, H. P. *Environ. Sci. Technol.* **2005**, *39*, 6435.
- [64] Tadros, T. F.; Lyklema, J. *J. Electroanal. Chem.* **1968**, *17*, 267.
- [65] Hu, K.; Bard, A. J. *Langmuir*, **1997**, *13*, 5114.
- [66] Lyklema, J. *Fundamentals of interface and colloid science Vol. II*. Elsevier Academic Press, **2005**.
- [67] Duval, J.; Lyklema, J.; Kleijn J.M.; van Leeuwen, H.P. *Langmuir* **2001**, *17*, 7573.
- [68] Duval, J.; Kleijn, J.M.; Lyklema, J.; van Leeuwen, H.P. *J. Electroanal. Chemistry* **2002**, *532*, 337.
- [69] Ong, S.W.; Zhao, X.L.; Eienthal, K.B. *Chem. Phys. Lett.* **1992**, *191*, 327.
- [70] Wang, B.; Abdulali-Kanji, Z.; Dodwell, E.; Horton, J.H.; Oleschuk, R.D. *Electrophoresis* **2003**, *24*, 1442.



# Chapter 6

## **Contact mechanics of UV/ozone treated PDMS by AFM and ATD techniques: Mechanical performance from nano- to micrometer length scales<sup>§</sup>**

In this *chapter*, the Young's modulus of cross-linked poly(dimethylsiloxane) (PDMS) surface as a function of UV/ozone treatment time across different length scales has been quantitatively investigated. AFM was used to probe PDMS surface mechanical properties at a nanometer lengthscale. Young's modulus of each sample was compared with different continuum contact mechanics theories (Hertz and JKR) as well as different tip shape models (spherical and hyperboloid). These data suggested that consideration of the adhesion energy at the tip-sample interface and tip shape was very important for consistent elastic modulus determination of soft materials. Moreover, a custom-built adhesion testing device (ATD) set-up was used which allows monitoring simultaneously the load, the contact area, and the relative displacement between a lens (PDMS elastomer or Si<sub>3</sub>N<sub>4</sub>) and the surface treated PDMS film, upon loading and unloading on the micrometer to sub-millimetre length scales. The measured modulus of PDMS increased with increasing treatment time as obtained from AFM and ATD techniques. Furthermore in comparison with PDMS bulk modulus, obtained from a tensile test, the surface modulus was enhanced. The characteristic length-scale effects on mechanical properties has not been studied quantitatively to great extent despite the widespread use of untreated and surface treated PDMS. Hence, we discussed the variation in modulus due to the indentation size effects considering indenter size and indentation depth. It is shown that the modulus decreased with the increase of the characteristic length scale.

---

<sup>§</sup> Part of this *chapter* will be submitted for publication.



## 6.1 Introduction

Mechanical properties of surfaces and interfaces are important for the understanding of the behavior of adhesive and sliding contacts.<sup>1</sup> In addition, mechanical response of elastomers is one of other important concerns in some applications such as tunable microdoublet lenses<sup>2</sup> and dielectric elastomer actuators.<sup>3</sup> A widely used elastomer, cross-linked PDMS, has been applied in several modern areas such as thin films and coatings, soft lithography, biomedical applications, optical system, nanotribology, nanofluidics, MEMS/NEMS, etc. Therefore, quantitatively characterized mechanical properties of PDMS become more and more important.

As we know, surface treatment can result in changes of interfacial properties. In *chapter 5*, the changes of surface chemistry and ionization state of PDMS exposed to UV/ozone irradiation have been reported. It has been shown that, during treatment-dependent surface modifications of PDMS, silanol groups were introduced at the surface. Oxidative cross-linking via Si–O bridges was found to cause the gradual formation of a continuous "silica-like" barrier layer of SiO<sub>2</sub>. The oxidation process within the top 10 nm of the surface has been extensively investigated by X-ray photoelectron spectroscopy (XPS), proving the existence of this silica-like layer. This thin silica-like layer may affect the mechanical properties of the treated PDMS surface. In addition, as the characteristic dimensions of the mechanical tests are reduced, the obtained surface properties may change greatly. On the above accounts, quantitative analysis of PDMS surface mechanical properties across different length scales as a function of treatment level is necessary.

Recently, indentation techniques have been extensively used for mechanical characterisation of materials. Development of instrumented indentation techniques at low and ultra low load levels has improved their utility for understanding the mechanical responses of solids at micro and nano scales. In this *chapter*, two indentation devices, AFM and ATD, were chosen to investigate the influence of surface treatment upon the elastic modulus of PDMS obtained from nano and micro indentations. Advances of AFM enable the examination of surface mechanical properties with substantially improved force and spatial resolution, and enable quantitative measurements of surface mechanical properties. Here, the analysis methods, the Hertz and JKR model have been applied in order to interpret the experimental data. Subsequently, the ATD technique provided a direct evaluation of elastic modulus at a micro meter length scale. Finally, a comparison of PDMS's response against nano and micro-

deformation to its bulk properties was reported. Hence we anticipate that, our study of PDMS near-to-surface mechanical properties would be valuable for material selection and design improvements in a number of practical applications.

## **6.2 Surface Young's modulus at a nanoscopic length scale**

There are two different methods commonly adopted for the measurement of indentation which are called "imaging method" and "compliance method". In the imaging method, the indenter, under a specified load is made to penetrate the test surface and withdrawn after a specified residence or dwelling time. The diameter or diagonal of the residual image of the indentation trace is then measured by optical or other means. However, this method has some inherent limitations. The imaging of the residual indent becomes inexact as the indentation size is scaled down. Therefore, this method provides primarily the plastic response of the material and is not very suitable for obtaining elastic and viscoelastic-plastic properties of organic polymers which creep in the indentation region significantly after unloading. In addition, no information regarding the elastic response of the sample is directly available with this method.

Nevertheless, this difficulty has been largely overcome with the broad introduction of the "compliance method". It is now commonly utilized for polymers and elastomeric systems. This method does not rely upon the measurement of the residual indent cross section; the surface mechanical properties such as stiffness, hardness and elastic modulus are obtained from the analysis of the load-displacement data recorded during loading–unloading indentation cycles performed upon material surfaces.

AFM applies the compliance method which is developed to eliminate the need to visualize the indents and has been used with success to study properties of polymeric materials with small dimensions (e.g. thin films and nano/micro structures) with lower indentation load.<sup>4, 5</sup> Several recent publications have demonstrated that reproducible and quantitative results could be obtained for a variety of polymers.<sup>6-16</sup> Various nano-mechanical properties of polymer thin films, including elasticity,<sup>17, 18</sup> hardness,<sup>19</sup> and viscoelasticity<sup>20, 21</sup> were studied. In this section, we demonstrate the use of the AFM indentation technique to study the Young's modulus of UV/ozone treated PDMS surface at the nanometer length scale. The elastic modulus was deduced directly from the indentation force curves.

AFM tip is considered as a probing indenter.<sup>8, 9, 14</sup> Quantitative measurements require the knowledge of cantilever spring constants.<sup>22, 23</sup> In AFM experiment, measurements are displacement controlled. The sample is displaced against a cantilever indenter via a piezoelectric actuator and forces are inferred from the measured deflection of the cantilever and its known spring constant. A schematic picture of nanoindentation with an AFM tip is shown in Figure 6.1a. During indentation, a typical force distance curve of tip deflection signal as a function of the vertical displacement of the piezo actuator is recorded and reproduced in Figure 6.1b. The slope of a force distance curve describes the elastic properties of a sample in a qualitative way. Experiment on an infinitely stiff sample, the deflection  $d$  of the cantilever is identical to the movement of the piezo in  $Z$  direction.

$$d = Z. \quad (\text{Eq. 6-1})$$

In the case of a soft sample, the tip will indent the sample. This indentation  $\delta$  leads to a smaller deflection resulting in a force curve with a smaller slope.

$$d = Z - \delta \quad (\text{Eq. 6-2})$$

Because Hooke's law connects the deflection of the cantilever and the applied loading force via the force constant  $k$  of the cantilever, the loading force can be written as

$$F = kd = k(Z - \delta) \quad (\text{Eq. 6-3})$$

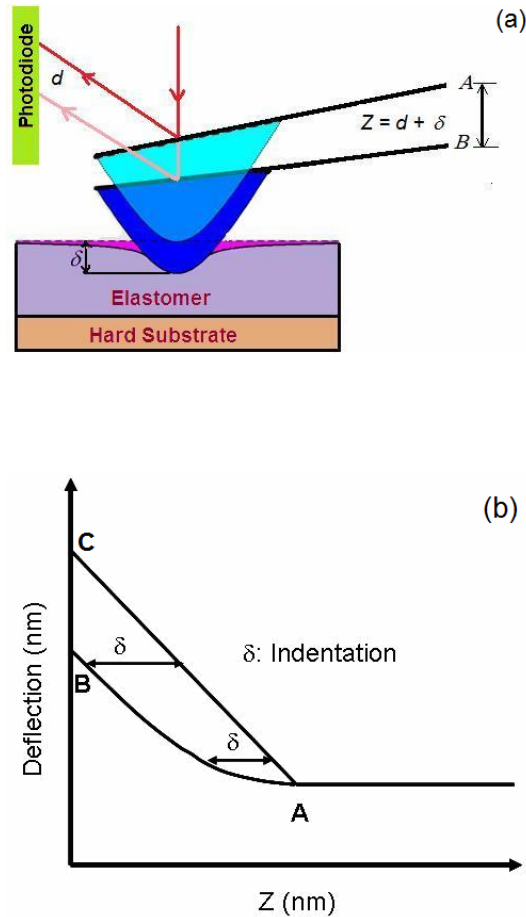


**Figure 6.1** (a) Schematic diagram of nanoindentation with an AFM probe;  $d$  is cantilever deflection change;  $\delta$  is indentation depth;  $Z$  is base movement. (b) Diagram of retracting force vs. distance curves of soft and hard materials.  $AC$  represents the contact portion of a stiff sample;  $AB$  represents the contact portion of a soft sample.

After contact is made between the probe tip and the sample surface, piezo displacement results in both probe tip deflection and sample indentation, the amount of which depends on the relative stiffness of the sample and the cantilever probe. Thus, the indenter spring stiffness must be matched to the contact stiffness in order to get a measurable deformation in the sample itself, rather than simple deflection of the cantilever spring. Tsukruk<sup>6</sup> defined a standard to choose the spring constant of the cantilever. The limits of detection of surface deformation were determined by analysing the ratio of materials elasticity and spring constant of cantilevers. If the cantilever is too stiff, the vertical deflection of the AFM cantilever is very small compared to the vertical displacement of the piezo actuator. In this case, the ratio of indentation depth to vertical deflection can approach an upper limit of detection, e.g.  $\delta/d = 10$ . However, if the material is much harder than the cantilever stiffness,

then a lower limit of observation,  $\delta/d = 0.1$  can be approached. Figure 6.2 shows the range of applicability of the cantilevers within this limit. This condition takes into account the usual level of noise and non-linearity of a commercial mechanical systems, and provides an acceptable signal level which can be separated from the background.<sup>6</sup>

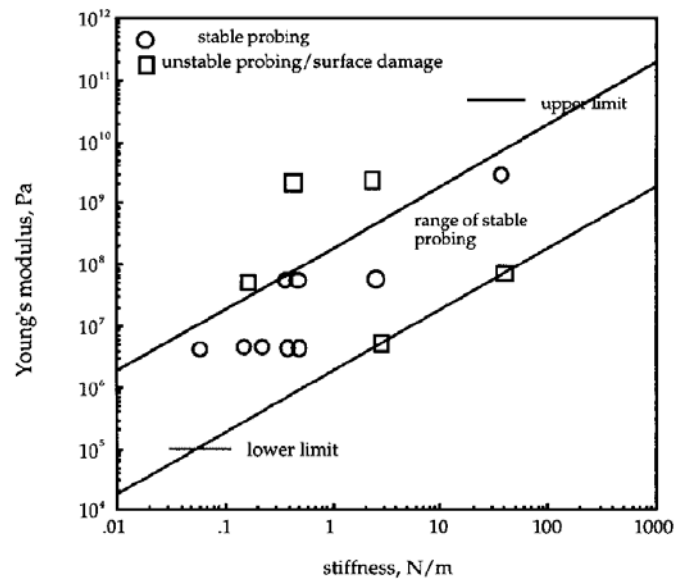


**Figure 6.2** Range of applicability of cantilevers with different stiffness with limits  $\delta/d = 0.1$  (upper limit) and  $h/d = 10$  (lower limit) and tested cantilevers for various materials (adapted from ref.<sup>6</sup>).

Using this deflection/indentation condition, we estimated the value of the cantilever spring constant which satisfied the measurement limits discussed above. As is clear from the plot presented, choosing the spring constant within the range of 0.18-0.28 N/m should allow measurements of elastic moduli from tens of KPa to tens of MPa. It is suitable for our PDMS measurements since the estimated bulk modulus is around 1-3 MPa (Sylgard-184A : Sylgard-184B = 10 : 1).

In addition to properly choosing of the indenter, another issue should be considered. Most AFMs, including the standard multi-mode AFM, plot forces vs. a calculated Z position based on the anticipated response of the Z-piezo to a given voltage. However, undesirable piezo properties such as creep, hysteresis, and nonlinearity can make this position axis inaccurate, especially for irregular, non-cyclic force plots. Thus, depth of penetration is difficult to determine due to piezo creep and hysteresis effects.<sup>24</sup> The new PicoForce scanner (Veeco-Digital Instruments (DI), Santa Barbara, CA) incorporates a Z axis capacitive sensor

for closed loop positioning within 0.5 nm RMS over 20  $\mu\text{m}$  of travel toward and away from the sample stage. The closed-loop low-noise Z-axis sensor accomplishes the goal of plotting the forces against an accurate position axis.

### 6.2.1 Young's modulus

In this section, we report on the initial results from model studies on nanomechanical properties of PDMS based on classical theories of elastic contacts, i.e. the Hertz and the Johnson-Kendall- Roberts (JKR) theories. These models were tested for a set of untreated and UV/ozone treated PDMS films. By applying known relationships between normal load  $F$  and indentation depth,  $\delta$ , offered in elastic contact models, one can obtain analytical expressions of Young's modulus for each model.<sup>16, 25</sup>

#### *Hertz model*

Hertz proposed a continuum mechanics model to describe the contact between two elastic spheres under external load in the absence of adhesion. We used the Hertz theory in the beginning to model the elastic part of the loading curve. In the Hertz theory, the applied load and the deformation of the sample are related by Equation 6-4:

$$F = k_c d = \sqrt{R} \delta^{3/2} K \quad (\text{Eq. 6-4})$$

where  $F$  represents the externally applied loading force, and  $R$  is the relative radius,

$$\frac{1}{R} = \frac{1}{R_{\text{tip}}} + \frac{1}{R_{\text{sample}}} \quad (\text{Eq. 6-5})$$

$K$  is the combined elastic modulus and  $\delta$  is the indentation depth.

$$K = 4/3 \left[ \left(1 - \nu_{\text{tip}}^2\right) / E_{\text{tip}} + \left(1 - \nu_{\text{sample}}^2\right) / E_{\text{sample}} \right]^{-1} \quad (\text{Eq. 6-6})$$

where  $E$  is the elastic modulus and  $\nu$  is the Poisson ratio, respectively. Since the value of the Young's modulus for  $\text{Si}_3\text{N}_4$  tips is about 220 GPa, while Young's modulus of the sample of interest in this work is only about several MPa, Equation 6-6 could be simplified as

$$K = \frac{4}{3(1 - \nu_{\text{PDMS}}^2)} E_{\text{PDMS}} \quad (\text{Eq. 6-7})$$

Moreover, in Equation 6-4 it has been assumed that the indenting tip has a spherical shape. Correction factors can be used to take into account the effect resulting from the nonspherical shape, e.g., conical, paraboloidal, hyperboloidal shape of the tip.<sup>26</sup> Adhesion effects are excluded from the Hertz model (adhesion induced indentation will be discussed in the JKR model), and the indentation depth is relatively small compared to the tip radius. Thus, only spherical tip configuration was assumed for the analysis.

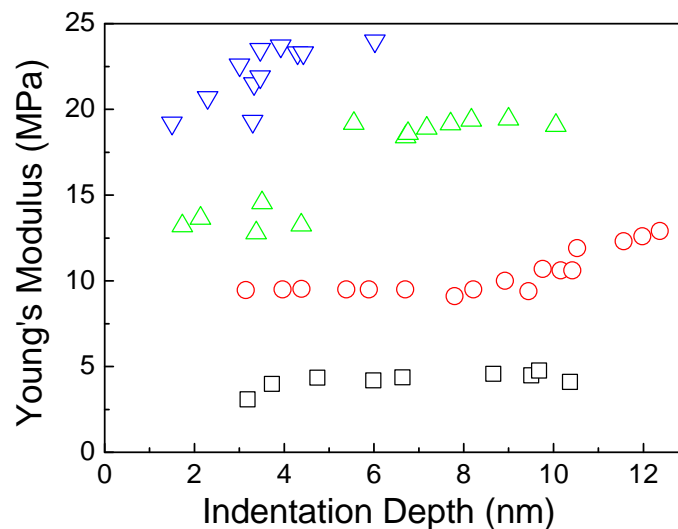


**Figure 6.3** Young's modulus of PDMS calculated with the Hertz model at different indentation depths. (□) untreated; (○) 15 min treated; (△) 30 min treated; (▽) 60 min treated.

Figure 6.3 shows the Young's modulus calculated by Hertz model using Equation 6-4. The contact point was defined as the minimum of the force curve on approach. The elastic value predicted by this model remains relatively constant over a broad indentation range. The thus estimated modulus of untreated PDMS was  $3.4 \pm 0.4$  MPa. With increasing the value of the surface treatment time, the surface Young's modulus increased. After 60 min UV/ozone treatment, the surface modulus increased to  $22 \pm 2.4$  MPa.

### JKR model

Adhesion forces must be taken into account when their contribution becomes significant as compared to purely elastic forces. The JKR, Maugis-Dugdale (MD) and extended viscoelastic JKR models are commonly used in adhesive contact mechanics.<sup>27-29</sup>

Unfortunately, the determination of the zero contact point in AFM indentation experiments using these adhesive contact models is not well described. In this *chapter*, the initial contact is the point where the interaction becomes attractive as defined by Walker and co-authors for PDMS study (shown in Figure 6.4a, point "a").<sup>30</sup>

A typical AFM force-distance curve of untreated PDMS is given in Figure 6.4a. When the gradient of the interaction force exceeds the force constant of the cantilever, the tip will jump in contact with surface. The maximum value of the attractive force is defined as pull-on force. Once the tip contacts the surface, the tip penetrates into the sample due to the adhesive force between the tip and PDMS film.<sup>30</sup> When the AFM tip retracts from a soft sample, the AFM tip can pull and deform the sample by the adhesive interaction. The pull-off force, i.e., the product of maximum contact cantilever deflection and  $k_c$ , is equal to the adhesion force,  $F_{ad}$ . In Figure 6.4c, a typical force distance curve of 60 min treated PDMS film is shown. Compared to untreated PDMS, the value of the pull-on force was decreased from 5.89 nN to 0.16 nN and pull-off force was decreased from 43.05 nN to 1.72 nN. Subsequently, the force plots were converted into corresponding force vs. indentation plots in Figure 6.4c and 6.4d. In the force-indentation plot, one important point should be mentioned here. At point "o" (an example is shown in Figure 6.4b), where AFM tip is pulled into the sample surface due to the adhesive interaction, the stored elastic energy and the surface energy are balanced; hence, there is a zero external force on the AFM cantilever. The indentation between the initial contact point "a" and point "o" is defined as the adhesion-induced indentation. Figure 6.4 e and 6.4 f summarize that the pull-on force and adhesion induced indentation decreased with increasing treatment time.



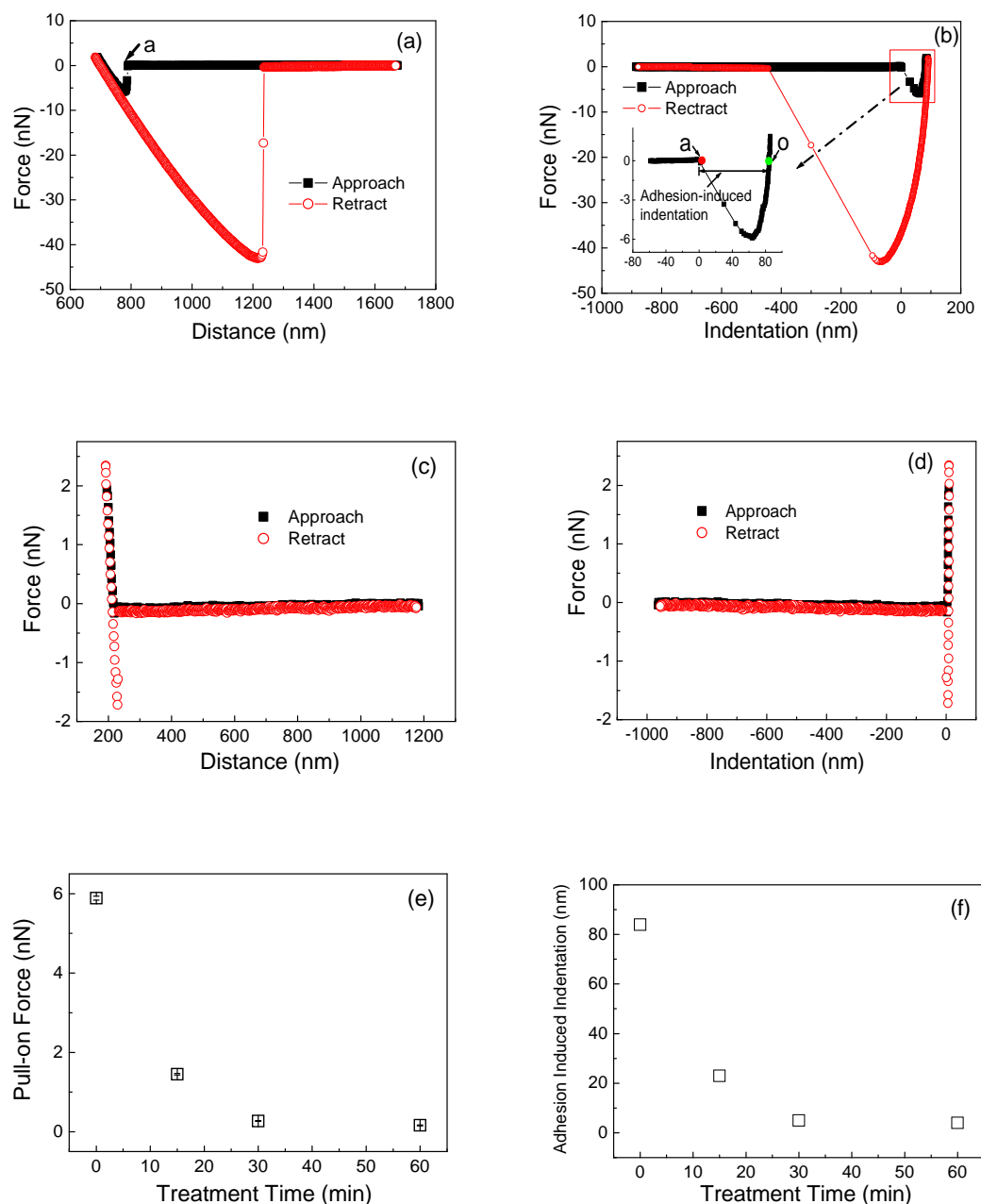


**Figure 6.4** a) A typical force distance curve of pure PDMS. b) A converted force indentation curve of pure PDMS. c) A typical force distance curve of 60 min treated PDMS. d) A converted force indentation curve of 60 min treated PDMS. Z scan size was set as  $1 \mu\text{m}$ . Z scan rate was 1 Hz. A commercial  $\text{Si}_3\text{N}_4$  tip was used. To minimize the capillary force effect, all the force distance curves were obtained under water. The value of the relative trigger is set to 20 nm.

The details of surface roughness of PDMS films characterization can be found in a previous study.<sup>31</sup> For untreated and oxidized PDMS films, the average surface roughness ( $R_a$ ) obtained by AFM topography analysis (scan area is  $5 \times 5 \mu\text{m}$ ) is in the range of 1 to 2 nm. In addition, the mean roughness was not influenced by the UV/ozone exposure. These smooth

sample surfaces can simplify the collection of force curves because the topographical effect is minimized.

AFM as a means of obtaining mechanical properties can be rather complex. A complete description of the mechanical behavior of the soft material and an analysis model to interpret AFM experiments are thus necessary. In the following section, a detailed description of the Young's modulus calculation used in this work is introduced.

First we briefly review some of the main conclusions of the JKR theory. As two elastic spheres contact, the adhesion and the external load cause an elastic deformation and a contact area forms between the two elastic bodies. According to the JKR theory, the contact radius  $a$  of the contact area and indentation depth are given by

$$a^3 = \frac{R}{K} \left[ P + 3\pi R W_{12} + \left( 6\pi R P W_{12} + (3\pi R W_{12})^2 \right)^{1/2} \right] \quad (\text{Eq. 6-8})$$

$$a_0^3 = 6W_{12}\pi R^2 / K \quad (\text{Eq. 6-9})$$

$$\delta = \frac{a^2}{R} \left[ 1 - \frac{2}{3} \left( \frac{a_0}{a} \right)^{3/2} \right] \quad (\text{Eq. 6-10})$$

(The meaning of the parameters is defined in *chapter 2*.)

The elastic modulus can be derived either by a two-point method which directly calculate the value from the known variables or by a two-parameter fitting of a force vs. indentation curve (i.e. by fitting  $K$  and  $W_{12}$ ). Our analysis has been focused on the approaching curves. We defined point "t" as an arbitrary point on the contact portion of the approaching curve.

The two-point JKR method provides an easy way to observe the elastic modulus over the indentation depth. Combining points "o" and "t", the modulus can be obtained by solving Equation 6-8 to Equation 6-10.  $\delta_o$ ,  $\delta_t$ ,  $P_o$  and  $P_t$  are known from the force plots. One then can obtain:

$$a_t^3 = \frac{R}{K} \left[ P_t + a_o^3 K / 2R + \left( P_t a_o^3 K / R + (a_o^3 K / 2R)^2 \right)^{1/2} \right] \quad (\text{Eq. 6-11})$$

Figure 6.5a shows the Young's modulus calculated with the two point JKR model for different indentation depths of treated and untreated PDMS films. It was found that Young's moduli were independent of indentation depth over the range of the first 80 nm.

Moreover, the values of thermodynamic *work of adhesion* ( $W_{12}$ ) and combined *elastic modulus* ( $K$ ) can also be obtained by fitting the recorded approach part of force distance curve with Equation 6-8. The obtained Young's moduli of PDMS are shown in Figure 6.5b. Similar results to the two-point JKR method were obtained.

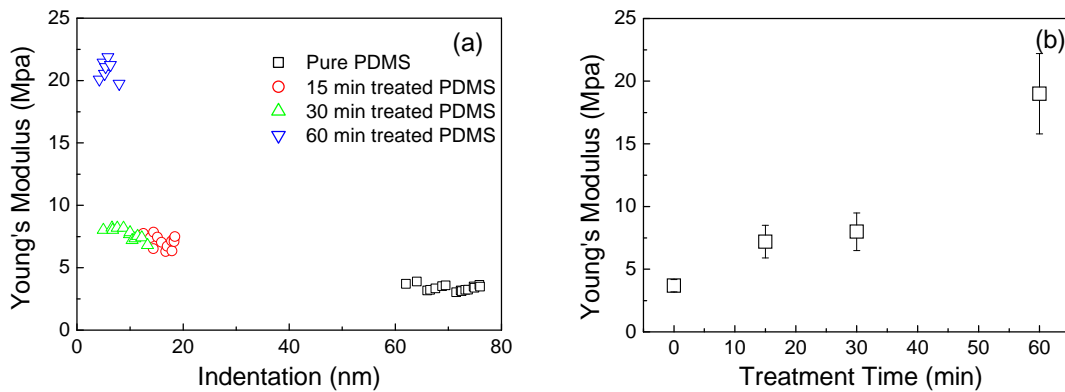


**Figure 6.5** a) Young's modulus calculated with two point JKR model on different indentation depth. b) Young's modulus calculated with the JKR fitting method.

The obtained moduli with the Hertz model are larger than those obtained from the JKR model. This is understandable as the Hertz model neglects adhesion effect. Thus, for the same contact area, the external load is overestimated. Hence, larger elastic modulus values are obtained.

For the above analysis, the AFM tip is treated as a sphere. The JKR theory for the elastic contact is valid only for contact radius values which are much smaller than the tip radius ( $R = 50$  nm). This is not true especially for soft untreated PDMS film, which can have larger contact radius values under a zero load. For instance, when the external force is zero, the adhesion-induced indentation of a tip into an untreated PDMS sample is about 83 nm, which is much larger than the 50 nm tip radius, see Figure 6.6a. For UV/ozone treated PDMS, especially for full oxidized PDMS, adhesion induced indentation of the tip is small (see Figure 6.6b).

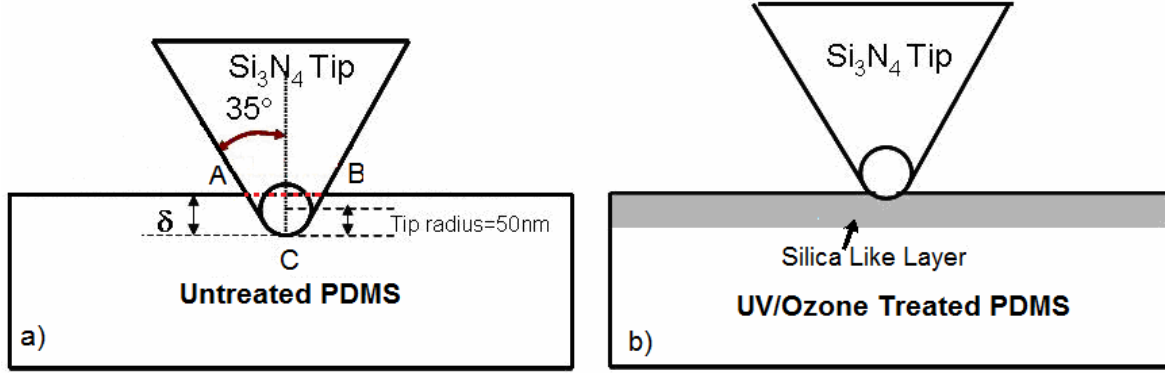


**Figure 6.6** Schematic representation (not to scale) of a tip indenting due to the adhesive interaction. a) untreated PDMS; b) UV/ozone treated PDMS.

Thus, the real tip shape must be considered when characterizing very soft samples. The  $\text{Si}_3\text{N}_4$  tip shape could be modeled by a hyperboloid.<sup>30</sup> The profile function for a hyperboloid shape tip is given by

$$f(x) = R \cot^2 \alpha \left( \left( \frac{ax}{R \cot \alpha} \right)^2 + 1 \right)^{1/2} - 1 \quad (\text{Eq. 6-12})$$

where  $R$  is the radius of the curvature of the tip apex,  $\alpha$  is the tip semivertical angle as shown in Figure 6.6a, and  $x$  is the vertical distance to the tip apex (at point C,  $x = 0$ ). To solve the dependence of the load and indentation on the contact radius, we applied Griffith's criterion<sup>32</sup> and the method proposed by Sneddon<sup>33</sup> and obtained

$$\delta = \frac{aA}{2R} \left[ \frac{\pi}{2} + \arcsin \left( \frac{(a/A)^2 - 1}{(a/A)^2 + 1} \right) \right] - \left( \frac{2a\pi(1-\nu^2)W_{12}}{E} \right)^{1/2} \quad (\text{Eq. 6-13})$$

$$P = \frac{2E}{1-\nu^2} \left[ \frac{A}{2R} \left[ aA + \frac{a^2 - A^2}{2} \left( \frac{\pi}{2} + \arcsin \frac{(a/A)^2 - 1}{(a/A)^2 + 1} \right) \right] - a \left( \frac{2a\pi(1-\nu^2)W_{12}}{E} \right)^{1/2} \right] \quad (\text{Eq. 6-14})$$

where  $R$  is the tip radius of curvature,  $A = R \cot(\alpha)$ ,  $\alpha$  is the tip semivertical angle,  $\nu$  is the Poisson ratio of the PDMS,  $\nu_{\text{PDMS}} = 0.5$ .  $E$  is the elastic modulus of PDMS,  $a$  is the contact radius, and  $W_{12}$  is the interfacial energy of the tip and the sample. The sample elasticity can be obtained based on Equation 6-13 and Equation 6-14 by combining point "o" and any other point at the contact portion of approaching curves "t".

At point "o", the external load  $P_o = 0$  and indentation  $\delta = \delta_o$ , so from Equation 6-13, one obtains

$$\frac{A}{2R} \left[ a_o A + \frac{a_o^2 - A^2}{2} \left( \frac{\pi}{2} + \arcsin \frac{(a_o/A)^2 - 1}{(a_o/A)^2 + 1} \right) \right] - a_o \left( \frac{2a_o \pi (1-\nu^2) W_{12}}{E} \right)^{1/2} = 0 \quad (\text{Eq. 6-15})$$

And Equation 6-14

$$\frac{a_o A}{2R} \left[ \frac{\pi}{2} + \arcsin \left( \frac{(a_o/A)^2 - 1}{(a_o/A)^2 + 1} \right) \right] - \left( \frac{2a_o \pi (1-\nu^2) W_{12}}{E} \right)^{1/2} - \delta_o = 0 \quad (\text{Eq. 6-16})$$

Thus, one can resolve  $a_o$  and  $(W_{12}/E)$  from Equation 6-15 and Equation 6-16.

At point  $t$ , the external load  $P = P_t$  and indentation  $\delta = \delta_t$  so from Eq 6-15 and 6-16, one obtains

$$\frac{a_t A}{2R} \left[ \frac{\pi}{2} + \arcsin \left( \frac{(a_t/A)^2 - 1}{(a_t/A)^2 + 1} \right) \right] - \left( \frac{2a_t \pi (1-\nu^2) W_{12}}{E} \right)^{1/2} - \delta_t = 0 \quad (\text{Eq. 6-17})$$

$$\frac{A}{2R} \left[ a_t A + \frac{a_t^2 - A^2}{2} \left( \frac{\pi}{2} + \arcsin \frac{(a_t/A)^2 - 1}{(a_t/A)^2 + 1} \right) \right] - a_t \left( \frac{2a_t \pi (1-\nu^2) W_{12}}{E} \right)^{1/2} - P_t = 0 \quad (\text{Eq. 6-18})$$

Thus, combine Equation 6-17 and Equation 6-18 and  $(W_{12}/E)$  which was solved at point o and one can solve  $a_t$  and E at point "t". This approach has been summarized in ref.<sup>30</sup>

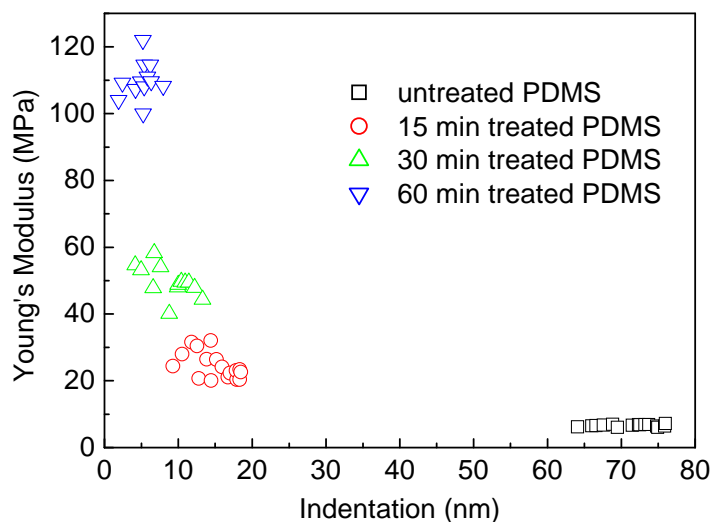


**Figure 6.7** Young's modulus calculated with hyperboloid shape tip model on different indentation depth. ( $\square$ ) pure PDMS; ( $\circ$ ) 15 min treated PDMS; ( $\triangle$ ) 30 min treated PDMS ( $\nabla$ ) 60 min treated PDMS.

Figure 6.7 gives the elasticity values calculated by assuming a hyperboloid tip shape for PDMS samples, showing how elasticity correlates with the treatment level. It shows that the value of the modulus increased with increasing treatment time. In addition, the magnitudes of the moduli obtained from the methods based on a hyperboloid tip shape are much higher than those based on a spherical shape. This can be understood as treating the tip as a sphere with a radius of the tip apex significantly overestimates the real contact radius when the indentation depth is large compared to the tip radius. Thus, underestimated modulus values are obtained. Furthermore, another issue should be noted as Hillborg and co-authors mentioned before.<sup>31</sup> As a thin silica-like layer was formed during the UV/ozone treatment, the obtained values do not reflect the true modulus of the silica-like layer but may rather be considered as the sum of a laminate structure, with a high modulus surface layer on top of the PDMS elastomer. The presented data indicate the formation of a surface structure, which differs significantly from that of silica which has an elastic modulus is around 70 GPa.<sup>34</sup>

When a sharp tip indents into a network, whether the continuum mechanics can hold is always a concern. As seen in Figure 6.6a, under an adhesion-induced stress, the cross-linked network A-B (80 nm) is stretched to A-C-B (150 nm), where  $\Delta l/l_0 = (150-80)/280 = 0.875$ . The stress-strain behavior in our experiment is still in the region where continuum mechanics

is expected to hold. PDMS samples can obey continuum mechanics under large deformation.<sup>35</sup>

It has been reported that when the indentation depth exceeds 10-25% of the thickness of the test film, effects of the supporting substrate underneath should be considered.<sup>36</sup> Since the thickness of the thin film samples used in this experiment is about 800 nm, the indentation depth should thus be less than 80 nm ~ 200 nm according to this criterion for the substrate to be observable. In our experiments, the maximum indentation depth was about 100 nm, i.e. effects of the substrate could be neglected.

### 6.3 Surface Young's modulus at a mesoscopic length scale

A custom built so-called adhesion-testing device (ATD) (or a JKR-type contact mechanical apparatus) has been introduced in *chapter 4*. The instrument simultaneously records the applied force, displacement, acquired contact area, real time, humidity and temperature. This measurement is a sensitive experimental method to obtain directly *work of adhesion* and *combined elastic modulus* from a fitting procedure. After exposed to UV/ozone, the surface energy for PDMS increased as a result of the introduction of polar groups in the surface as indicated by our previous study.<sup>37</sup> In the following section, we focus our attention on surface mechanical behavior of surface treated PDMS films on a micrometer length scale.

Conventionally, the ATD applies to study surface and interfacial properties between an elastomeric lens and a rigid substrate. The schematic plot of lens and film configuration is shown in Figure 6.8. Compared to hard substrate, a PDMS lens is easy to deform. In our experiment, a new stiff Si<sub>3</sub>N<sub>4</sub> indenter lens was also introduced and used against relatively thick (200 μm) PDMS films. This scheme is shown in Figure 6.8b. There are two advantages of using an Si<sub>3</sub>N<sub>4</sub> indenter. 1) It looks like an "unscaled" AFM tip-sample assembly: an enlarged AFM tip, Si<sub>3</sub>N<sub>4</sub> lens and tip-sample contact. Thus, length scale effects on surface modulus and adhesive force could be compared easily with continuum contact mechanics. 2) Combined modulus obtained from JKR fitting procedure could be simplified to the value of PDMS surface modulus without introducing a large error due to the high modulus of silicon nitride (220 GPa). However, there are still some disadvantages of using Si<sub>3</sub>N<sub>4</sub> lenses. The surface roughness of Si<sub>3</sub>N<sub>4</sub> lens is rather high ( $R_a = 3.4 \pm 0.5$  nm) compared to normal PDMS lenses ( $R_a = 1.0 \pm 0.3$  nm) which will affect interfacial energy and modulus values. Moreover,

$\text{Si}_3\text{N}_4$  is an opaque material and this would limit testing the experiments to transparent samples.

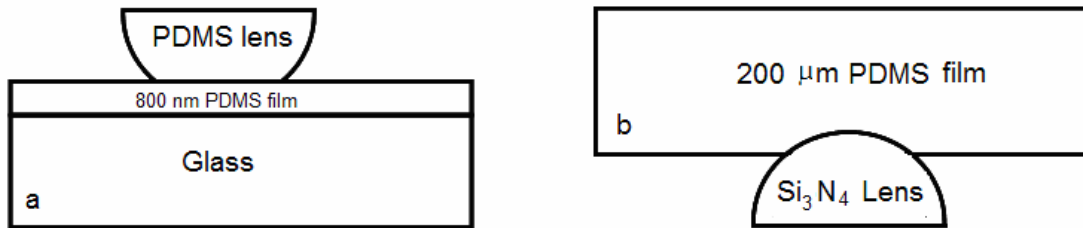


**Figure 6.8** Schematic plot (not to scale) of lens and substrate combination. a) PDMS lens b)  $\text{Si}_3\text{N}_4$  lens.

Figure 6.9 shows the Young's modulus of PDMS films obtained with two different lenses. A same trend was observed as before, i.e. the value of the Young's modulus increased with increasing sample treatment time. We attribute the increased modulus to the formation of a silica-like surface layer. In addition, with a PDMS lens, higher modulus values were obtained. This may be due to two reasons. 1) Against PDMS lens, 800 nm PDMS film coating on a glass substrate is a thin layer compared to the lens radius ( $a = 1.15$  mm). The modulus of PDMS lens is comparable with the substrate sample (treated PDMS) and rather low and during the loading procedure, a large deformation was formed. Conversely, the stiff  $\text{Si}_3\text{N}_4$  lens indented into the thick PDMS layer and its elastic deformation can be neglected. The maximum indentation depth is in this case around 3 micrometers (experimentally verified). This process thus yields information primarily about the sample bulk properties and hence the obtained values are smaller. 2) Increased roughness of  $\text{Si}_3\text{N}_4$  lens may affect the obtained modulus values.



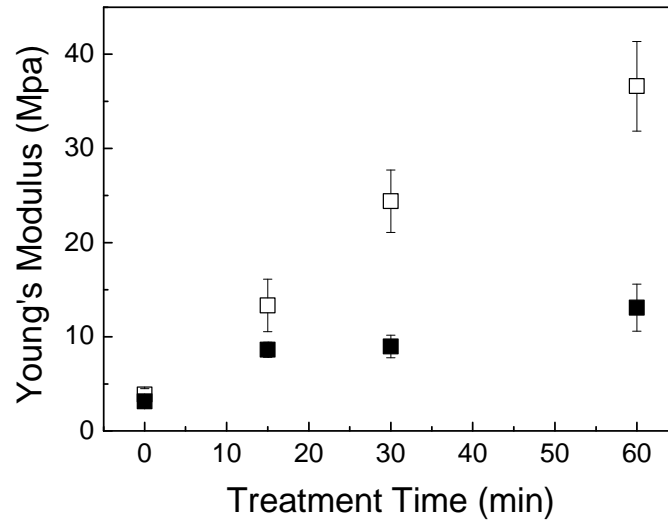


**Figure 6.9** Young's Modulus obtained with the ATD. (□) with PDMS lens (■) with Si<sub>3</sub>N<sub>4</sub> lens

## 6.4 Bulk modulus

Bulk mechanical properties are usually obtained by tensile tests and bending tests. When investigating the bulk mechanical response of materials on a macroscopic length scale, the strength of a material is often the primary concern. The strength of interest may be measured in terms of either the stress necessary to cause appreciable elastic or/and plastic deformation or the maximum stress that the material can withstand.

A tensile testing machine applies a known stress to a sample and measures the resulting strain. A load cell measures the force applied; an extensometer measures the extension of the sample. Analysis of force elongation or stress-strain curves can convey much information about the material being tested, and it can help in predicting its behaviour. For most tensile testing of materials, the initial portion of the curve is linear. In this linear region, the line obeys the relationship defined as "Hooke's Law" where the ratio of stress  $\sigma$  to strain  $\varepsilon$  is a constant. The slope of this linear region is called the *elastic modulus* or *Young's modulus*:

$$E = \sigma / \varepsilon \quad (\text{Eq. 6-19})$$

Figure 6.10 shows the stress-strain curve of treated and untreated PDMS samples. We could see that the Young modulus of untreated PDMS and 60 min treated PDMS are essentially identical. UV/ozone surface treatment does not affect the PDMS bulk mechanical properties.

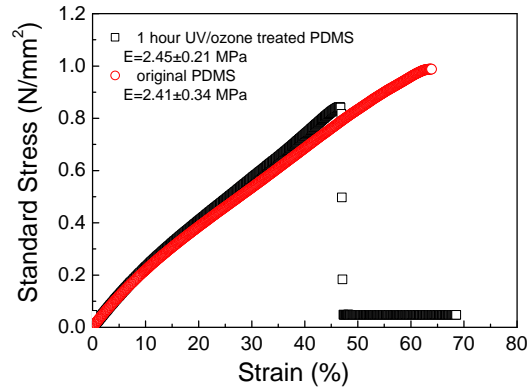


**Figure 6.10** The stress strain curves of untreated and 60 min treated PDMS.

## 6.5 Analysis of the length scale effects

The above sections discussed Young's modulus measurements with different techniques which obtained information of mechanical performance at different length scales. The summary of all results are shown in Table 6.1.

**Table 6.1** Young's elastic modulus obtained across different length scale.  $Si_3N_4$  tip and lens were used as indenter

Treatment Time (min)	Nano Indentation by AFM		Micro Indentation by ATD		Tensile Test (MPa)
	Young's Modulus (MPa)	Maximum Indentation Depth (nm)	Young's Modulus (MPa)	Maximum Indentation Depth ( $\mu m$ )	
0	$6.62 \pm 0.35$	86	$3.14 \pm 0.563$	3	$2.45 \pm 0.21$
15	$24.65 \pm 3.97$	19	$8.63 \pm 0.8$	2.8	-
30	$49.65 \pm 4.66$	13	$8.97 \pm 1.2$	2.5	-
60	$109.89 \pm 5.55$	9	$13.09 \pm 2.5$	2.4	$2.41 \pm 0.34$

Two trends can be observed in Table 6.1. First, with two surface mechanical techniques, AFM and ATD, the Young's modulus of UV/ozone treated PDMS films increased with increasing treatment time (treatment dose). This could be explained by assuming that a silica-like layer is formed after surface treatment, which changes surface properties.

Conversely, the bulk modulus was not significantly affected by the surface treatment. Second, the characteristic dimension has an influence on the obtained mechanical properties. With the same sample, comparing the AFM and ATD methods, the value of elastic modulus decreased with increasing the length scale (from nano- to micrometer). Surface moduli were enhanced compared to the sample bulk properties. Early experimental observations have indicated that the geometrical size of components has an influence on the mechanical properties of polymers, as well as in metals<sup>38</sup> and ceramics.<sup>39</sup> For example, Lam and Chong have shown that a length-scale parameter associated with strain gradient yielding is influenced by the cross-link distance in epoxies.<sup>40</sup> Experiments on both thermosets and thermoplastics have shown that the hardness evaluated from shallow indents is larger than that resulting from a deeper one. It was concluded that this was due to a higher plastic yield stress in the presence of larger strain gradients. In our experiments, elastic deformation of nanoindentation occurred in a small volume with a large strain gradient, where  $\Delta l/l_0 = (150-80)/280 = 0.875$  (shown in Figure 6.6a). For ATD measurements, the maximum contact radius is about  $90 \mu\text{m}$  and the maximum indentation depth is about  $3.3 \mu\text{m}$ , where  $\Delta l/l_0 \approx 0.5\%$ . Thus, nanoindentation yielded a larger modulus. In addition, adhesive forces play a significant role on a nanometer scale in indentation tests that will affect the real contact area during nanoindentation measurements. Furthermore, roughness of the indenter on a larger contact area will also affect the final results.

When micro and nanoindentations are produced upon polymeric surfaces, additional difficulties are caused by the complex viscoelastic-plastic response that is typical of such materials. Polymers have highly strain and strain rate-dependent properties and show substantially different behaviours when the indentations are produced under different contact conditions. This has been investigated by Loubet et al.<sup>41</sup> for certain ceramic systems and subsequently by Briscoe and Sebastian<sup>42</sup> and Ion<sup>43</sup> et al. in the context of organic polymers. In our experiments, we have focused on the loading or approaching part of data analysis. With a firm understanding of rate dependent effects on unloading part data analysis, a more quantitative evaluation of the indentation mechanics should be made in the future.

## 6.6 Conclusions

This *chapter* described a study on length scale dependencies of surface mechanical properties (surface Young's modulus) of UV/ozone treated PDMS films. AFM and ATD were

used to measure modulus from nano- to micro-meter indentation, which were compared with the bulk modulus. The similarities and differences of the models used, i.e. the Hertz and JKR models were shown along with a description of their limitations. The obtained Young's elastic modulus was varied with the size of the characteristic dimensions of the experiment. In addition, surface elastic modulus was observed to increase with increasing treatment time. Indentation testing for surface mechanical property studies is reasonably robust but the results must be interpreted with care and attention to the limitations of the analysis, limitations of the instrument and material behavior and length scale of the study.

## 6.7 Experimental section

**Tensile test.** The macroscopic mechanical properties of PDMS were evaluated with 5 mm × 5 mm × 100 mm polymer films. Tensile tests were carried out in duplicate at room temperature according to ASTM D882-91 specifications. A Zwick Z020 universal tensile tester equipped with a 500 N load cell was operated at a crosshead speed of 50 mm·min<sup>-1</sup>. The specimen deformation was derived from the grip-to-grip separation, which initially was 50 mm.

**Nanoindentation by AFM.** The nanoindentation tests were carried out using a NanoScope IV AFM (Veeco-Digital Instruments (DI), Santa Barbara, CA). Commercial silicon nitride tips (DI) were used as the indentors in the AFM indentation experiments. The cantilever specifications were as follows: length 350 μm, width 100 μm, thickness 13 μm, resonant frequency 50 kHz. The spring constants of the cantilevers ranged from 0.18 to 0.28 nN nm<sup>-1</sup>, as obtained by the thermal tuning method of Hutter and Bechhoefer.<sup>44</sup> The radius of Si<sub>3</sub>N<sub>4</sub> tip was verified by imaging suitable spherical gold colloid particles with a known diameter of 13 nm. From the measured width of the gold colloids, the effective radius of tip R, can be calculated based on geometrical considerations.<sup>45</sup>

AFM was operated in the force mode using a Z ramp rate of 1 Hz. Multiple force curves for each PDMS film were collected using the “point and shoot” mode of the AFM. Relative trigger thresholds were set to 20 nm. A series of automated indentations (up to 7 indents in 7 rows) were performed at different locations. Each individual force-distance curve was laterally separated by at least 1 μm from the preceding measurement to ensure that the observations are independent. All the nano indentation experiments were performed in aqueous environment.

An indent was made by forcing the tip into the surface until the required cantilever deflection was reached. For each indent, a plot of the cantilever deflection versus displacement in the  $Z$  direction was recorded. These graphs were transformed into force (nN) versus tip penetration curves. The applied load  $F$  was determined as  $F = \frac{k_c \Delta V}{S}$ , where  $k_c$  is the spring constant,  $\Delta V$  is the photodetector voltage change, and  $S$  is the cantilever sensitivity. The cantilever sensitivity was determined by taking force measurements using hard surfaces such as silicon. The algorithm outlined previously was used to extract Young's modulus from each dataset.

**PDMS film preparation.** All experiments were performed using an elastomeric PDMS kit manufactured by Dow Corning. Sylgard-184A (elastomer) and Sylgard-184B (curing agent) were used without modification and mixed at a mass ratio of 10:1. PDMS film preparation and UV/ozone treatment have been described in *chapter 5*. Samples with these different thickness values were used. PDMS films with thickness of 5 mm were applied in tensile tests. PDMS films with thicknesses of 200  $\mu\text{m}$  and 800 nm were used in ATD measurements. Finally, PDMS films with thicknesses of 800 nm were utilized in AFM nanoindentation experiments.

## References

- [1] Syed Asif, S. A.; Colton, R. J.; Wahl, K. J., In *ACS symposium Series*, Frommer, J.; Overney, R., Eds. Oxford University Press: Washington, DC, 2001; Vol. 781, p 198.
- [2] Jeong, K.-H.; Liu, G. L.; Chronis, N.; Lee, L. P., *Opt. Express* **2004**, *12*, 2494.
- [3] Pelrine, R.; Kornbluh, R.; Pei, Q.; Joseph, J., *Science* **2000**, *287*, 836.
- [4] Binnig, G.; Quate, C. F.; Gerber, C., *Phys. Rev. Lett.* **1986**, *12*, 930.
- [5] Sarid, D., *Scanning Force Microscopy*. Oxford University Press: New York, 1991.
- [6] Tsukruk, V. V.; Gorbunov, V. V.; Huang, Z.; Chizhik, S. A., *Polym. Int.* **2000**, *49*, 441.
- [7] Tranchida, D.; Piccarolo, S., *Polymer* **2005**, *46*, 4032.
- [8] Domke, J.; Radmacher, M., *Langmuir* **1998**, *14*, 3320.
- [9] Vanlandingham, M. R.; Villarrubia, J. S.; Guthrie, W. F.; Meyers, G. F., *Macromol. Symp.* **2001**, *167*, 15.
- [10] Vanlandingham, M. R.; McKnight, S. H.; Palmese, G. R.; Elings, J. R.; Huang, X.; Bogetti, T. A.; Eduljee, R. F.; Gillespie, J. W., Jr., *J. Adhesion* **1997**, *64*, 31.
- [11] Briscoe, B. J.; Fiori, L.; Pelillo, E., *J. Phys. D* **1998**, *31*, 2395.
- [12] Reynaud, C.; Sommer, F.; Quet, C.; El Bounia, M.; Duc, T. M., *Surf. Interface Anal.* **2000**, *30*, 185.
- [13] Chizhik, S. A.; Huang, Z.; Gorbunov, V. V.; Myshkin, N. K.; Tsukruk, V. V., *Langmuir* **1998**, *14*, 2606.
- [14] Du, B. Y.; Tsui, O. K. C.; Zhang, Q. L.; He, T. B., *Langmuir* **2001**, *17*, 3286.
- [15] Raghavan, D.; Gu, X.; Nguyen, T.; Vanlandingham, M. R.; Karim, A., *Macromolecules* **2000**, *33*, 2573.
- [16] Micro/Nanotribology and Its Applications. In *NATO ASI Series*, Bhushan, B., Ed. Kluwer Academic Publishers: Dordrecht, 1997.
- [17] Du, B. Y.; Liu, J.; Zhang, Q. L.; He, T., *Polymer* **2001**, *42*, 5901.
- [18] Du, B.; Zhang, J.; Zhang, Q.; Yan, D.; He, T.; Tsui, O. K. C., *Macromolecules* **2000**, *33*, 7521.
- [19] Drechsler, D.; Karbach, A.; Fuchs, H., *Appl. Phys. A* **1998**, *66*, S825.
- [20] Tanaka, K.; Takahara, A.; Kajiyama, T., *Macromolecules* **1998**, *31*, 5150.
- [21] Kaliappan, S. K.; Cappella, B., *Polymer* **2005**, *46*, 11416.
- [22] Overney, R.; Tsukruk, V. V., Scanning Probe Microscopy of Polymers. In *ACS symposium Series*, Ratner, B.; Tsukruk, V. V., Eds. American Chemical Society: Washington DC., 1998; Vol. 694, p 2.
- [23] Hues, S. M.; Colton, R. J.; Meyer, E.; Guntherodt, H.-J., *MRS Bull.* **1993**, *18*, 41.
- [24] Hues, S. M.; Draper, C. F.; Lee, K. P.; Colton, R. J., *Rev. Sci. Instrum.* **1994**, *65*, 1561.
- [25] Johnson, K. L.; Kendall, K.; Roberts, A. D., *Proc. R. Soc. London* **1971**, *A324*, 301.
- [26] Akhremitchev, B. B.; Walker, G. C., *Langmuir* **1999**, *15*, 5630.
- [27] Barthel, E.; Lin, X. Y.; Loubet, J. L., *J. Colloid Interface Sci.* **1996**, *177*, 401.
- [28] Lantz, M.; Shea, S. O.; Welland, M., *Phys. Rev. B* **1997**, *55*, 10776.
- [29] Giri, M.; Bousfield, D. B.; Unertl, W. N., **2001**, *17*, 2973.
- [30] Sun, Y. J.; Akhremitchev, B.; Walker, G. C., *Langmuir* **2004**, *20*, 5837.
- [31] Hillborg, H.; Tomczak, N.; Olah, A.; Schonherr, H.; Vancso, G. J., *Langmuir* **2004**, *20*, 785.
- [32] Swedlow, J. L., *Int. J. Fract. Mech.* **1975**, *1*, 210.
- [33] Sneddon, I. N., *Int. J. Eng. Sci.* **1965**, *3*, 47.
- [34] Kayne, G. W. C.; Laby, T. H., *Tables of Physical and Chemical Constants*. Longman: Essex, 1985.
- [35] Treloar, L. R. G., *The Physics of Rubber Elasticity*. Clarendon Press: Oxford, 1975.
- [36] Vanlandingham, M. R., *Microsc. Today* **1997**, *97-10*, 12.
- [37] Olah, A.; Hillborg, H.; Vancso, G. J., *Appl. Surf. Sci.* **2005**, *239*, 410.
- [38] Fleck, N. A.; Muller, G. M.; Ashby, M. F.; Hutchinson, J. W., *Acta Metall. Mater.* **1994**, *42*, 475.
- [39] Xu, Z.-H.; Rowcliffe, D., *Surf. Coat Tech.* **2002**, *161*, 44.
- [40] Lam, D. C. C.; Chong, A. C. M., *J. Mater. Sci.* **2001**, *16*, 558.
- [41] Loubet, J. L.; Georges, J. M.; Marchesini, O.; Meille, G., *J. Tribol.* **1984**, *106*, 43.
- [42] Briscoe, B. J.; Sebastian, K. S., *Proc. R. Soc. A* **1996**, *452*, 439.

- [43] Ion, R. H.; Pollock, H. M.; Roques-Carnes, C., *J. Mater. Sci.* **1990**, 25, 1444.
- [44] Hutter, J. L.; Bechhoefer, J., *Rev. Sci. Instrum.* **1993**, 64, 1868.
- [45] Engel, A.; Schoenenberger, C. A.; Muller, D. J., *Curr. Opin. Struct. Biol.* **1997**, 7, 279.

# Chapter 7

## "Smart" organometallic polymer brushes: Switching friction by electrochemical redox stimuli\*\*

In this *chapter* quantitative friction and adherence (adhesion) measurements between  $\text{Si}_3\text{N}_4$  tip and reversibly oxidized and reduced poly(ferrocenyldimethylsilane) (PFS) layers grafted to Au are reported. The experiments were carried out by an electrochemical atomic force microscopy (ECAFM). Thiol-end group containing PFS chains were used to obtain PFS monolayers immobilized on the substrate. AFM cantilever torsional calibration was performed by direct calibration method (the wedge calibration method) using a new calibration standard (originally introduced in our group). Corrections for fluid refraction have been introduced in the calibration protocol to obtain quantitative friction data in aqueous electrolyte. PFS is a redox active polymer featuring a main chain with ferrocene units. Chain stiffness, segment length and their effective change of this polymer were controlled in situ by electrochemistry. Measurements of interfacial friction as a function of applied load on the nanoscale revealed a significant change in friction between the oxidized and reduced PFS layers. The average friction coefficient (0.47) and adherence (0.61 nN) between oxidized PFS and  $\text{Si}_3\text{N}_4$  tip was found to be larger than that of neutral reduced PFS (0.3, and 0.03 nN, respectively). Issues related to the interpretation of observed friction and adherence changes were discussed. In particular, conformational changes of polymer chains and ionic interactions in the presence of  $\text{ClO}_4^-$  anions were considered. These measurements demonstrated an opportunity for this "smart" polymer for a reversible control of the conformation, chain stiffness and electrical charge of polymer chains to regularly alter interfacial friction and adhesion properties of surfaces for physico-chemical, or biological applications such as electrically controlled lubrication or grafting in bio-micro-electro-mechanical system (bio-MEMS).

---

\*\* Parts of this *chapter* have been published in the following article: Tocha, E. A.; Song, J.; Schönherr, H.; Vancso, G. J. *Langmuir* **2006**, 23, 7078 (lateral force spring calibration constant). Other parts (stimulus responsive behaviour) will be submitted for publication.



## 7.1 Introduction

Stimuli-responsive polymer interfaces, which switch their physical and chemical properties in response to changes in the external environment, offer great possibilities in many technologically important areas such as drug delivery,<sup>1, 2</sup> bioadhesion mediators,<sup>3-5</sup> surface patterning,<sup>6</sup> motors and actuators,<sup>7, 8</sup> microfluidic devices,<sup>9</sup> affinity separation and binding,<sup>10, 11</sup> etc. An ambitious challenge in material science is to design of smart surfaces with these dynamically controllable properties exhibiting fast response and local addressability on sub-micrometer length scales using macromolecules.<sup>12</sup> The classical framework is focused on triggering conformational and/or chemical changes in macromolecular layer grafted to, or physically attached to substrates upon environmental variations. These stimuli induced transformations are commonly a result of changes in temperature,<sup>13, 14</sup> electrochemical potential,<sup>15</sup> pH,<sup>16</sup> solvent,<sup>17</sup> or irradiation.<sup>18-20</sup> Redox processes represent an effective and fast way to control the interfacial properties such as surface charge density,<sup>21</sup> ion or molecule permeability,<sup>22</sup> electronic properties,<sup>23, 24</sup> hydration<sup>25</sup> and adhesion.<sup>26</sup> Redox-responsive poly(ferrocenyldimethylsilanes) (PFS) have attracted considerably attention because they exhibit interesting reversibly electrochemical oxidation/reduction properties owing to their unique backbone structure.<sup>27</sup> These organometallic polymers which consist of alternating ferrocene and silane units in the main chain combine the processing characteristics of organic polymers with the properties common for transition metals. It has been observed by cyclic voltammetry (CV) that PFS exhibits two reversible redox events resulting from oxidation of alternating ferrocene units.<sup>28-30</sup> In our group's previous study, immobilized PFS monolayers on gold surfaces were obtained by a self-assembly technique following the attachment of a thiol-end function to the high molar mass polymer chain. It has been shown that the electrochemical oxidation/reduction of the PFS coil manifests itself in morphology and volume changes due to the presence of electrostatic repulsion between the charged electroactive centers as well as due to changes of chain flexibility and effective segment length.<sup>21, 31, 32</sup> Moreover, it has been demonstrated by AFM based single molecule force spectroscopy that external electrochemical stimuli can be used to induce reversible elasticity changes of individual PFS chains attached to surfaces, and generate mechanical work as a model system of an electrochemically powered molecular motor.<sup>33, 34</sup> Although surface immobilized PFS monolayer constitute an interesting electrochemically responsive nanosystem, interfacial friction and adherence of PFS layer in response to electrochemical stimuli need to be demonstrated.

As devices shrink in size, the increased surface to volume ratio necessitates a full understanding of the surface forces occurring at the interface when materials are brought together, separated, or moved with respect to one another. Surface forces play a central role in many technological problems, including contact formation, wear, fracture, lubrication, nanoindentation, and machining on micro or nanoscale.<sup>35-39</sup> Research in the fields of hard coatings, vapor phase lubrication, self-assembled monolayers and polymeric coatings has begun to address these needs.<sup>40-42</sup> The surface force apparatus (SFA),<sup>43, 44</sup> scanning tunneling microscopy (STM),<sup>45</sup> atomic force microscopy (AFM),<sup>46</sup> friction force microscopy (FFM)<sup>47</sup> as well as quartz crystal microbalance (QCM)<sup>48, 49</sup> techniques are widely used in corresponding studies. Today, surface imaging of polymer thin films with chemical specificity by FFM or chemical force microscopy (CFM)<sup>50-52</sup> measurements has received increasing attention. Changes in ionic strength, pH, or solvent properties can lead to markedly different surface properties, such as surface energy, hydration, charge distribution.<sup>53, 54</sup> However, the great majority of these reports focused on polymer lubrication effects and contact formation.<sup>54-57</sup> Although studies of reversible friction control is much less developed, scientists and engineers working on small-scale mechanical devices (MEM or NEM) may find the idea of friction control from molecular to macroscopic length scales attractive. In this *chapter*, the switchable interfacial friction and adhesion between immobilized PFS and Si<sub>3</sub>N<sub>4</sub> tips have been investigated using in-situ electrochemical lateral force microscopy (ECLFM). Imaging with high spatial resolution and friction mapping of PFS grafted surface was compared between the oxidized, charged polymer and its reduced neutral state. Quantitatively, friction forces were calculated using a revised universal lateral force calibration platform. Force volume images were analyzed by custom-built LabVIEW<sup>TM</sup> software and adherence histograms were obtained. Changes in polymer chain conformation, counter ion adsorption, differences in tribological and adhesive properties of electrochemical oxidized/reduced polymers were sought. The fast switching and good reversibility of interfacial friction and adherence of the PFS layers showed that this interface might have applications in micro/nano fluidic systems. Furthermore, it was further tempting to consider the relevance of this finding for other systems, particularly in nature, where charged polymers at biological surfaces are ubiquitous. This interface illustrated that such polymer-based smart interfaces may have great potential in biomimetics such as biological actuators, controlled permeation membranes, separation, immobilized biocatalysts, interfacial engineering, responsive filters, and so on.

## **7.2 Tuning of tribological behavior of stimulus responsive PFS by electrochemistry and its study using in-situ electrochemical lateral force microscopy**

Electrochemical atomic force microscopy (ECAFM) has been used to observe, in situ, the topography and adhesive force changes that occur to redox species bound to gold electrode surfaces.<sup>58</sup> However, nanotribology studied by AFM related to the electrochemical reactions at an electroactive polymer thin film has not been reported. Electrochemical lateral force microscopy (ECLFM) provides valuable insights into the thermodynamics of redox processes, the kinetics of electron transfer reactions, and adsorption processes by a potentiostat control. Further, the acquisition of interfacial friction data with high spatial resolution establishes the role which various phenomena that occur between interacting surfaces, such as surface energy, structural rearrangement, and adhesion have upon electrochemical reaction kinetics. A schematic of the ECAFM set up used in this study is shown in Figure 7.1.

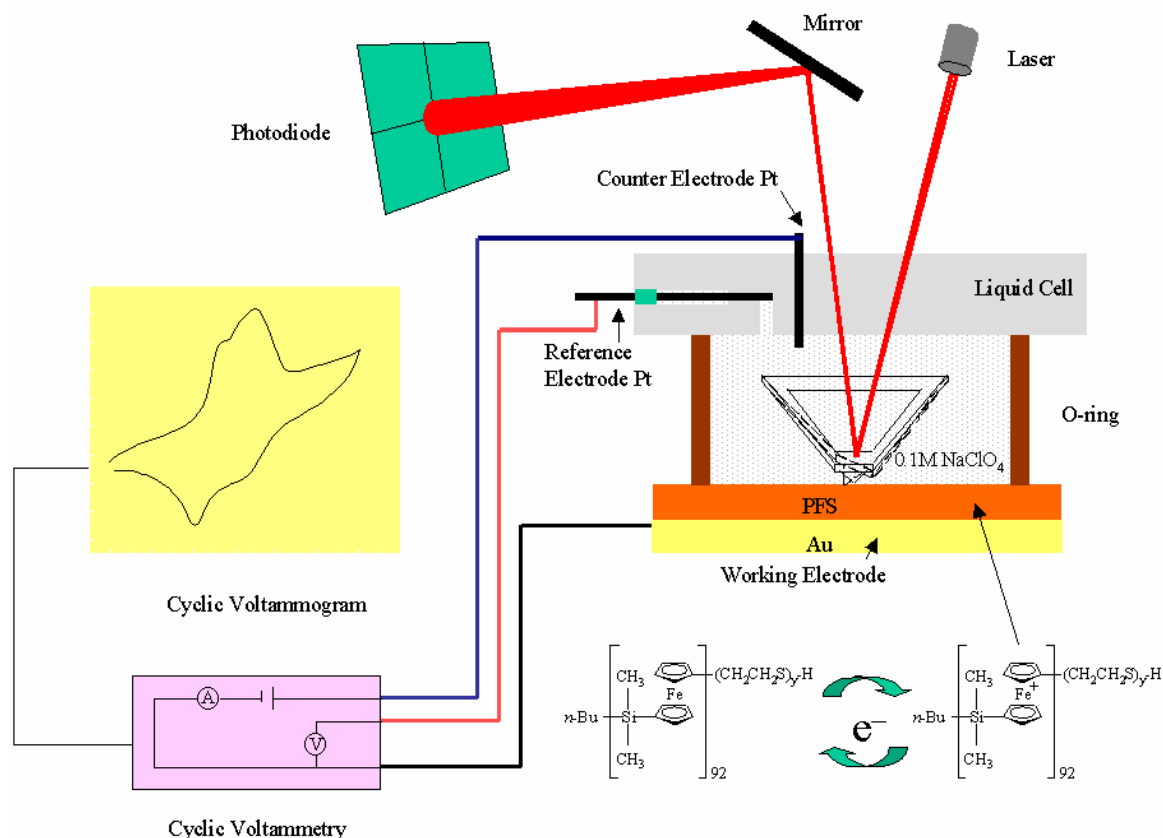


**Figure 7.1** Schematic illustration of in situ ECAFM measurements on end functionalized PFS attached to Au surfaces.

The AFM used in the lateral force microscopy mode was connected with an external potentiostat which apply potential to the sample. The gold substrate with immobilized PFS layer plays the role of the working electrode. The reference (Pt wire) and counter (Pt wire) electrodes can be mounted through the holes of the special electrochemical liquid cell. 0.1M NaClO<sub>4</sub> served as electrolyte which was injected or drained through the inlet or the outlet of the liquid cell. In the ECAFM experiment, the sample surface is scanned with a Si<sub>3</sub>N<sub>4</sub> tip at an angle of 90° with respect to the long axis of the cantilever. The torsion of the cantilever is detected by the four quadrant photodiode detector. During the measurement, the friction image and morphological image are displayed together, recorded simultaneously with the voltammogram (current versus potential). The friction image can be recorded at a constant potential or a sweep potential. Thus, electrochemically induced friction changes can be monitored in situ at the electrode/electrolyte interface.

### 7.2.1 Calibration of AFM friction force signals in liquid media

Measurements of lateral (friction) forces have taken a central role both in fundamental studies of (nano)tribology<sup>59-66</sup> as well as in compositional mapping of patterned or multiphase organized thin film assemblies.<sup>67-69</sup> The *quantitative* determination of nanotribological properties in liquid environment is also essential for the understanding, among others, of various biological systems, as well as for several applications such as MEMS valves, micropumps, and micromotors.<sup>70-72</sup>

Despite its obvious importance, the reliable calibration of friction forces in AFM remained a difficult task until recently. The frequently applied two-step calibration methods<sup>73-75</sup> based on the determination of the cantilever lateral spring constant  $k_L$  and the lateral photodiode sensitivity  $S_L$  may be highly inaccurate, as shown recently,<sup>76</sup> due to poorly defined cantilever material properties, the imprecise determination of the cantilever thickness and the inaccuracy in estimating  $S_L$ . These limitations are overcome in the direct calibration procedure called wedge calibration method, which was introduced by Ogletree et al.<sup>77</sup> and further improved by Varenberg et al.<sup>78</sup> In this method, the friction signal is recorded as a function of the applied load on a calibration sample with two well-defined slopes. The friction force calibration factor is determined from the lateral force relations measured on differently sloped surfaces, thus enabling one to convert the experimentally obtained photodiode response in Volts, as a measure of the torsion moment, into the corresponding friction force expressed in Newtons. The calibration of all types of probes cantilevers independent of cantilever geometry and tip radius can be performed with an error of only *ca.* 5% using the universal calibration specimen recently introduced by our group.<sup>76</sup>

In spite of this success, this method suffers similar to the reference techniques, i.e. the two-step, and direct procedures, from the fact that calibration factors obtained in ambient air or defined gas atmospheres cannot be a priori utilized in AFM experiments carried out in liquid media for most commercial AFM instruments. As considered here explicitly for the first time, in such cases, refraction of the laser light (used in the beam deflection detection) leads to systematic errors. As shown in this section, the altered laser light path, as a result of refraction, can be accounted for using a simple model and a correction factor can be introduced that relates the photodiode response for measurements in air and in a given liquid (with a given refractive index). This correction can be applied for all three classes of calibration procedures. Thus, the systematic error described can be conveniently eliminated.

The direct application of the friction force calibration factor (or  $S_L$ ) determined in air for the friction force calibration of experimental data obtained in liquids results in an overestimate of the friction forces. The path of the laser beam from the cantilever apex to the photodiode for experiments in liquid is different compared to the situation in air due to refraction caused by the different refractive indices of the different media traversed by the light (Figure 7.2). Consequently, this will change the photodiode response to the bending and twist the angles of the cantilever that correspond to the movement of the laser spot on the photodiode in vertical and horizontal direction, respectively. In conventional contact mode AFM height imaging and in force-volume data acquisition, this effect can be corrected for not too soft samples in situ by determining the photodiode sensitivity  $S_N$  in f-d curves.  $S_N$  is obtained by estimating the slope of the linear compliance region, where the tip and the sample are in hard wall contact.

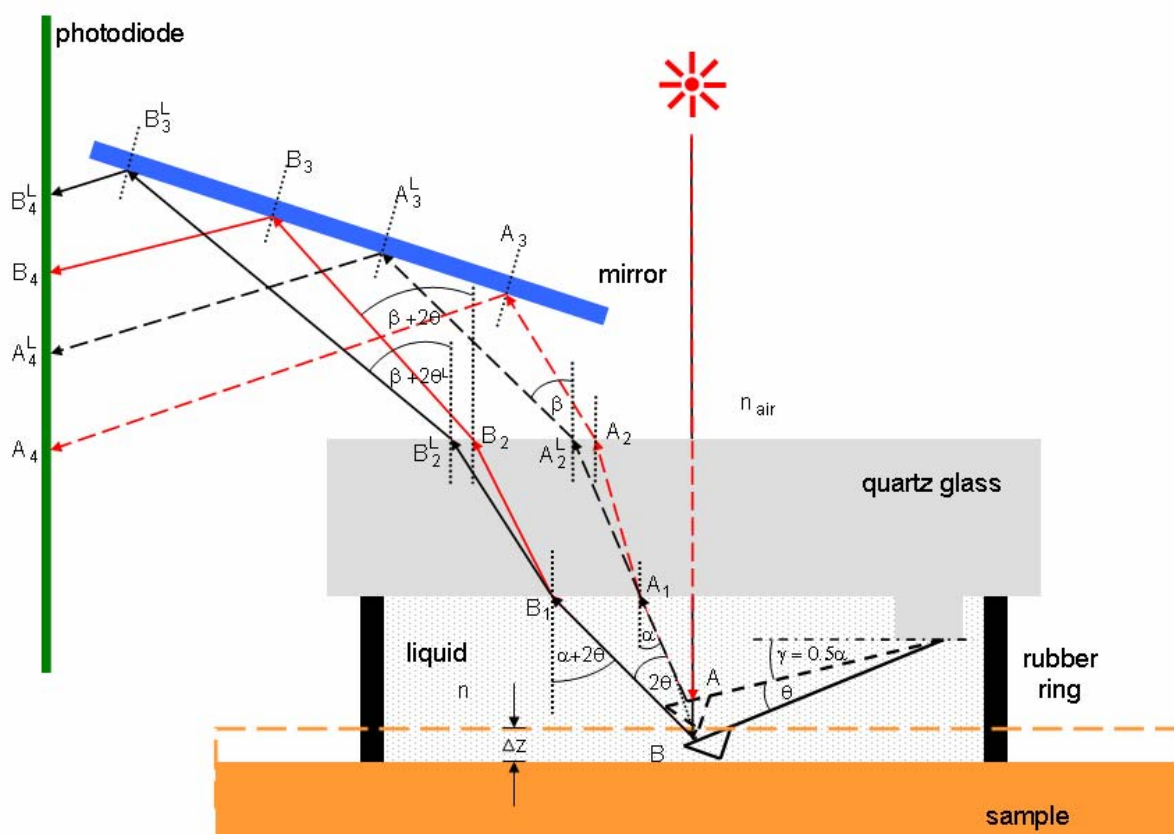


**Figure 7.2** Simplified side-view schematic (not to scale) of an AFM experiment carried out using a liquid cell: The light paths for two cantilever deflections are indicated for media with different refractive indices (normal bending signals: black line represents light path in liquid and red line represents light path in air). We denote the cantilever bending angle  $\theta$  and the angle between cantilever and holder  $\gamma = 1/2\alpha$ .  $n$ ,  $n_{\text{air}}$  and  $\alpha$ ,  $\beta$  stand for the refractive indices of the liquid and air, and the entry / exit angles for light propagating through the liquid-quartz and quartz-air interfaces, respectively.

However, for LFM the corresponding sensitivity  $S_L$  cannot be easily obtained in situ. The precise and reliable calibration methods available have not been used in liquid even though there are no fundamental reasons not to use them in conjunction with a liquid cell. Instead the set-up is usually calibrated in air and the calibration factors are used for the liquid cell experiments. As shown below, depending on the liquid medium (refractive indices may range from 1.25 to 1.74 for perfluorohexane and diiodomethane, respectively; water has a refractive index of 1.36), the determined friction coefficients are overestimated by a systematic error in range of 25% to 74% (36% for water).<sup>79</sup>

### ***Determination of the correction factor***

The correction factor taking into account the refraction effect mentioned above can be derived based on an analysis of the altered laser light path. The optical paths of laser light reflected off the cantilever are schematically shown in Figure 7.1 for measurements in air and in a liquid. In most of the commercial AFM set-ups the laser beam enters the liquid cell approximately vertically (at an angle of  $\sim 90^\circ$  with respect to the liquid cell surface) and the optical path will thus not be influenced by different refractive indices of the different media. The path of the reflected beam, however, is affected by the refractive index of the different media. We denote the path travelled by the light before and after bending the cantilever by an angle  $\theta$  with  $AA_1A_2A_3A_4$  and  $BB_1B_2B_3B_4$ , respectively; the situation for the light traversing the liquid-filled cell we denote with superscript L (compare Figure 7.2). The lateral shifts of the optical paths due to refraction at the medium-quartz and quartz-air surface for air and in liquid are small and can hence be faithfully neglected. For a comparison: the thickness of the liquid cell is  $\sim 65$  mm compared to the typical length of the optical path of 320 mm.

The normal photodiode sensitivity  $S_N$  in nm/V is inversely proportional to distance between the two laser light reflections on the photodiode in air  $A_4B_4$ , which can be expressed as a function of the cantilever bending angle  $\theta$ :

$$A_4B_4 = 2\theta (AA_1 + A_1A_2 + A_2A_3 + A_3A_4) = 2\theta AA_4 \quad (\text{Eq. 7-1})$$

In addition, we can approximate the distance between the two reflected paths in liquid  $A_4^L B_4^L$  using the following relation:

$$A_4^L B_4^L = 2\theta^L (AA_1 + A_1A_2^L + A_2^L A_3^L + A_3^L A_4^L) = 2\theta^L AA_4^L \quad (\text{Eq. 7-2})$$

The different refractive indices of air and the liquid medium will result in refraction, as indicated in Figure 7.2. Instead of leaving the liquid cell under an angle  $\alpha + 2\theta$ , the light leaves under an increased angle  $\beta + 2\theta^L$ . This effect can be described using Snell's law, as shown in Equation 7-3:

$$\frac{n_{\text{air}}}{n} = \frac{\sin\alpha}{\sin\beta} = \frac{\sin(\alpha + 2\theta)}{\sin(\beta + 2\theta^L)} \quad (\text{Eq. 7-3})$$

where  $n$ ,  $n_{\text{air}}$  and  $\alpha$ ,  $\beta$  denote the refractive indices of the liquid and air, and the entry / exit angles for light propagating through the liquid-quartz and quartz air interfaces, respectively. As mentioned above, the refraction due to the quartz cell can be faithfully neglected owing to the very short path length.

Different mirror positions that are required to reflect the light towards the photodiode result in equal lengths of the laser path for measurements in air and in liquid:

$$AA_4 \cong AA_4^L \quad (\text{Eq. 7-4})$$

This equality is quantitatively captured in a simple model shown below. The corresponding optical path of the laser light for normal bending of the cantilever in air and in liquids is sketched in Figure 7.3 approximately to scale.



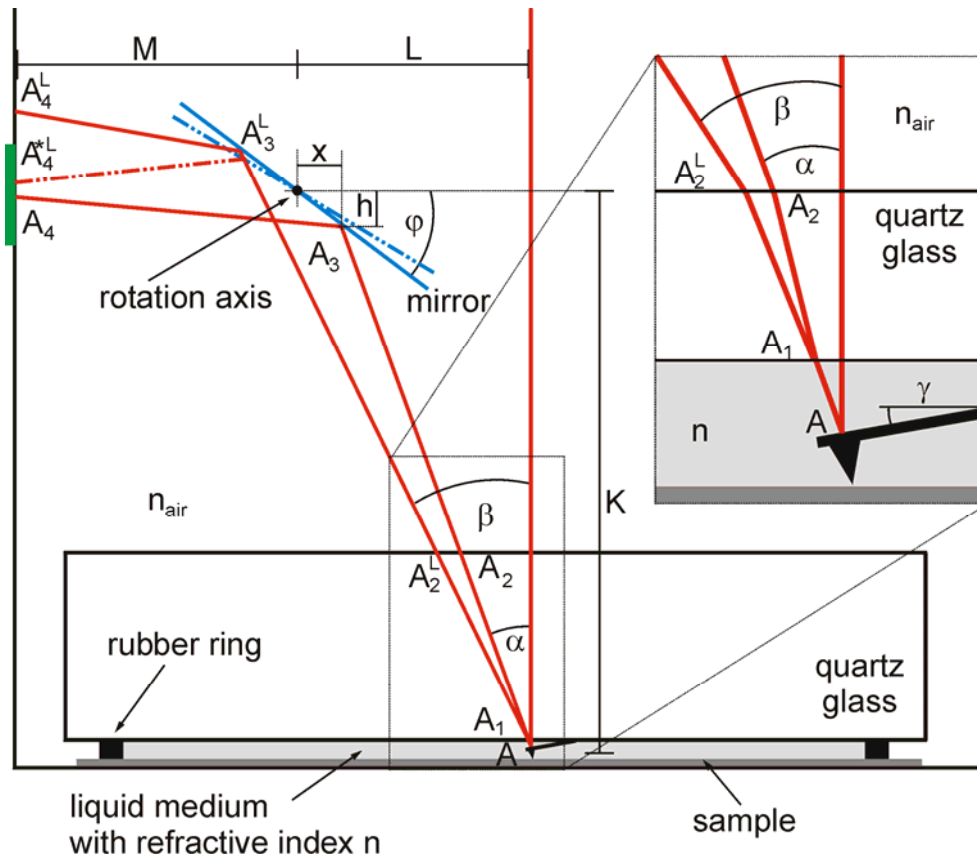


**Figure 7.3** Schematic (approximately to scale) of an AFM experiment carried out using a liquid cell in scale. The light paths for normal cantilever deflection are indicated for media with different refractive indices.  $n$ ,  $n_{\text{air}}$  and  $\alpha$ ,  $\beta$  denote the refractive indices of the liquid and air, and the entry / exit angles for light propagating through the liquid-quartz and quartz-air interfaces, respectively. We denote the mirror rotation angle as  $\varphi$ , the vertical distance between cantilever apex and the mirror rotation axis as  $K$ , the horizontal distance between photodiode and the mirror rotation axis as  $M$ , the horizontal distance between incident beam and the mirror rotation axis as  $L$ , and the angle between cantilever and holder  $\gamma = 1/2\alpha$ .  $x$  and  $h$  stands for the horizontal and vertical distance of reflected laser beam on the mirror relative to the rotation axis.

The precise path length  $AA_4$  and  $AA_4^{*L}$  can be determined from dimensions of the optical head as a function of mirror rotation angle  $\varphi$ . The superscript  $*$  indicates the laser path after adjusting the mirror. Further we denote the vertical distance between cantilever apex and the mirror rotation axis as  $K$ , the horizontal distance between photodiode and the mirror rotation axis as  $M$ , the horizontal distance between incident beam and the mirror rotation axis as  $L$ , and the angle between cantilever and holder  $\gamma = 1/2\alpha$ .

The horizontal and vertical distance of reflected laser beam on the mirror relative to the rotation axis  $x$  can be approximated in air and in liquid, respectively, as:

$$x \cong L - Ktg\alpha \quad (\text{Eq. 7-5})$$

and

$$h(\varphi) \cong xtg\varphi = (L - Ktg\alpha)tg\varphi \quad (\text{Eq. 7-6})$$

Similarly we can write:

$$x^L \cong L - Ktg\beta \quad (\text{Eq. 7-7})$$

and

$$h^L(\varphi) \cong x^Ltg\varphi = (L - Ktg\beta)tg\varphi \quad (\text{Eq. 7-8})$$

where  $\beta$  is determined by Equation 7-3.

Since the length of  $AA_2 \cong AA_2^L$  is significantly smaller than  $A_2^L A_4^L$ , and since  $\beta$  can be obtained from Equation 7-3, we can describe the path length in air and in liquid as:

$$AA_4(\varphi) = \frac{K-h}{\cos\alpha} + \frac{M+x}{\sin(\alpha+2\varphi)} \quad (\text{Eq. 7-9})$$

$$AA_4^{*L}(\varphi) = \frac{K-h^L}{\cos\beta} + \frac{M+x^L}{\sin(\beta+2\varphi)} \quad (\text{Eq. 7-10})$$

The determined path length in air and liquid are identical to within an error of 1 %, which is negligible (Table 7.1).

**Table 7.1** Comparison of laser path length for air and liquid measurements, calculated for media with different refractive indexes:

	n	$\varphi$	$AA_4$ [mm]	$AA_4^{*L}$ [mm]
air	1.00	37	31.4	-
water	1.36	31	-	31.8
ethanol	1.34	31	-	31.8
iodomethane	1.53	28	-	31.8
diiodomethane	1.74	25	-	31.8

Calculated with following values:  $K = 20$  mm,  $M = 10$  mm,  $L = 8.5$  mm, and  $\alpha = 16$  deg.

From Equations 7-1 to 7-3, the relative change of the vertical photodiode response ( $A_4^L B_4^L / A_4 B_4$ ) between liquid and air can be derived:

$$\frac{A_4^L B_4^L}{A_4 B_4} = \frac{S_N}{S_N^L} = \frac{n}{n_{\text{air}}} \frac{\cos \alpha}{\sqrt{1 - \left(\frac{n}{n_{\text{air}}}\right)^2 \sin^2 \alpha}} \quad (\text{Eq. 7-11})$$

where  $\alpha$  is twice the value of the constant inclination angle  $\gamma$  between cantilever and cantilever holder.

The optical paths of laser light reflected off the cantilever as a means to determine the lateral deflection of the cantilever are schematically shown in Figure 7.4 for measurements in air and in a liquid.

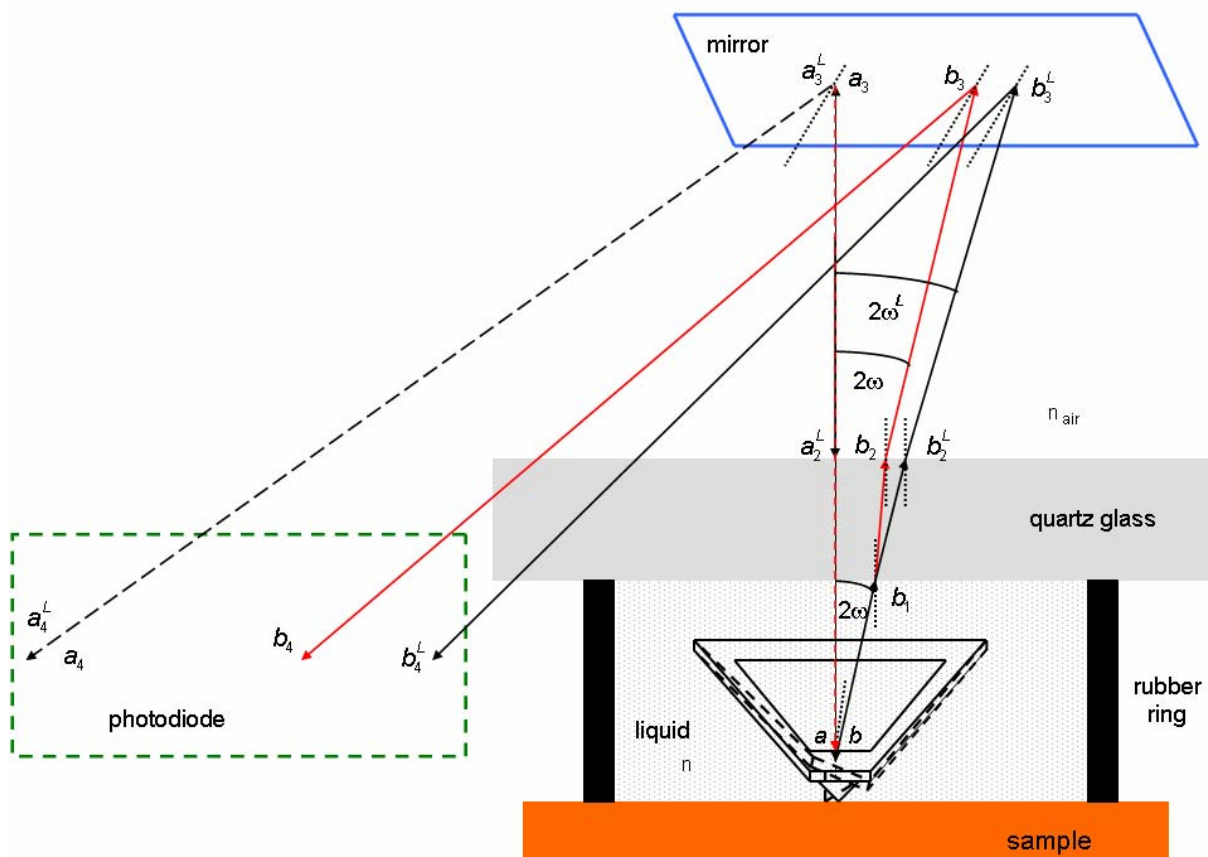


**Figure 7.4** Simplified schematic (not to scale) of a friction-force AFM experiment carried out using a liquid cell: The light paths for cantilever deflection are indicated for media with different refractive indices (lateral torsion signals: black line: light path in liquid; red line: light path in air). The cantilever torsion angle is denoted as  $\omega$ .

The *lateral* photodiode sensitivities  $S_L$  and  $S_L^L$  expressed in nm/V are inversely proportional to the distance between the corresponding laser light reflections on the photodiode in air  $a_4b_4$  and in liquid  $a_4^Lb_4^L$ , which can be described as a function of the cantilever torsion angle  $\omega$  and refracted beam  $\omega^L$ , respectively:

$$a_4b_4 = 2\omega (aa_1+a_1a_2+a_2a_3+a_3a_4) = 2\omega aa_4 \quad (\text{Eq. 7-12})$$

$$a_4^Lb_4^L = 2\omega^L (aa_1+a_1a_2^L+a_2^La_3^L+a_3^La_4^L) = 2\omega^L aa_4^L \quad (\text{Eq. 7-13})$$

where the refracted beam  $\omega^L$  for liquid measurements is described in Equation 7-14:

$$\frac{n_{\text{air}}}{n} = \frac{\sin 2\omega}{\sin 2\omega^L} = \frac{\omega}{\omega^L} \quad (\text{Eq. 7-14})$$

Since the length of the laser light path for both normal and lateral signals is identical, as reported recently<sup>73,76</sup> and as can be seen in Equation 7-4, we can approximate equal lengths of the laser path for measurements in air and in liquid:

$$AA_4 = aa_4 = aa_4^L = bb_4 = bb_4^L. \quad (\text{Eq. 7-15})$$

Consequently, the relative change of lateral photodiode response between liquid and air ( $a_4^Lb_4^L/a_4b_4$ ) is equal to the relative changes of refractive indexes of different media.

$$\frac{a_4^Lb_4^L}{a_4b_4} = \frac{S_L}{S_L^L} = \frac{n}{n_{\text{air}}} \quad (\text{Eq. 7-16})$$

Thus, calibration factors determined in air can be converted to the correct calibration factors  $\alpha^L$  (for liquid) by multiplication with  $n_{\text{air}}/n_{\text{liquid}}$ .

Consequently, if we substitute  $\alpha$  in Equation 7-11 with zero (as is the case for the lateral deflection in the absence of cantilever torsion), we obtain Equation 7-16. The excellent agreement of the measured ratios  $S_N/S_N^L$  and the calculated ones (based on tabulated refractive indices) show that our models correctly relate vertical, and hence also lateral, photodiode responses between air and liquid. Thereby Equation 7-16 enables one to utilize re-scaled friction force calibration factors determined in air<sup>76</sup> for AFM experiments carried out in liquid. In addition, the slight offset of the constant force set point in conventional contact mode height imaging in media with different refractive indices, in case that  $S_N$  has not been calibrated in situ, can be accounted for by a similar rescaling procedure.

The hitherto overlooked effect of laser light refraction for friction force AFM measurements in liquid media and the dependence of the calibration factors on the refractive index of the imaging medium are quantitatively described in a simple model derived in this *chapter*. By multiplication with the factor  $n_{\text{air}}/n_{\text{liquid}}$  one can conveniently re-scale the values of lateral photodiode sensitivity obtained in air  $S_L$  employing, e.g., the improved wedge calibration method using a universal calibration specimen, to obtain the correct value for  $S_L^L$ . Hence a simple, yet precise calibration of lateral forces is now feasible also for AFM in liquids.

### 7.2.2 Nanotribology on PFS films

Topographic and frictional changes on the surface of PFS in 0.1 M NaClO<sub>4</sub> electrolyte were recorded during charge and discharge in an ECLFM experiment. To obtain friction data, the tip was scanned back and forth in the X direction in contact with the sample at a constant load while the lateral deflection of the lever was monitored by the lateral segments of the photodetector. Thus, the calibration factor, which is detector sensitivity to the twist of the cantilever coupled with the torsional force constant of the cantilever, can be correlated with the friction force at the tip sample microcontact. The details of the frictional calibration factor in liquid media have been discussed in section 7.2.1. CV experiments were performed while holding the potential at either negative or positive values, corresponding to the reduced and oxidized forms of the polymer respectively. Figure 7.5a shows a friction image recorded at a constant potential of 0.50 V (vs. Pt) at which the polymer is positively charged and oxidized while at -0.1 V (vs. Pt) is recorded in Figure 7.5b (neutral, reduced form of the polymer).

Ideally, the surface should be as flat as possible for the frictional measurements. Since lateral forces can also be applied to the tip by large vertical variations in topography, it can be difficult to acquire frictional data on rough surfaces. One way to “separate” the topography information from the frictional information is to subtract the trace image from the retrace image, producing an image with two vertical levels. The higher friction area will be displayed as bright, and the lower friction areas as dark. The contrasts of different friction images can be seen more clearly in this case. Quantitatively, friction data was obtained by evaluating the so-called friction force loops, by taking the average friction force between the forward and reverse scan directions. The typical friction loops of oxidized and reduced PFS are presented in Figure 7.5(c-d), respectively.

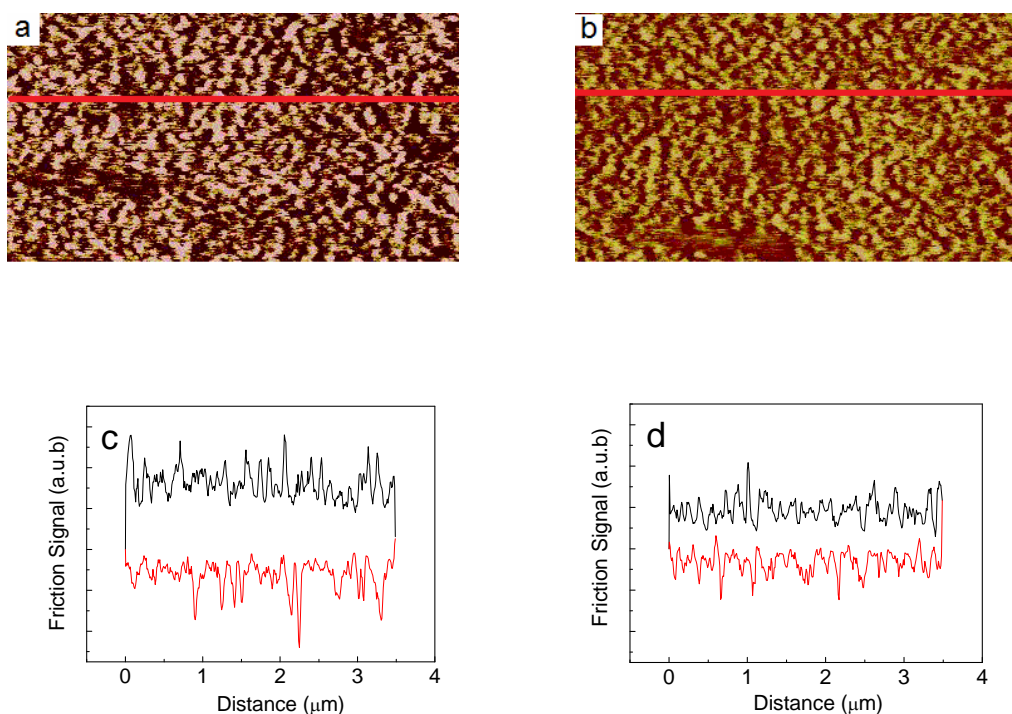


**Figure 7.5** ECLFM images obtained for ES-PFS<sub>100</sub> layers on gold. (scan area is  $3.5 \times 2 \mu\text{m}$ ). a) Friction image (trace-retrace) of oxidized ES-PFS<sub>100</sub> layers. b) Friction image (trace-retrace) of reduced ES-PFS<sub>100</sub> layers. c) Friction loop corresponding to cross-section shown in (a). The black line corresponds to the friction trace signal of ox-PFS<sub>100</sub>. The red line corresponds to friction retrace signal of ox-PFS<sub>100</sub>. d) Friction loop corresponding to cross-section shown in (b). The black line corresponds to friction trace signal of re-PFS<sub>100</sub>. The red line corresponds to friction retrace signal of re-PFS<sub>100</sub>.

The measured friction force as a function of the applied normal force is shown in Figure 7.6. The measurements were performed using a Si<sub>3</sub>N<sub>4</sub> probe tip with a scan velocity of  $2.5 \mu\text{m/s}$ . Before friction measurements were made, force-distance curves were captured and the set point adjusted to control the value of normal force. The upper curve ( $\square$ ) was determined at an electrode potential of  $+0.5\text{V}$  while the lower curve ( $\circ$ ) was determined at an electrode potential of  $-0.1\text{V}$ . A linear increase of the friction force signal with increasing the normal forces was observed for both potentials. The friction coefficient values were determined for both oxidized and reduced PFS surface as the electrode potential was varied. The friction coefficient was determined by assuming a linear relation between the lateral force  $F_L$  and the normal force  $F_N$ .

$$F_L = F_0 + \mu F_N \quad (\text{Eq. 7-17})$$

where  $F_0$  is a constant friction force arising from adhesion between the tip and the sample and  $\mu$  is the normal friction coefficient. The value of  $F_0$  usually correlates, but is not equal, to adhesion forces obtained from approaching-retracting measurements. The value of  $\mu$  was calculated to be 0.47 and 0.30 for oxidized and reduced PFS respectively, giving an increase of  $\mu$  of 57% upon oxidation. These data showed that the surface properties of the oxidized and reduced PFS surface at the tip-sample microcontact has a profound effect on the resulting friction.

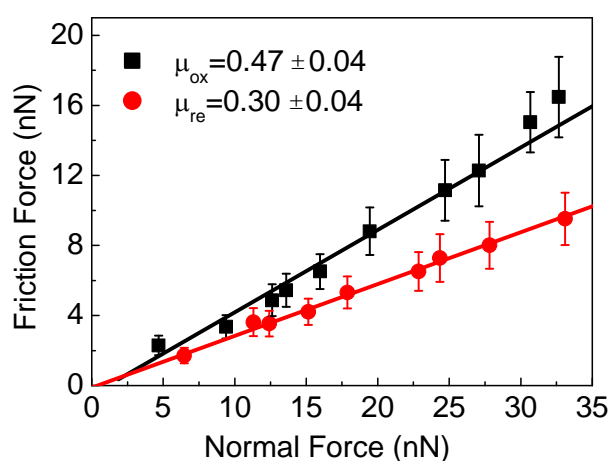


**Figure 7.6** Friction force vs. normal force for ox-re PFS<sub>100</sub>.

Repeated experiments were performed to check the reversibility of friction control. Friction coefficients were measured by a simple switching procedure of the oxidizing and reducing potentials respectively. Figure 7.7 shows the friction coefficient values in four consecutive electrochemical cycles.

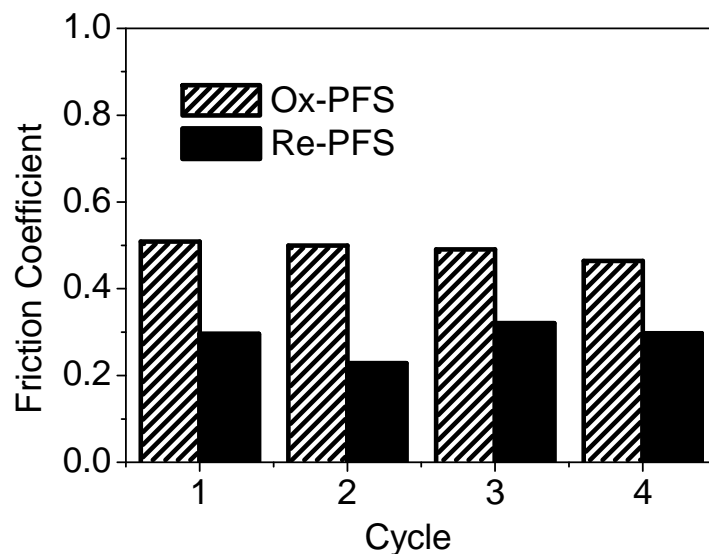


**Figure 7.7** Tribological behavior of stimulus PFS in subsequent electrochemical cycles.

As Figure 7.7 demonstrates the repetitive cycling of the potential between the limits given resulted in a switchable, relatively stable friction coefficients of the PFS monolayer.

Figure 7.8 records the aforementioned four cycles of cyclic voltammetric current-potential ( $i$ - $E$ ) curves for the oxidized and reduced of PFS film. These curves were obtained at scan rate of 50 mV/s and a potential window between  $-0.1$  and  $+0.5$  V.

As earlier stated, applied potentials ( $E_{\text{apply}}$ ) were held at 2 values ( $-0.1$  V and  $0.5$  V) for friction measurements. Due to the presence of the ferrocene units in the polymer main chain, PFS exhibits two reversible redox peaks, which appear at the  $E$  values of  $0.18$  V and  $0.28$  V.<sup>80</sup> It has been proposed that these two oxidation waves result from the stepwise oxidation behavior of polymer where the alternating ferrocene centers along the chain are oxidized, first in alternation and then for all remaining sites as observed in previous studies.<sup>21, 28</sup> The surface coverage of ferrocene sites ( $\Gamma_{\text{Fc}}$ ) for all layers in our study were determined from electrochemistry using Equation 7-18:

$$\Gamma_{\text{Fc}} = \frac{Q_{\text{Fc}}}{nFA} \quad (\text{Eq. 7-18})$$



where  $\Gamma_{Fc}$  is the charge passed for the oxidation/reduction of ferrocene sites,  $n$  is the number of electrons involved in the electron transfer process ( $n = 1$ ),  $F$  is the Faraday constant, and  $A$  is the geometric surface area of the electrode. The charge passed in the redox reaction was determined by integrating the area under the redox peaks. The number of grafted chains per unit area ( $\Gamma$ ) was calculated by dividing  $\Gamma_{Fc}$  by the known value of the degree of polymerization. The calculated surface coverage of PFS100 chains gave the value of  $\Gamma = 0.13$  chains/nm<sup>2</sup>.

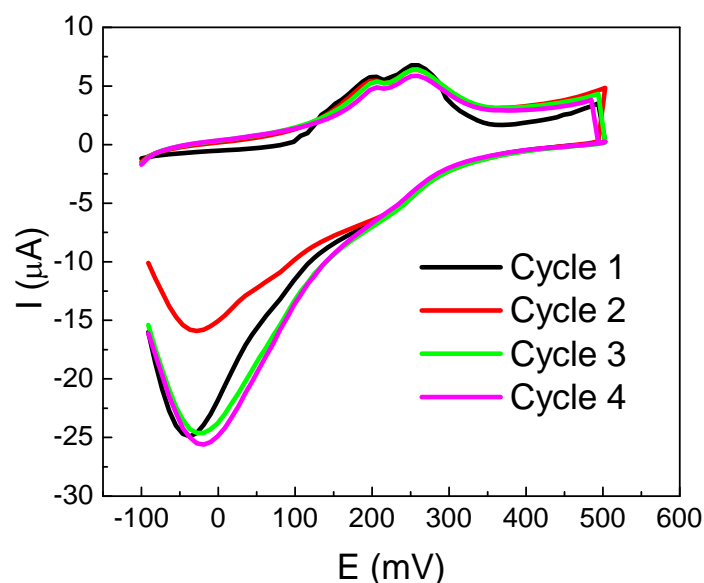


**Figure 7.8** Cyclic voltammograms of end functionalized PFS on gold. All experiments were measured in 0.1 M NaClO<sub>4</sub><sup>-</sup>, hold at 0.5 V and -0.1V for 1 hour between scans, area = 0.36 cm<sup>2</sup>.

### 7.3 Dependence of adherence of stimulus responsive PFS on the electrical potential by electrochemical atomic force microscopy

Several recent studies using surface force apparatus, or atomic force microscopy, have suggested a connection between adhesion and friction resulting from a common energy dissipation mechanism.<sup>81</sup> Therefore, we proposed that the potential-dependent variation in friction observed in Figure 7.5 should be accompanied by similar changes in adherence. Force measurements between PFS film and Si<sub>3</sub>N<sub>4</sub> tip were performed in a 0.1M NaClO<sub>4</sub> aqueous solution with a pH of 6.7. To facilitate data acquisition and improve the accuracy of the measured adhesion force, a force volume image mode available in the NanoScope controller

(III) (Veeco-Digital Instruments, Santa Barbara) was used. The resulting array of force curves was imported into a custom built labview analysis program. Statistical analysis of over 4096 consecutive force curves for each type (plotted as a histogram fitted by a Gaussian distribution) yielded an average adhesion force of 0.031 nN for the reduced polymer films, and 0.61 nN for the oxidized polymer films, respectively. A representative set of force curves are presented in Figure 7.9 (c-d). We conclude that the adherence between tip and PFS film was increased following the conversion of the ferrocenyl group to its ferrocenium form as the electrode potential was held at +0.50 V. Thus, the variation of the magnitude of the pull-off force can be controlled by the electrochemical potential during PFS oxidation in a manner similar to friction control.

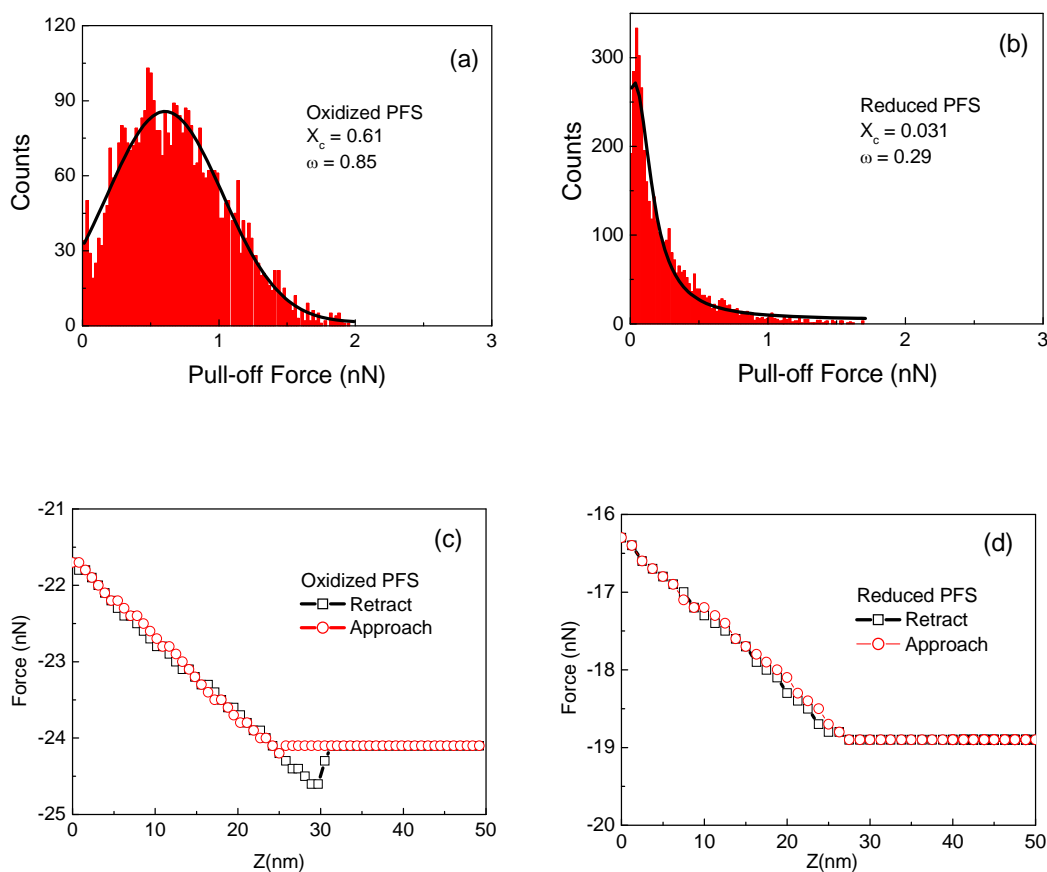


**Figure 7.9** Representative histograms of pull-off force recorded for oxidized and reduced PFS films in  $\text{NaClO}_4$  solutions over an area of  $500 \text{ nm} \times 500 \text{ nm}$  (4096 force curves per histogram). The histograms were fitted using a Gaussian distribution. Electrochemical potential: a) +0.5 V; b) -0.1 V. Representative force curves between the  $\text{Si}_3\text{N}_4$  tip and PFS under potential control are shown in c) +0.5 V; d) -0.1 V. The cantilever used had a normal spring constant,  $k_N$ , of 0.126 nN/nm.

## 7.4 Discussion

Friction force of polymers has been studied by in-situ electrochemical techniques with force microscopy in a few cases.<sup>82-84</sup> Known examples include polypyrrole thin films featuring planar anions (ref.<sup>82</sup>, Chyla, et al.), electro-sensitive poly(2-acrylamide-2-methylpropane sulfonic acid (ref.<sup>83</sup> Song, et al.) and thin film of sulfonate derivatized poly(aniline) (ref.<sup>84</sup> Hillier, et al.). Influence of the electrochemical potential on other interfacial properties such as pull-off force or adhesion force (adherence) has been reported by several authors. An early examination of the force between two metal wires in an electrolyte solution illustrated a potential-dependent repulsive force. Hillier and co-workers<sup>84</sup> measured the force between a silica sphere affixed to a tip and a gold electrode as a function of the applied potential and the electrolyte composition. Green et al.<sup>58</sup> demonstrated the ability to monitor in real-time the electrochemical transformations of a redox active surface species. These authors showed a variation of adherence with electrode potential suggesting that an electrostatic component dominated the adhesion process. Hudson and Abruna<sup>85</sup> concluded that variation of adherence in electrochemical systems can be attributed to differences in solvation energies. According to these authors, the ability to break the microcontact is easier when the surface is more solvent compatible. In our PFS system we also found a clear variation in pull-off force at the two different applied electrode potentials. This variation can be understood by considering the various interactions at the tip substrate interface during contact. In general, the total adhesion force between an AFM tip and a sample surface include van der Waals forces, electrostatic forces, specific chemical interactions, etc. When considering the long range interactions between macroscopic surfaces in liquids, four important forces should be taken into account: solvation, structural, hydration and steric forces. However, the origins of the overall measured surface forces in experiments are often difficult to discern. In our case, the most likely source of the force change observed include electrostatic forces and solvation forces, thus these will be discussed in the subsequent sections.

First, a brief overview of what is known from other techniques on the processes that accompany electron transfer in ferrocenyl groups will be presented to place the results shown in sections 7.2 and 7.3 into context. Contact angle measurements have shown that surfaces of monolayers of 15-(ferrocenylcarbonyl)pentadecanethiol attached to Au substrates are more hydrophilic after ferrocene oxidation, presumably due to the more polar character of the ferrocenium species.<sup>86</sup> CV and electrochemical QCM measurements have firmly established

that the oxidation of surface bound ferrocene is accompanied by a strong association of  $\text{ClO}_4^-$  with the ferrocenium to form a 1:1 ion pair at the monolayer solution interface if  $\text{NaClO}_4$  electrolyte is used. The formation of ferrocenium cations and their association with  $\text{ClO}_4^-$  anions result in changes in the wetting properties of the monolayer.<sup>87</sup> Film structural changes have also been reported. In situ ellipsometry of  $\text{FcC}_{11}\text{S-Au}$  demonstrated that oxidation of the terminal ferrocene moieties results in an increase in the film thickness.<sup>88</sup> Similarly, in the study of Pèter et al., covalently end-grafted PFS layers on gold exhibited morphological and thickness changes depending on the potential applied by ECAFMs.<sup>21</sup>

Generally, the grafting density, the solvation of ferrocenyl unit, electrostatic interactions and excluded volume effects determine the conformation of neutral PFS. The contour length of the  $\text{PFS}_{100}$  polymer chain can be estimated as  $\sim 58$  nm using the assumed mean length of the repeat unit as  $6.3 \text{ \AA}$  multiplied by the degree of polymerization ( $\text{D.P.}=92$ ). The extension distance representing the elastic response of the polymer was  $55$  nm which was estimated by performing single molecular force microscopy to the maximum attainable, stretched from of the chains to the maximum attainable stretched form of the chains.<sup>33, 34, 89</sup> The thickness of  $\text{PFS}_{100}$  film measured by SPRS in  $0.1\text{M NaClO}_4$  electrolyte is  $7$  nm.<sup>21, 31, 32</sup> The calculated surface coverage of  $\text{PFS}_{100}$  chains was  $\Gamma = 0.13 \text{ chains/nm}^2$  obtained from CV experiments. Moreover, neutral PFS films were hydrophobic as shown by water contact angle experiment results ( $\theta_a(\text{PFS}) = 96^\circ$ ).<sup>89</sup> The electrochemical experiments were performed in aqueous  $\text{NaClO}_4$  electrolytes, which is a bad solvent for the neutral polymer chains. It is difficult for the electrolyte molecules and counter-ions to penetrate the hydrophobic film since the polymer chains in the films are packed close to each other. After oxidation, PFS chains will slightly swell and elongate due to electrostatic repulsion forces between the  $\text{Fc}^+$  in the polymer chain. Moderate swelling and water uptake of the film is a result of polarity changes, i.e. the oxidized PFS is more hydrophilic due to the more polar character of the ferrocenium species. Oxidized PFS becomes even soluble in some polar organic solvents.<sup>90</sup>

The presence of ions can result in specific interactions between the ions involved and the charged PFS polymer brush, as recently reported in the literature.<sup>91</sup> The differences in the electrostatic environment introduced by ion-pairing effects were also monitored by changes in frequency and dissipation measurements on a quartz crystal coated with a poly(2(methacryloyloxy)ethyltrimethylammonium chloride) monolayer using a quartz crystal microbalance with dissipation (QCM-D).<sup>91</sup>

Specific interactions of counter ions with macromolecules has already been observed more than 100 years ago, and the phenomenon has been named the Hofmeister effect<sup>92, 93</sup> after its inventor. Irrespective of common use, the underlying principles of the Hofmeister effect are not yet completely understood. The Hofmeister series goes as follows:  $\text{ClO}_4^- > \text{SCN}^- > \text{I}^- > \text{NO}_3^- > \text{Br}^- > \text{Cl}^- > \text{CH}_3\text{COO}^- > \text{HCOO}^- > \text{F}^- > \text{OH}^- > \text{HPO}_4^{2-} > \text{SO}_4^{2-}$ . The anions on the left of chloride in the above series are chaotropic, which exhibit weaker interactions with water than water itself. On the other hand, the ions on the right of chloride are kosmotropic which exhibit strong interactions with water. Anions increase the solubility with decreasing the hydration entropy according to the Hofmeister series ( $\text{ClO}_4^-$   $-57 \text{ J K}^{-1} \text{ mol}^{-1}$  and  $\text{SO}_4^{2-}$   $-200 \text{ J K}^{-1} \text{ mol}^{-1}$ ).<sup>94</sup> Electrolyte solutions correlate well with the hydration entropy of the counter anion giving also the conclusion that the least hydrated counter anion binds strongest to the polyelectrolyte.<sup>95</sup>  $\text{ClO}_4^-$  ions are rarely hydrated, large and highly polarizable species, consequently, they can interact very strongly with the ferrocium group through ion-pairing interactions, promoting differences in the physicochemical properties of the PFS brush.

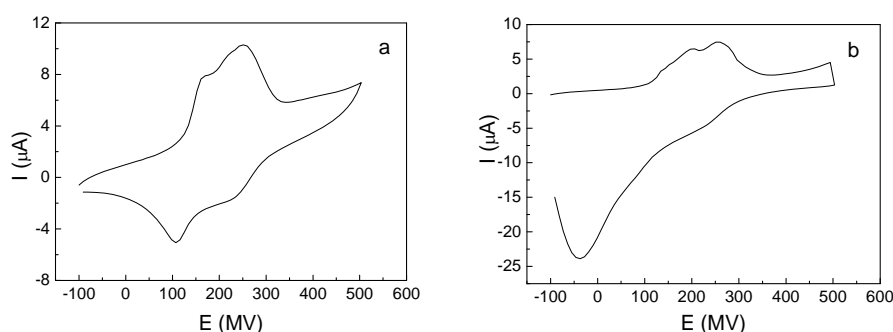
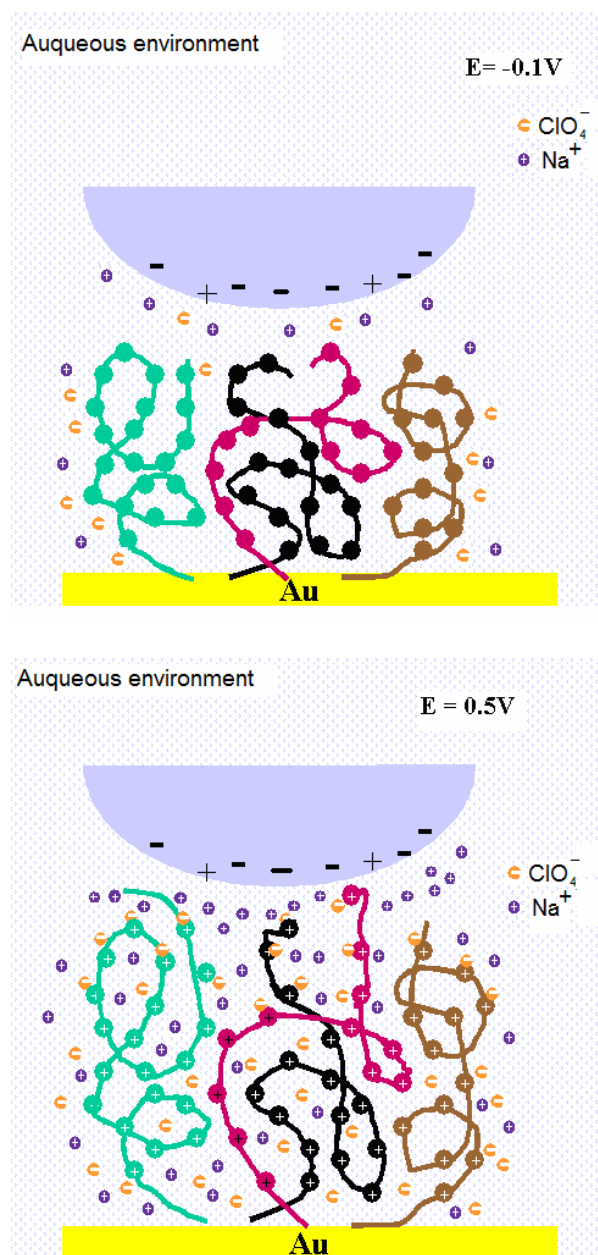


**Figure 7.10** Cyclic voltammograms of end functionalized PFS on gold. All experiments were measured in  $0.1 \text{ M NaClO}_4^-$ . a) Normal scan b) sample held at  $0.5 \text{ V}$  and  $-0.1 \text{ V}$  for 1 hour between scans.

Figure 7.10a shows a typical CV scan of a PFS film. Compared to Figure 7.10b, which was recorded following holding the potential at  $0.5 \text{ V}$  and  $-0.1 \text{ V}$  for 1 hour respectively, a relatively large cathodic current can be observed at the  $0.5 \text{ V}$  following oxidation reflecting a structural change of the grafted polymer layer. The counter ions adsorbed at the positively charged surface maybe the reason for the observed non Faradaic current.

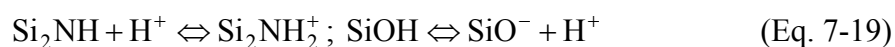
We argue that oxidized PFS bearing cationic groups undergo ion-pairing interactions in the presence of  $\text{ClO}_4^-$  anions. Recently reported electron paramagnetic resonance

spectroscopy experiments showed that tightly bound species like  $\text{ClO}_4^-$  can promote large changes in the collective motion of polyelectrolyte chains. This change is accompanied by conformational transitions of surface confined polymers. Within the traditional picture of charged polymer brushes, the collapse is seen as a result of electrostatic screening of pendant charges by counter ions. However, in the case of the ion paired  $\text{ClO}_4^-$  species the brush experiences not only an electrostatic change, but also a chemical change (hydrophobic to hydrophilic). A schematic illustration of the chain conformation and charge distribution before and after the electrochemical oxidation of PFS layer is shown in scheme 7.1.



**Scheme 7.1** Illustration of interactions between  $\text{Si}_3\text{N}_4$  tip and end immobilized PFS at different potentials.

Bearing this picture in mind, the origin of the friction force and adhesion change after electrochemical change can now be addressed. First, it is clear that the monolayer structure/state is ostensibly different in the oxidized/reduced forms. The  $\text{Si}_3\text{N}_4$  probe is negatively charged, as can be seen from the following argument. The pH of the electrolyte used was 6.7. Raiteri and co-workers<sup>96</sup> determined the isoelectric point (IEP) of  $\text{Si}_3\text{N}_4$  to be at pH 6 ~ 6.5. It has also been established that the charge behavior of the surface of silicon nitride in an aqueous environment is governed by protolytic reactions involving two major types of functional groups: namely silanols which are bearers of acidic properties and secondary amino groups bearing basic properties.



Both the hydrolytic instability of the surface and its affinity to oxidation lead to gradual development of a silica layer covering the surface of silicon nitride. The thickness of this layer may reach several nanometers.<sup>97</sup> For silicon oxide the surface charge is determined by the second reaction. Thus, in our experimental conditions, the  $\text{Si}_3\text{N}_4$  tip at pH = 6.7 is negatively charged. The reason for the surface force change is partly due to electrostatic force resulting from that the positive surface charges of oxidized PFS. Radmacher and coworkers measured local electrostatic interactions between the  $\text{Si}_3\text{N}_4$  tip and positively or negatively charged surfaces.<sup>98</sup> For  $\text{PFS}^+\text{ClO}_4^-$  ion pairs, as suggested by recent theoretical results reported by Winkler et al., ion-pairing effects in polyelectrolytes should be associated with the appearance of dipole moments.<sup>99</sup> An alternative explanation may be that the adhesion results from induced dipolar interactions.

According to the JKR theory of contact mechanics the force required to separate a sphere and a flat surface ( $F_{\text{pull-off}}$ ) is related to the *work of adhesion* ( $W_{\text{adh}}$ ).

$$F_{\text{pull-off}} = -\frac{3}{2}\pi R_{\text{T}}W_{\text{adh}} \quad (\text{Eq. 7-20})$$

The *work of adhesion* can be related to the surface free energies of the various system interfaces.

$$W_{\text{adh}} = r_{13} + r_{23} - r_{12} \quad (\text{Eq. 7-21})$$

The change in adhesion upon the electrochemical transformation of the ferrocenyl groups can be in part attributed to a change in the miscibility of the terminal groups at the corresponding

surfaces. That is, the reduced, more hydrophobic form of the ferrocenyl group is less miscible with aqueous electrolyte than the oxidized, less hydrophobic ferrocenium group. In this case, one can readily assert that the surface tension for the cationic (i.e., oxidized) form of the ferrocenyl group will be greater than that for its neutral (i.e., reduced) form, an assertion supported by an exploration of the potential dependent wetting of a monolayer formed at gold from 15-(ferrocenylcarbonyl)pentadecanethiol. This study found that the advancing contact angle for water decreased from  $71^\circ$  to  $43^\circ$  upon the oxidation of the ferrocenyl group.<sup>86</sup> The above analysis provides an explanation for the change in  $F_{ad}$  that results from the redox conversion of the PFS monolayer from an energetic perspective will be one source for the measured differences in  $W_{adh}$  and, consequently,  $F_{pull-off}$ .

In our case, only a small differences in water contact angles have been observed (on the order of a few degrees and  $<10^\circ$ ). This observation indicates some contribution by solvation effects, however this is likely met the dominating mechanism. While it is known that the work performed during sliding friction of a freshly prepared interface ultimately ends up as heat (via the generation of phonons) and/or surface structural modification (plowing and wear), the details of the correspondences energy dissipation processes, including the energy loss pathways and the rates with which these processes occur, are still not well understood. Identifying these dissipative mechanisms requires kinetic analysis in involving rate and temperature dependent measurements, dynamic mechanical analysis and dielectric spectroscopy.<sup>100</sup> Israelachvili and co-workers find a quantitative relation between friction and adhesion hysteresis.<sup>81</sup> In our experiment, friction and adhesion hysteresis generally change in the same direction as the applied potential changed. For reduced PFS, during adhesional loading and unloading, there is little adhesion hysteresis due to the low pull-off force. For oxidized PFS, as the two surfaces come into contact or slide past each other, is significant increase in adhesive forces across the interface as well as local rearrangements of surface molecular groups, polar-nonpolar group reorientations, etc. This results in an increased adhesion hysteresis. The friction force would be higher for similar reasons. However, at this stage, no quantitative correlation between friction and adherence variations can be made.



## 7.5 Conclusions

In conclusion, we have demonstrated that sulphur end functionalized PFS can be efficiently grafted onto Au surfaces with a grafting density of 0.13 chains/nm<sup>2</sup>. These grafted chains form a robust, stable predominately monomolecular layer, which shows a stimulus responsive behavior under electrochemical control. Using the Au substrate as electrode, the adherence and friction of these films can be reversibly controlled and switched between an oxidized (high adhesion, high friction) and a reduced neutral (low adhesion, low friction) state, respectively. Adherence and friction behavior was studied using an AFM and utilizing nanoscale contacts. The results indicate that the value of *friction force* at the contact formed between an Si<sub>3</sub>O<sub>4</sub> AFM probe tip and the PFS film increases as the ferrocenyl groups are converted by one-electron reactions from their reduced neutral to their oxidized forms. Consistent with the same trend, a comparison of a histogram plot of adhesion (from AFM pull-off force measurements) versus applied potential revealed that changes in adhesion accompanied the changes of friction force. This increase is consistent with an increase in the interfacial surface tension at the nanometer scale contact. Changes in adhesion and friction are primarily attributed to changes of the electrostatic and induced electrostatic interactions between AFM tip and PFS film. A variation of solubility of the PFS film with oxidation vs. reduction also plays a role.

## 7.6 Experimental

**Materials.** Ethylene sulfide end-functionalized PFS was synthesized as described previously.<sup>21, 31, 32</sup> The subscript number of the polymers PFS<sub>100</sub> corresponds to the monomer/initiator ratios. The molar mass data were determined by GPC in THF, referenced to a polystyrene calibration standard. Molecular characteristics of end-functionalized PFS<sub>100</sub> are ( $M_n = 22.6$  kg/mol,  $DP_n = 92$ ,  $M_w/M_n = 1.13$ ).

**Substrates and samples.** (a) Gold substrates (11 × 11 mm<sup>2</sup>, 250 nm Au on 2 nm Cr on borosilicate glass) for ECAFM measurements were purchased from Metallhandel Schroer GmbH (Lienen, Germany). Prior to use, the substrates were cleaned in piranha solution (mixture of 1:4 of 30% H<sub>2</sub>O<sub>2</sub> and 70% concentrated H<sub>2</sub>SO<sub>4</sub>), then rinsed with Milli-Q water and ethanol and dried in a nitrogen stream. *Caution! Piranha solution is a very strong oxidant, which reacts violently with organic materials and therefore should be handled with the utmost*

*care!* The samples were prepared by immersing gold substrate into  $8 \times 10^{-6}$  M PFS toluene solution overnight to ensure the maximum coverage. The samples were cleaned by placing them in toluene (20 mL) and dichloromethane (20 mL) for 10 min, respectively, followed by drying in a stream of nitrogen. The PFS solutions were deaerated with Argon gas and sealed with Teflon film to prevent oxidation. All the glassware were cleaned with Piranha solution and subsequently rinsed with large amount of Milli Q water.

***In-situ electrochemical lateral force microscopy.*** A NanoScope IVa scanning probe microscopy (Veeco-Digital Instruments (DI), Santa Barbara, CA) was used in combination with an Autolab PGSTAT10 potentiostat (Ecochemie, Utrecht, The Netherlands). The electrochemical measurements were carried out using a three-electrode arrangement. The sample functioned as a single working electrode. A platinum coil served as a counter electrode. Another platinum wire acted as a reference electrode; all voltages are given with respect to this reference electrode. The supporting electrolyte was 0.1 M  $\text{NaClO}_4$  (aq). Cyclic voltammograms were recorded between (-0.1V vs Pt) and (+0.5V vs. Pt) with a scan rate of 100 mV/s. Prior to the experiments, the electrolyte was deaerated by passing nitrogen gas through the solution for 5 min. An external potential of +0.5 V was maintained during friction measurements to ensure the complete oxidation of PFS molecules. Nanotribology experiments were performed by in situ AFM in liquid environment fitted with a DI liquid cell (volume  $\sim 50 \mu\text{L}$ ). Commercially available V-shaped  $\text{Si}_3\text{N}_4$  cantilevers (DI) were used. Each cantilever was calibrated after a given experiment by measuring the thermal excitation of the tip to compute its spring constant.<sup>101, 102</sup> Adhesion force curves were collected at a ramp size of 500 nm and scan rate of 1 Hz. Overall, time required to mount the sample, fill the electrochemical cell with electrolytic solution, and allow for instrumental thermal equilibration were typically a few hours.

## References

- [1] Gupta, P.; Vermani, K.; Garg, S., *Drug Discov. Today* **2002**, *7*, 569.
- [2] Yoshida, R.; Sakai, K.; Okano, T.; Sakurai, Y., *Adv. Drug Deliver Rev.* **1993**, *11*, 85.
- [3] Ista, L. K.; Lopez, G. P., *J. Ind. Microbiol. Biot.* **1998**, *20*, 121.
- [4] Yamato, M.; Konno, C.; Utsumi, M.; Kikuchi, A.; Okano, T., *Biomaterials* **2002**, *23*, 561.
- [5] Cunliffe, D.; Alarcon, C. D.; Peters, V.; Smith, J. R.; Alexander, C., *Langmuir* **2003**, *19*, 2888.
- [6] Bohanon, T.; Elender, G.; Knoll, W.; Koberle, P.; Lee, J. S.; Offenhausser, A.; Ringsdorf, H.; Sackmann, E.; Simon, J.; Tovar, G.; Winnik, F. M., *J. Biomat. Sci.-Polym. E.* **1996**, *8*, 39.
- [7] Urry, D. W., *Biopolymers*, **1998**, *47*, 167.
- [8] Hoffmann, J.; Plotner, M.; Kuckling, D.; Fischer, W. J., *Sensor Actuat. A-Phys.* **1999**, *77*, 139.
- [9] Barker, S. L. R.; Ross, D.; Tarlov, M. J.; Gaitan, M.; Locascio, L. E., *Anal. Chem.*, **2000**, *72*, 5925.
- [10] Chen, J. P.; Yang, H. J.; Hoffman, A. S., *Biomaterials* **1990**, *11*, 625.
- [11] Stayton, P. S.; Shimoboji, T.; Long, C.; Chilkoti, A.; Chen, G. H.; Harris, J. M.; Hoffman, A. S., *Nature* **1995**, *378*, 472.
- [12] Yerushalmi, R.; Scherz, A.; van der Boom, M. E.; Kraatz, H. B., *J. Mater. Chem.* **2005**, *15*, 4480.
- [13] Kawaguchi, H.; Fujimoto, K.; Mizuhara, Y., *Colloid Polym. Sci.* **1992**, *270*, 53.
- [14] Snowden, M. J.; Chowdhry, B. Z.; Vincent, B.; Morris, G. E., *J. Chem. Soc. Faraday T.* **1996**, *92*, 5013.
- [15] Robinson, L.; Isaksson, J.; Robinson, N. D.; Berggren, M., *Surf. Sci.* **2006**, *600*, L148.
- [16] Matthews, J. R.; Tuncel, D.; Jacobs, R. M. J.; Bain, C. D.; Anderson, H. L., *J. Am. Chem. Soc.* **2003**, *125*, 6428.
- [17] Ionov, L.; Minko, S.; Stamm, M.; Gohy, J. F.; Jerome, R.; Scholl, A., *J. Am. Chem. Soc.* **2003**, *125*, 8302.
- [18] Natansohn, A.; Rochon, P.; Gosselin, J.; Xie, S., *Macromolecules* **1992**, *25*, 2268.
- [19] Bunker, B. C.; Kim, B. I.; Houston, J. E.; Rosario, R.; Garcia, A. A.; Hayes, M.; Gust, D.; Picraux, S. T., *Nano Lett.* **2003**, *3*, 1732.
- [20] Natansohn, A.; Rochon, P.; Ho, M. S.; Barrett, C., *Macromolecules* **1995**, *28*, 4179.
- [21] Peter, M.; Hempenius, M. A.; Kooij, E. S.; Jenkins, T. A.; Roser, S. J.; Knoll, W.; Vancso, G. J., *Langmuir* **2004**, 891.
- [22] Maksymiuk, K., *Electroanal.* **1996**, *8*, 661.
- [23] Gittins, D. I.; Bethell, D.; Schiffrin, D. J.; Nichols, R. J., *Nature* **2000**, *408*, 67.
- [24] Miller, C.; Gratzel, M., *J. Phys. Chem.* **1991**, *95*, 5225.
- [25] Inzelt, G.; Baetskai, J., *J. Electroanal. Chem.* **1991**, *308*, 255.
- [26] Jiang, J. H.; Kucernak, A., *Electrochim. Acta.* **2000**, *45*, 2227.
- [27] Petersen, R.; Foucher, D. A.; Tang, B. Z.; Lough, A.; Raju, N. P.; Greedan, J. E.; Manners, I., *Chem. Mater.* **1995**, *7*, 2045.
- [28] Rulkens, R.; Lough, A. J.; Manners, I.; Lovelace, S. R.; Grant, C.; Geiger, W. E., *J. Am. Chem. Soc.* **1996**, *118*, 12683.
- [29] Foucher, D. A.; Tang, B. Z.; Manners, I., *J. Am. Chem. Soc.* **1992**, *114*, 6246.
- [30] Brandt, P. F.; Rauchfuss, T. B., *J. Am. Chem. Soc.* **1992**, *114*, 1926.
- [31] Peter, M.; Hempenius, M. A.; Lammertink, R. G. H.; Vancso, G. J., *Macromol. Symp.* **2001**, *167*, 285.
- [32] Peter, M.; Lammertink, R. G. H.; Hempenius, M. A.; van Os, M.; Beulen, M. W. J.; Reinhoudt, D. N.; Knoll, W.; Vancso, G. J., *Chem. Commun.* **1999**, *4*, 359.
- [33] Zou, S.; Hempenius, M. A.; Schönherr, H.; Vancso, G. J., *Macromol. Rapid Comm.* **2006**, *27*, 103.
- [34] Zou, S.; Korczagin, I.; Hempenius, M. A.; Schönherr, H.; Vancso, G. J., *Polymer* **2006**, *47*, 2483.
- [35] Bhushan, B.; Israelachvili, J. N.; Landman, U., *Nature* **1995**, *374*, 607.
- [36] Wahl, K. J.; Stepnowski, S. V.; Unertl, W. N., *Tribol. Lett.* **1998**, *5*, 103.
- [37] Bhushan, B., *P. I. Mech. Eng. J-J. Eng.* **1998**, *212*, 1.
- [38] Johnson, K. L., *Langmuir* **1996**, *12*, 4510.

- [39] Bhushan, B.; Sundararajan, S., *Acta Mater.* **1998**, *46*, 3793.
- [40] Sundararajan, S.; Bhushan, B., *Wear* **1999**, *229*, 678.
- [41] Abdelmaksoud, M.; Bender, J. W.; Krim, J., *Tribol. Lett.* **2002**, *13*, 179.
- [42] Xu, S.; Miller, S.; Laibinis, P. E.; Liu, G. Y., *Langmuir* **1999**, *15*, 7244.
- [43] Israelachvili, J. N.; Tabor, D., *Wear* **1973**, *24*, 386.
- [44] Israelachvili, J. N.; McGuiggan, P., M.; Homola, A. M., *Science* **1988**, *240*, 189.
- [45] Binnig, G.; Rohrer, H.; Gerber, C.; Weibel, E., *Phys. Rev. Lett.* **1982**, *49*, 57.
- [46] Binnig, G.; Quate, C. F.; Gerber, C., *Phys. Rev. Lett.* **1986**, *56*, 930.
- [47] Mate, C. M.; McClelland, G. M.; Erlandsson, R.; Chiang, S., *Phys. Rev. Lett.* **1987**, *59*, 1942.
- [48] Widom, A.; Krim, J., *Phys. Rev. B* **1986**, *34*, 1403.
- [49] Krim, J.; Widom, A., *Phys. Rev. B* **1988**, *38*, 12184.
- [50] Frisbie, C. D.; Rozsnyai, L. F.; Noy, A.; Wrighton, M. S.; Lieber, C. M., *Science* **1994**, *265*, 2071.
- [51] Noy, A.; Frisbie, C. D.; Rozsnyai, L. F.; Wrighton, M. S.; Lieber, C. M., *J. Am. Chem. Soc.* **1995**, *117*, 7943.
- [52] Noy, A.; Vezenov, D.; Lieber, C. M., *Annu. Rev. Mater. Sci.* **1997**, *27*, 381.
- [53] Nap, R.; Gong, P.; Szleifer, I., *J. Polym. Sci. Pol. Phys.* **2006**, *44*, 2638.
- [54] Butt, H. J.; Cappella, B.; Kappl, M., *Surf. Sci. Rep.* **2005**, *59*, 1.
- [55] Meyer, E.; Overney, R.; Brodbeck, D.; Howald, L.; Luthi, R.; Frommer, J.; Guntherodt, H. J., *Phys. Rev. Lett.* **1992**, *69*, 1777.
- [56] O Shea, S. J.; Welland, M. E.; Rayment, T., *Appl. Phys. Lett.* **1992**, *61*, 2240.
- [57] Bhushan, B.; Dandavate, C., *J. Appl. Phys.* **2000**, *87*, 1201.
- [58] Green, J. B. D.; McDermott, M. T.; Porter, M. D., *J. Phys. Chem.* **1996**, *100*, 13342.
- [59] Carpick, R. W.; Salmeron, M., *Chemical Reviews* **1997**, *97*, 1163.
- [60] Schwarz, U. D.; Allers, W.; Gensterblum, G.; Wiesendanger, R., *Physical Review B* **1995**, *52*, 14976.
- [61] Enachescu, M.; van den Oetelaar, R. J. A.; Carpick, R. W.; Ogletree, D. F.; Flipse, C. F. J.; Salmeron, M., *Physical Review Letters* **1998**, *81*, 1877.
- [62] Mate, C. M.; McClelland, G. M.; Erlandsson, R.; Chiang, S., *Physical Review Letters* **1987**, *59*, 1942.
- [63] Liley, M.; Gourdon, D.; Stamou, D.; Meseth, U.; Fischer, T. M.; Lautz, C.; Stahlberg, H.; Vogel, H.; Burnham, N. A.; Duschl, C., *Science* **1998**, *280*, 273.
- [64] Gnecco, E.; Bennewitz, R.; Gyalog, T.; Loppacher, C.; Bammerlin, M.; Meyer, E.; Güntherodt, H. J., *Physical Review Letters* **2000**, *84*, 1172.
- [65] Bhushan, B., *Handbook of Micro/Nano Tribology*. CRC Press: New York, 1999.
- [66] Hurley, C. R.; Leggett, G. J., *Langmuir* **2006**, *22*, 4179.
- [67] Sun, S.; Leggett, G. J., *Nano Lett.* **2004**, *4*, 1381.
- [68] Schonherr, H.; Vancso, G. J., Scanning Probe Microscopies Beyond Imaging: Manipulation of Molecules and Nano-structures. In Samori, P., Ed. Wiley-VCH: Weinheim, 2006; p 275.
- [69] Frisbie, C. D.; Rozsnyai, L. F.; Noy, A.; Wrighton, M. S.; Lieber, C. M., *Science* **1994**, *265*, 2071.
- [70] Zhang, W. M.; Meng, G. A., *Microsystem Technologies-Micro-And Nanosystems-Information Storage And Processing Systems* **2006**, *12*, 283.
- [71] Wang, C. H.; Lee, G. B., *Biosensors & Bioelectronics* **2005**, *21*, 419.
- [72] Zhang, W. M.; Meng, G.; Li, H. G., *Microelectronics Reliability* **2005**, *45*, 1230.
- [73] Liu, E.; Blanpain, B.; Celis, J. P., *Wear* **1996**, *192*, 141.
- [74] Noy, A.; Frisbie, C. D.; Rozsnyai, L. F.; Wrighton, M. S.; Lieber, C. M., *Journal of the American Chemical Society* **1995**, *117*, 7943.
- [75] Schwarz, U. D.; Köster, P.; Wiesendanger, R., *Review of Scientific Instruments* **1996**, *67*, 2560.
- [76] Tocha, E.; Schönherr, H.; Vancso, G. J., *Langmuir* **2006**, *22*, 2340.
- [77] Ogletree, D. F.; Carpick, R. W.; Salmeron, M., *Review of Scientific Instruments* **1996**, *67*, 3298.
- [78] Varenberg, M.; Etsion, I.; Halperin, G., *Review of Scientific Instruments* **2003**, *74*, 3362.
- [79] Lide, D. R., *CRC Handbook of Chemistry and Physics*. 87 ed.; CRC press: Boca Raton, 2006/2007.

- [80] Foucher, D.; Ziembinski, R.; Petersen, R.; Pudelski, J.; Edwards, M.; Ni, Y. Z.; Massey, J.; Jaeger, C. R.; Vancso, G. J.; Manners, I., *Macromolecules* **1994**, *27*, 3992.
- [81] Maeda, N.; Chen, N. H.; Tirrell, M.; Israelachvili, J. N., *Science* **2002**, *297*, 379.
- [82] Chyla, A. T.; Ryley, S.; Walton, D. J.; Liu, X.; Chetwynd, D. G., *Adv. Mater. Opt. Electr.* **1998**, *8*, 87.
- [83] Song, W.; Sun, T.; Song, Y.; Bai, Y.; Liu, F.; Jiang, L., *Talanta* **2005**, *67*, 543.
- [84] Campbell, S. D.; Hillier, A. C., *Langmuir* **1999**, *15*, 891.
- [85] Hudson, J. E.; Abruna, H. D., *J. Am. Chem. Soc* **1996**, *118*, 6303.
- [86] Abbott, N. L.; Whitesides, G. M., *Langmuir* **1994**, *10*, 1493.
- [87] Soudaghuethorst, J. A. M.; Fokkink, L. G. J., *Langmuir* **1994**, *10*, 4380.
- [88] Ohtsuka, T.; Sato, Y.; Uosaki, K., *Langmuir* **1994**, *10*, 3658.
- [89] Zou, S.; Ma, Y. J.; Hempenius, M. A.; Schönherr, H.; Vancso, G. J., *Langmuir* **2004**, *20*, 6278.
- [90] Arsenaault, A.; Fleischhaker, F.; von Freymann, G.; Kitaev, V.; Miguez, H.; Mihi, A.; Tetreault, N.; Vekris, E.; Manners, I.; Aitchison, S.; Perovic, D.; Ozin, G. A.
- [91] Azzaroni, O.; Moya, S.; Farhan, T.; Brown, A. A.; Huck, W. T. S., *Macromolecules* **2005**, *38*, 10192.
- [92] Hofmeister, F., *Arch. Exp. Pathol. Pharmacol.* **1888**, *24*, 247.
- [93] Hofmeister, F., *Arch. Exp. Pathol. Pharmacol.* **1890**, *27*, 395.
- [94] Zhang, Y. J.; Furyk, S.; Bergbreiter, D. E.; Cremer, P. S., *J. Am. Chem. Soc.* **2005**, *127*, 14505.
- [95] Salomaki, M.; Tervasmaki, P.; Areva, S.; Kankare, J., *Langmuir* **2004**, *20*, 3679.
- [96] Raiteri, R.; Margesin, B.; Grattarola, M., *Sensor Actuat. B-Chem.* **1998**, *46*, 126.
- [97] Zhmud, B. V.; Meurk, A.; Bergstrom, L., *Colloids Surf. A* **1999**, *158*, 327.
- [98] Rotsch, C.; Radmacher, M., *Langmuir* **1997**, *13*, 2825.
- [99] Winkler, R. G.; Gold, M.; Reineker, P., *Phys. Rev. Lett.* **1998**, *80*, 3731.
- [100] Perry, S. S.; Tysoe, W. T., *Tribol. Lett.* **2005**, *19*, 151.
- [101] Hutter, J. L.; Bechhoefer, J., *Rev. Sci. Instrum.* **1993**, *64*, 3342.
- [102] Sader, J. E., *J. Appl. Phys.* **1998**, *84*, 64.

## Outlook

This Thesis summarizes our efforts to design and engineer desired surface properties of selected polymers and to characterize them by various experimental techniques from nano- to mesoscale. The results obtained in this work are relevant for a broad spectrum of scientific issues ranging from fundamental to technological applications. Here we would like to present a number of points which may be worthwhile to consider for further research in different polymer systems.

When micro and nanoindentations are produced upon polymeric surfaces, difficulties are caused by the complex viscoelastic–plastic response that is typical of such materials. Polymers have highly strain and strain rate-dependent properties and show substantially different behaviours when the indentations are produced under differing contact conditions. This has been investigated by Loubet et al<sup>1</sup> for certain ceramic systems and subsequently by Briscoe and Sebastian<sup>2</sup> and Ion<sup>3</sup> et al. in the context of organic polymers. In our experiments, we have focused on the loading or approaching part of data analysis. With a firm understanding of rate dependent effects on unloading part data analysis, a more quantitative evaluation of the indentation mechanics should be made in the future. In addition, other surface properties, such as friction and adhesion could be compared by different techniques (eg. AFM and ATD) across the different length scales.

In *chapter 7*, quantitative friction and adhesion measurements between Si<sub>3</sub>N<sub>4</sub> tip and stimuli-responsive PFS interfaces in response to external electrochemical signal were reported. This interface shows that such PFS-based smart polymer may have great potential such as biological actuators, interfacial engineering, nano-motors, and so on.<sup>4-6</sup> However, it is still a big challenge to devise an efficient approach for fabricating smart interfaces that respond to different stimuli simultaneously. In our experiments, changes in adhesion and friction are primarily attribute to the changes of the electrostatic and induced electrostatic interactions between AFM tip and PFS film. Some other external stimuli such as solution pH, ionic strength, and different functionalized AFM tips may also affect this intelligent polymer surface property. Through reversibly modulating different environmental conditions, PFS film surfaces may be a potentially interesting material for multi-functional actuators.

## References

1. Loubet, J. L.; Georges, J. M.; Marchesini, O.; Meille, G., *J. Tribol.* **1984**, 106, 43.
2. Briscoe, B. J.; Sebastian, K. S., *Proc. R. Soc. A* **1996**, 452, 439.
3. Ion, R. H.; Pollock, H. M.; Roques-Carmes, C., *J. Mater. Sci.* **1990**, 25, 1444.
4. Schneider, H. J.; Kato, K.; Strongin, R. M., *Sensors* **2007**, 7, 1578.
5. Zou, S.; Hempenius, M. A.; Schönherr, H.; Vancso, G. J., *Macromol. Rapid Comm.* **2006**, 27, 103.
6. Nath, N.; Hyun, J.; Ma, H.; Chilkoti, A., *Surface Science* **2004**, 570, 98.

## Summary

The aim of the present Thesis is to enhance characterization and surface engineering approaches to test and control physico-chemical changes on modified hydrophobic (LDPE and PDMS) and stimulus-responsive (PFS) polymers across different length scales. [Here LDPE denotes low density polyethylene, PDMS stands for poly(dimethylsiloxane), and PFS for poly(ferrocenyldimethylsilanes)]. Efforts have been made to design and engineer desired surface properties of selected polymers and to characterize the chemical composition, electrokinetic and mechanical properties by various experimental techniques from the nano to the meso scale. Furthermore, a comparison of these techniques has been carried out in order to understand the aforementioned issues.

In *chapter 2* details are provided regarding essential issues for the scientific and technological background necessary to introduce the scope and the state of the art for this Thesis. Recent advances of modern approaches to surface analysis, as well as the state-of-the-art of corresponding instrumentation are reviewed. A high priority has been given to the investigation of adhesion and adherence across the length scales from micro- to nanometer contact areas. The physical principles and theories of polymer adhesion, and the various experimental approaches used in adhesion studies are introduced. Finally, some new developments of adhesion applications in polymer science are reviewed.

Flame-treatment has been developed to modify the surface properties of LDPE in order to yield valuable finished products. The relationship between surface chemistry and morphology of flame-treated LDPE by various characterization techniques across different length scales has been described in *chapter 3*. The surface concentration of hydroxyl, carbonyl and carboxyl groups, as well as surface wettability as a function of the number of flame-treatment passes (which is proportional to the treatment time) was obtained. In addition, surface topography of LDPE (before and after flame-treatment) was examined by atomic force microscopy (AFM). Carboxyl functional groups were specifically identified by fluorescent labeling and the results were compared with time-of-flight secondary ion mass spectrometry (ToF-SIMS) data. The effective surface  $pK_a$  values of carboxylic acid ( $-COOH$ ) were revealed by chemical force titration curves and the effective surface  $pK_a$  values were found to be around 6.



*Chapter 4* demonstrates the effects of the flame-treated LDPE on the *work of adhesion* ( $W$ ) and *energy release rate* ( $G$ ) as assessed by a custom-built adhesion testing device (ATD). ATD measurements were performed between extracted PDMS lenses prior to, and following UV/ozone treatment (PDMS and PDMS<sub>OX</sub>) and LDPE films with different treatment level. *Work of adhesion* and pull-off force were studied as functions of treatment numbers. The dependence of the measured values of the *energy release rate* on the rate of separation, dwelling time (time in contact), flame-treatment effects, were also considered. The difference between the *energy release rate* and the thermodynamic *work of adhesion*, which is defined as the adhesion hysteresis ( $G-W$ ) increased systematically with increasing treatment numbers. The source of adhesion hysteresis observed was attributed to specific bonding of surface functional groups and viscoelastic effect.

UV/ozone irradiation has been adopted for controlling the wettability of PDMS for a wide variety of applications. Studies of the surface chemistry and ionization state of cross-linked PDMS exposed to UV/ozone as a function of treatment time using various complementary and independent experimental techniques are presented in *chapter 5*. It was found that the top 1-2 nm surface layer was dominated by silanol groups ( $-SiOH$ ) for which the concentration increased with increasing treatment dose as unveiled by quantitative studies using ToF-SIMS. The lateral distributions of the silanol groups were analyzed on the nanometer length scale by means of AFM with chemically functionalized tip probes in aqueous buffer solutions at varying pHs. The protolytic properties of oxidized PDMS surfaces in the presence of sodium chloride and phosphate electrolytes were further analyzed by streaming potential measurements as a function of the UV/ozone treatment time. The electrokinetic data were quantitatively interpreted on the basis of a classical double layer model that combined the Gouy-Stern picture and the site dissociation theory. A characteristic  $pK_a$  constant of silanol groups was found to be a function of treatment time. We concluded that this shift was primarily due to the hydrophobic environment, which has a stabilizing effects on the surface ionization. The broadening of the  $pK_a$  range that was also observed with increasing treatment dose was interpreted as a result of a mixed contribution of increasing probability of intermolecular hydrogen bonding and specific ion adsorption.

*Chapter 6* presents the investigation of the dependence of the Young's modulus of UV/ozone treated PDMS across different length scales. AFM has been used to probe PDMS surface mechanical properties at the nanometer length scale. The values of the Young's modulus of each sample was calculated by comparing different continuum contact mechanics

theories (Hertz and JKR) as well as different tip shape models (spherical and hyperboloid). Moreover, a custom-built ATD has been used to study the modulus at the micrometer length scale with PDMS using a  $\text{Si}_3\text{N}_4$  lens. The modulus of PDMS increased with increasing treatment time as unveiled by both AFM and ATD techniques. Moreover, in comparison with PDMS bulk modulus values which were obtained by tensile tests, we showed that the modulus decreased with the increase the characteristic length scales of the different approaches. These surface mechanical properties studies of UV/ozone treated PDMS provide new insights into the contact performance used in surface engineering and tribological applications.

*Chapter 7* describes quantitative friction and adherence (adhesion) measurements between  $\text{Si}_3\text{N}_4$  tips and reversibly oxidized and reduced poly(ferrocenyldimethylsilane) (PFS) layers. Corrections for fluid refraction have been introduced in the calibration protocol of cantilever spring constants to obtain quantitative friction data in aqueous electrolytes. Measurements of interfacial friction as a function of applied load on the nanoscale revealed a significant change in friction between the oxidized and reduced PFS layers. The average friction coefficient (0.47) and adherence (0.61 nN) between oxidized PFS and  $\text{Si}_3\text{N}_4$  tip was found to be larger than that of neutral PFS (0.3, and 0.03 nN, respectively). Issues related to the interpretation of observed friction and adherence changes were discussed. In particular, electrostatic force, conformational changes of polymer chains and ionic interactions in the presence of  $\text{ClO}_4^-$  anions were concerned.

As shown in this Thesis, "surface engineering" can provided polymer surfaces with specific properties to suit wide applications without affecting the bulk properties. In-depth understanding of the chemical and physical properties of polymer surfaces is, however, essential to further improve those in surface modification techniques. New characterization approaches across the length scales from sub millimeter to nanometer can contribute to a significant enhancement of our understanding of surface properties, and optimizing treatment procedure. Specifically, with the advent of nanoscale surface analysis technique, such as AFM, the gap between atomic/molecular scale properties and bulk (ensemble average) performance has been significantly narrowed.



## Samenvatting

Het doel van dit proefschrift is het verbeteren van technieken voor oppervlaktekarakterisatie alsmede technieken voor “surface engineering” welke dienst zullen doen voor het testen en reguleren van fysisch-chemische veranderingen van gemodificeerde hydrofobe polymeren (LDPE en PDMS) als ook op stimuli reagerende polymeren (PFS) over verschillende lengteschalen [Hierbij staat LDPE voor low density polyethyleen, PDMS voor poly(dimethylsiloxaan) en PFS voor polyferrocenyldimethylsilaan]. Tijdens dit onderzoek zijn oppervlakken van de bovengenoemde polymeren ontwikkeld met specifieke oppervlakte-eigenschappen. Deze zijn vervolgens gekarakteriseerd met behulp van verschillende technieken en op verschillende lengteschalen op basis van chemische samenstelling, elektrokinetiek en mechanische eigenschappen. Bovendien zijn de eerdergenoemde technieken en oppervlakte-eigenschappen met elkaar vergeleken.

In *hoofdstuk 2* wordt een gedetailleerd overzicht gegeven van de essentiële wetenschappelijke en technologische achtergrond die noodzakelijk is voor een goed begrip van de onderwerpen die aan bod komen in dit proefschrift. Verder worden de “state of the art”-ontwikkelingen op het gebied van instrumentatie en moderne benaderingen op het gebied van oppervlakte-analyse besproken. In dit proefschrift heeft het onderzoek naar adhesie met contactoppervlakken op de micro- en nanometerschaal hoge prioriteit gekregen. De fysische principes en theorieën van polymeeradhesie en de verscheidene experimentele benaderingen die gebruikt worden voor het bestuderen van adhesiekrachten worden geïntroduceerd. Verder wordt er een overzicht gegeven van nieuwe ontwikkelingen op het gebied van de analyse van adhesiekrachten in de polymeerchemie.

“Flame treatment” – of ook wel vlambehandeling – is een methode waarbij oppervlakte-eigenschappen gemodificeerd kunnen worden met behulp van de vlammen die ontstaan bij de verbranding van een gas. Deze methode is gebruikt om de oppervlakte-eigenschappen van LDPE zodanig te modificeren dat een economisch waardevol product ontstaat. De relatie tussen oppervlaktechemie en morfologie van vlambehandeld LDPE is beschreven in *hoofdstuk 3*. Hierbij worden verschillende karakterisatietechnieken en verschillende lengteschalen vergeleken. In dit hoofdstuk wordt ook de oppervlakteconcentratie van hydroxyl, carbonyl en carboxylgroepen, als ook de

oppervlaktebevochtiging (“wettability”) als functie van het aantal repeterende vlambehandelingsstappen (welke evenredig is met de behandeltijd van het oppervlak) uitgebreid besproken. Bovendien is de topografie van het oppervlak van LDPE voor en na de vlambehandeling onderzocht met behulp van de atomic force microscoop (AFM). Carboxylgroepen zijn geïdentificeerd en bestudeerd via fluorescente labeling en de resultaten zijn vergeleken met “time of flight secondary ion mass spectrometry” (ToF-SIMS) data. De effectieve oppervlakte  $pK_a$  waarden van carbonzuren ( $-\text{COOH}$ ) zijn bepaald met behulp van chemical force titratiecurves en bleken een waarde van ongeveer 6 te hebben.

*Hoofdstuk 4* geeft een overzicht van de effecten van de vlambehandeling op de *adhesie-arbeid* ( $W$ ) en de *energy release rate* ( $G$ ) welke bepaald zijn met behulp van een zelfontwikkeld adhesion testing device (ATD). ATD-metingen zijn uitgevoerd met PDMS lenzen zowel voor als na UV/ozon-behandeling (PDMS en  $\text{PDMS}_{\text{OX}}$ ) en dunne films van LDPE met verschillende behandeltijden. *Adhesie-arbeid* en pull-off krachten als functie van het aantal behandelingen is onderzocht. De afhankelijkheid van de gemeten data van de *energy release rate* als functie van de scheidingsafstand, de contacttijd en de vlambehandelingseffecten is hierbij ook meegenomen. Het verschil tussen de *energy release rate* en de *thermodynamische adhesie-arbeid* ( $G-W$ ; ook wel hysteresis), neemt systematisch toe met het aantal behandelingen. Dit effect valt toe te schrijven aan de specifieke bindingen van functionele oppervlaktegroepen en het visco-elastisch effect.

De bevochtiging (“wettability”) van PDMS kan gecontroleerd worden met behulp van UV/ozon behandeling. Er is onderzoek verricht naar de oppervlaktechemie en ionisatietoestand van gecrosslinked PDMS welke behandeld werd met UV/ozon als functie van de behandeltijd. Hierbij wordt een vergelijk gemaakt van verscheidene complementaire en onafhankelijke experimentele technieken. Een compleet overzicht van dit onderzoek is weergegeven in *hoofdstuk 5*. Uit dit onderzoek is gebleken dat de bovenste 1-2 nm van het oppervlak hoofdzakelijk silanolgroepen bevat ( $-\text{SiOH}$ ), waarvan de concentratie nog eens toeneemt naarmate de dosis UV/ozon toeneemt tijdens de oppervlaktebehandeling (vastgesteld via ToF-SIMS metingen). De laterale distributie van silanolgroepen op de nanometerschaal is geanalyseerd met behulp van AFM door middel van chemisch gefunctionaliseerde AFM tips in waterachtige bufferoplossing bij verschillende pH-waarden. De protolytische eigenschappen van geoxideerde PDMS oppervlakken in aanwezigheid van natriumchloride en fosfaatelektrolyten zijn in meer detail geanalyseerd met behulp van stromingspotentiaalmetingen als functie van de UV/ozon behandeltijd. De elektro-kinetische

data is kwantitatief geanalyseerd op basis van het klassieke dubbellaagmodel als ook het Gouy-Stern dubbellaagmodel en de site-dissociatietheorie. Karakteristieke  $pK_a$ -waarden voor silanolgroepen zijn bepaald als functie van de behandel tijd. De verschuiving in  $pK_a$ -waarden kan primair worden toegewezen aan de hydrofobe omgeving die een stabiliserend effect op de oppervlakte-ionisatie heeft. Een verbreding van het  $pK_a$ -bereik kon worden vastgesteld als functie van de toename in de dosis UV/ozon tijdens de oppervlaktebehandeling. Dit kan geïnterpreteerd worden als het resultaat van een gecombineerde bijdrage van specifieke ion-adsorptie en door een toename van de kans op de vorming van intermoleculaire waterstofbruggen.

*Hoofdstuk 6* beschrijft het onderzoek naar de afhankelijkheid van de Young's modulus van PDMS dat is behandeld met UV/ozon voor verschillende lengteschalen. AFM-metingen zijn gebruikt voor het meten van de mechanische eigenschappen op nanometerschaal. De waarden van de Young's modulus van elk monster zijn berekend door middel van een vergelijking van de mechanische contacttheorieën (Hertz en JKR) als ook verschillende modellen van de tipgeometrie (sferisch en hyperbolisch). Verder is de zelfontwikkelde ATD gebruikt voor de bestudering van de modulus op micrometerschaal, waarbij gebruik gemaakt is van PDMS en een  $Si_3N_4$  lens. Zowel met behulp van de AFM als de ATD kan vastgesteld worden dat de modulus van PDMS toeneemt met toenemende behandel tijd. Bovendien is de PDMS-bulkmodulusdata (verkregen met trek-rek-experimenten) vergeleken met de PDMS-modulus bepaald via AFM en ATD. Hierbij wordt gedemonstreerd dat de modulus afneemt met een toename in de karakteristieke lengteschaal voor de verschillende benaderingen. Het onderzoek naar de oppervlaktmechanische eigenschappen van PDMS dat behandeld is met UV/ozon geeft nieuwe inzichten in het contactgedrag voor tribologische toepassingen en in "surface engineering".

*Hoofdstuk 7* beschrijft de kwantitatieve frictie- en adhesiemetingen tussen  $Si_3N_4$  tips en reversibel geoxideerde en gereduceerde poly(ferrocenyldimethylsilaan)-lagen (PFS). Correctie voor de brekingsindex van het vloeistofmedium waarin de meting is uitgevoerd is geïntroduceerd in het meetprotocol voor het kalibreren van de veerconstante van de AFM-cantilever, zodat kwantitatieve frictiedata in waterachtige elektrolyten gemeten kan worden. Metingen van de frictie van het raakvlak als functie van de toegepaste kracht op de nanometer-lengteschaal laten een significante verandering van de frictie tussen geoxideerd en gereduceerd PFS zien. De gemiddelde frictiecoëfficiënt (0.47) en adhesie (0.61 nN) tussen geoxideerd PFS en de  $Si_3N_4$  tip blijkt veel groter dan voor neutraal PFS (0.3 en 0.03 nN,

respectievelijk). Verder wordt de interpretatie van de geobserveerde weerstand en adhesieveranderingen behandeld waarbij specifiek aandacht wordt besteed aan de elektrostatische krachten, de conformatieveranderingen van de polymeerketens en de ionische interacties in de aanwezigheid van  $\text{ClO}_4^-$  anionen.

Dit proefschrift toont aan dat met behulp van “surface engineering” polymere oppervlakken met specifieke eigenschappen voor een breed spectrum aan toepassingen gefabriceerd kunnen worden, zonder bulkeigenschappen te modificeren. Een gedetailleerd begrip van chemische en fysische eigenschappen van polymere oppervlakken is echter essentieel voor verdere ontwikkelingen van technieken op het gebied van oppervlaktomodificatie. Nieuwe karakterisatietechnieken met verschillende lengteschalen variërend van de sub-millimeter lengteschaal tot de nanometer-lengteschaal kunnen bijdragen aan een significante verbetering van het begrip van oppervlakte-eigenschappen en kunnen leiden tot geoptimaliseerde protocollen voor de behandeling van deze oppervlakken. Vooral analysetechnieken op de nanometer-lengteschaal – en AFM in het bijzonder – zullen bijdragen aan het overbruggen van de kloof tussen atomaire eigenschappen en het gedrag van bulkmateriaal.

## Acknowledgements

Looking back over last four and half years, I have the feeling that it was one of the most pleasant and intensive periods of my life. This Thesis is the end of my long journey in obtaining my Ph.D degree. However, to come to this end would not have been possible without the help of many people. I want to thank all those who have been generous to me and helped me by any means during these years.

First and foremost, I want to extend deep sense of gratitude to my promoter, Prof. G. Julius Vancso for offering me the opportunity pursuing my Ph.D study in MTP group at University of Twente. I truly appreciate the chances you gave me to develop myself professionally and consequently personally. Your invaluable guidance, scientific support and encouragement helped me in all the time of research for and writing of this Thesis. My sincere thank also goes to Klára for your hospitality and kindness.

I would also like to thank the other members of promotion committee who made the effort to read this Thesis and provide me with valuable comments.

I have great pleasure in expressing my gratitude to Dr Holger Schönherr for your ever-ready helping attitude which was the constant motivating factors for me to complete this Thesis. I want to thank Dr. Mark Hempenius for your help in the lab and all the chemistry related issues. I would like to express my gratitude to Ing. Clemens Padberg for your constant help with computers, SEM measurements, all the equipments.

I would like to thank Geneviève, Cindy, Gerda, Karin and Thelma for your enormous help with all type of paperwork, for your patience. Special thanks to Geneviève for our nice chats and benefit from your art sense. I also thank Zlata for your assistance. Life would be much harder without all your help during the last four years.

Special thanks to Yujie and Qi for accepting to be my paranimfens and for being my good friends. We share together the good and difficult moments.

I would like to thank In Yee, Davide, Janet, Rui, Yujie and Qi for giving corrections to this Thesis. I am grateful to Anika and Mark for their devoted help to translate the summary into Dutch.



In this Thesis, there are numerous people who contribute to the research. I owe my appreciation to the following collaborators who made it possible to perform the various studies reported in this dissertation. In particular, I would like to express my gratitude to Dr. Jerome F. L. Duval for the electrostatic study. I am grateful to Dr. Nikodam Nomczak for the software development of the force volume analysis. I also would like to acknowledge Albert van der Berg and Mark Smithers for the XPS, SEM related work. Dr. Ullrich Gunst deserves my sincere thanks for the ToF-SIMS study and analysis. I owe many thanks to Dr. Henrik Hillborg who contributed with many ideas and work to the UV/ozone treatment of the PDMS.

I would like to thank all past and present MTP members during my stay in Twente University for their patience, understanding and cheering up during busy periods in a alphabetical order: Anika, Attila, Barbi, Beáta, Béla Junior, Chuanliang, Concetta, Cynthia, Denis, Dorota, Douwe-Wiebe, Eugenia, Ewa, Edmondo, Emila, Hong, Henrik, Igor, In Yee, Ivan, Janet, Johannes, Joris, Joost, Lanti, Maria, Marina, Melba, Monique, Nina, Nikodem, Ramon, Oya, Qi, Sandra Sasha, Szczepan, Shan, Shuying, Steffi, Weiqing, Yujie and many many others. I also appreciate all nice moments with members of other groups: PBM, RBT and SMCT.

During these years, many Chinese friends have given me this or that help. Dear Lanti, Hao, Shan, Yuguo, Tian, Xin, Zheng, Xiao, Wei, Zhao Wei, Rui, Hongmei, Zhou Wei, Yang, Bai Wei, Dongsheng, Chen Wei, Wenbin, Xiaohua, Bon-Hua, Alu, Haosen, Hui, Yan, Chunlin, Chao, Rong, and Jiang, I have many great memories of things we did together, beside working. Without you guys, these four years in Enschede would have never been the same.

Finally, I would like to express my deepest gratitude to my parents Song Xiaohua and Wu Yaju for their endless love and constant support who gave me a good education and unlimited support in everything I have done. I would like also to share this moment of happiness with my sister, Song Xin. She gave me enormous support during the whole period of my research.

I hope you enjoyed reading this Thesis and I wish to all of you the best!

*Jing Song*

Enschede, Nov, 2007

## Curriculum Vitae

Jing SONG was born in Tianjin, China. In 1992, she entered chemical engineering department, Tianjin University (Tianjin, China). Four years later, she obtained her Bachelor's degree. In 1997, she joined the research group of Prof. dr. Ming Zhou to pursue her Master Degree in Chemical Engineering Research Center, Tianjin University. With research on the enhancement of mass transfer in adsorptive distillation process, she graduated in 1999. In the same year, she continued her studies at the National University of Singapore in Prof. Hidajat Kus's group on the topic of novel catalytic membrane reactor. She received her M. Eng. Degree in 2001. Thereafter, she joined the Data Research Institute in Singapore, working as a research engineer. In 2003, she started her Ph. D work at University of Twente under the supervision of Prof. Dr. G. J. Vancso. The aim and the results of her project, "New Approaches in the Engineering and Characterization of Macromolecular Interfaces Across the Length Scales: Applications to Hydrophobic and Stimulus Responsive Polymers" are described in this Thesis. Starting from 7<sup>th</sup> July, 2007, she is working in the same group as a postdoctoral researcher.



# Bibliography

## Journal Papers and Conference Proceedings

- **Song, J.;** Vancso, G. J. “Effects of flame treatment on the interfacial energy of polyethylene by contact mechanics” Submitted (2007).
- **Song, J.;** Tranchida, D.; Vancso, G. J. “Contact mechanics of UV/ozone treated PDMS by AFM and ATD techniques: Mechanical performance from nanometer to micrometer length scale” In preparation (2007).
- **Jing Song,** Ewa Tocha, Weiqing Shi, Holger Schönherr, G. Julius Vancso "Smart" organometallic polymer brushes: Switching friction by electrochemical redox stimuli” In preparation (2007).
- **Jing Song,** Ullrich Gunst, Heinrich F. Arlinghaus and G. Julius Vancso “Flame treatment of low-density polyethylene: Surface chemistry across the length scales” *Applied Surface Science*, **253**, 9489 (2007).
- Tocha, E.A.; **Song, J.;** Schönherr, H.; Vancso, G. J. “Calibration of Friction Force Signals in Atomic Force Microscopy in Liquid Media” *Langmuir* **23**, 7078 (2007).
- **Song, J.;** Duval, J. F. L.; Cohen-Stuart, M. A. C.; Hillborg, H.; Gunst, U.; Arlinghaus, H. F.; Vancso, G. J. “Surface Ionization State and Nanoscale Chemical Composition of UV-Irradiated Poly(dimethylsiloxane) Probed by Chemical Force Microscopy, Force Titration, and Electrokinetic Measurements” *Langmuir* **23**, 5430 (2007)
- Xia, Q. H.; **Song, J.;** Kawi, S.; Li, L. L. “Characterization and morphological control of beta zeolite synthesized in a fluoride medium” *Recent Advances In The Science and Technology of Zeolites and Related Materials, PTS A - C Studies in Surface Science and Catalysis* **154**, 195 (2004).
- Xia, Q.H.; Shen, S.C.; **Song, J.;** Kawi, S.; Hidajat, K. “Structure, morphology, and catalytic activity of beta zeolite synthesized in a fluoride medium for asymmetric hydrogenation” *Journal of Catalysis* **219**, 74 (2003).

- **Song, J.** Hidajat, K. “Catalytic membrane reactor for high purity hydrogen for fuel cell applications” *Engineering with membranes*, June 3-6, I-137. (2001)
- Cheng, H.; **Song, J.** Zhou, M. “Application of digital-image correlation method to experimental measurement of fine particle velocity and concentration” *The 9th National Conference on Chemical Engineering-NCCE* (1998).

## List of Abbreviations

AFM	Atomic force microscopy
AR-XPS	Angle resolved X-ray photoelectron spectroscopy
ATD	Adhesion testing device
ATIR	Attenuated total internal reflection
CA	Contact angle
CFM	Chemical force microscopy
CV	Cyclic voltammetry
DLVO	Derjaguin-Landau-Verwey-Overbeek
DMT	Derjaguin-Muller-Toporov
DSC	Differential scanning calorimetry
DSI	Depth sensing indentation
DSIMS	Dynamic secondary ion mass spectroscopy
ECAFM	Electrochemical atomic force microscopy
ECLFM	Electrochemical lateral force microscopy
EDX	Energy dispersive X-ray
EDC	Ethyl-3-(dimethylamino)-propylcarbodiimide
ESCA	Electron spectroscopy for chemical analysis
FECO	Fringes of equal chromatic order
FFM	Friction force microscopy
FM	Fluorescence microscopy
FV	Force volume
IEP	Isoelectric point
iHp	Inner Helmholtz plane
JKR	Johnson-Kendall- Roberts
LDPE	Low density polyethylene
LMWOM	Low molecular weight oxidized materials
LSR	Least square regression
MEMS	Micro-electro-mechanical system
NHS	N-hydroxysuccinimide
oHp	Outer Helmholtz plane
PDMS	Poly(dimethylsiloxane)
PDMS <sub>ox</sub>	Oxidized poly(dimethylsiloxane)
PFS	Poly(ferrocenyl dimethylsilane)
QCM	Quartz crystal microbalance
QCM-D	Quartz crystal microbalance with dissipation
RH	Relative humidity
SEM	Scanning electron microscopy
SFA	Surface force apparatus
SIMS	Secondary ion mass spectroscopy
SSIMS	Static secondary ion mass spectroscopy
STM	Scanning tunnelling microscopy
ToF-SIMS	Time-of-flight secondary ion mass spectrometry
WLF	Williams-Landel-Ferry
XPS	X-ray photoelectron spectroscopy